A Search for Neutrinos from Gravitational Collapse with the MACRO Experiment

Thesis by

Kate Scholberg

In Partial Fulfillment of the Requirements

for the Degree of

Doctor of Philosophy

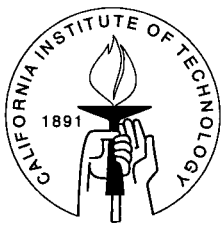

California Institute of Technology

Pasadena, California

1997

(Submitted September 30, 1996)

Acknowledgements

First, I would like to thank my advisors. Charlie Peck has been a wonderful teacher and a kind and patient advisor always willing to share his inexhaustible supply of physics knowledge. Barry Barish has provided guidance and support; many times he has pointed me in the right direction. I have learned a great deal from both of them and I appreciate very much their time and advice.

I would like especially to thank the members of the Pisa group, Carlo Bemporad, Alessandro Baldini, Fabrizio Cei, Roberto Pazzi, Marco Grassi, Gianrossano Giannini and Donato Nicolò, for their hospitality during my trips to Pisa and for sharing their time and expertise.

My fellow students and MACRO collaborators have helped in many ways with this thesis. I cannot possibly list them all (and I am certainly forgetting some here). I can point in particular to Alec Habig (for collaboration on the monitor), Francesco Ronga and Sandro Marini (for monitor support), Alessandra di Credico (for making tapes), and Mike Kelsey (for many PAW and LaTeX tricks). Thanks to Chuck Bower for Figure 6.9, to Chris Walter for Figure 5.11, to Fabrizio Cei for many of the PHRASE-related figures, and to Ashutosh Sanzgiri and Alec Habig for a number of other figures. In addition, I am grateful to Rich Baker, Ed Diehl, Alec Habig, John Hong, Erik Katsavounides, Ed Kearns, Dan Levin, Rongzhi Liu, Nat Longley, Doug Michael, Stuart Mufson, Jim Musser, Bob Nolty, Greg Tarlé, and Chris Walter for valuable discussions and input. Bob Nolty and Stuart Mufson provided comments on parts of this thesis, and Jim Panetta gave comments on the whole thing. Thanks also to the "beepersitters": Alec Habig, Erik Katsavounides, Stu Mufson, Doug "I left it in the car" Michael, and Chris Walter.

I'm grateful to friends both in California and Italy (especially Skelly) who have made my life in grad school enjoyable, and to my mother Ann and brother Tom in Canada. And finally, thanks to Chris for love, support and food preparation.

Abstract

A Search for Neutrinos from Gravitational Collapse with the MACRO Experiment

Thesis by Kate Scholberg

Thesis Advisor: Dr. Charles W. Peck

The MACRO experiment, an underground scintillator/streamer tube array at the Gran Sasso Laboratory in Italy, is capable of detecting a burst of neutrinos from a stellar gravitational collapse using its 560 tons of liquid scintillator. The detector is sensitive to a collapse event in or nearby our galaxy. Two redundant circuits trigger on GC neutrino-like events. This thesis will describe a search for a gravitational collapse burst with MACRO over a time period starting July 24, 1995 and ending February 8, 1996, using both trigger systems. No candidate bursts were observed over this time.

Since neutrinos emerge from a collapsing star promptly after core collapse whereas electromagnetic radiation can follow hours or days later, the MACRO detector can provide an early warning to optical astronomers that a supernova event may appear. MACRO's redundant online supernova watch systems will also be described.

Contents

List of Figures

List of Tables

Chapter 1 Introduction

1.1 Gravitational Collapse Neutrinos

The famous supernova SN1987A brought the field of gravitational collapse neutrino astrophysics to life. The supernova seen on February 24, 1987 was produced by a gravitational collapse (GC) event in the Large Magellanic Cloud (LMC) outside our galaxy, 50 kpc away. SN1987A was a tremendously exciting event for optical astronomers and brought much new knowledge about the life and death of stars. In addition, SN1987A was the first gravitational collapse event in modern times to occur close enough to Earth to have its neutrino signal detected. Several neutrino detectors were operational at the time: two water Čerenkov detectors, Kamiokande II and IMB, detected 20 events between them [1, 2, 3]. In addition, the Baksan scintillator detector saw 5 events [4].[1] The SN1987A neutrino data, although sparse, was sufficient to confirm the baseline model of gravitational collapse and put some limits on neutrino properties, such as neutrino mass, as well. We await a more copious neutrino signal from a closer GC event in our galaxy to be able to make distinctions between different theoretical models of core collapse and supernova explosions, and to be able to extract more information about neutrino properties.

When a massive star at the end of its life collapses to a neutron star, it radiates almost all of its binding energy in the form of neutrinos, most of which have energies in the range 5–30 MeV. These neutrinos come in all flavors, and are emitted over a timescale of several tens of seconds. The energy emitted in the form of neutrinos by a gravitational collapse-driven supernova is typically $\sim$100 times the sum of the kinetic energy of the debris and the energy emitted in photons. Neutrino detectors with active masses in the $\sim$1 kton range are capable of detecting a burst of neutrinos

[1] Another scintillator detector, the Mont Blanc detector, saw 5 events several hours early [5], but the significance of this signal is controversial.

from a gravitational collapse event in or nearby our galaxy.

Neutrinos interact via the weak interaction only, whereas photons interact electromagnetically; neutrinos are extremely hard to detect, and photons are not. Despite the fact that a stellar collapse produces neutrinos much more copiously than photons, the observable neutrino signal is far more sparse. One might be tempted to ask why it is interesting to look for a neutrino signal from a supernova when it is much easier to observe electromagnetic radiation. There are several answers to this question. The penetrating nature of neutrinos which makes them so difficult to detect also allows them to transmit information which is inaccessible from photon observations. For instance, the core of a collapsing star is much more transparent to neutrinos than to photons, so the inner processes of gravitational collapse can be probed by looking at the neutrino signals. Optical observations can only probe the outer layers of a collapsing star. The combination of neutrino and optical observations of a stellar collapse yields a deeper understanding of the physical processes.

Furthermore, by looking for neutrino signals it is possible to look for gravitational collapse events in regions of the sky which are obscured by dust. In addition, there may be no optical supernova displays at all for some core collapses: some collapsing stars may never produce electromagnetic fireworks. In fact, the rate of gravitational collapse may exceed the rate of visible supernovae by some fairly significant factor.

Another benefit of looking for a neutrino signal is that neutrinos emerge from the star *promptly* after core collapse: the neutrino signal is expected to precede the visible signal by several hours, due to the time required for the shock wave to make its way out of the collapsed star's envelope. This means that a prompt detection of a neutrino can be used as an early warning of the appearance of a supernova event, giving astronomers a better chance to observe the early turn-on of the supernova.

Finally, a GC event provides a neutrino source for studies of the properties of neutrinos themselves.

Estimates of the frequency of GC occurrence in our galaxy have large uncertainties and vary quite widely, ranging from 1 per 10 years to 1 per 250 years. However, estimates from several methods give answers of $\sim$1 per 30 years, so it is not unreasonable

to hope for a GC event in our galaxy during the next ten years.

1.2 Detecting GC Neutrinos with MACRO

A number of detectors of different types (scintillator, water Čerenkov, radiochemical) capable of detecting GC neutrinos are in operation or under construction around the world. One such detector is the MACRO detector, a large area underground scintillator/streamer tube array located in Italy at the Gran Sasso National Laboratory. MACRO's primary physics goal is the detection of magnetic monopoles; however MACRO's 560 tons of liquid allow good sensitivity to gravitational collapse in our galaxy.

A burst of neutrinos from a GC at 10 kpc (near the center of the galaxy) is expected to induce a total of approximately 180 events above 7 MeV in MACRO's scintillator within a few tens of seconds. The sensitivity of MACRO to a burst of GC neutrinos is determined by the rate of background events which produces "fake" bursts from Poissonian fluctuations. The background rate in MACRO is mainly due to cosmic ray muons and natural radioactivity from the surrounding rock and concrete. The background rate decreases rapidly with increasing energy threshold, such that the rate in the GC neutrino signal energy regime of interest ($\sim$ 50 mHz with energy greater than 10 MeV) is much lower than the expected signal rate. A burst of neutrinos from beyond the opposite edge of our galaxy should stand out well above background in the MACRO data; however the LMC is out of MACRO's sensitive range.

In MACRO, two independent triggers provide sensitivity to GC neutrino events. In both cases, trigger decisions are made based on energy deposition in a scintillator counter. Both the PHRASE (Pulse Height Recorder and Synchronous Encoder), built by MACRO collaborators from the University of Pisa specifically for GC neutrino detection, and the ERP (Energy Reconstruction Processor), built at the University of Michigan, provide approximately a 7 MeV energy threshold.

Since the neutrino signal from a core collapse can arrive hours or days earlier than the optical signal, a prompt neutrino burst alarm signal can alert both astronomers

and other neutrino observatories. Unfortunately, no directional information may be extracted from MACRO's signal alone; however, information from several detectors may be able to provide pointing.

For MACRO, special "spy" software looks at data coming in from the acquisition and does a preliminary analysis and searches for bursts of neutrino-like events over short ($\sim$10 s) timescales. If a sufficiently low probability burst of hits is found, an alarm message is generated, and relayed to an "on-call" physicist via a wireless communications system. There are two redundant GC monitor systems: one which looks at the Phrase data (with alarm messages sent within Italy) and one which looks at the ERP (with alarm messages sent to the U.S.).

1.3 Outline of the Thesis

This thesis will discuss neutrinos from gravitational collapse and their detection, focusing on detection of GC neutrinos in liquid scintillator and MACRO's capabilities. Chapter 2 will cover the physics of gravitational collapse and neutrino emission and Chapter 3 will discuss the nature of the expected neutrino signal in more detail and the various detection techniques. The knowledge obtained from the SN1987A will be covered in these two chapters. Chapter 4 gives a general description of the MACRO detector. Chapter 5 describes calibration and event reconstruction procedures for MACRO's two GC trigger systems; further details about the GC electronics are given in Appendix C. Chapter 6 gives information about the expected neutrino signal in MACRO, MACRO's specific capabilities, and the general procedure for searching for bursts of neutrinos. Chapter 7 discusses the burst search data analysis performed, and specific issues involved in combining information from the two redundant trigger systems. Results of the burst search are also presented in this chapter. Finally, Chapter 8 describes MACRO's redundant online GC burst alarm systems.

Appendix H is a glossary of terms, acronyms and symbols used frequently in the thesis.

Some parts of this thesis report in detail on the work of people besides the author

who have contributed both directly and indirectly to gravitational collapse studies with MACRO. Such material is included here for clarity and completeness, where it is relevant to the topic under discussion. In particular, the sections focusing on the PHRASE in large part represent the work of the members of the Pisa group (with the exception of the sections referring specifically to combined ERP/PHRASE analysis, for which the work was done by the author). The ERP circuit was built by members of the University of Michigan group, and the ERP standard calibrations were developed and performed primarily by the Indiana group. The parts of this thesis describing work not done by the author are noted as such and wherever possible contain references to the appropriate MACRO internal memos.

Chapter 2 Supernovae and Gravitational Collapse

A supernova is defined as a highly energetic outburst resulting in the complete disruption of a star. A gravitational collapse is defined as the inward collapse of the core of a massive star which has exhausted its nuclear fuel. A gravitational collapse event is expected to produce copious amounts of neutrinos, and it is with this type of event that this thesis is concerned. Gravitational collapse and supernova events may often be associated with one another; however, not all gravitational collapse events necessarily result in supernovae, and not all supernovae result from gravitational collapse events.

2.1 Classification of Supernovae

Supernovae are classified by astronomers into two main types, Type I and Type II, according to their optically observed properties. Supernova types are distinguished on the basis of their electromagnetic spectra and their "light curves", i.e. their luminosities as a function of time. Reference [6] gives a recent review of the classification of supernovae. Type I supernovae are further subclassified into Types Ia and Ib, and Type II supernovae into Types II-L and II-P. The standard astronomical classification scheme is purely phenomenological, so the classes do not necessarily correspond exactly to physical processes.

2.1.1 Type I Supernovae

The primary classifying feature of a Type I supernova is the absence of hydrogen lines in its spectrum at maximum light output. The light curves of Type I supernovae tend to show features which are quite uniform from event to event. After maximum light, the luminosity declines steeply for a period of about 30 days, after which the shape changes to a fairly clean exponential with a time constant of about 70 days. Figure 2.1

shows a typical Type I supernova light curve. The spectra of Type I supernovae tend to change in a characteristic way over time as well. Typically, the spectrum fits a blackbody distribution well at early times with a few characteristic superimposed absorption and emission lines, whereas at late times the spectrum is less dominated by the blackbody continuum and exhibits a rich emission line structure.

Type I supernovae occur in both elliptical and spiral galaxies with approximately equal frequency. They are thought to arise from relatively old, low mass stars, known as Population II stars. Type I supernovae are not often accompanied by compact remnants, such as pulsars.

The standard model for a Type I supernova is a white dwarf star which has lost its hydrogen envelope and which is accreting matter from a companion star. When a critical mass is reached, a thermonuclear explosion is ignited, which is seen as a supernova explosion. The lack of hydrogen lines is explained by assuming that the star's initial hydrogen envelope was blown off long before the explosion. Negligible neutrino emission is expected for supernovae which arise from this type of physical process.

2.1.2 Type II Supernovae

Type II supernovae are identified by the presence of hydrogen lines in their spectra at maximum light. Type II supernovae have light curves and spectra which show much more variation from supernova to supernova than do the light curves and spectra of Type I supernovae. The light curves of Type II supernovae are broader than those of Type I supernovae: the maxima tend to be less bright than the Type I maxima by some magnitudes[1], but the tails of the light curves tend to extend out for a longer period of time. Also, typical expansion velocities of material expelled in the explosion (as measured by the Doppler shifting of spectral lines) are smaller for Type II than for Type I supernovae.

Type II supernovae tend to occur almost exclusively in the arms of spiral galaxies.

[1]Magnitude referred to here is the absolute magnitude given by $M = -2.5log_{10}L + K$, where L is the luminosity and K is a constant.

Spiral arms contain stars which are more likely to be massive, hot and bright, and also generally young, since a large stellar mass implies a short lifetime; these stars are known as Population I stars. Type II supernovae are also occasionally associated with compact remnants, observed as pulsars.

Figure 2.1 shows a "typical" Type II supernova light curve.

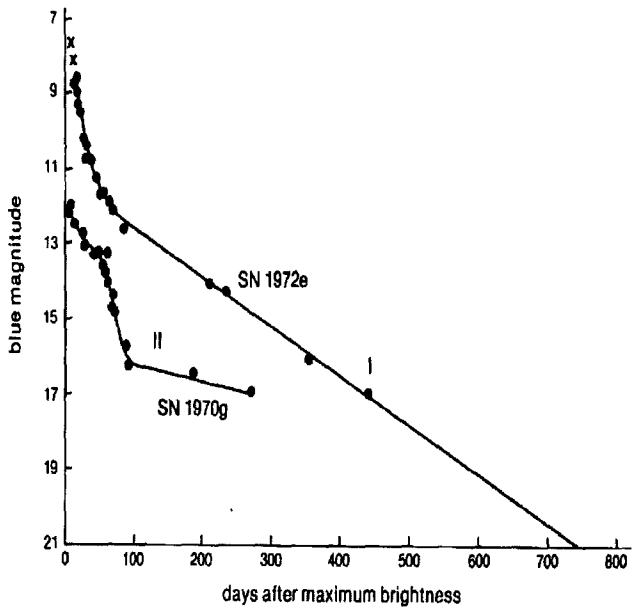

Figure 2.1: Light curves for typical Type I (upper) and Type II (lower) supernovae. From Bowers and Deeming.

The standard model for a Type II supernova is a massive star which has reached the end of its evolution such that the pressure from fusion reactions in its core can no longer support the weight of the outer layers. The star collapses inwards, and when the density of the core reaches approximately nuclear density the collapse "bounces" and a shock wave propagates outward. The interaction of this shock wave with the outer material may power part of the explosion seen in photons. Neutrinos streaming from the core most likely deposit enough energy in the outer material to contribute more significantly to the explosion. After bounce, the core continues to collapse until a neutron star, or possibly a black hole, is formed.

In this model, the explosion energy is expected to be only a small fraction of

10^{53} ergs, the total binding energy of the resulting neutron star. The remainder of the binding energy— approximately 99% of it— is carried away by neutrinos.

Gravitational collapse models and neutrino emission will be discussed extensively in Section 2.2 and Chapter 3.

It is interesting to note that the explosion energies seen in the form of photons and kinetic energy for both main types of supernovae are of the same order of magnitude, about 10^{51} ergs, even though the energy sources are quite different for Types I and II. This approximate equivalence of explosion energy from the two types of supernovae is coincidental: for Type I supernovae the energy source (thermonuclear explosion) is relatively weak but produces photons which interact strongly with the surrounding matter (via the electromagnetic interaction), whereas for Type II supernovae the energy source (the gravitational binding energy of a neutron star) is strong but produces mostly neutrinos which interact only weakly with the surrounding matter.

2.1.3 Subclassifications

Type I and II supernovae, as distinguished by the presence or absence of hydrogen lines, can be further subclassified according to features of their spectra and light curves. Figure 2.2 summarizes the standard phenomenological supernova classification scheme.

Recent research shows that the members of some of the subclasses may not correspond exactly to the generic physical interpretations of Type I and Type II supernovae given above.

Some supernovae classified as Type I due to the absence of hydrogen lines at maximum light do not have other characteristic Type I features in their spectra. Type I supernovae which have strong silicon lines in their maximum light spectra are designated as Type Ia, whereas those without silicon are designated as Type Ib or Ic, according to whether or not they have helium lines in their spectra.

There is some possibility that the physical mechanism behind Type Ib and Ic supernovae is a gravitational collapse event. For these types of events, the supermassive

star may have blown off its hydrogen envelope before core collapse, which accounts for the lack of observable hydrogen lines.

Type II supernovae are subclassified according to their light curves. Those for which the light curve flattens out are designated as Type II-P (plateau), whereas those for which the light curve falls more rapidly are designated as Type II-L (linear). Type II-L and II-P supernovae also have different characteristic spectra at maximum light. Recent work suggests that Type II-L supernovae may have underlying mechanisms which are similar to those of Type Ia supernovae [6].

Some supernovae defy classification according the standard scheme. These may represent progenitors with atypical compositions, mass distributions and solar winds.

In fact, the phenomenological classification probably has more to do with the radius, elemental abundances, envelope mass and stellar winds of the progenitor star than the explosion mechanism. The fact that GC events tend to result in Type II supernovae simply reflects the fact that stars which are candidates for gravitational collapse are massive and are more likely to have followed evolutionary paths resulting in compositions and envelopes that produce Type II light curves and spectra when 10^{51} ergs of energy are dumped into them. By the same token, white dwarf stars which are candidates for thermonuclear explosion events are likely to possess compositions and envelopes which will result in Type I observed supernovae.

2.2 The Physics of Gravitational Collapse

This section will describe a standard model for the processes which are believed to occur during a gravitational collapse, which may result in a visible Type II, Ib or Ic supernova (or no supernova at all). Various models exist for the process of gravitational collapse, differing in some specific details; however, they have many common features. These general features will be described here, and main differences between competing models will be pointed out where appropriate. References [7], [8], and [9] give reviews of the subject.

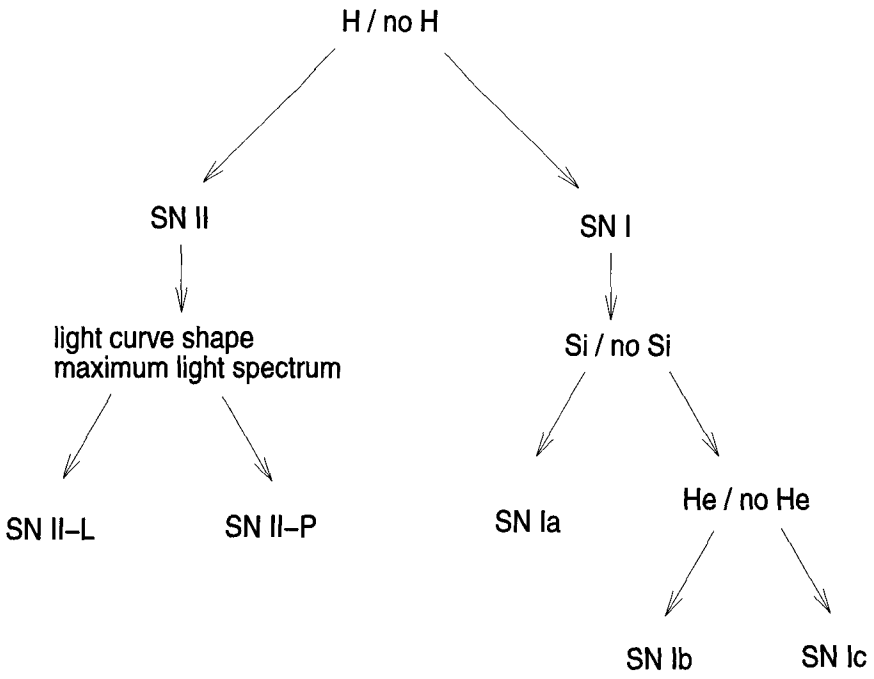

Figure 2.2: Phenomenological supernova classification scheme, based on observations at maximum light. After Harkness and Wheeler.

2.2.1 Standard Stellar Evolution

In principle, the evolutionary path of a star can be predicted knowing only the star's mass and chemical composition; in practice, poorly understood effects such as convection and internal mixing of stellar matter decrease the power of the predictions of the standard theory. Nevertheless, many of the general features of stellar evolution are quite well understood, and predictions of the theory match many aspects of observed distributions of stars very well.

At the beginning of its life, a star condenses from a cloud of protostellar matter, consisting mainly of hydrogen and helium with some small admixture of heavier elements. As the cloud contracts, it heats up. When the temperature exceeds the requirement for initiating nuclear fusion (at $\sim 10^7$ K), hydrogen burning ignites. The thermal pressure from the nuclear burning reactions provides a balancing force counteracting the inward gravitational attraction, resulting in a state of hydrostatic equilibrium.

Eventually, the supply of hydrogen in a star decreases, and the pressure gener-

ated by its burning can no longer support the overlying mass of material. When this happens, the stellar core starts to contract. If the star is massive enough, the gravitational binding energy released by the contraction will increase the star's core temperature enough to start fusion reactions involving the helium products of the initial hydrogen burning reaction, which halts further contraction. A helium burning stage of the star's life then begins. At this point the star consists of a helium core surrounded by an outer hydrogen envelope, with fusion reactions mostly occurring on the interface between the hydrogen and helium regions.

When the helium supply diminishes so as to be unable to fuel the support of the overlying mass, the same thing happens again: the star contracts, heats up, and a subsequent burning reaction involving the fusion of higher Z atoms ignites. This process is repeated, with the fusion of increasingly heavy elements igniting at every step, until the star is made of concentric shells of successive products of nuclear burning, with the heaviest elements in the center and hydrogen in outer envelope. This is the famous "onion-skin" structure shown in Figure 2.3.

Note that for each successive burning stage to be initiated, the energy provided by gravitational contraction must be sufficient to ignite the next fusion reaction; if the star is not massive enough, the star will simply contract until electron degeneracy pressure stops the collapse and will start cooling down. (In fact, very low mass "stars" will not even ignite hydrogen fusion after their initial contraction). The star then becomes a "burned out" white dwarf, with further contraction halted only by the degeneracy pressure of its electrons. Only stars of initial mass greater than $\sim 6M_{\odot}$ are able to continue the contraction and ignition cycle to its final stages.

Each burning stage takes less time than the one preceding it. For massive stars (greater than $10M_{\odot}$), hydrogen burning lasts for several million years; however, the last few stages last only a few years or months. The final burning stage of a pre-supernova star lasts only about a day.

2.2.2 The Pre-Supernova Star

If the star is massive enough, in the final stage of its life it is burning heavy elements like oxygen and silicon and producing ^{56}Fe. ^{56}Fe is the most strongly bound of all elements, so adding more nucleons in further fusion reactions involving this isotope will only result in the absorption, rather than the production, of energy. Therefore ^{56}Fe does not burn, but accumulates in the core of the star. The standard picture of the star at this point involves a relatively tiny core of iron at the center, surrounded by shells of successively lighter elements. For example, first there will be shells of silicon, then neon and oxygen, carbon, helium and finally an outer shell of unburned hydrogen.

During the final day of a massive star's life, a thin shell of silicon being converted to iron surrounds the innermost core, slowly adding iron to the core's inert mass. For masses greater than the Chandrasekhar mass limit M_{Ch}, the degeneracy pressure of the electrons in the core can no longer support the pressure of its own mass. The Chandrasekhar mass limit is given by

$$M_{Ch} = 5.8 Y_e^2 M_\odot, \tag{2.1}$$

where Y_e is the fraction of electrons per nucleon ($Y_e = Z/A$, Z is the average charge, A is the average atomic number) and $M_\odot$ is one solar mass. For an iron-nickel core, $M_{Ch} \sim 1.2 M_\odot$. When the inert core exceeds this mass, the core will start to compress under its own gravity.

2.2.3 Core Collapse

Under normal stellar evolution circumstances, an increase in temperature from the gravitational binding energy would increase the pressure and slow the contraction. However, in the final stage of evolution, counterintuitively the pressure does *not* increase as gravitational energy is dumped into the core. This is due to two effects: first, *photodisintegration* reactions occur, e.g.

$$\gamma + {}^{56}\mathrm{Fe} \rightarrow 13\,{}^{4}\mathrm{He} + 4\mathrm{n} \tag{2.2}$$

and

$$\gamma + {}^{4}\mathrm{He} \rightarrow \text{nucleons.} \tag{2.3}$$

Although this reaction increases the number of particles present which would tend to increase the pressure in the core, it is an endothermic reaction which requires energy, so the average kinetic energy of the particles decreases. Overall, the pressure decreases.

The other effect contributing to the destabilization of the core collapse is *electron capture.* As core densities rise, so do rates of the reaction

$$e^{-} + p \rightarrow n + \nu_e. \tag{2.4}$$

Electron capture is also referred to as *neutronization.* Because in the initial stages of the collapse, the neutrino mean free path is much greater than the size of the star, the electron neutrinos escape, so this reaction decreases the number of particles in the core and so tends to decrease the pressure. According to more recent models, electron capture tends to dominate over photodisintegration as the primary mechanism which accelerates the collapse.

The electron neutrinos produced by reaction 2.4 will represent less than one percent of the total number of neutrinos eventually emitted by the supernova.

2.2.4 Neutrino Trapping

The core collapse continues until sufficiently high densities are reached that not even neutrinos can escape. The density at which this occurs is approximately $\rho \sim 4 \times 10^{11}$ g/cm^3, which is the density at which the mean free path for neutral current ν_e scattering becomes less than the size of the core. At this point, all energy becomes trapped in the core, within a radius of approximately 30 km. The spherical shell at this radius, separating the inner region which is opaque to neutrinos and the

outer region which is transparent to neutrinos, is known as the *neutrinosphere*. The neutrinosphere radius r_ν is defined more precisely as the radius at which the density of matter is such that the distance between that radius and infinity is one neutrino interaction mean free path. For $r < r_\nu$ a neutrino is trapped, whereas for $r > r_\nu$ a neutrino is free to propagate outward.

After neutrino trapping occurs, collapse continues and the core density continues to increase.

2.2.5 Bounce and Generation of the Shock Wave

When, finally, the density of matter in the core reaches the density of nuclear matter, at around $\rho \sim 2.7 \times 10^{14}$ g/cm^3, the nuclear equation of state becomes "stiff": the matter cannot compress any further under its own gravity due to nucleonic degeneracy pressure. When this happens, a "bounce" occurs: after the core has been squeezed down as much as possible, a shock wave starts inside the core and begins propagating outward and interacting with the outer layers of matter, which are still falling inward towards the core. The shock wave is a discontinuity in pressure, density and temperature, and its effect is to compress and heat the matter it passes through. The shock starts at a radius of approximately 10 km, and moves outward with a velocity of about 70 km/ms.

2.2.6 Neutrino Breakout

About a millisecond after bounce, the shock hits the neutrinosphere. After this has happened, the neutrinos formed in the wake of the high-temperature shock wave (from both electron capture and cooling reactions) are free to stream outward. This is called "neutrino break-out", or sometimes "neutrino flash" or "neutronization burst" (since ν_e neutrinos from neutronization reactions predominate).[2]

[2]Note that it is primarily neutrinos formed *by* the shock wave that break out at this point; before the shock hits the neutrinosphere, any neutrinos formed by its energy deposition are still trapped, whereas after the shock hits the neutrinospheres, neutrinos created are free, giving the appearance of a "breakout".

Immediately following breakout, other flavors of neutrinos also start to stream out of the core, as cooling reactions begin to produce them (see Section 2.2.8). The timescale for emission of break-out neutrinos is less than a second.

2.2.7 Explosion

The next stage of a gravitational collapse event is known as the "explosion". This is the process by which the star's material gets disrupted, and it is the source of the photons which eventually get seen as a supernova. The explosion is the least well understood part of the supernova process and is currently a topic of interest and development in theoretical astrophysics. If the infalling outer core matter does not get blown away from the core within several hundred milliseconds of bounce, then the matter is doomed to continue falling inward and to accrete onto the core. The electromagnetic fireworks of a supernova explosion may then simply fizzle out, and in many models the explosion fails to happen at all.

Two general types of explosion mechanisms are described in the literature. For a "prompt" or "direct" type explosion, the shock wave itself deposits enough energy in the star's envelope to create a supernova explosion. However, according to most models, by itself the shock wave generated by core bounce is not sufficient to propel the star's outlying matter to escape velocities. The shock wave must move through regions with high densities of heavy nuclei, and photodissociation reactions can sap its energy. Also, the phenomenon called "neutrino damping" can come into play: $\nu_e\bar{\nu}_e$ production from neutrino-cooling type reactions (Section 2.2.8) occurring after the shock hits the neutrinosphere can remove enough energy to significantly weaken the shock [8]. For most simulations of shock-driven explosions, unless the shock is very strong or model parameters are tuned unrealistically, the explosions die at a radius of several hundred kilometers.

The other type of explosion mechanism is known as a "delayed" mechanism. One relatively recent idea for a delayed mechanism has been quite successful at producing supernova models that explode: these models are known as "neutrino heating"

models. In these models, neutrinos diffusing out of the core after breakout manage to transfer enough of their momentum to the envelope to reheat it and revive the shock wave, via scattering from electrons and nuclei [10].

Thermonuclear reactions ignited by the passage of the shock wave may also lead to the disruption of outlying matter. Inert or weakly burning shells of nuclear fuel may ignite or dramatically increase their energy production following a temperature increase brought on by interaction with the shock.

Some models use fluid dynamics effects such as convection to explain how energy could be released into the envelope to power the explosion. Other models include such things as magnetic effects and asymmetrical explosions (e.g. [11]). Many complicated phenomena which may be important for explosion are poorly understood at this time, and it is likely that unknown effects come into play.

2.2.8 Cooling

After the explosion, the "cooling" stage takes place over a timescale of tens of seconds. Most of the collapse event's neutrinos are emitted during this stage. The star sheds its binding energy during this stage, almost completely in the form of neutrinos of approximately 15 MeV each.

Neutrinos of all flavors are emitted during cooling, as $\nu\bar{\nu}$ pairs. The reactions which produce the cooling neutrinos are both neutral current (for all flavors) and charged current (for $\nu_e\bar{\nu}_e$). A few such reactions are shown below:

- Pair annihilation:

$$e^+ + e^- \rightarrow \nu + \bar{\nu} \tag{2.5}$$

- Plasmon decay:

$$plasma\ excitation \rightarrow \nu + \bar{\nu} \tag{2.6}$$

- Photoannihilation:

$$e^- + \gamma \rightarrow e^- + \nu + \bar{\nu} \tag{2.7}$$

- Bremsstrahlung:

$$e^- + (Z, A) \rightarrow (Z, A) + e^- + \nu + \bar{\nu}. \tag{2.8}$$

After the neutrino cooling stage, according to the standard gravitational collapse model, the core is a young, hot neutron star. If enough mass accretes to the proto-neutron star that the nucleon degeneracy pressure cannot support the gravitational pressure (such as possibly for the case when explosion fails to occur and outlying matter continues to fall inward), then further collapse to a black hole will occur. If this happens, the neutrino flux will terminate abruptly.

2.2.9 Aftermath

After explosion, the shock wave continues to move outward into the envelope. Various kinds of electromagnetic radiation result from the interaction of the shock with the outlying matter. The intensities and spectra of the light coming from observed supernovae as a function of time are studied intensively by optical astronomers.

The first signal visible to optical astronomers emerges from the star's envelope some hours after the neutrino burst has occurred. The exact timescale depends on the nature of the envelope.

A summary of some relevant parameters for the different processes occurring during gravitational collapse is shown in Table 2.1.

2.3 Expected Frequency of Gravitational Collapse

An important concern for those studying gravitational collapse events is the frequency with which observable gravitational collapse events are expected to occur. There are several approaches towards making estimates of the frequency of gravitational collapse, and the results from these different approaches vary quite widely.

Stage	Time scale	Core density (g/cm^3)	ν production
Presupernova	-1 day	10^9	none
Core infall	0 s	10^9 to 4×10^{11}	some ν_e
Neutrino trapping	few ms	4×10^{11} to 2.7×10^{14}	negligible
Bounce	10 ms	2.7×10^{14} (oscillates)	negligible
Neutrino breakout	100 ms	2.7×10^{14}	$mostly \nu_e$
Explosion	600 ms	2.7×10^{14}	all flavors
Cooling	600 ms - 50 s	2.7×10^{14}	all flavors
Visible supernova	several hours	2.7×10^{14} (or black hole)	none

Table 2.1: Relevant parameters for gravitational collapse processes. Times are given with respect to the time of the start of core collapse.

2.3.1 Visible Supernovae in History

One approach to determining the frequency of gravitational collapse involves examining the supernovae which have been seen by astronomers in the past, and estimating a rate of gravitational collapse in our galaxy based on these observations.

Table 2.2 shows a list of the supernovae occurring in our galaxy which have been recorded over the past two thousand years. (The list includes one recent remnant, CasA, for which no supernova was observed). All of these events were observed in the relatively small region of the galaxy accessible for viewing by historical astronomers. By assuming that the rate of supernovae in the whole galaxy is the same as that in the historically observable region, one can obtain estimates for the expected rate of supernovae in the galaxy from 1/30 yr to 1/60 yr [12].

Unfortunately, the sample of observed events is very small, and our knowledge of these events is very sketchy due to the fact that all of them occurred before astronomical techniques were very advanced. The best data were recorded by Tycho Brahe and Johannes Kepler, and were sufficient to determine that the last two observed supernovae in this list were almost certainly of Type I; however not enough information is available in the historical record to determine the classification of the others (although the presence of a pulsar remnant associated with the 1054 supernova location suggests a Type II or Ib supernova). Therefore it is difficult to estimate relative rates

Date	Probable Type	Observed By	Remnant, if known
185	unknown	Chinese	possible radio,optical
393	unknown	Chinese	possible radio
1006	unknown	Chinese,Japanese,Koreans,Arabs	radio,Lupus Loop
1054	unknown	Chinese,Japanese	Crab nebula,pulsar
1184	Type I	Chinese,Japanese	radio
1572	Type I	Tycho Brahe,Chinese,Koreans	radio,optical,x-ray
1604	Type I	Kepler,Chinese,Koreans	radio,optical
1660	Type Ib	remnant only observed	CasA

Table 2.2: Known recent supernovae in our galaxy. Compiled from Clark and Stephenson.

of Type I and Type II supernovae by this method.

2.3.2 Supernovae in Other Galaxies

Other galaxies are routinely scanned for supernova events, and some tens of supernovae are discovered every year in the visible universe. It is possible to obtain an estimate of the supernova rates in our own galaxy from the measured rates in other galaxies.

Various assumptions are required in order to make this estimate. First, it is necessary to make large corrections for obscuration effects and the angle of inclination of galaxies with respect to our solar system, so assumptions about amounts of obscuration and distributions of inclination angles must be made. Next, the estimate depends on the value of the Hubble constant, since one must know the distances of galaxies in order to determine their sizes. Finally, the rates of different types of supernovae depend significantly on galaxy type. Therefore, in order to use the measured extragalactic rates to determine a rate for our own galaxy it is necessary to know the type and size of our own galaxy.

Reference [13] gives a recent estimate based on extragalactic supernova frequencies of 1/50 yr, for an assumed Hubble constant 50 km s^{-1} Mpc^{-1}, and assumed luminosity 2.3×10^{10} $L_{\odot}$ and type Sbc for our own galaxy. About 85% of these supernova events are expected to be due to gravitational collapse and should give rise to bursts of

neutrinos.

Tammann et al. [13] also give a combined estimate using both extragalactic and galactic observations of 1/40 yr.

2.3.3 Supernova Remnants

Radio and Gamma Ray Emitters

Another approach to the estimation of frequency of gravitational collapse involves scanning our galaxy for supernova remnants. After a supernova event, the expanding shell of blown-out matter interacts with the interstellar medium, producing radio emission and possibly other types of electromagnetic radiation. On the basis of counts of these remnant objects and knowledge of the ages of galaxies, one can make an estimate of the frequency of supernova events. Fairly large uncertainties come into these types of estimates due to the fact that the characteristics of supernova remnants depend strongly on the detailed composition of the interstellar medium surrounding the supernova. For instance, radio-emitting supernova remnants are much more likely to be found near the galactic plane where the density of matter is greater, which implies that supernovae occurring in the spiral arms of galaxies are unlikely to be represented among the radio remnant population.

Leahy and Wu [14] give a recent estimate of galactic SN rate based on radio supernova remnant surveys of 1 per $f \times (18-42)$ yr, where f is some factor less than unity but of the order of unity.

Pulsars

A special kind of supernova remnant which is thought to be associated only with gravitational collapse is a pulsar. Pulsars are strong sources of highly periodic radio signals, and are thought to be rotating magnetic neutron stars. Certainly some young pulsars have been found to be associated with supernova remnants (e.g. the Crab pulsar), lending credence to the idea that pulsars are compact remnants from core collapse events. However, although the only known way for a pulsar to be formed is

via gravitational collapse, it is probably not true that all gravitational collapse events necessarily result in the creation of a pulsar. No pulsar has been found in SN1987A's remnant, suggesting that some fraction of gravitational collapse events do not result in pulsars. Therefore the rate of pulsar formation may represent a lower limit on the gravitational collapse rate.

Several hundred pulsars have been discovered in the galaxy. Using data from pulsar surveys and taking into account the ages of the pulsars from their measured rotation periods (the period of a pulsar's radio signal increases with time as the pulsar "spins down" after the formation of a neutron star), one can estimate the rate of formation of pulsars in the galaxy. Narayan and Ostriker [15] and Lorimer et al. [16] give recent estimates for the pulsar formation rate of 1 per 100 yr, and 1 per $124 - 250$ yr respectively. However, Wakatsuki [17] gives an estimate of 1 per $4.4 - 14$ yr, so clearly large uncertainties are involved in these estimates.

2.3.4 Heavy Element Abundances

By assuming that all heavy elements in the universe were manufactured by stellar evolution and dispersed by supernova explosions, one can estimate the average frequency with which gravitational collapse would have to have occurred over the history of the universe on the basis of estimates of the composition and age of the universe. According to Tammann et al. [13], who use the estimates of iron abundance in the universe found in Arnett et al. [18] the average rate of supernova occurrence (85% of which are core collapse events) in our galaxy is approximately 1 per 16 yr.

Of course, it is possible that the rate of supernovae has not remained constant throughout the lifetime of the universe, so that the time-average rate provided by estimates based on heavy element abundances is not equal to the current supernova rate. In fact, it is thought that the rate of dispersal of iron by supernovae in the past was greater than it is now, making the above estimate an upper limit on current supernova rates.

2.3.5 Stellar Evolution Rates

Rates of stellar evolution are fairly well understood. Based on knowledge of the distribution of star masses and types in the galaxy, one can find the rate with which massive stars are expected to reach the ends of their lifetimes. Bahcall and Piran [19] estimate a gravitational collapse rate of 1/11 yr by this method, while Ratnatunga and van den Bergh [20] estimate 1/45 yr. The main uncertainties in these calculations involve the distribution of star masses in the galaxy, which is imperfectly known.

2.3.6 Neutrinos

The Baksan detector (see Section 3.2.3) is an underground neutrino detector which has observed no bursts of neutrino events consistent with a gravitational collapse over a period of 5.5 years. This experiment's search puts a limit on the rate of gravitational collapse in the galaxy of 1/2.4 yr at the 90% confidence level.

Furthermore, other neutrino detectors (see Chapter 3) have been operational over the last ten years. Tammann et al. [13] quote a combined limit for the Kamiokande, Baksan, Mont Blanc and IMB experiments of 1 event per 12 years at the 1σ level. This number represents a negative search for a total combined time interval of more than 10 years.

Table 2.3 gives various examples of estimates of the mean interval between supernovae in the galaxy. The column labeled 'GC only' refers to estimates of gravitational collapse events; the column labeled 'All supernovae' refers to estimates of supernovae of all types.

Estimate	Mean interval (yr)		Reference
	GC only	All supernovae	
Observed galactic events		30-60	Clark and Stephenson [12]
Extragalactic events	37-74	32-63	Tammann et al. [13]
Radio remnants		$\leq$ 18-42	Leahy and Wu [14]
Gamma ray remnants		16-25	Hartmann et al. [21]
Pulsars	100		Narayan and Ostriker [15]
	125-250		Lorimer et al. [16]
	4-14		Wakatsuki [17]
Iron abundance	> 19	> 16	Arnett et al. [18], Tammann [13]
Stellar death rates	45		Ratnatunga and van den Bergh [20]
Neutrinos	> 12		Tammann [13]

Table 2.3: Some estimates of the mean interval between supernovae in the galaxy by various methods.

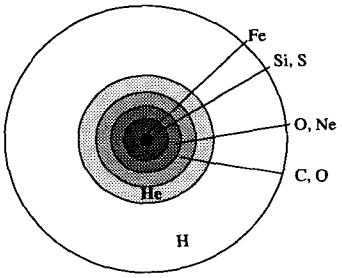

PRE-SUPERNOVA

The 'onion-skin' picture of a star near the end of its life. (The radii of successive layers are not shown to scale here).
The central core radius is 5000-6000 km.

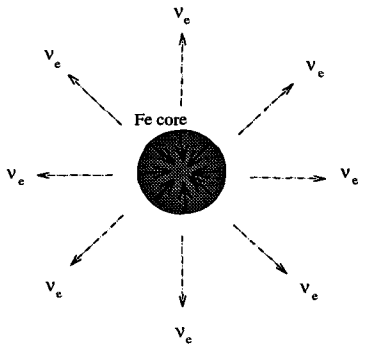

COLLAPSE

The collapse of the star's iron core. Electron neutrinos from electron capture reactions escape.

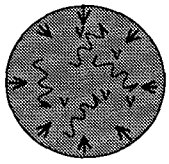

TRAPPING

Neutrinos trapped inside the collapsing core. All flavors of neutrinos can be present, although electron neutrinos from infall capture dominate the neutrino population immediately after trapping occurs.
Trapping occurs at about 30 km radius.

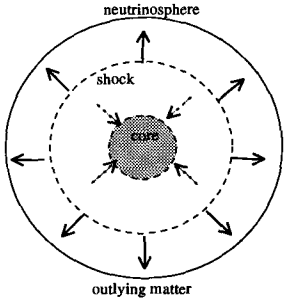

CORE BOUNCE

'Bounce' occurs when the density of collapsing core reaches nuclear density. "Maximum scrunch" occurs at 5-10 km radius. A shock front forms and travels outward into the surrounding infalling matter.

Figure 2.3: Early stages of stellar collapse, from pre-supernova to core bounce. The pictures are not to scale.

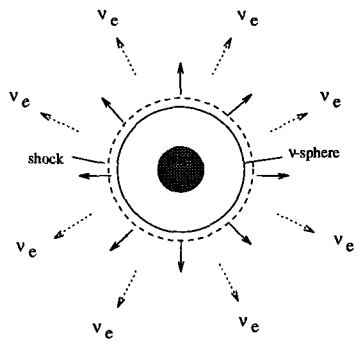

BREAKOUT

Neutrinos generated in the shock-heated matter stream out when the shock reaches the neutrinosphere at about a 30 km radius. A "neutrino flash" occurs consisting primarily of electron neutrinos.

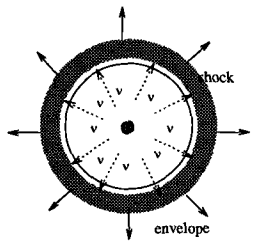

EXPLOSION

The shock wave moves out at about 70 km/ms, depositing energy in the outlying matter. Neutrinos streaming from the core may contribute to the disruption of the star's matter.

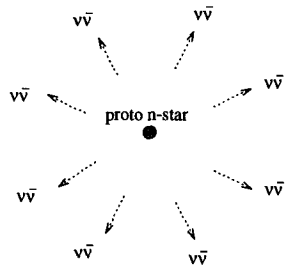

COOLING

Neutrino-antineutrino pairs carry away most of the binding energy of the collapsed core.
The neutron star remnant has a radius of about 10 km.

Figure 2.4: Later stages of stellar collapse.

Chapter 3 Neutrino Emission from Gravitational Collapse

As stated in Chapter 2, nearly all of the total gravitational binding energy of a neutron star will be emitted in the form of neutrinos. A back-of-the-envelope calculation yields an estimate of this energy:

$$E_b \sim \frac{GM_{core}^2}{R}, \tag{3.1}$$

where E_b is the binding energy of the neutron star, G is the gravitational constant, M_{core} is the mass of the core which collapses (also the mass of the resulting neutron star) and R is the final radius of the neutron star. Plugging in approximate values for the parameters ($M_{core} \sim M_\odot$, $R \sim$ 10 km), we get for the energy radiated in neutrinos $E_b \sim 3 \times 10^{53}$ ergs. Less than 1% of this energy is expected to be released in the form of optically visible radiation. The remainder of the binding energy is radiated in neutrinos, of which approximately 1% will be electron neutrinos from the neutronization burst and the remaining 99% will be neutrinos from the cooling reactions, equally distributed among flavors. Average neutrino energies are expected to be about 12 MeV for electron neutrinos, 15 MeV for electron antineutrinos, and 18 MeV for all other flavors (following the notation of Burrows [22], muon and tau neutrinos and antineutrinos will be denoted collectively as "ν_μ").

The physical processes occurring during gravitational collapse leading to the emission of neutrinos have already been described in the previous chapter. In the following section, the expected neutrino signal from a typical gravitational collapse event will be described in much more detail.

3.1 The Expected Neutrino Signal

In this section, a "baseline" model of neutrino production from gravitational collapse will be described. Much of the information presented here is taken from the "generic neutrino signature" of Burrows et al. [22], which uses a model which incorporates features from various "standard" gravitational collapse models. The Burrows et al. draws on work from references [23], [24], [25] and [26], and is an amalgam of specific spectral and luminosity assumptions patched together for different time periods. The "generic neutrino signature" is well summarized in Figures 3.1 and 3.2. Figure 3.1 shows the neutrino luminosities as a function of time for different neutrino flavors, with 3.1(a) showing the first second after collapse, and 3.1(b) showing the luminosity after collapse on a 50 second timescale. Figures 3.2 (a) and (b) show the average energies for the different neutrino flavors as a function of time over the same two timescales.[1]

Full predictions of the neutrino luminosities and energy distributions require detailed numerical simulation. However, in the following sections some qualitative justifications for the shapes of these generic curves will be presented.

3.1.1 Core Infall and Neutrino Trapping

In Figures 3.1 (a) and 3.2, the start of core infall occurs at -100 milliseconds (where $t = 0$ is the time of maximum neutrino luminosity). For the next 100 milliseconds, the neutrino luminosity consists entirely of ν_e which come from electron capture occurring during the initial stages of core collapse. The ν_e luminosity increases as the core density increases and more protons and electrons get squeezed together.

3.1.2 Bounce and Neutrino Breakout

After core bounce, the shock wave races outwards. It reaches the neutrinosphere at about 50 ms after the start of infall. Neutrino breakout occurs on a timescale of a few tens of ms, and the neutrino luminosity increases enormously as the neutrinos

[1]These plots show average neutrino energies; a typical spectrum is shown in Figure 6.4.

produced by the high temperatures of the shock are free to stream out, whereas those produced inside the neutrinosphere (before the shock hit it) are trapped. Maximum luminosity occurs at around 100 ms after infall. The breakout peak is dominated by ν_e, the products of electron capture. However, other flavors of neutrinos, products of early neutral current cooling reactions, also exhibit breakout peaks in their respective luminosity curves when the shock hits their corresponding neutrinospheres, as shown in Figure 3.1. Muon and tau neutrinos and antineutrinos have deeper neutrinospheres than electron neutrinos because they interact less readily than ν_e with the proto-neutron star matter; this means that "ν_μ" will have longer mean free paths than ν_e. Therefore, spectra of the non-electron neutrinos which emerge from the core are harder than the electron neutrino spectrum since the "ν_μ" neutrinospheres are deeper within the core where temperatures and pressures, and so average particle energies, are higher.

3.1.3 Explosion

Whether or not an explosion clears overlying mass away from the core immediately after core bounce is crucial to the subsequent supernova's visibility in the electromagnetic spectrum. On the other hand, the success or failure of the explosion has a much less significant effect on the neutrino signal. However, whether a prompt, delayed or failed explosion occurs can have a measurable effect on the time dependence of the observed neutrino luminosity. (Figures 3.1 and 3.2 represent a delayed explosion model).

If a prompt explosion mechanism succeeds, i.e. the shock wave manages to propel itself through the outer layers of the star without losing too much energy, then matter will get blown away from the core and relatively little mass will fall back onto the core. In this case, neutrino fluxes will drop off quite steeply immediately after bounce since relatively little mass will accrete to the core and therefore less overall gravitational binding energy will be released. In addition, when less mass accretes to the core than for the delayed explosion case, the core is less opaque to neutrinos and r_ν decreases,

causing neutrinos to emerge from deeper and hotter regions of the core. Therefore, for prompt explosions, the neutrino spectrum will harden abruptly when the explosion occurs.

On the other hand, if the prompt explosion fails, more mass surrounding the collapsing core will accrete to the core than for the successful prompt explosion case. In this delayed explosion case, the neutrino luminosity will tend to be higher than for a prompt explosion due to the additional gravitational binding energy released. The ν_e breakout flash will tend to be stronger for a delayed explosion due to additional neutronization occurring as the extra matter falls inward. In some models in which the prompt explosion fails, additional bounces of much smaller magnitude than the initial core bounce can occur: this is known as "core ringing". Since the density and therefore the neutrino opacity oscillates over time, the ringing of the core may be reflected in the neutrino luminosity emerging from the core. In the model of Burrows et al. [22], the ν_e and $\bar{\nu}_e$ luminosities vary by 19% due to accretion oscillations with an 80 ms period, over a timescale of 10-500 ms after bounce; the luminosities of other neutrino flavors also oscillate with a smaller amplitude. This effect is shown in Figure 3.1. If a delayed explosion mechanism such as neutrino heating then produces an explosion, the neutrino energy spectrum will harden suddenly just as for a prompt explosion. The increase in average neutrino energy at explosion for all flavors is shown in Figure 3.2.

3.1.4 Cooling

After explosion, the cooling core of the proto-neutron star releases its energy in the form of neutrinos, according to the processes described in Section 2.2.8. The baseline model of Burrows et al. [22] includes two cooling phases: immediately after explosion neutrinos from cooling reactions are released from the outer regions. The time constant for neutrino emissions for this first phase is around 4 seconds. The second part of cooling phase lasts tens of seconds, and the neutrinos emitted come from cooling reactions in the core. During this time period, the neutrino luminosity decays accord-

ing to a power law. Over this phase, the average energy of the neutrinos gradually decreases.

3.1.5 Very Late Phases

According to the Burrows et al. model, the emission of neutrinos from the cooling core stops after some tens of seconds. At this point the core has become essentially transparent to neutrinos, and densities and temperatures have decreased such that cooling reactions are no longer possible. The luminosity cutoff will occur at different times for different neutrino flavors, according to the relative opacities of the core to the different flavors: "ν_μ" luminosities should cut off first, followed by the $\bar{\nu}_e$ and ν_e luminosities.

Black Hole Formation

Stars with very massive cores and generous envelopes, and whose shock waves fail to produce an explosion, such that there are unusually high rates of accretion to the core, may collapse beyond the point where nucleon degeneracy pressure can hold the core stable, and may become black holes. According to [22], for such cases, black hole formation occurs shortly after bounce, and the duration of the neutrino signal is very short— perhaps 1-2 seconds long. The breakout and cooling phases of a typical gravitational collapse neutrino signal would be absent if black hole formation follows accretion, and for such a case the neutrino luminosity would cut off sharply soon after bounce. A gravitational collapse leading to black hole formation would emit neutrinos of relatively lower energy, due to the loss of energy to the relatively dense matter accreting to the core before the final collapse.

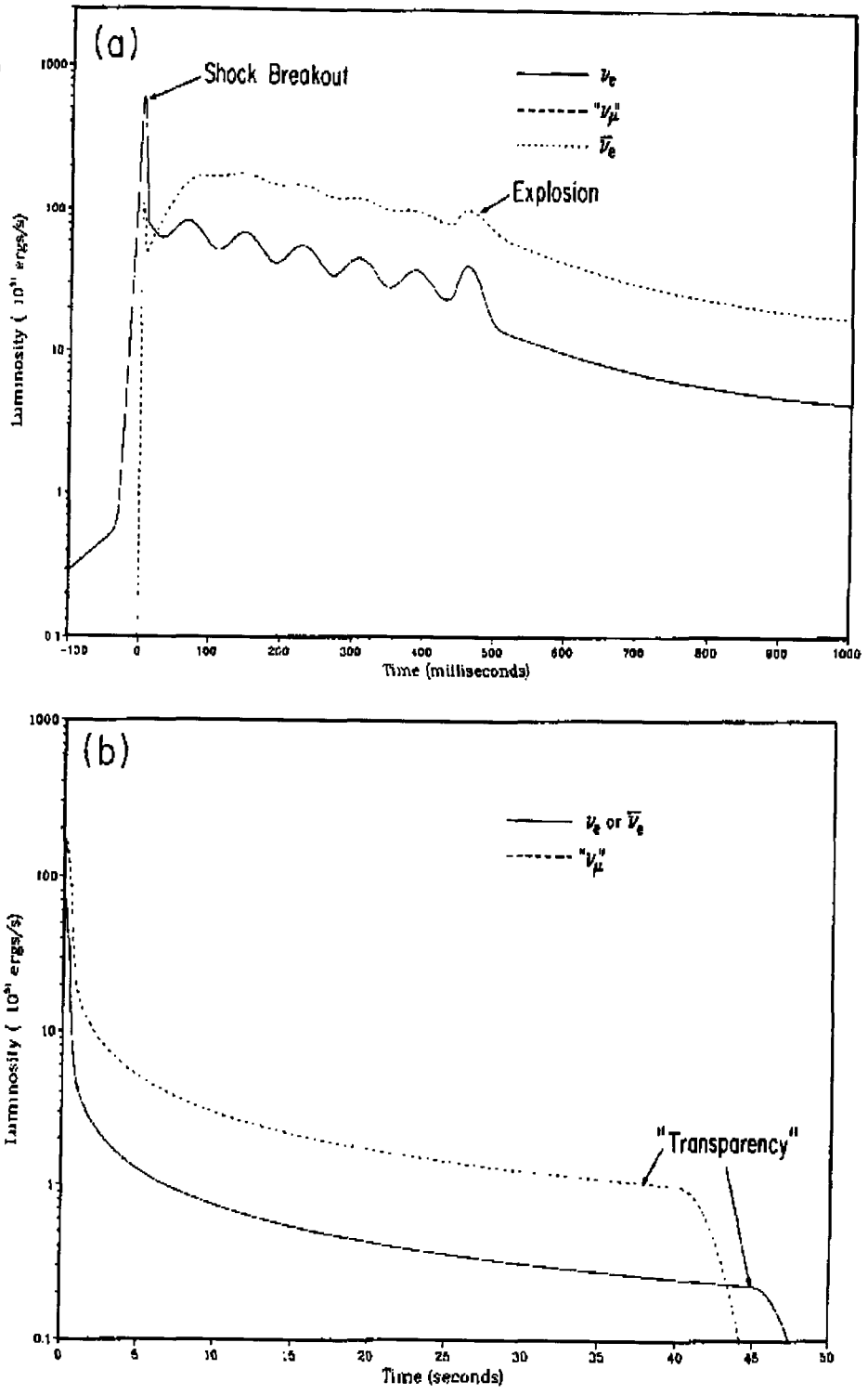

Figure 3.1: Expected neutrino luminosity as a function of time for various neutrino flavors. From Burrows et al..

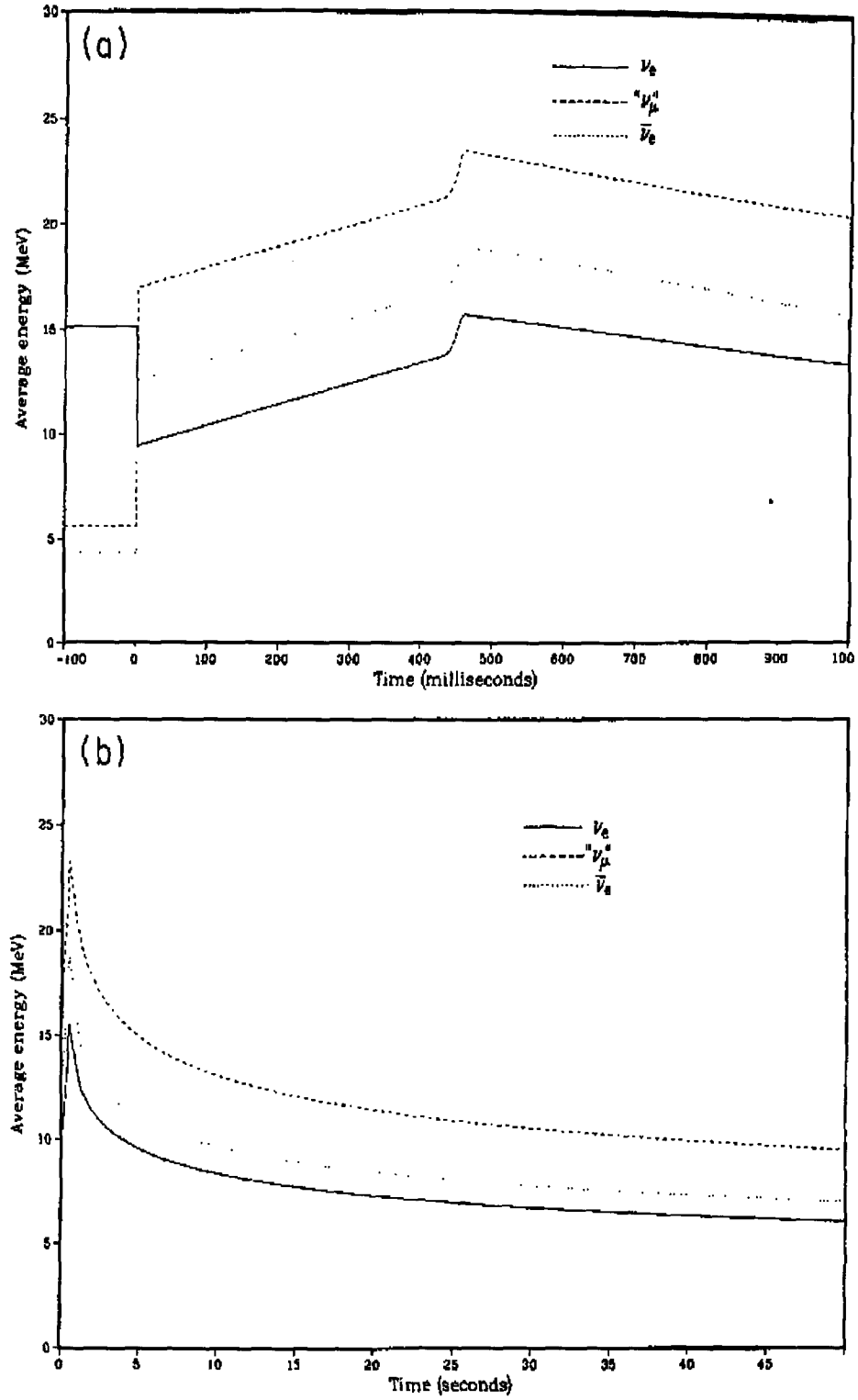

Figure 3.2: Expected average energy in MeV of neutrinos as a function of time for various neutrino flavors, for a "baseline model". From Burrows et al..

3.2 The Detection of Neutrinos from Gravitational Collapse

This section will discuss the detector characteristics required for seeing a GC neutrino signal in our galaxy, and will describe existing types of detectors. The potential physics results from a GC burst detection will be covered, as well as the past detected signal from SN1987A.

3.2.1 Neutrino Interaction Cross-sections

At the energies expected for a gravitational collapse neutrino signal, in the energy range 1 – 50 MeV, calculated cross-sections for the interaction of neutrinos with matter are extremely small. In general they are in the range of 10^{-44}–10^{-40} cm^2, typically increasing rapidly with neutrino energy. One of the most important of these reactions for neutrino experiments is the charged current reaction

$$\bar{\nu_e} + p \rightarrow e^+ + n. \tag{3.2}$$

This reaction has a threshold energy of $E_{\bar{\nu_e}}$ >1.8 MeV. It is often referred to as the "inverse beta decay" reaction.

Other reactions with relatively large cross-sections include the neutral current breakup of deuterium, and the charged current capture of neutrinos on nuclei such as ^{37}Cl and ^{40}Ar, and neutrino-electron scattering (which proceeds via charged current channels for electron neutrinos, and via neutral currents for all neutrino flavors). Some of these experimentally significant reactions will be discussed in more detail in the following sections. A few experimentally important cross-sections are plotted in Figure 3.3 [27, 28].

3.2.2 Detector Characteristics

The primary requirement for a neutrino detector is a very large active mass. Although the expected flux from a gravitational collapse is very large, the cross-sections

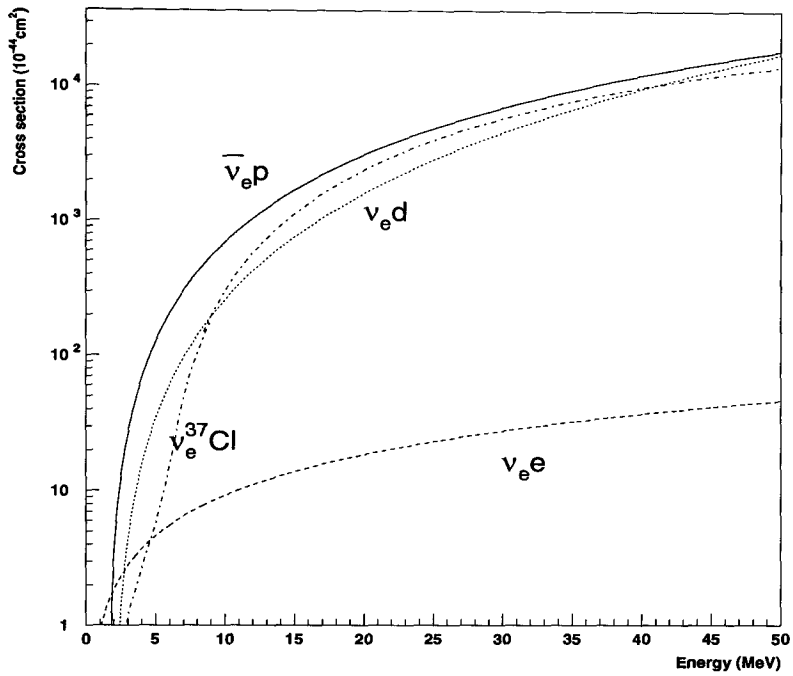

Figure 3.3: Examples of neutrino interaction cross-sections important for low-energy gravitational collapse neutrino detectors.

for neutrino interactions for the energy range of gravitational collapse neutrinos are so small that a very large quantity of material is required for a reasonable event rate. A back-of-the-envelope calculation yields the approximate mass required: the approximate number of $\bar{\nu}_e$ interactions per target particle for a gravitational collapse event at distance R is

$$N \sim \sigma\left(\frac{1}{6}\right)\left(\frac{E_b}{15\ \mathrm{MeV}}\right)\left(\frac{1}{4\pi R^2}\right). \tag{3.3}$$

For $E_b \sim 2 \times 10^{53}$ ergs and $R \sim 8.5$ kpc (the center of the galaxy), and assuming an inverse beta decay cross-section of 10^{-41} cm^2, we obtain $N \sim 10^{-30}$. Therefore, the number of protons N_p required for ~ 100 interactions in the detector is $N_p \sim 10^{32}$. For substances such as water and hydrocarbons, this translates to a required detector mass of $\sim$1 kton.

The time scale over which a gravitational collapse occurs is tens of seconds, and

the highest rate occurs in the first second: therefore the neutrino signal rate for a galactic center collapse will be in the range $10-100$ Hz. Any detector designed for the purpose of detecting gravitational collapse neutrinos must then have a background rate lower than the expected rate for a gravitational collapse signal. Therefore, an underground location where the cosmic ray background is greatly reduced is desirable, as is a low ambient radioactivity background.

A high neutrino-interaction cross-section material should be chosen to optimize the signal to background ratio. The ability to measure the times of neutrino signals relative to each other (for mapping the time structure of the signal) and to an absolute standard (for comparing times with other neutrino and optical observations) is required. In addition, good energy resolution for measurement of the energy distribution of the signal neutrinos is desirable. These criteria will be discussed with respect to specific detectors in the following sections.

The ability to point back to where the neutrinos come from is certainly desirable. Detectors exploiting the neutral current electron scattering reaction for neutrino detection, for which information about the direction of the incoming neutrino is retained by the scattered electron, have some hope of reconstructing the neutrino source direction. In addition, if more than one neutrino detector is able to measure enough events to determine the turn-on time of the neutrino pulse to a few milliseconds precision, some directional information may be obtained by triangulation methods [22].

3.2.3 Types of Detectors

There are several classes of detectors capable of detecting neutrinos from gravitational collapse. Table 3.1 gives an overview. Most of these take advantage of the charged current inverse beta decay reaction 3.2, but many use other reactions as well. Some specific detectors will be discussed in this section.

Scintillation Detectors

The active agents in scintillation detectors are organic molecules which emit light when excited by the passage of particles. The most common scintillator type for gravitational collapse neutrino detection is the organic molecule pseudocumene dissolved in a clear liquid hydrocarbon such as mineral oil or kerosene. A volume of this mix is viewed by photomultiplier tubes. Usually it also contains wavelength shifting substances to shift the frequency of the light to match the best response of the phototubes and to reduce absorption in the medium. Liquid scintillator is composed entirely of carbon and hydrogen (apart from contaminants) and so is rich in free protons, giving it a high cross-section for the charged current antineutrino absorption reaction 3.2. The neutron from reaction 3.2 may also be detectable via the fusion reaction

$$n + p \rightarrow d + \gamma\ (2.2\ \text{MeV}), \tag{3.4}$$

where the γ can be detected in the scintillator by its Comption scattering. The average moderation time for the neutron is $\sim$10 μs, and the average capture time is 170 μs. Therefore, a time-delayed coincidence of a $\sim$10 MeV pulse with a 2.2 MeV signal can provide a signature for the absorption of GC $\bar{\nu_e}$ in liquid scintillator detectors.

Neutrino-electron scattering, equation 3.5, is also detectable by scintillation detectors, although cross-sections are much lower than for inverse beta decay.

$$\nu_x + e^- \rightarrow \nu_x + e^-, \tag{3.5}$$

where ν_x represents a neutrino of any flavor. For electron neutrinos, the scattering can take place via the exchange of either a W or a Z boson; for muon and tau neutrinos the scattering takes place via Z boson only. (Sensitivity to ν_e is valuable for detection of the initial neutronization burst which contains primarily electron neutrinos). The neutral current reaction is sensitive to all neutrino flavors. There is no energy threshold for this reaction. However, for scintillation detectors scattering cross-sections are very low (see Figure 3.4).

The superallowed neutral current excitation of ^{12}C by neutrinos of all flavors also plays a role in scintillator detection of gravitational collapse neutrinos. The reaction is

$$\nu_x + {}^{12}\mathrm{C} \rightarrow \nu_x + {}^{12}\mathrm{C}^*. \tag{3.6}$$

The ^{12}C subsequently de-excites giving a 15.11 MeV gamma ray. The detection of this gamma could provide a signature of a neutral current reaction in the scintillator.

Figure 3.4 shows cross-sections for neutrino interactions with scintillator over the energy regime of interest [29]. Energy thresholds for liquid scintillator detectors are typically 6–7 MeV or lower.

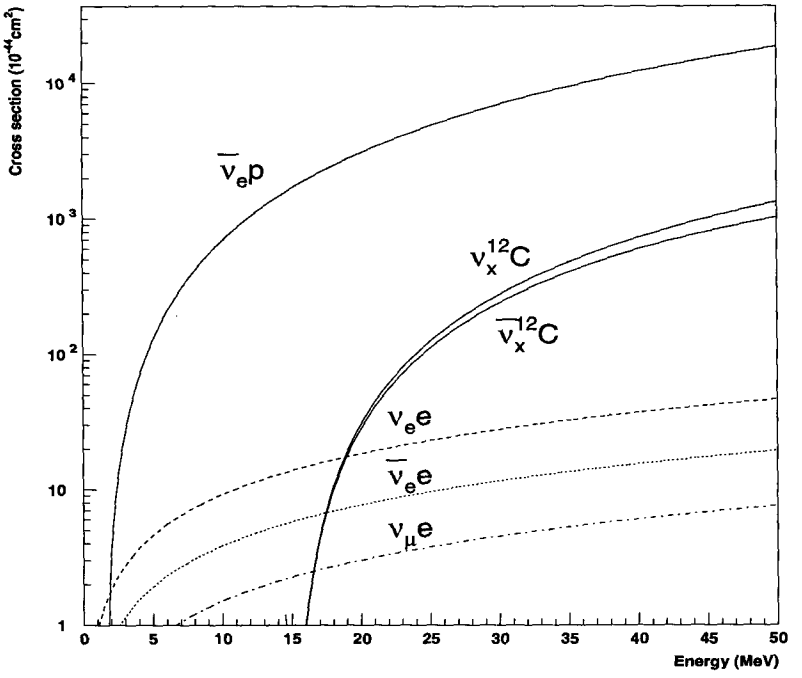

Figure 3.4: Cross-sections for interactions of neutrinos with scintillator.

Scintillator detectors are not able to measure the directions of the incoming neutrinos. The positron products of the predominant inverse beta decay reaction are isotropic; in addition, the geometrical configurations of many scintillation neutrino detectors (such as MACRO) are such that directions of short-pathlength charged

particles passing through them are difficult to determine anyway.

Some examples of liquid scintillation detectors (currently running and past) are MACRO at the Gran Sasso Laboratory in Italy (the properties of which will be discussed in detail in Chapter 4), the Large Volume Detector (LVD) also at the Gran Sasso [30], the Baksan detector in Russia [31], LSND at Los Alamos [32], and the LSD detector under Mont Blanc [33]. Other scintillation detectors currently under construction include Borexino at the Gran Sasso [34] and the Palo Verde detector in Arizona [35].

Light Water Čerenkov Detectors

Water Čerenkov detectors consist of large volumes of water viewed by photomultiplier tubes. Charged particles moving inside the water volume with velocity greater than the velocity of light in water produce a cone of Čerenkov light. The Čerenkov photons are then detected by the photomultiplier tubes on the outside of the volume. The particle velocities can be determined from the angle of the Čerenkov cone, and energy deposited can be determined from the number of photons detected. The energy threshold for electron or positron detection for most current experiments using this method is about 5-10 MeV.

This type of detector also takes advantage of the standard inverse beta decay reaction, reaction 3.2 for supernova neutrino detection, since there are plenty of free protons available in the water. In this case, the Čerenkov light from the positron emerging from this interaction is detected. Light water Čerenkov detectors are also capable of seeing the neutrino electron scattering reactions 3.5. The electron scattering reactions are of particular significance for water Čerenkov detectors, because unlike the products of the inverse beta decay reaction, the electrons scattered by neutrinos retain some of the direction information of the incoming neutrinos. Information about the direction of motion of the scattered electron is available from the Čerenkov light cone, so a Čerenkov detector observing this reaction has some potential for reconstructing the direction from which gravitational collapse neutrinos came.

Some examples of light water Čerenkov detectors are the IMB detector in the United States [36], the Kamiokande II [3] (now Kamiokande III) and Superkamiokande [37] detectors in Japan, and part of the SNO detector presently under construction in Canada [38]. These detectors were primarily designed with the detection of proton decay or solar neutrinos in mind; however, they all have very good gravitational collapse neutrino detection capability.

Heavy Water Detectors

At present, the only example of a heavy water supernova neutrino detector is the SNO detector [38]. The idea behind a heavy water neutrino detector is to exploit the relatively high cross-sections for the interaction of neutrinos with deuterium. Two classes of reactions are relevant here.

1. The neutral current interaction of all flavors of neutrinos with deuterium:

$$\nu_x + d \rightarrow n + p + \nu_x. \tag{3.7}$$

   In this case the neutron is detected. No energy or neutrino direction is available for this reaction; however, the reaction is sensitive to all flavors of neutrinos.

2. The charged current interaction of electron neutrinos and antineutrinos with deuterium:

$$\nu_e + d \rightarrow p + p + e^- \tag{3.8}$$

$$\bar{\nu_e} + d \rightarrow n + n + e^+. \tag{3.9}$$

   In these cases, the electron or positron can be detected by its Čerenkov light, and energy and directional information can be extracted. In addition, the neutrons from the antineutrino reaction can be detected with a time-delayed coincidence.

Other Detector Types

A few other types of detectors also have sensitivity to gravitational collapse neutrinos.

- Liquid Argon:

  The proposed ICARUS detector to be built at the Gran Sasso laboratory [39] would have quite good sensitivity to gravitational collapse neutrinos (although it is designed primarily for solar neutrino detection.) This is a very large liquid argon drift chamber which can take three dimensional "pictures" of interaction events. Electron neutrinos interact via

$$\nu_e + {}^{40}\mathrm{Ar} \rightarrow {}^{40}\mathrm{K}^* + \mathrm{e}^-. \tag{3.10}$$

  The final state electron is detected, and in addition the de-excitation gamma rays from $^{40}\mathrm{K}^*$ can also be detected.

  A detector such as ICARUS would have very good sensitivity to the initial neutronization burst of a gravitational collapse.

- Calcium Carbonate:

  SNBO [40] is a proposed gravitational collapse neutrino detector which would consist of a large quantity of calcium carbonate rock in conjunction with BF_3 neutron counters. The neutrino detection reaction is

$$\nu_x + (A, Z) \rightarrow (A-1, Z) + n + \nu_x. \tag{3.11}$$

  The relevant nucleus would be calcium, and the neutron would be detected. This reaction, being neutral current, is also flavor-blind.

- Radiochemical Detectors:

  Radiochemical detectors such as the classic $^{37}\mathrm{Cl}$ solar neutrino detector at the Homestake mine [41], the gallium solar neutrino detectors such as GALLEX [42] and SAGE [43], or a possible $^{127}\mathrm{I}$ detector [44], will register counts if gravitational collapse neutrinos interact inside them. Since the sensitive chemicals are only extracted at very long time intervals ($\sim$ weeks or months), they have no time (or energy) resolution and are of limited value for a gravitational collapse

search. However, if a burst of gravitational collapse neutrinos were confirmed in one or many of the real-time neutrino detectors, radiochemical experiments could perform prompt extractions to determine whether any counts over the background were registered during the relevant time period.

A summary of the properties of the main types of gravitational collapse neutrino detectors is given in Table 3.1.

3.3 Potential Physics Results

The detection of a significant neutrino signal from a gravitational collapse event could yield important information about gravitational collapse physics and neutrino properties.

3.3.1 Constraints on Supernova Models

As will be discussed in Section 3.4, the neutrino measurements from SN1987A by the IMB and Kamiokande II experiments were sufficient to establish that the general view of gravitational collapse is correct. However, the neutrino events seen by those two experiments were too few to provide enough information to distinguish between details of competing models of gravitational collapse. A high statistics observation of a burst of neutrinos from a nearby supernova would be very valuable for determining the exact nature of the processes occurring during a gravitational collapse. The ability to measure neutrino energies as a function of time is particularly useful for looking into the heart of a supernova. For instance, as mentioned in Section 3.1.3, a sharp hardening of the neutrino spectrum at early times could imply that a prompt rather than a delayed explosion occurred. Observed oscillations in the neutrino signal immediately after breakout could yield information about the amount of matter accreting to the core before and after explosion. Neutrino flavor information is also valuable: the size of the neutronization peak, as seen in electron antineutrinos, gives information about infall and explosion; "ν_μ" neutrinosphere radii can be determined

Detector type	Examples	Material	Energy	Time	Point	Flavor
scintillator	MACRO (R) LVD (R) Baksan (R) LSND (R) LSD (P) Borexino (F) Palo Verde (F)	C,H	y	y	n	$\bar{\nu}_e$
water Čerenkov	IMB (P) KIII (R) SuperK (R) SNO (F)	H_20	y	y	y	$\bar{\nu}_e$
heavy water	SNO (F)	D_20	NC: n	y	n	all
			CC: y	y	y	ν_e,$\bar{\nu}_e$
liquid argon	Icarus (F)	Ar	y	y	y	ν_e
calcium carbonate	SNBO (F)	$CaC0_3$	n	y	n	all
radio-chemical	Homestake (R) Homestake (F) Gallex (R) SAGE (R)	^{37}Cl ^{127}I ^{71}Ga ^{71}Ga	n	n	n	ν_e

Table 3.1: Properties of various types of gravitational collapse neutrino detectors (see the text for references). The columns labeled "Energy", "Time" and "Point" indicate whether the detector type can make measurements of incoming neutrino energies, times or directions (yes/no); the column labeled "Flavor" gives the primary neutrino flavor sensitivity. "R" after the specific detector name indicates that the detector is currently running; "P"(past) indicates that the detector is no longer running and "F" (future) means that the detector is either proposed or under construction.

from their respective breakout peaks, etc. And finally, as described in Section 3.1.5, a sharp cutoff in neutrino luminosity would indicate that the neutron star had undergone further collapse to a black hole.

3.3.2 Neutrino Physics

By making some reasonable assumptions about gravitational collapse physics, it is possible to extract information about the properties of neutrinos themselves by examining the detected neutrino events. Many people attempted to do this for the SN1987A observations. However, statistics were low in that case and only a moderate amount of information was obtained (although hundreds of papers were written about it!). The detection of an order of magnitude more events could provide much more interesting results.

Neutrino Mass Measurement

The basic idea behind this measurement is that if neutrinos have non-zero mass, then their times of flight will vary according to their energies. Therefore, since neutrinos are emitted from the gravitational collapse with a distribution of energies, the signal seen at Earth will be spread out in time if neutrinos have mass.

The extra time ΔT_0 it takes a massive particle of mass m and energy E to travel a distance D compared to a massless particle of the same energy is given by

$$\Delta T_0 \;=\; D\left(\frac{1}{v}-\frac{1}{c}\right) \;\simeq\; \frac{1}{2}\frac{D}{c}\left(\frac{mc^2}{E}\right)^2 \tag{3.12}$$

in the relativistic limit $E \gg m$, where v is the speed of the particle and c is the speed of light.

If two neutrinos are observed at distance D away at times ΔT apart, and we assume that that they have mass m_ν and were emitted by the gravitational collapse at the same time but with different energies E_1 and E_2, then m_ν can be obtained

from:

$$m_\nu c^2 = \left(\frac{2\Delta T c}{D}\right)^{1/2} E_1 E_2 (E_2^2 - E_1^2)^{-1/2}. \quad (3.13)$$

However, the mass of neutrinos determined by looking at a gravitational collapse neutrino signal depends on the assumption of the spread in time over which the neutrinos are emitted by the supernova. Thus, we can only get an upper limit on the mass of neutrinos, corresponding to the assumption of a delta-function spread in emission time.

Mass limits have been obtained for electron antineutrinos using the SN1987A neutrino data. For the above assumption of a delta function for the emission times, one obtains a conservative upper mass limit of [45]

$$m_{\bar{\nu_e}} < 30 \text{ eV}. \quad (3.14)$$

By making some reasonable assumptions about the spread in emission times of the neutrinos that were seen by IMB and Kamiokande II, it is possible to calculate a more stringent limit. Many people have done this, and typical limits (e.g [46], [47]) are in the range

$$m_{\bar{\nu_e}} < (10 - 20) \text{ eV}. \quad (3.15)$$

However, these limits are not better than limits which have already been obtained by other methods. For example, the current limit on ν_e mass from double beta decay measurements is $m_{\nu_e} < 0.68$ eV at 90% C.L. [48] (for Majorana neutrinos). Less stringent but more model independent limits come from tritium beta decay endpoint experiments, e.g. references [49], [50] give a limit of $m_{\nu_e} < 7.2$ eV at 95% C.L..

If neutrinos have mass, different flavors of neutrinos may have different masses (i.e. $m_{\nu_e} \neq m_{\nu_\mu} \neq m_{\nu_\tau}$). In this case, an experiment which is sensitive to all flavors via neutral current reactions could see three bursts in succession corresponding to electron, muon and tau neutrinos (if the different flavor masses are different enough from each other), for a high statistics neutrino signal (see, e.g. [51]).

Number of Neutrino Flavors

It is possible to use a gravitational collapse neutrino signal to set a limit on the number of neutrino families. If one assumes that the gravitational collapse neutrino luminosity is equally distributed among the different neutrino flavors, which is true to a very good approximation for almost all models, then the more flavors that exist, the fewer events are expected per flavor. Even if an experiment is primarily sensitive to only one flavor of neutrino, assuming a maximum total luminosity makes it possible to calculate a maximum number of neutrino flavors. Such a result would be greatly strengthened by having sensitivity to multiple flavors.

The limit obtained from the SN1987A data was $N_\nu < 6$ [45], which is not as stringent as current limits from accelerator experiments [52] (for $m_\nu < m_{Z_0}/2$) or earlier limits from big-bang nucleosynthesis [53].

Neutrino Lifetime Measurement

The fact that neutrinos reached the Earth at all from a gravitational collapse event has some bearing on the neutrino lifetime: if neutrinos had decayed in flight, then the flux observed at Earth would have been reduced. Since the measured neutrino luminosity matches the expected luminosity (based on the binding energy of a neutron star), one can estimate the minimum lifetime of neutrinos (e.g. [45, 28]) to be

$$\gamma\tau_\nu > D/c, \tag{3.16}$$

where D is the distance to the supernova, γ is the relativistic factor and τ_ν is the neutrino lifetime. The result for SN1987A, 50 kpc away, is

$$\gamma\tau_{\bar{\nu}_e} > 1.6 \times 10^5 \text{ yr}, \tag{3.17}$$

The SN1987A result implies that neutrino decay is not a solution to the solar neutrino problem: the deficit in the predicted flux of neutrinos reaching the Earth from the sun cannot be explained by the neutrinos having decayed in flight (for $\tau_{\bar{\nu}_e} = \tau_{\nu_e}$).

Note that this limit will not be improved by future measurements of GC neutrinos in our galaxy.

Neutrino Charge Measurement

Neutrinos with a non-zero charge would take differing paths in the galactic magnetic field on their way to Earth according to their different energies. Therefore, just as in the mass limit case, the observed burst would be more spread out in time than the initial emission time distribution if neutrinos had charge.

The upper limit from SN1987A for the charge of the electron antineutrino is [28, 45]:

$$Q_{\bar{\nu}_e} \; < \; 3 \times 10^{-17} |e|. \tag{3.18}$$

Neutrino Oscillations

With sensitivity to neutral current, flavor-blind, neutrino reactions, it may be possible to make measurements of neutrino oscillations between different flavors. With a very high statistics signal, experiments with modest neutral current sensitivity can hope to look for evidence for neutrino oscillations [54]. Again, any such analysis depends strongly on assumptions made about the neutrino emission processes in the supernova (including possible neutrino mixing in the supernova core), and limit results are unlikely to be competitive with direct measurements.

With sensitivity to $\bar{\nu}_e$ only, in principle it is possible to extract some information about neutrino oscillation by considering the observed $\bar{\nu}_e$ energy spectrum. For example, "ν_μ" flavors are expected to have harder energy spectra than ν_e and $\bar{\nu}_e$, so if $\bar{\nu}_\mu$ or ν_τ oscillate into $\bar{\nu}_e$, the observed $\bar{\nu}_e$ energies would be higher than if no oscillation occurred. However, even with very good statistics it would be difficult to draw conclusions from $\bar{\nu}_e$ data alone, and any such conclusions would depend on neutrino emission assumptions.

Neutrino Magnetic Moment Measurement

One somewhat more exotic limit that might be obtained from gravitational collapse neutrino data is a limit on neutrino magnetic moment. Many gravitational collapse models involve large magnetic field effects, and predict significant effects on emitted neutrino properties and distributions if neutrinos have magnetic moments. Such anomalies were not observed for SN1987A. The SN1987A limit on the magnetic moment of the neutrino obtained in [55] is

$$\mu_\nu < 10^{-12}\mu_B. \tag{3.19}$$

However, such limits on neutrino properties are highly dependent on the exact gravitational collapse models adopted, and magnetic field effects in collapsing stars are currently not very well understood. Measurements from $\bar{\nu_e}$ scattering at reactors give less stringent (but more certain) limits of $\mu_\nu < 2 \times 10^{-10}\mu_B$ [56].

3.4 Supernova 1987A

No discussion of supernova neutrino detection would be complete without a detailed description of the famous detection of neutrinos from Supernova 1987A. This event was a Type II supernova which occurred in the Large Magellanic Cloud, 50 kpc away, on February 24, 1987 (UT). It was first recognized optically on February 24, 1987. It was the first supernova observable with the naked eye since Kepler's supernova in 1604.

Astronomers detected hydrogen lines in the supernova spectrum, immediately allowing them to identify the supernova as a Type II. The light curve was also consistent with that expected for a Type II supernova. The explosion energy was measured to be about 10^{51} ergs [57].

The progenitor star, Sanduleak -69 202, had been catalogued previously. Unexpectedly, the progenitor was a *blue* supergiant rather than a red one, and had a lower metallicity and smaller radius than was thought previously to be typical for a

pre-supernova star. However, the properties of this particular progenitor star are not inconsistent with models of gravitational collapse, given some assumptions about the star's composition and history (it is assumed to have been a former red supergiant which had blown off much of its mass).

No pulsar has been seen in the supernova remnant location so far (some early reports of pulsar detection [58] were withdrawn).

This gravitational collapse neutrinos were not noticed promptly by neutrino detectors. However, when the data from two large water Čerenkov detectors were analyzed a few days after the optical observations, bursts of neutrino events were seen at times consistent with the expected core collapse time for the optically observed supernova. The IMB detector saw eight events above its energy threshold of 29 MeV [1, 2], and the Kamiokande II detector saw 11 events above its energy threshold of 8.5 MeV [59, 3].[2]

In addition, two liquid scintillator detectors reported detecting events coincident with the supernova burst. The Baksan detector saw five events [4] (although the expected number of events was only one). The LSD detector under Mont Blanc, despite its very small mass (90 tons), saw two events in coincidence with the burst observed by the other experiments [5]. In addition, LSD recorded a highly statistically significant burst of five events five hours before the burst events seen by the other detectors. This early burst is rather controversial, because no other detector recorded it. Furthermore, the number of events expected in the LSD detector from a gravitational collapse at the distance of SN1987A was less than one.

Table 3.2 gives a summary of the relevant parameters of the detectors which observed neutrino events near the time of SN 1987A.

The SN 1987A explosion was first discovered optically at a UT time of 10:53 on February 24, and it had been photographed on February 24 at 10:40 UT time, some 3 hours after the neutrino signal. This time delay between neutrino and optical signals is entirely consistent with the predictions of supernova explosion theory.

The energy and time distributions of the events seen by Kamiokande II and IBM

[2]The energy thresholds here are defined as the positron energy at which 50% detection efficiency is attained.

Detector	Type	Mass (kton)		Thresh.	Events	Events	UT Time
		Total	Fid.	(MeV)	seen	expected	Feb 24 1987
K II	water Č	3	2.1	8.5	12	~ 15	7:35
IMB	water Č	5	3.3	29	8	~ 5	7:35
Baksan	scint.	0.2	0.13	10	5	~ 1	7:35
LSD	scint.		0.09	7	5	0	2:52
					2	<1	7:35

Table 3.2: Masses and energy thresholds of neutrino detectors which saw events near the time of SN 1987A, on February 24, 1987, and some details of the events seen.

are shown in Figure 3.5.

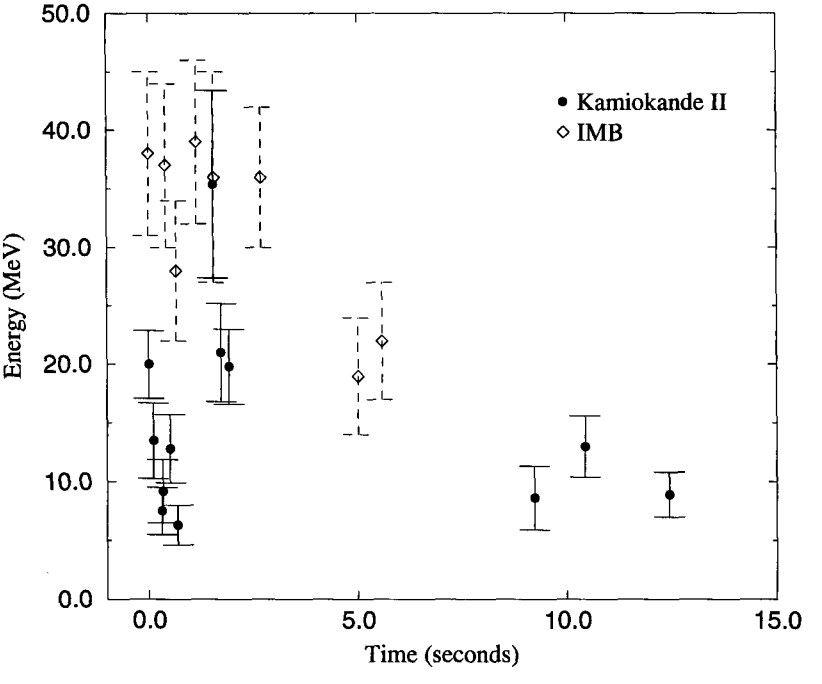

Figure 3.5: Energies and times of the events detected by Kamiokande II and IMB during SN 1987A.

The events observed by Kamiokande II and IMB show energy and time distributions well in line with what is expected from a minimal gravitational collapse model: the energies are of the right order of magnitude, the decrease with time of the average energies is as expected, and the decrease in rate with time is as expected (compare qualitatively to Figures 3.1 and 3.2). Furthermore, the number of events observed

is quite consistent with the estimated release of binding energy of this gravitational collapse, some 2×10^{53} ergs. In this respect, the data from IMB and Kamiokande II well confirm the basic theory of gravitational collapse. However, statistics are lacking if one wants to be able to distinguish between the details of differing models. Also, as detailed in Section 3.3.2, some constraints on neutrino properties, such as mass and number of families, were set using the detected events from Kamiokande II and IMB. However, such constraints were generally weaker than corresponding laboratory measurements due to the small number of neutrino events detected.

Although statistics are very low, the Baksan neutrino events are not inconsistent with a baseline gravitational collapse model (although they are greater in number than would be expected from the mass of the detector). The Mont Blanc events present more of a problem due to their early arrival time and the fact that no other experiment measured a coincident burst. In addition, no really satisfactory model has been proposed to explain them, and the opinion of several astrophysicists (e.g. Bahcall [28], Schramm [45]) is that this observed burst was not actually correlated with the SN1987A event.

Chapter 4 The MACRO Experiment

4.1 General Description

The MACRO (Monopole, Astrophysics and Cosmic Ray Observatory) detector is a large array of scintillator and streamer tubes located in the underground Gran Sasso Laboratory near l'Aquila, Italy. The main goal of the MACRO experiment is the detection of magnetic monopoles; however several other kinds of physics, including the detection of gravitational collapse neutrinos, can be investigated using the MACRO detector.

The MACRO experiment is the result of an Italian-American collaboration, involving about 150 people from several institutions in both countries. The MACRO author list is given in Appendix I.

4.2 The Gran Sasso Laboratory

A map showing the location of the Gran Sasso Laboratory (Laboratori Nazionali del Gran Sasso) [60] is shown in Figure 4.1. The underground laboratory is accessible from the A24 highway running through the Gran Sasso mountain. The minimum overburden is ~3200 m.w.e.; the muon flux at this depth is reduced by a factor of about 10^6 compared to the surface level flux. The MACRO experiment is located in Hall B of the underground laboratory. Figure 4.2 shows the layout of the experimental halls.

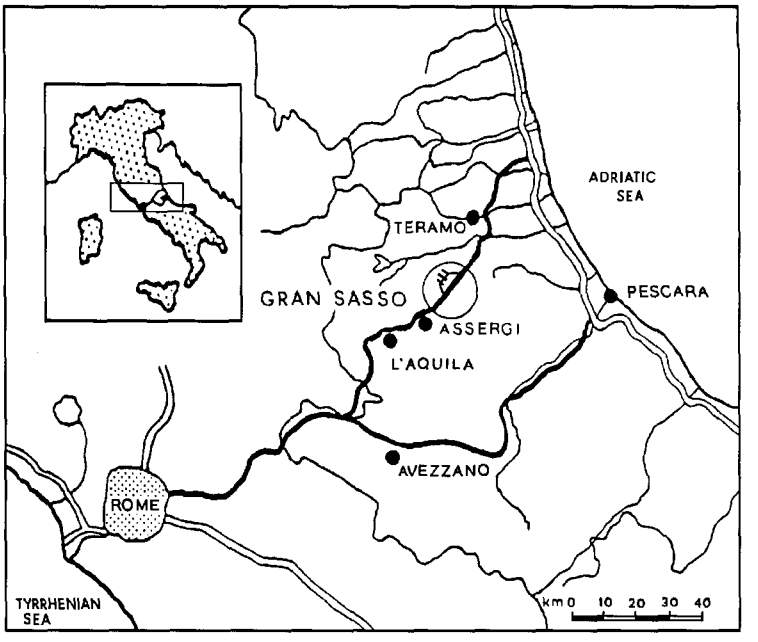

Figure 4.1: Location of the Gran Sasso laboratory.

4.3 Physics Goals

4.3.1 Magnetic Monopoles

The primary motivation for the construction of MACRO is the detection of magnetic monopoles, and the optimization of potential monopole signals motivates the basic design of the experiment. The primary features of MACRO — an underground large area, multi-instrument, tracking, timing and charge-measuring device — are dictated by the need to obtain an unambiguous, redundant signal for a through-going monopole. Because the monopole search is what motivates the design of MACRO, monopole detection will be briefly described in this section.

According to theoretical models, magnetic monopoles may be slowly moving, possibly down to $\sim 10^{-4}c$. MACRO contains three horizontal layers of liquid scintillator counters, as well as scintillator counters along its side walls. Scintillator provides nanosecond timing timing resolution for time of flight measurements, as well as measurements of energy deposition. The time of flight within a single scintillator counter of a monopole can be measured by looking at the pulse width of the scintillator sig-

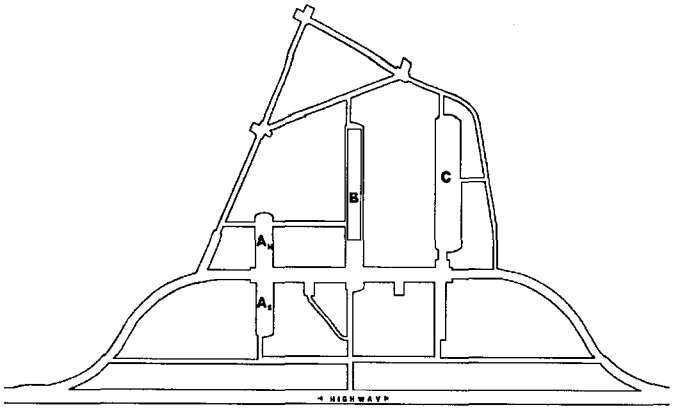

Figure 4.2: The Gran Sasso Laboratory.

nal. In addition, the time of flight of a monopole between two different counters can be measured by looking at the signals in the different faces of MACRO. Consistency between times of flight measured within a counter and between counters can be required, as well as consistency between measured and expected dE/dx given the measured velocity of the monopole candidate.

Monopoles are also expected to produce signals in streamer tubes: helium-filled streamer tubes should have very good sensitivities to very slow monopoles according to the Drell-Penning predictions [61] for monopole interactions in helium. The streamer tubes of MACRO are configured in horizontal parallel planes, and also in vertical planes along the sides of the detector, in order to record the tracks of passing monopoles. This tracking allows a check of the flight path of a monopole which left signals in the scintillation counters. In addition some timing ($\sim \mu$s) is available from the streamer tube signals for very slowly moving particles, and some charge information is available allowing an additional measurement of energy loss.

A third component of MACRO is the track-etch detector. Layers of special plastic are installed in the central plane of MACRO and on the side walls. Monopoles traversing these plastics should produce defects in its molecular structure, and these defects can then be made visible by an etching procedure. If a monopole candidate is detected by the scintillator and/or streamer tube systems of the detector, the track etch

plastic at the appropriate locations can be pulled out, etched and examined for the presence of a hole confirming the passage of a monopole. Two different kinds of track etch plastic, CR-39 and Lexan, with different velocity sensitivities, are employed.

A wide area detector is desirable for the detection of monopoles, for large acceptance: MACRO's total acceptance for an isotropic flux is $\sim$10000 m^2sr.

4.3.2 Gravitational Collapse Neutrinos

Another important capability of the MACRO detector is the detection of neutrinos from gravitational collapse, which is the subject of this thesis. As discussed in Chapter 3.2, liquid scintillator is sensitive to GC neutrinos, primarily due to the inverse beta decay reaction of electron antineutrinos. Although the MACRO detector's scintillator elements are relatively unshielded against radioactive background, energy and timing capabilities are quite good (see Section 5.4) and the active mass of 560 tons of liquid scintillator provides good sensitivity to GC within our galaxy. MACRO's capabilities for GC neutrino detection will be discussed in detail in Chapter 6.

4.3.3 Other Physics Topics

The MACRO detector can address several other issues of current interest in physics:

- Upward-going muons seen in MACRO are produced from high-energy neutrino interactions occurring below the detector. Upward-going muons yield information on neutrino oscillations of atmospheric neutrinos and WIMP annihilations in the Earth or the sun [62]. In addition searches can be made for astronomical neutrino point sources.

- Various cosmic ray muon studies can be done by measuring the properties of downward-going muons seen in the detector. Multiplicity, space and time distributions of cosmic ray muons are sensitive to primary cosmic ray composition and interactions in the upper atmosphere (e.g. references [63], [64]). Searches for astronomical muon point sources and large scale anisotropies in muon arrival

directions can also be made ([65], [66]).

- Searches for exotic particles such as nuclearites or other highly ionizing particles, or fractionally charged particles can be made ([67], [68]).

These topics will not be addressed in this thesis.

4.4 Detector Description

This section will contain a description of the MACRO detector, with emphasis on those elements important for a GC search. The scintillator system of MACRO will be described in detail because its active mass provides the means of detection of the GC $\bar{\nu}_e$ signal (as described in Section 3.2.3). The streamer tube system, which can be used to reduce background for a GC search by vetoing cosmic ray muons from the data sample (Section 6.2.1), will be described in somewhat less detail. Complete descriptions of the track etch and TRD systems will omitted because these systems are not relevant to the subject of this thesis. Detailed information about technical aspects of the experiment can be found in reference [69].

4.4.1 General Description

The MACRO detector is divided into 6 "supermodules", each of dimensions 12 m $\times$ 12 m $\times$ 9 m. These supermodules are laid end to end in Hall B, and the full detector is 76 meters long. Each supermodule is further subdivided into two "modules", each 6 meters wide.

MACRO liquid scintillator is contained in 12 m long PVC counters arranged in layers. Each supermodule has three horizontal layers of scintillator counters. The counters belonging to the horizontal layers will be denoted as "horizontal counters". The bottom layer sits about 1 m above the concrete on the floor of Hall B, the center layer sits on top of a layer of crushed rock absorber, and the top layer sits 5 meters above that. Between the center and top layers is a gap, which houses the detector electronics racks and maintenance shacks.

Vertical planes of scintillator counters cover the sides of the detector on the east and west, and on the bottom parts of the north and south faces. These counters are known as "vertical counters". The scintillator counter configuration will be described in more detail in Section 4.4.2.

Each layer of scintillator counters is sandwiched between planes of streamer tubes chambers. The bottom half of the detector contains ten layers of streamer tube planes and readout strips in between layers of crushed rock. Vertical scintillator counters are also sandwiched between layers of streamer tubes. The streamer tube configuration will be described in more detail in Section 4.4.3.

The track etch layer is horizontal and located in the lower detector about half way between the bottom and central scintillator planes. It contains two types of track etch plastic, CR-39 and Lexan, separated by a layer of iron. CR-39 track etch also covers half of the vertical sides of the detector. The track etch is not used for GC neutrino studies.

In addition, three TRD modules occupy a 6 m×6 m×2 m space inside the upper part of the detector. These detectors measure energies of the muons passing through them, for 100 GeV< E_μ <1 TeV. The TRD modules are also not used for GC neutrino studies.

Figure 4.3 shows a drawing of the full MACRO detector.

4.4.2 The Scintillator System

MACRO's total mass of liquid scintillator is 0.56 kton, contained in 12 m long counters.

The Scintillator Counter Configuration

Figure 4.4 shows one supermodule in cross-section (not to scale). The bottom and center horizontal layers each contain 16 counters. Each horizontal counter has outside dimensions of 12 m×0.75 m×0.26 m, and is viewed at each end by photomultiplier tubes, two per tankend. The counters are laid out on a metal support structure side

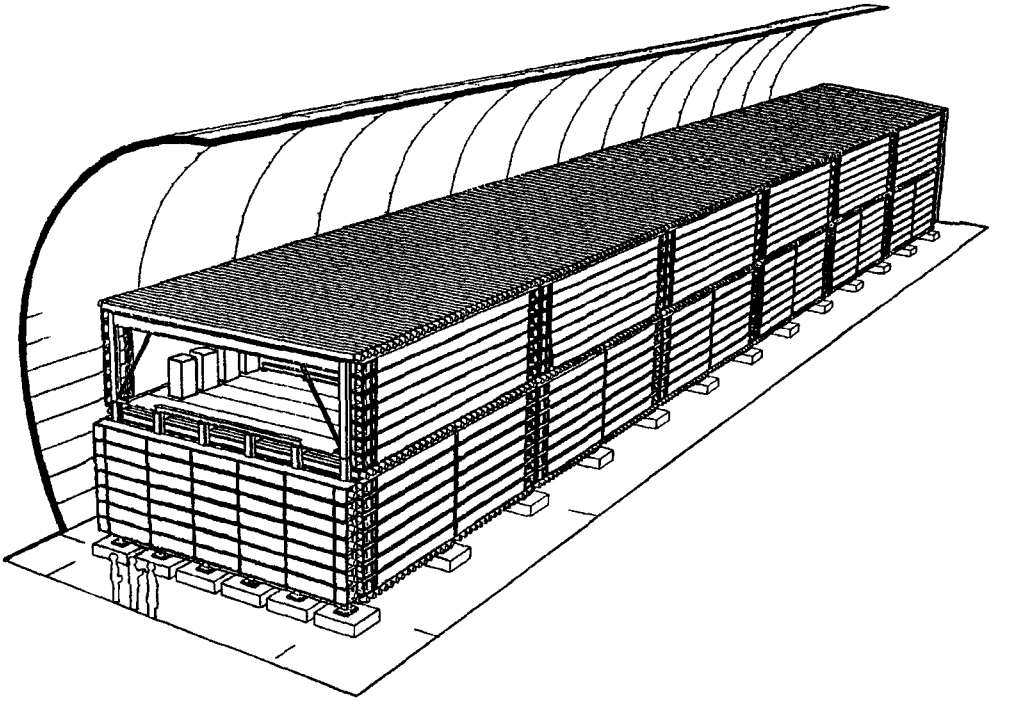

Figure 4.3: Drawing of the full MACRO detector in Hall B.

by side along the east-west axis. There is a small gap between each module (set of 8 counters) in the bottom and center layers. However the top layer (the "attico") contains no gaps and each supermodule contains 17 top layer counters.

The sides of the detector are covered by vertical counters. These are taller and narrower than the horizontal counters, with outside dimensions 12 m$\times$0.23 m$\times$0.47 m. The vertical counters are viewed at each end by one photomultiplier tube. The verticals on the east and west planes are laid out on top of one another in a north-south direction; on the north and south planes the verticals are laid out east to west. There are seven counters on each side of each supermodule in the lower part of the detector for all planes, and an eighth counter just above the center horizontal scintillator layer for the east and west planes. These "eighth layer" counters (12 in all) are shorter by 10 cm than the other vertical counters. There are six more counters (called the "attico verticals") between the center and top layers for the east and west planes on each side of each supermodule.

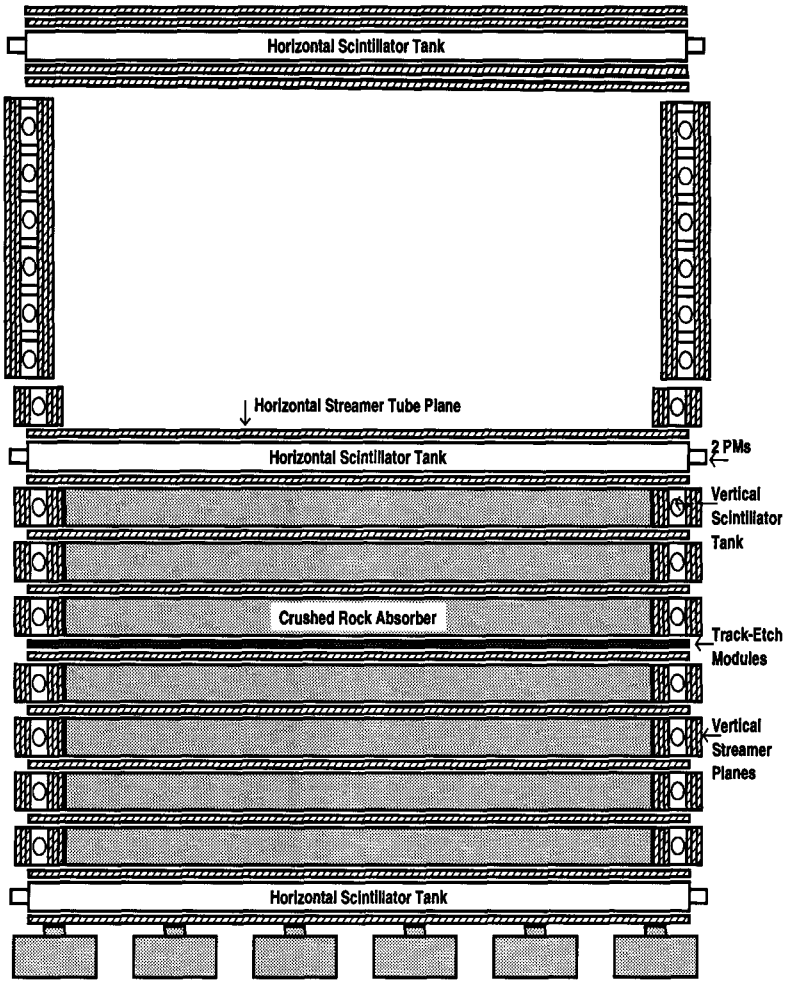

Figure 4.4: Cross-section of the MACRO detector, seen from the end (not to scale).

The counters are made of molded PVC, with walls 0.63 cm thick, and are coated on the inside by a vinyl-FEP reflective material with $n = 1.33$. Light produced inside the counter undergoes total internal reflection for angles less than $\sim 25.6°$ in mineral oil with $n = 1.475$. The counter liner material is resistant to degradation by the chemicals in the scintillator.

Each counter has a clear PVC window at each end separating the main scintillator volume from the end chambers which house the photomultiplier tubes. The counters are filled with scintillator oil to within a few centimeters of the tops of the counters, so that the total fill dimensions are 1120 cm (from end-window to end-window) $\times$ 73 cm (breadth) $\times$ 19 cm (scintillator fill level) for horizontal counters, and 1119 cm

$\times$ 22 cm $\times$ 43.5 cm for vertical counters. The fill level can vary by several millimeters from counter to counter.

The MACRO scintillator counter naming convention is given in Appendix A.

The Liquid Scintillator

The liquid scintillator used in MACRO is composed of very clear ($>$ 20 m attenuation length) mineral oil mixed with scintillation agent. Pseudocumene ($1,2,4-$ trimethylbenzene, C_9H_{12}) is the main scintillation agent; PPO ($2,5-$diphenyl-oxazole) is also added. Since pseudocumene emits scintillation light peaking in the ultraviolet at about 290 nm, mainly in a wavelength regime where the photomultiplier tubes are quite insensitive, wavelength shifters which absorb and then reemit light with a longer wavelength ($\sim$420 nm) are added to the mixture. The wavelength shifters used is bis-MSB (p-bis[o-methylstyryl]benzene). The scintillator mixture also contains an antioxidant to minimize degradation of scintillator light emission due to dissolved oxygen. The density of the scintillator is 0.87 g/cm^{-3}.

The concentration of pseudocumene used was chosen so as to optimize the light yield of the scintillator for particles depositing energy at the far end of the counter. A higher concentration of pseudocumene will increase the number of photons produced for a given energy deposition; however, higher concentrations also decrease the attenuation length so that fewer photons actually get to the phototubes for far end events. By measuring signal size as a function of pseudocumene concentration using muons traversing the far end, the optimum concentration of pseudocumene was chosen to be 3.6 % [69].

The typical attenuation length of MACRO scintillator in the counters is 11 meters, although there is some variation from counter to counter.[1] The light response curve can be well described by a sum of exponentials for the region more than 1 meter away from the phototubes, and by a polynomial near the ends of the counters: see Figure 5.5.

[1]Attenuation lengths can vary from $\sim$ 7-12 m; attico counter attenuation lengths are more likely to be low, due to a relatively cloudy batch of oil that was put into them.

Scintillator Counter Ends

The horizontal counter end chambers (known as "tankends"), illustrated in Figure 4.5, contain two phototubes each. A clear PVC window separates the counter from the end chamber, which is made of the same PVC material as the rest of the counter. The horizontal tankends extend 23 cm beyond the PVC window, and two cylindrical containers are attached to the outside of each end chamber to house the anode-end parts of each phototube.

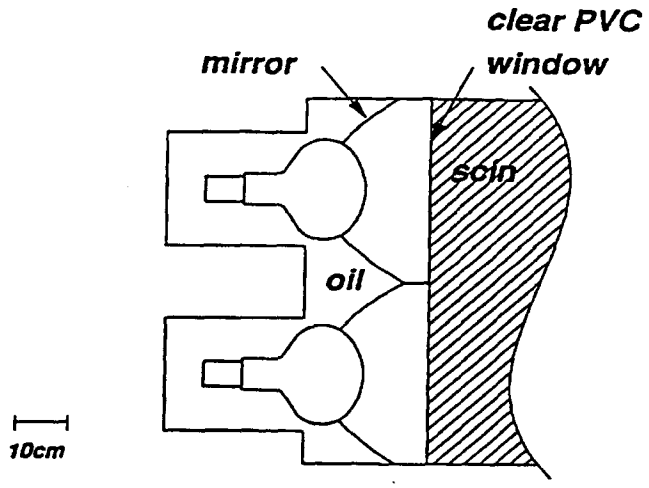

Figure 4.5: Horizontal counter end chamber.

Each phototube is held in place by styrofoam pieces and is also surrounded by a steel magnetic shield which protects it from ambient magnetic fields. The hemispherical photocathode of each phototube looks out into a cone shaped aluminized plastic mirror, designed to optimize light collection at the end of the counter. The tankends are filled with clear mineral oil to improve the optical coupling between the scintillator and the phototubes. Signal sizes from events depositing energy in the counter's main scintillator-filled chamber increase by a factor of $\sim$2 when oil is present in the tankend, due to improved optical coupling; however the fact that clear oil is used in the tankends rather than scintillator ensures that sizes of signals from particles depositing energy very near the phototubes are limited.

Since MACRO phototubes are run with negative high voltage (so that the anode signal does not need to be capacitively coupled), the photocathode is at high volt-

age. Sparking occurring between the photocathodes and the mirrors or the magnetic shields can cause damage to the phototubes; in addition the light from sparking can cause background for a GC search in the data (see Section 6.2.4). The presence of mineral oil in the tankends does suppress, but does not eliminate, tankend sparking. To eliminate the sparking, the magnetic shield and mirrors of the horizontal tankends are brought up to high voltage via a system of connectors inside the tankend (called a "spark kit").

Vertical tankends contain only one phototube (see Figure 4.6). Like horizontal tankends, they have a clear PVC window and are filled with mineral oil. Unlike horizontal tankends, they have a metal mirror and no magnetic shields (it was shown that magnetic fields in the hall are oriented such that they do not have a significant effect on the vertical face tubes). The verticals contain no spark suppression kits, since sparking in vertical tankends has not been problematic (probably due to lack of magnetic shields).

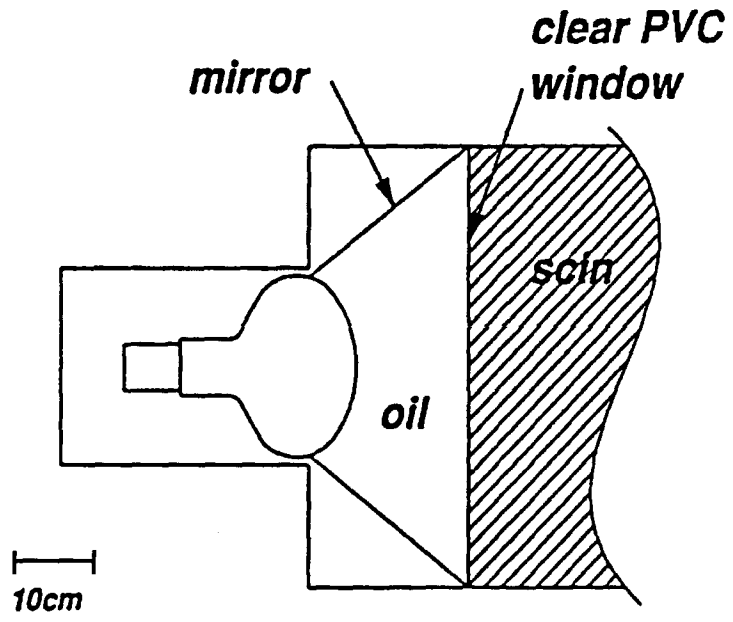

Figure 4.6: Vertical tankend.

Negative high voltage is provided to the phototube bases via a multi-channel LeCroy 1440 system. Because there is only one high voltage channel available per

tankend, for the horizontal tankends, which contain two phototubes, a "splitter box" is employed. The splitter box contains a resistor which provides the correct voltage drop for the tube of the pair which requires the lower voltage. The splitter box is connected to the tankend on the outside.

For the horizontal tankends, the two phototube signals are summed. The anode signals from the phototubes are brought from the tankends to the electronics racks via 30 meter long RG-58 cables. At the electronics racks, six copies of the analog phototube signals are produced by custom-built fast-signal linear fan-outs, for use by the various trigger and pulse recording systems (see Section 4.5.1.)

The Photomultiplier Tubes

Two types of photomultiplier tubes are installed in MACRO. EMI 9350 KA 8" phototubes are installed in all counters of the horizontal layer as well as all of the lower vertical counters. A smaller number of Hamamatsu R1408 8" phototubes are installed in the attico vertical counters.[2] Quantum efficiencies are about 25%.

The two types of phototubes have different single photoelectron (spe) characteristics. Whereas the spe spectra are not particularly important for GC-energy signals and background (which contain at least tens of photoelectrons), they are important for doing monopole physics, since one possible signature of the passage of a slow monopole is a train of spe signals. The custom waveform digitizers are capable of recording such a spe train, and for this reason the gains of the phototubes are set in order that spe signals fall at a level which exceeds the waveform digitizer and slow monopole trigger discrimination level of approximately 2 mV. Phototube gain-setting methods are described in Appendix B.

[2]These Hamamatsu tubes are the same tubes that were installed in the first supermodule during the first prototype running period (see Section 4.7)). They were were chosen at the time because they were the only type available; later, the EMI tubes with their superior single photoelectron performance became available.

Scintillator Calibration Hardware

MACRO employs lasers and light emitting diodes (LEDs) to provide light to the counters for the calibration of the phototubes and their corresponding electronics.

The Laser System

The laser system is used for pulse height and timing calibrations. There are six nitrogen lasers located underneath the detector, serving the bottom and center layers and the lower verticals, as well as three lasers located on top of the attico, serving the top layer and the attico verticals. The lasers produce several ns width pulses of UV light of 337 nm wavelength. The laser pulse properties were chosen to match the timing and spectral properties of ionization-induced light in the scintillator as closely as possible (although laser pulses do tend to be narrower in width for the same number of photons than ionization pulses; see Section 5.3.2). Quartz optical fibers carry laser light to the center of each counter. A stepping-motor-driven light attenuator adjusts the light level for each laser. In addition, reference phototubes view the laser light before and after the attenuator before the light is sent to the counters; the reference signals are used for various triggering and calibration purposes, as will be described in Chapter 5. Laser light flashes and attenuator levels are controlled via Camac through the acquisition computer.

The LED System

The LED system is used for timing calibrations (see Section 5.2.2) and the simulation of various types of events in the counters.

Red LEDS are installed in each tankend, glued onto each tankend mirror. Although the characteristic light spectrum of red LEDs does not match the optimum response of the phototubes, their timing response is quite fast which is necessary for adequate simulation of short-risetime monopole signals. The LED firing patterns are set via a system of specially designed switchbox modules, whose output patterns are controlled via Camac. For calibration runs, the LED switchboxes are pulsed using a programmable pulse generator.

The scintillator calibration hardware is described in more detail in references [69]

and [70]. Calibration procedures for reconstruction of GC-energy level events will be discussed in detail in Chapter 5.

4.4.3 The Streamer Tube System

Plastic streamer tubes operated in limited streamer mode allow for the tracking of charged particles passing through the MACRO detector. They are used for muon veto purposes for a gravitational collapse search (Section 6.2.1).

The streamer tubes are box-like chambers made of plastic and lined on three sides with resistive graphite which acts as a cathode. The chambers are arranged as eight-compartment modules, with each chamber having the dimensions 3.2 cm $\times$ 25 cm $\times$ 12 cm. An anode wire runs along the length of each compartment and picks up signals from streamers induced by passing particles. In addition, for each plane of streamer tubes, metal pickup strips run at a angle of 26.5° to the tubes: these allow two-dimensional readout for each plane of tubes. Multiple horizontal planes of tubes then allow three-dimensional reconstruction of particle tracks. Figure 4.7 shows a cross-section of one of the eight-compartment streamer tube modules. The vertical planes have only strip readout.

The streamer tube gas mixture used consists of 73% helium with 27% n-pentane; helium was chosen to exploit the predicted Drell-Penning effect [61] in the interaction of magnetic monopoles, and the gas mixture was optimized for maximum efficiency.

MACRO streamer tubes run with the very low background noise rate of 40 Hz/m^2. The efficiency for picking up a single ionization is very high, around 20%.

Further information about construction and operation of the MACRO streamer tubes can be found in references [69] and [71].

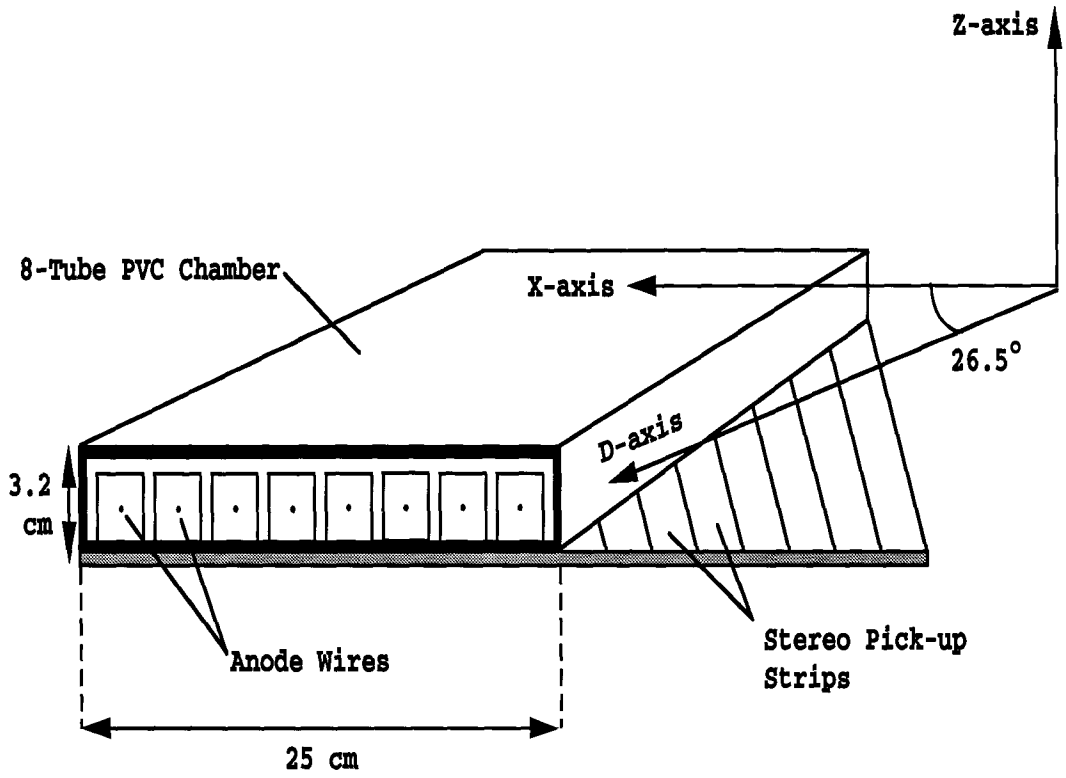

Figure 4.7: MACRO streamer tube chambers and strips.

4.5 Electronics

4.5.1 Scintillator Electronics

There are several specialized trigger systems designed to record MACRO scintillator information for physically interesting processes. Scintillator information is stored as digitized waveforms and in digitized integrated charge form. Specialized electronics systems exist for triggering on slow-moving monopole-like events (the SMT system), fast-moving monopole-like events (the FMT system), lightly ionizing particles (the LIP system), and muons (the ERP and CSPAM). Most of MACRO's scintillator trigger/pulse recording systems are not employed for the detection of gravitational collapse neutrinos, and will not be described here. More detailed descriptions of these systems can be found in reference [69]. In most cases a separate trigger system operates on each supermodule.

There are two specialized trigger systems in MACRO designed to trigger on the

types of pulses that would be seen during a gravitational collapse event. These will be briefly introduced in this section, and described in much more detail in Appendix C.

Due to the light attenuation in the scintillator (such that a given energy deposition can cause signals differing in size by a factor of ~ 3 on the two ends of the counter for a near-tankend event), a simple trigger based on coincidence of pulses from the two sides, each discriminated at a constant threshold, would cause non-uniform triggering as a function of counter longitudinal position z. In other words, the trigger energy threshold and therefore the trigger rate would be a function of z. A uniform energy threshold as a function of z is desirable. Therefore the goal of both trigger circuits is to provide uniform triggering along the length of a counter based on energy deposition.

The PHRASE

The PHRASE (Pulse Height Recorder and Synchronous Encoder) circuit was designed with the detection of gravitational collapse neutrinos as its primary objective; it is described in detail in Section C.1. The nominal energy threshold of the PHRASE is ~ 7 MeV. A uniform energy threshold across the length of a scintillator counter is achieved by means of an analog compensation for light attenuation in the electronics. A unique feature of this circuit is the "secondary threshold": following a trigger the energy threshold is automatically lowered to a lower level of ~ 1.5 MeV to allow the detection of the 2.2 MeV gamma rays from neutron capture following a GC neutrino interaction, equation 3.2. The PHRASE's secondary threshold capability will be described in Sections 6.5 and C.1.3. Waveforms (with 10 ns sampling) are recorded internally to the PHRASE for each trigger.[3]

Unlike any other scintillator electronics system, the PHRASE operates with its own independent data acquisition system: separate microVAXes take care of readout of the PHRASE circuits, and the PHRASE data is combined with the rest of the data by the main acquisition system at a later stage (see Section 4.5.4). The advantage of

[3]For future reference, in this thesis, a "hit" in the PHRASE refers to one primary-threshold triggered waveform pulse in one box, usually corresponding to a single muon or radioactivity event. In the data analysis of this thesis, an "event" is defined as the set of hits (ERP or PHRASE) with reconstructed times within 1 ms of each other.

this configuration is that the detector can still run independently for GC detection even when other parts of the detector are experiencing problems, undergoing maintenance, etc. This configuration has served MACRO well in the past for keeping GC livetime high, especially during construction phases of the experiment.

The PHRASE electronics is described in detail in Appendix C.

The ERP

The ERP (Energy Reconstruction Processor) system is a general-purpose ADC/TDC system whereas the PHRASE is specialized. The ERP was designed as the primary trigger for muons traversing MACRO and measures time and integrated charge information for muons (and any ionizing particles). It also yields a complementary trigger and hit information for GC neutrinos. Like the PHRASE, the ERP triggers on events in a counter which deposit more than a given amount of energy. In this case, however, uniform energy triggering across the length of a counter (i.e. taking into account the position-dependent light attenuation) is accomplished with a digital system: phototube pulse height and timing signals from each side of each counter are integrated onto capacitors, and the integrated signal digitized by means of flash ADC's (FADC). The FADC values for each side are used as addresses for a look up table (LUT), in which corresponding energy and trigger information is stored, and the decision of whether or not to trigger and save the event information is made on the basis of the contents of the LUT.

The ERP uses two separate energy thresholds: the "muon" level corresponds to $\sim$12 MeV, and phototube signals exceeding that threshold are stored in the "muon buffer", which is read out promptly. The muon energy threshold is $\sim$ 1/3 typical muon energy deposition, so that trigger efficiency is high for muon detection. At energies lower than the muon threshold, trigger rates increase rapidly with decreasing energy threshold due to radioactivity (Section 6.2.2). In order not to saturate the muon buffers, events with energy deposition exceeding a lower "GC" energy threshold (nominally $\sim$7 MeV) have their ADC and TDC information stored in a "GC buffer" memory, and are read out in batches of 818 events (approximately every 5-10 minutes)

on each supermodule. The ERP is read out by the main acquisition.[4]

The ERP system is described in detail in Appendix C.

The CSPAM

The CSPAM scintillator trigger is mentioned briefly here because it is used as part of the muon veto for GC hits (described in Section 7.1.5). The CSPAM uses scintillator plane coincidences and is used primarily as a fast particle veto for the FMT system. Because it triggers on through-going fast particles (with <1 μs time of flight in the detector) it is useful for identifying muons.

The Waveform Digitizer

MACRO's custom-built 200 MHz waveform digitizer (WFD) system will be described briefly here because of its usefulness for studies of ERP and PHRASE low energy background (see Section 7.3.3).

MACRO's WFD system [72, 73] is designed to capture waveforms of events with monopole-like signals with high precision and efficiency. To cover the full range of possible monopole velocities, the dynamic range of possible signal sizes covers the range from few mV signals (for recording single photoelectron trains expected for slow monopoles with velocities of $10^{-4}c$) up to several volts (for recording very large pulse heights expected for fast $v \sim c$ monopoles). To accomplish this, the WFD front-end makes use of a specially designed amplifier system with three nearly-linear regimes. The response is calibrated for every channel using known pulse sizes. The waveform digitized pulse heights for each 5 ns time bucket are stored in 8-bit words.

The MACRO WFD system is VME-based, with each card having four channels capable of recording four waveforms. Each channel accepts four inputs and fans in signals for four different tankends (from alternate counter numbers, so that the signals going into each channel are from non-adjacent counters). Therefore each WFD module is capable of serving eight scintillator counters. To distinguish which of the

[4] An ERP "hit" refers to one signal (two-end coincidence) in one box, corresponding to one set of digitizations.

fanned-in inputs corresponds to the recorded waveform, each input has a discriminator bit set when the signal seen exceeds a 2 mV threshold.

Waveforms are stored in an on-board memory, and the readout into the main acquisition is controlled by an in-crate VME computer which allows flexibility for reading out different time intervals and channels for different trigger configurations. For instance, ERP muon triggers cause readout of 1 ms of information from the hit counters following the trigger time. The waveform data read out are zero-suppressed. ERP and PHRASE GC trigger events do not cause any waveform readout under normal circumstances, although this has been done for special runs (see Section 7.3.3).

4.5.2 Streamer Tube Electronics and Tracking

This subject will be addressed only briefly. The streamer tube information is relevant for gravitational collapse studies primarily for use as a muon veto to reduce background for GC burst searches (Section 6.2.1).

The streamer tubes wires and strips are read out separately (lower detector vertical counters have only wire read out). Readout cards are connected directly to the hardware (8-channel for the wires, 32-channel for the strips). The signals go through shift registers along the side of the detector to be fed into the trigger electronics

Streamer tube triggers are formed by various logic combinations of the signals from the different planes, using flexible EPROM-type circuits. Due to the low background noise rate in the streamer tubes, simple plane ORs are used for "muon"-type triggers. The "Bari" trigger is one such trigger: a trigger condition is set when various predetermined configurations of planes fire within approximately 1 microsecond: for instance the trigger condition is fulfilled when 5 out of 10 horizontal planes fire, when 5 out of 8 internal contiguous horizontal planes fire, or when 3 horizontal and 3 vertical planes fire. (The exact trigger conditions are fairly complicated and, being programmed onto an EPROM chip, are easily modifiable and have not been consistent throughout the history of MACRO. See reference [69].)

Streamer tube charge and time information is also recorded using custom-designed

electronics for monopole studies.

The spatial resolution of an individual streamer tube hit is 1.1 cm for the wires and 1.6 cm for the strips. For through-going muons, the wires fire with a typical efficiency of ~95% for each plane traversed by the particle, and the strips fire with ~90% efficiency. It is possible to reconstruct tracks of through-going particles with an instrumental angular resolution of 0.48°. Track reconstruction is performed by the DREAM software package (Section 4.6.1).

4.5.3 The UTC Clock

An additional important piece of equipment associated with MACRO is the universal time clock for determining absolute times of events. This clock, a commercial rubidium oscillator, is located outside the underground laboratories at the external facilities. Its signal is shared by the several experiments at the laboratory. The external master clock signal drives internal slave clocks inside the lab via 8 km long optical fibers. The absolute time scale is set using Italian television signals. The clock signal time is accurate to within 100 μs of the actual UTC time. The data acquisition latches and reads out the UTC clock time signal for most triggers (with the amount of jitter depending on the particular trigger system). The latched information is available with a least count of 100 ns.

4.5.4 Data Acquisition

Most of the MACRO trigger electronics is Camac, with the exception of the waveform digitizer system which is a VME system. The data is read out from Camac or VME via six microVAX computers, which are arranged in a modular fashion. Figure 4.8 shows the overall configuration.

Three of the microVAXes are "main acquisition" microVAXes and serve all of the electronics — scintillator and streamer tube — with the exception of the PHRASE electronics. The PHRASE system has its own separate acquisition system consisting of three microVAXes, to reduce dead time for gravitational collapse detection.

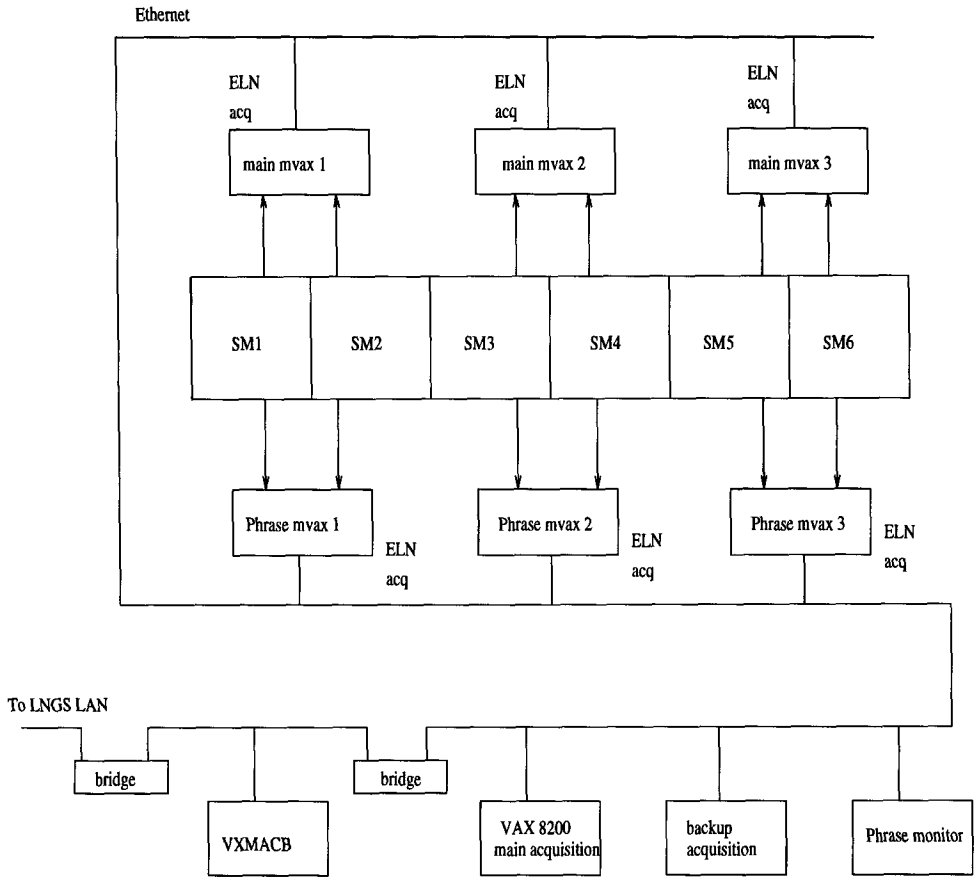

Figure 4.8: MACRO data acquisition microVAX configuration

MicroVAX Configuration

Each group of two adjacent supermodules (1/2, 3/4, 5/6) is served by two independent microVAXes. One microVAX of each pair, known as the "main acquisition microVAX", takes care of "main" electronics. The other microVAX serving each pair of supermodules is dedicated for the readout of the PHRASE electronics. DEC software called VAXELN runs on the microVAXes to perform Camac or VME readout and network tasks. The microVAXes ship data to the main acquisition computer via an Ethernet/DECNET system.

Main Acquisition VAX Computers

The central acquisition computer (VXMACA) is a VAX8200 machine running VAX/VMS. This computer performs data coordination and logging tasks: events from the main microVAXes and the PHRASE microVAXes are combined and the data is written to disk (for temporary storage). The main acquisition computer also serves as the user interface: console software runs on it, as well as various monitoring and spy software. Two separate VAXstations can run the acquisition software and serve as backup computers if the VXMACA main acquisition computer is down or being used for other purposes (e.g. for calibration runs). Runs for which data was taken using the backup acquisition computers are numbered differently.

Additional monitoring software runs on an auxiliary VAX computer (VXMACB). In particular, the software which performs ERP GC "spy" monitoring runs on this computer; this software will be described in detail in Chapter 8.

Networks

The main acquisition computer is linked fully to the rest of the world. Inside Hall B, the local computers are linked by Ethernet and communicate via DECNET protocol. The inside of the tunnel is then linked to the rest of the world via a DEC bridge and an FDDI optical fiber link. DECNET and TCP/IP protocols are used for communication with the outside.

Data Distribution

Before July 1995, MACRO data was written to 8 mm tapes (holding about 2 Gb each) after being copied out of the tunnel, and distributed to all MACRO collaborators. With the addition of the waveform digitizer information to the data stream in summer of 1995, the data rate increased by a factor of about five, to about 1 Gb per day. Starting at the end July 1995, data was written to DLT tapes (holding 10–20 Gb each) as well as 8 mm tapes, and data distribution switched to DLT tape exclusively in November 1995.

4.6 Collaboration Software

4.6.1 DREAM

A standard collaboration software package, known as DREAM (Data Reduction and Event Analysis for MACRO) [74], performs decoding of raw data and event reconstruction for most of MACRO's electronics systems. A streamer tube tracking package is also included, which reconstructs tracks from streamer tube wire and strip information. For the data analysis in this thesis, standard DREAM software is used for tracking and for retrieval of raw ERP data; a modified version is used for PHRASE event reconstruction (see Chapter 7).

4.6.2 CALMOD

A package called CALMOD [75] is used for manipulation of scintillator calibration constant databases. Sets of calibration constants are stored on a run by run basis, changing every few weeks. Standard ERP constants are included, as well as converted PHRASE constants [76].

4.7 MACRO Construction and Running History

The construction of the MACRO detector first started in 1986 after the excavation of Hall B of the Gran Sasso laboratory. By 1989, a single supermodule prototype, in the form of the lower half of the first supermodule of the detector, was completed. It was instrumented with Hamamatsu phototubes and prototype versions of the electronics. The first data was taken in the spring of that year. The first supermodule prototype run lasted from 1989 through 1991, during which time the lower parts of the other five supermodules were being constructed and instrumented. In 1991 the streamer tube system for the six lower supermodules was turned on. Much of the scintillator system of the SM 1 prototype was taken apart and rebuilt to conform to the new standards of the other five supermodules: EMI tubes, magnetic shields and spark kits were

installed, as well as new versions of the electronics. In 1992 the final instrumentation and tuning of the lower 6 supermodules was completed, and in November 1992 the "Six Month Run", a relatively stable running period, began, and lasted until June 1993. The attico structure was added to the detector in 1992 and 1993 and scintillator system instrumentation work for the attico was performed after the six month run period. The Hamamatsu phototubes were installed in the attico verticals, and EMI phototubes were installed in the top layer. During 1993, 1994 and 1995, various systems and extensions of systems were added to the detector and integrated into the acquisition.

Commissioning of the six-supermodule PHRASE system started in 1990; the lower parts of six supermodules were instrumented with PHRASE electronics by 1992 and the attico was fully instrumented by April 1994. Commissioning of the complete six supermodule ERP system was completed in 1994, and full detector running with the ERP system started in in March 1994. All slow monopole trigger, LIP and waveform digitizer electronics was added by the fall of 1995, and the complete "full detector run" started in 1995.

The time period of gravitational collapse analysis covered by this thesis extends from July 1995 (as the waveform system was being added) through February 1996. All GC electronics was fully operational during this period.

Chapter 5 Calibration and Event Reconstruction

5.1 Energy and Time Reconstruction Requirements for a GC Search

MACRO is capable of providing time and energy information for GC neutrino-induced interactions. Good energy resolution is clearly required for mapping the energy structure of a GC neutrino pulse, and for separating signal from noise; a resolution of a few MeV in the signal regime of 5-20 MeV is desirable. Timing is also important for several purposes. First, it is necessary to be able to stamp absolute times on hits for comparison with signals from other neutrino and optical supernova detectors, preferably to within milliseconds (see Chapter 8). Furthermore, relative times between the separate hits in a neutrino burst are required, for mapping the time structure of the burst. For a GC at the center of the galaxy, maximum rates of $\sim$50 Hz are expected, so that minimum separation times between events should be in the few tens of ms range; therefore ms timing accuracy is adequate for determining GC neutrino burst time structure.

In addition, relative tankend timing, at the ns level, is required in order to calculate longitudinal positions of events in the counter; these positions are then used to correct for light attenuation in the counter for determining energies. In addition, relative times between hit counters need to be known in order to veto through-going muons, which have a maximum detector crossing time of about 270 ns.

This chapter will describe how MACRO's GC trigger electronics is calibrated so that energies and positions of recorded events may be reconstructed. The ERP and PHRASE, being fundamentally different pieces of electronics, have quite different calibration and reconstruction procedures. The reader should refer to Appendix C for details on the operation of the ERP and the PHRASE.

5.2 ERP Calibrations and Reconstruction

Full GC event reconstruction entails determination of a hit's energy, position within the counter, and absolute time.

As described in Section C.2, the ERP provides four ADC and four TDC measurements for each hit recorded in the GC buffer. For each side of the counter, there is an ADC and an attenuated ADC value, as well as a TDC and a low-threshold TDC value, all of these values measured with the same high precision ADC. The goal of the ERP calibration procedure is to translate the ADC and TDC values into an energy deposition and longitudinal position, as well as to determine the time of each hit relative to UTC time.

The "standard" ERP calibration procedure is tuned to reconstruct the times of flight and energies of muons, which typically deposit about 40 MeV in a counter. However, GC neutrinos are expected to deposit less energy than typical muons, and the energy regime from 5-20 MeV is of the most interest for GC data analysis. Some elements of standard calibrations are used for reconstructing events of low energy deposition; however, some special procedures are necessary to reconstruct ERP events in the GC regime for consistency between ERP and PHRASE. Standard ERP calibration procedures were developed by the University of Indiana group (and some others) are described in references [77, 78].

To compensate for slow drifts in phototube properties and electronics response, new ERP calibration constants are generated approximately every few weeks on a routine basis, or when apparatus conditions change (e.g. after phototube gain resetting). Special laser and LED calibration runs are performed on a weekly basis.

5.2.1 Absolute Time Reconstruction for the ERP

The times of the ERP hits relative to UTC are obtained using the UTC times read out for each muon trigger and the internal ERP clock time. Unlike muon triggers, ERP GC-level triggers which are present only in the GC buffer and not in the muon buffer do not have UTC clock times associated with them. Therefore their absolute times

must be reconstructed using nearby ERP muon triggers which have both internal ERP clock times and UTC times associated with them. The UT/ERP time fit procedure is not part of the standard calibration procedure and will be described in more detail in Chapter 7.

5.2.2 ERP Timing Calibrations

The longitudinal position of a hit in a MACRO counter can be reconstructed from the difference between the times of arrival of the pulses from the two ends of the counter:

$$z = \frac{v}{2}(T_1 - T_0) \tag{5.1}$$

where z is the longitudinal position ($z = 0$ corresponds to the center of the counter), T_0 is the time of arrival of the pulse on side 0 of the counter, and T_1 is the time of arrival of the pulse on side 1 of the counter. Here, v is an effective longitudinal velocity of light in the counter, taking into account the optical properties of the scintillator and the various ray paths from energy deposition site to the phototube. For the purpose of ERP timing reconstruction, v is given as

$$v = \frac{c}{n_{eff}}, \tag{5.2}$$

where n_{eff} is the "effective index of refraction".

The ERP TDC system is a common stop system, so that the earlier the pulse the larger the TDC value. TDC calibrations involve the determination of the conversion from TDC value to time. It is assumed that the TDC value is linear in time (see equation 5.5). For computing positions within a counter, and times of flight between counters (the latter of importance for muon timing studies), time differences rather than absolute times are important. Therefore the intercept (i.e. the offset, representing pedestal of the TDC circuit as well as delays in signal production and cables) in the TDC calibration need not be such that the time values obtained are absolute: the intercept can contain a global offset which cancels out when time differences between

tankends and counters are taken.

Four types of calibration constants are used to reconstruct ERP counter positions and times of flight between counters: timewalk corrections, slopes, offsets and effective index of refraction n_{eff}. Information from LED, laser and muon light in the counters is used to determine the calibration constants. These timing calibration constants will be discussed in turn in the following subsections.

Timewalk Corrections

"Timewalk" in a time measurement at a fixed discriminator threshold is due to the effect of different relative threshold-crossing times for different total pulse sizes: large pulses have steeper rising edges and start the TDC earlier whereas small, shallower pulses start the TDC later for the same particle arrival time. For ~10 MeV pulses, timewalk corrections are in the several ns range. Figure 5.1 illustrates the situation.

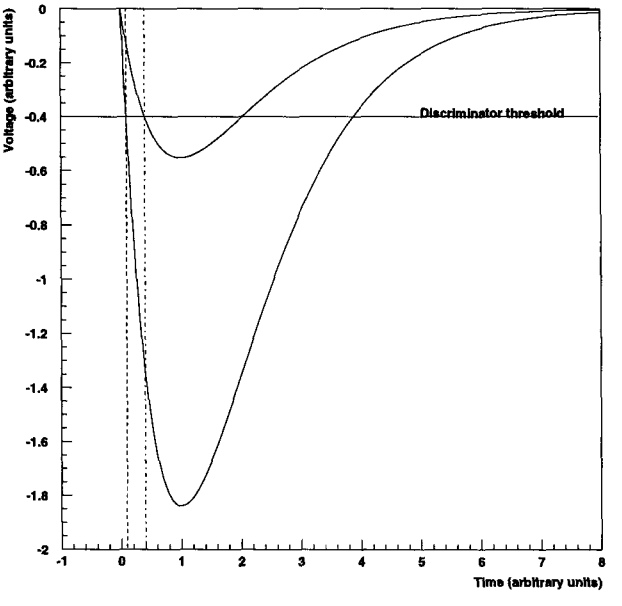

Figure 5.1: Illustration of the timewalk effect: the relative discriminator firing time shifts as a function of pulse size. The solid horizontal line represents the discriminator threshold, and the two vertical lines are the threshold crossing times. The distance between the two vertical lines is the timewalk shift.

The timewalk effect in the ERP TDC data is measured using laser flashes to

produce pulses of varying sizes (it is assumed that the timewalk function is the same for laser and ionization pulses). The laser calibration system causes the ERP system to get its common TDC stop at a fixed time relative to the time of the light in the counter. (The fixed time delay is accomplished by means of a pulse from the laser unattenuated reference phototube going to a "fake box" spare channel in the ERP, timed such that it provides an early global stop). Therefore, differences in TDC value for different pulse heights must be due to the timewalk effect. For each side i of each counter, a fit is made to TDC_i versus ADC_i with the functional form

$$TDCd_i = \frac{TW1_i}{\sqrt{ADC_i}} + \frac{TW2_i}{ADC_i}, \tag{5.3}$$

where $TDCd_i$ is the timewalk correction for side i, ADC_i is the pedestal-subtracted ADC value, and $TW1_i$ and $TW2_i$ are the calibration constants, calculated for each side of each counter. The fit is done separately for low and high threshold TDC values. Note that the functional form is purely phenomenological and not physically motivated.

Real events then have their TDC values corrected by

$$TDCcorr_i = TDC_i - TDCd_i, \tag{5.4}$$

where $TDCd_i$ is given by equation 5.3.

Once the timewalk correction has been applied, times can be reconstructed using

$$T_i = S_i(TDCcorr_i) - T0_i, \tag{5.5}$$

where S_i is the TDC slope for that channel, and $T0_i$ is the offset.

TDC Slopes

During LED calibration runs, LEDs are flashed in the counter with known time delays with respect to a global ERP stop in order to calibrate the TDC slopes S_i for each side of each counter. The global ERP stop is produced by a signal from the LED

pulser which fires an ERP "fake box" (spare channel of the ERP); the LED fake box signal is timed to be early enough that its pretrigger (MBT) makes the global stop. The TDC slope calibration is done separately for both high and low threshold TDC values. Typical values of S_i are 1/6 ns per TDC count.

TDC Offsets

The TDC offset $T0_i$ used in equation 5.5 takes into account relative delays between the TDC times measured by the different channels (due to differences in phototube signal production times, cable lengths, S/H electronics, etc.). The TDC offset calculation is fairly complex, and tuned for upward-going muon timing concerns. Note that the timing offsets $T0_i$ are relative, not absolute.

The TDC offset calibration uses a sample of ERP muon hits for which non-showering single tracks were measured in the streamer tube system. The first step involves determination of the relative timing offset between the two ends of the counter, for each counter, by requiring that the average value of the difference between the counter timing position (equation 5.1) and the measured streamer tube position (resolution $\sim$ 1 cm) be minimized.

For the next step, the relative offsets between the different counters in the supermodule (ERP system) are determined. The streamer tube tracks are used to calculate expected times of flight between the pairs of counters, assuming that the muons travel with $\beta = 1$. An iterative procedure is then used to adjust the offsets of each counter such that the average difference between calculated streamer tube time of flight and measured ERP time of flight is minimized. (Times of flight of muons which pass through more than one supermodule are measured with a separate TDC system; a similar procedure using muons is used to calibrate the inter-supermodule timing offsets.)

Effective Index of Refraction

The final step in the ERP timing calibration involves determination of "effective" refractive indices n_{eff} (used in equation 5.2) for each counter. In this step, the previ-

ously determined offsets $T0_i$ (after the tankend balancing and time of flight steps) are used to reconstruct counter positions, and the average value of the difference between measured streamer tube position and timing counter position is minimized for each counter, now with the refractive index as the free parameter. Typical values of n_{eff} for MACRO counters are $\sim$ 1.5–1.6.

ERP Relative Timing Resolution

With the final set of timing calibrations, the two-tankend relative timing resolution for muons is about 0.5 ns, corresponding to a position resolution of about 10 cm. This position resolution contributes only about 1-2% to the energy resolution σ_E/E (which is typically 10% at 10 MeV). Clearly, the inter-box timing resolution is more than sufficient to veto through-going muons and to reconstruct time structure of GC burst candidates.

5.2.3 Standard ERP Energy Calibrations

Energies are reconstructed from charge measurements from side i of a counter according to

$$E_i = pe_i/R(Z), \tag{5.6}$$

where pe_i is the number of photoelectrons seen at tankend i and $R(Z)$ gives the light attenuation factor for an event occurring distance Z away from the tankend (equation 5.9).

Using the two measurements from the two sides of the counter, the reconstructed energy is a photoelectron-statistics weighted average of the two sides:[1]

$$E = \frac{E_0\sqrt{pe_0} + E_1\sqrt{pe_1}}{\sqrt{pe_0} + \sqrt{pe_1}} \tag{5.7}$$

The charge seen at the phototube is proportional to the number of photoelectrons, and the ERP ADC value gives a measure of the charge. We assume the the ADC

[1] In fact for optimal energy resolution, the weighting $E = (E_0 * pe_0 + E_1 * pe_1)/(pe_0 + pe_1)$ should be used; however the use of equation 5.7 is historical and built into the standard software.

value is linear in photoelectrons (which has been shown to be a good approximation up to muon light levels):

$$pe_i = G_i(ADC_i - ped_i), \tag{5.8}$$

where the gains and the pedestals are the channel-specific calibration constants to be determined by the calibration procedure. The pedestals ped_i give the ADC value at zero light, and the gains G_i give pe per ADC count.

Pedestals

ERP pedestals ped_i are determined using the laser system. Figure 5.2 shows a block diagram of the laser pedestal calibration setup. The laser is fired at the center of each counter at several different light levels, determined by the laser attenuator setting. The chosen light levels start at or below the level where the ERP barely starts to trigger at GC-level (corresponding to $\sim$ $5-6$ MeV) and go up to muon level. Approximately 100 pulses are fired at each setting. The reference phototube views the attenuated light directly out of the attenuator (Section 4.4.2) and the size of its pulse should be proportional to the amount of laser light in the counter. The pulse from this reference phototube is integrated and digitized by a reference ADC, whose pedestal has been determined independently. The reference ADC measurement is assumed to be linear in light and its pedestal value is assumed to represent the level of zero light in the counter.

For each side of each counter, at each attenuator setting the pedestal-subtracted reference ADC and ERP ADC values are averaged. A linear fit is made of ERP ADC versus reference ADC, and ERP ADC values are then extrapolated to zero light to determine the ERP pedestals. Figure 5.3 shows an example of a laser pedestal fit for one side of one counter.

Gains

The ERP gain calibration constants G_i, which set the overall ERP energy scale, are determined using muon data. For each counter, a sample of ERP hits with associated

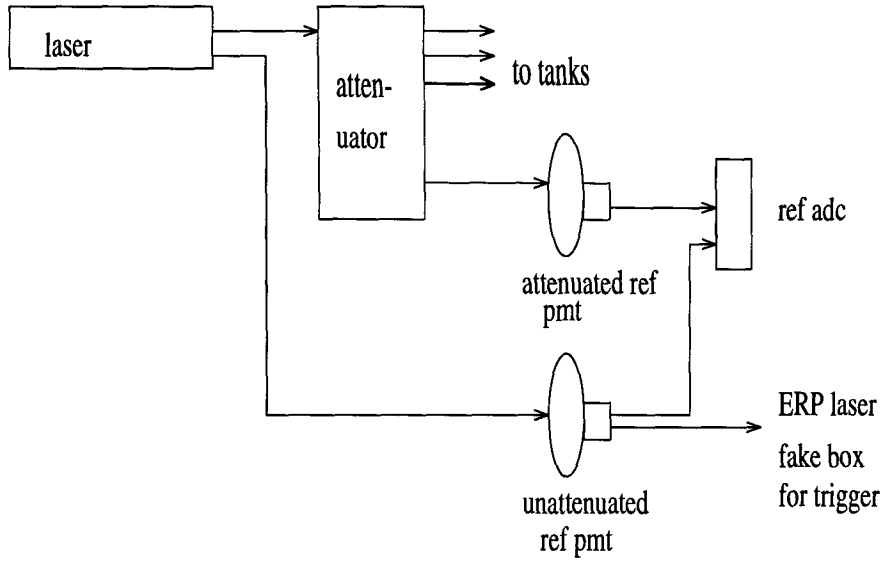

Figure 5.2: Block diagram showing the setup for laser pedestal calibrations, for each supermodule. (There is an additional setup for the attico counters for every pair of supermodules).

non-showering single track muons is selected. The energies are calculated according to equations 5.6 through 5.8 (using the previous set of calibration constants). Energies are then corrected for the muon pathlength in the scintillator counter, using streamer tube track information. Next, the energy distribution is fit to a "pseudo-Landau" distribution which describes the energy loss of a highly relativistic particle in a thin absorber.[2] The fit is weighted such that the peak of the fit pseudo-Landau matches well to the peak of the distribution. An example of such a fit is shown in Figure 5.4.

The ERP gains G_i are then chosen in order to put the peak of the Landau function at a calculated value of 1.8 MeV/cm of pathlength, for each side of the counter.

The gains and pedestals for the ERP attenuated ADC values are determined in the same way as for the unattenuated values. The ERP attenuated ADC (attenuated by a factor of 10 with respect to the unattenuated value) is used for very large pulse charges which enter into the non-linear regime of the ERP response (not relevant for low energy gravitational collapse studies).

[2]The function is a "pseudo-Landau" and not a true Landau distribution because the width parameter (which should be fixed) is allowed to vary freely in the fit, in order to simulate the effect of photoelectron statistics broadening the peak. Detailed studies which include pe statistics broadening have shown that the pseudo-Landau fit peak position is within a few percent of the true peak value.

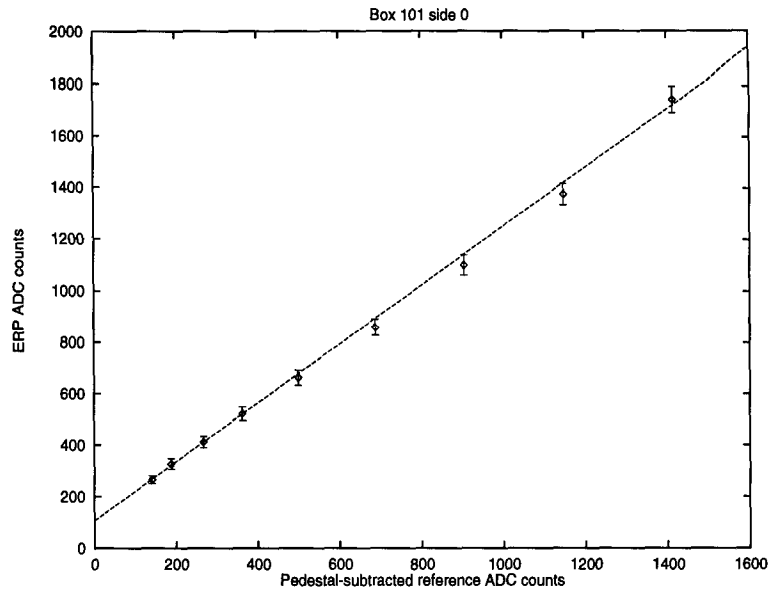

Figure 5.3: Laser pedestal fit for one side of one counter.

Response functions

The response function gives the fraction of light reaching the phototube as a function of distance from the phototube. To first approximation the function can be described by an exponential; it is more accurately described by the 5-parameter semi-empirical function

$$R(Z) = A\exp(-Z/B) + C\exp(-Z/D) + E/Z^2, \tag{5.9}$$

where Z is the distance from the tankend. The $1/Z^2$ term is included to describe the light response function at small Z, where it tends to steepen rapidly; simple exponential fits determined for the central counter region may not work well near the tankend. The response function, shown in Figure 5.5, is determined using a sample of muons with single non-showering streamer tube tracks. Each counter is divided into 12 equal bins, and for each bin the average *pe* value of the muons whose streamer tube position falls into that bin is calculated. Then a fit is performed using equation 5.9. The same fit is used for both ends of the counter.

For the ERP calibration, in practice the "pe" number given by equation 5.8 does not give the true number of photoelectrons; however it is *proportional* to the true number of photoelectrons (with the same proportionality constant for both ends of a

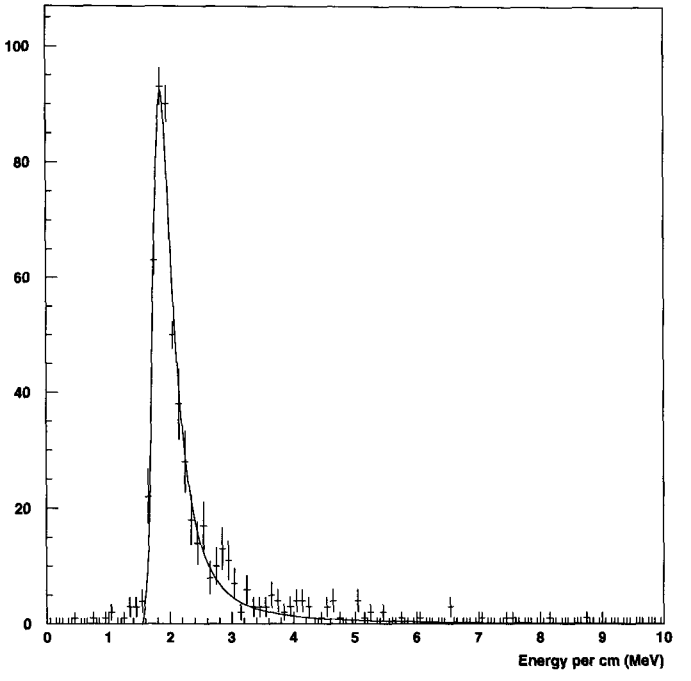

Figure 5.4: Pathlength corrected energy distribution showing the Landau peak from a sample of single muons going through one counter.

counter). The response curve normalization in equation 5.9 is such that the energy calculated from equation 5.6 has the correct value.

The standard ERP calibrations were optimized for analysis of muons, which deposit some 40 MeV in a counter; they were not optimized for low energy events. For this reason the standard calibrations may give somewhat incorrect answers for ERP hits with energies in the regime of interest for GC studies, as will be shown in Section 7.2.3. In particular, for most counters the ERP pedestals are such that the reconstructed energies in the 5–15 MeV regime disagree with the PHRASE energies by 1–2 MeV, on a counter by counter basis. A method which compensates for these discrepancies and provides comparable energies for the purpose of matching ERP and PHRASE events is described in Section 7.2.3.

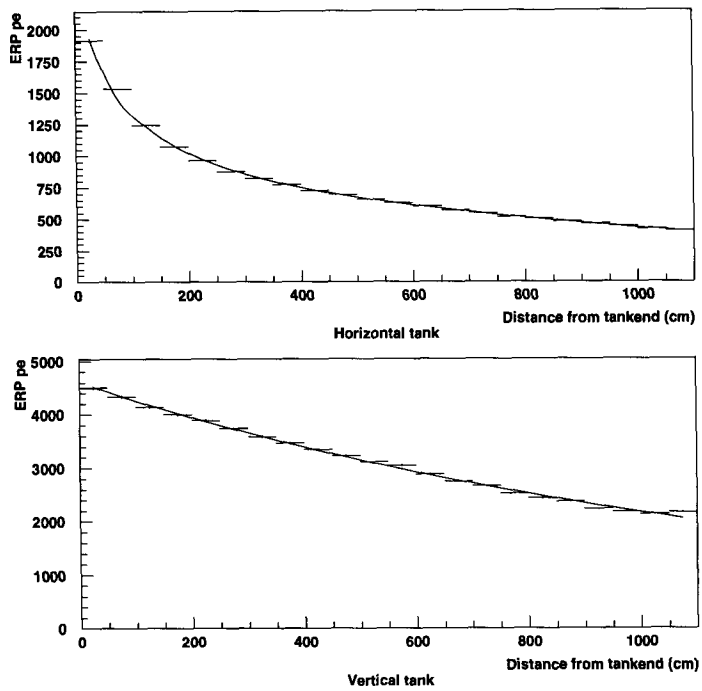

Figure 5.5: ERP response curve fit: average number of pe's for a counter slice versus distance from the tankend calculated from streamer tube position for a sample of single muons. The top plot shows a horizontal counter fit and the bottom plot shows a vertical counter fit.

Counter Longitudinal Position from Pulse Heights

The counter longitudinal position can also be calculated using pulse size measurements from the two ends of the counter. For the ERP, the position calculated using ADC measurements is designated ADCZ (whereas position calculated from TDC information is designated TDCZ).

The ADCZ value is found using the counter response curve information and the ratio of ERP *pe* values (from equation 5.8), by finding the position z such that

$$\frac{pe_0}{pe_1} = \frac{R(z + L/2)}{R(z - L/2)}, \tag{5.10}$$

where z is measured from the center of the counter, L is the counter length, and $R(Z)$ is the response function given in equation 5.9.

5.3 PHRASE Calibrations and Reconstruction

Energy, time and position calibrations and reconstruction for the PHRASE differ in many respects from ERP calibrations. The PHRASE data consists of waveforms sampled at 10 ns intervals, with additional fast clock information. The PHRASE calibration procedure, described in detail in reference [79], was developed by the University of Pisa group.

As for the ERP, new PHRASE calibration constants are generated at several week intervals.

5.3.1 Time Reconstruction

Reconstruction of Absolute Times

The PHRASE internal clock is set to zero by a synchronization pulse for all supermodules at the beginning of every run. For some of the data, the PHRASE global external 100 MHz clock was phase-locked to the UT clock signal. For this data, absolute time reconstruction should be straightforward: the times need merely be reconstructed from the PHRASE GA clock times (Section C.1.4) according to the known clock periods, and referenced to the header time of a single event per run. However, until early 1996 the PHRASE external clock was not synchronized to the UTC clock signal, and so the time measured by this clock was subject to the drift of a free-running crystal oscillator which amounted to a few tens of microseconds over the course of a several hour run. By matching muon events observed by both the ERP and the PHRASE, a secular time correction to the PHRASE time was obtained for each run. This UT time reconstruction procedure was developed for this analysis and will be described more fully in Section 7.1.4.

Reconstruction of Relative Tankend Times

For the purpose of calculating counter positions, relative tankend times are determined for each hit using the GA clock times and the fast clock words (see Sec-

tion C.1.4). Due to the 30 mV front-end threshold of the PHRASE, timewalk does affect the measured PHRASE times. Timewalk is corrected for in the PHRASE using a function of the form,

$$\Delta t = \frac{a}{f}(sph^b - C^b), \tag{5.11}$$

where the time is corrected by $t + \Delta t$, a, f, C and b are constants, and sph is the "sum pulse height", the sum of the individual FADC values of digitizations in the waveform (charge response corrected, see Section 5.3.2). A PHRASE timewalk correction function is measured with the laser using a method similar to that used for the ERP. However in the PHRASE case a universal timewalk correction function is used for all counters.

The overall PHRASE relative timing resolution is 1.6 ns.

5.3.2 Energy Reconstruction

Charge Response

PHRASE energies are reconstructed from the integrated individual digitizations in a waveform, designated the "sum pulse height". The flash ADC's of the PHRASE waveform digitizer saturate for input pulse heights exceeding 262 mV (approximately the 15 MeV level). However, because the widths of the pulses increase monotonically with increasing energy deposition through a large dynamic range, it is possible to write a relation between the input pulse charge (proportional to energy deposition so long as the phototube/fanout does not saturate) and the PHRASE sum pulse height,

$$C = kU(sph), \tag{5.12}$$

where C is the pulse charge, sph is the sum pulse height and k is a proportionality constant depending on the gain of the phototube.

This charge response function U (known as the "linearization" function in Pisa analyses) is used universally for all tankends. It was measured using a Tektronix TDS620 2 GHz digital oscilloscope, by recording waveforms for muon pulses in both

the PHRASE and the oscilloscope. Using the measured waveforms, the sum pulse height in the PHRASE as a function of true input charge was obtained, taking into account the appropriate PHRASE signal transfer function (due to the PHRASE's 50 Mz low-pass input filter). The charge response function for muons is shown in Figure 5.6.

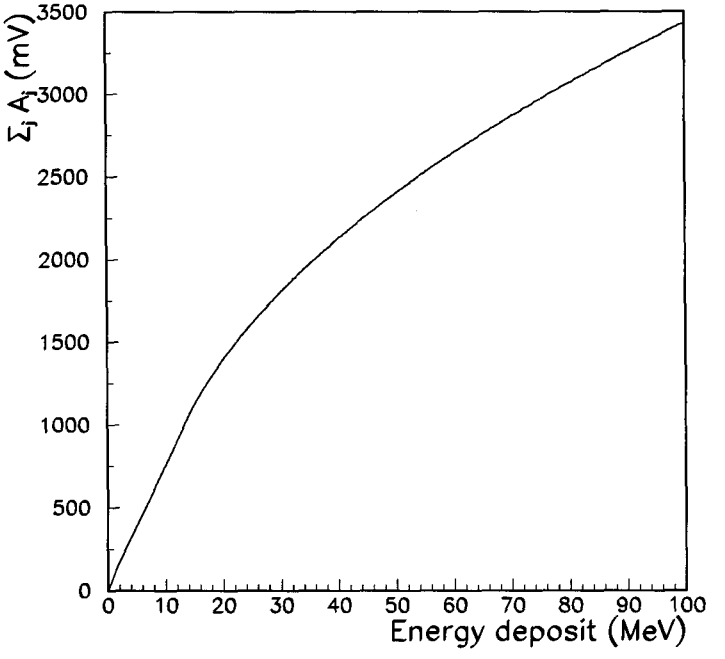

Figure 5.6: PHRASE charge response curve for ionizing particles. The x-axis shows energy deposited and the y-axis shows PHRASE sum pulse height. (F. Cei).

The reliability of this method of determination of the charge response function was tested by measuring the charge response function for laser pulses. For a given pulse charge, laser light produces a narrower pulse shape than an ionizing particle, due to the different physical processes involved; therefore the charge response curve is different. The laser charge response function for several counters is shown in Figure 5.7. The digital-scope-measured laser charge response function did indeed match the independently measured function determined using the laser attenuator setting as a measure of input light, giving confidence that the method is valid.

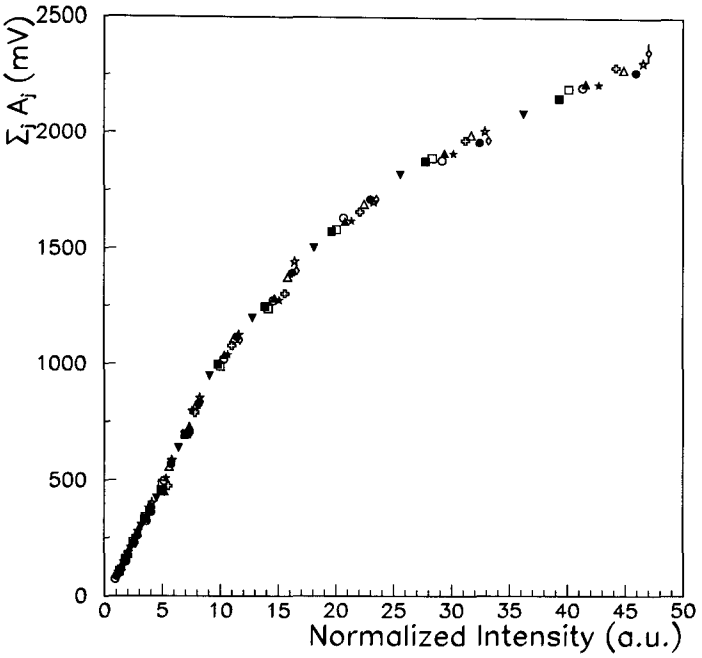

Figure 5.7: PHRASE charge response curve for laser light. The x-axis shows light intensity (A.U.) and the y-axis shows PHRASE sum pulse height. The different symbols represent different counters. (F. Cei).

Tankend Balancing

After charge determination, the relative gains of the two ends of each counter are determined. This is done by looking at the pulse charges seen on each side of the counter for light originating at the center of the counter. Light at the center of the counter used for this calibration can be generated by either the laser (the fibers go to the center of the counter) or by cosmic ray muons, by selecting a sample of muons which go through a narrow bin at the center of the counter. Both methods have been used. The mean ratio of pulse heights for center of counter events is used to calculate the relative gain factors C_0 and C_1 for the two sides of the counter.

Position Response Function

Just as for the ERP, the PHRASE sum pulse heights for each side of the counter are corrected for light attenuation in the counter with a response function $R(Z)$. This function is measured independently for the PHRASE. The functional form used for the PHRASE calibration omits the $1/Z^2$ term:

$$R(Z) \;=\; A\,(exp(-Z/B) \;+\; C(exp(-Z/D))\,, \tag{5.13}$$

where A,B,C, and D are constants.

This function is determined with muons using a similar method to that used for the ERP (although muon position is determined using the PHRASE timing position data itself rather than using streamer tube information). Figure 5.8 shows some examples. The PHRASE response curve shapes generally agree quite well with the ERP response curves, although there are typically ~10-20% discrepancies within a few meters of the tankends.

Energy Scale Normalization

Presently the observation of a distinctive spectral feature due to the 2.6 MeV γ emitted by ^{208}Tl is the standard method for setting the PHRASE energy scale. This method is described in references [80] and [81]. Figure 5.9 shows the differential energy spectrum in the underground laboratory taken with a sodium iodide detector, which has much higher energy resolution than possible with MACRO counters. Figure 5.10 shows the spectrum of PHRASE secondary threshold events. The change of slope in this spectrum corresponds to the ^{208}Tl line at 2.6 MeV seen more clearly in the NaI spectrum. The location of this change in slope can be used to determine the absolute energy scale at the energy of the line (with detector effects and effects of the nearby lines accounted for using a Monte Carlo simulation, such that the change in slope is shifted to ~2.4 MeV.).

This thallium line calibration can be done quickly for all counters (in $\sim$ 1 day) with

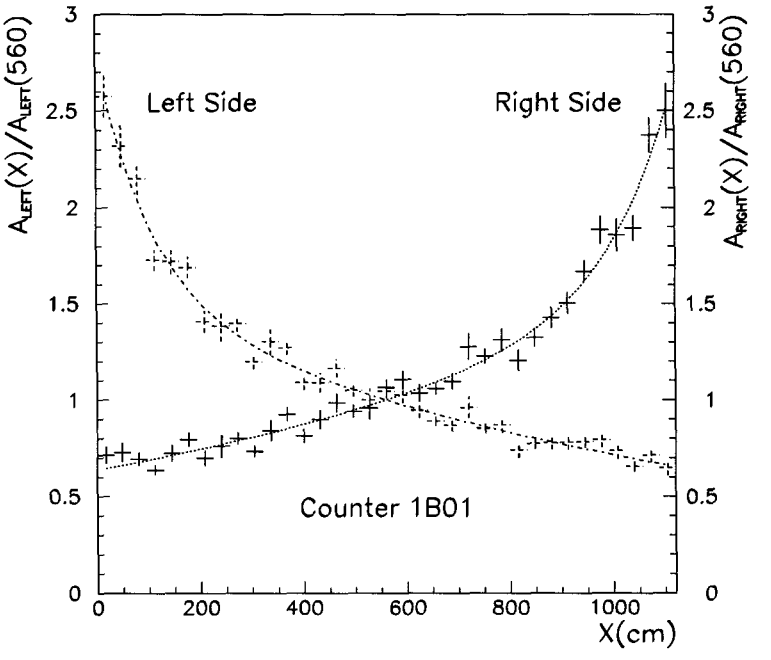

Figure 5.8: PHRASE response curves for the two sides of one counter. (F. Cei).

special runs for which the primary threshold is triggered externally. However such special runs are quite disruptive to data-taking, so they are done only infrequently. More routinely the natural radioactivity background is used to generate the secondary events required for the calibration. About two weeks of data is required for a full thallium line calibration.

The PHRASE secondary thallium line measurement has been checked independently by C. Walter using MACRO's custom 200 MHz waveform digitizers (Section 4.5.1), which have a very low front-end discriminator threshold of 2 mV [68]. The pulses in the 1 ms of data recorded following each muon (for counters not hit by the muon) can be used to measure a low energy spectrum with better resolution than the PHRASE secondary threshold. Figure 5.11 shows the WFD low energy spectrum: the thallium line is visible as a bump in the waveform spectrum at 2.5 MeV (shifted to slightly lower energies due to detector effects and contributions from other nearby lines; this number was calculated independently from the Pisa Monte

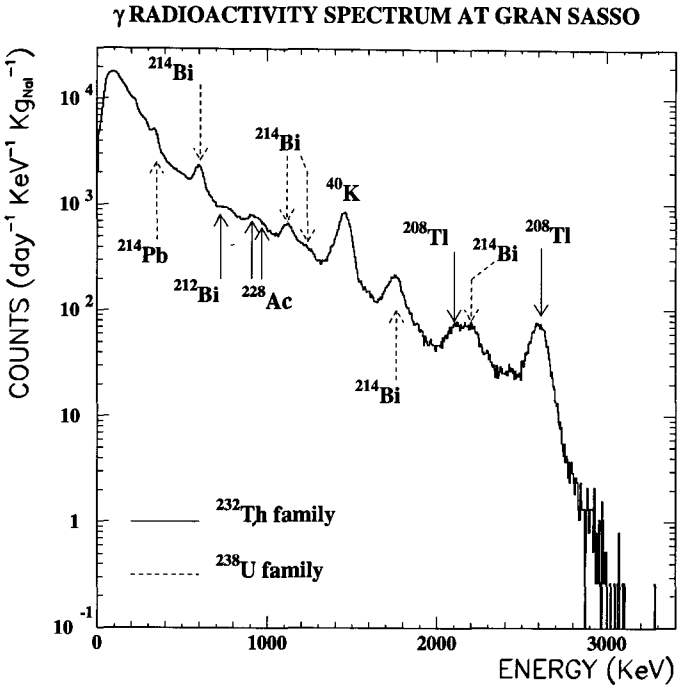

Figure 5.9: Differential energy spectrum measured with a sodium iodide detector, with prominent lines labeled. (F. Cei).

Carlo calculation with a separate Monte Carlo). In addition a ^{40}K line is visible at 1.3 MeV.

The energy scale normalization from the thallium line calibration can be checked using the known energy deposition of muons [79]. For this check a sample of muons is selected, and the resulting distribution is compared to the expected Landau distribution of pathlength-corrected energy losses, calculated by a Monte Carlo method to take into account detector effects. For each counter, the energy scale can be normalized in order that the measured muon energy distribution match the expected one. The expected ratio of the muon peak energy to the thallium line energy is expected to be $\sim$ 15; for a Gaussian fit to the distribution over horizontal counters, the mean ratio of muon peak energy to Tl energy is 14.9 for horizontal counters and 14 for vertical counters. The sigma of the ratio distribution is 0.9 for horizontals and 4 for verticals.

An Am/Be source used to check the efficiency of secondary neutron detection (see

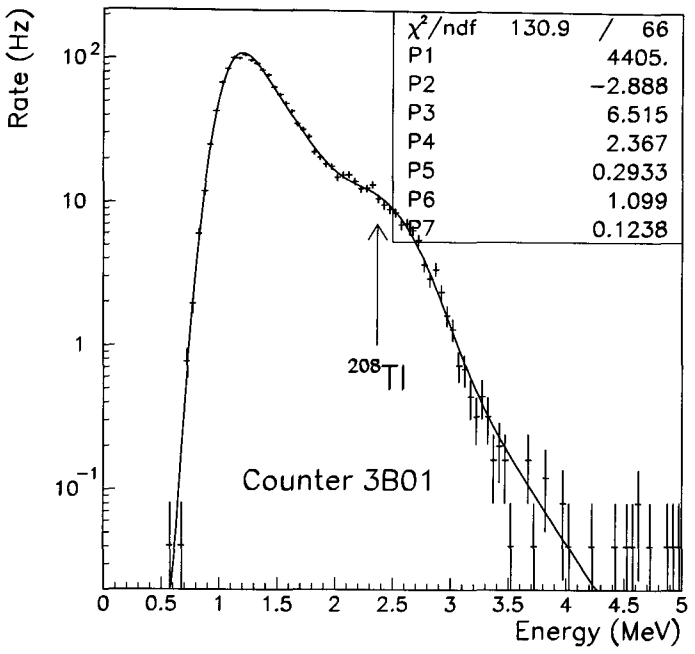

Figure 5.10: Differential energy spectrum measured with the secondary threshold of the PHRASE. (F. Cei).

section 6.5) has also been used to check the PHRASE energy scale calibration [82] during the first supermodule prototype running period. The reconstructed peak energies using muon energy normalization were 4.4 and 2.2 MeV as expected (Figure 6.15), confirming that the calibration procedure was correct. Unfortunately the source check is too disruptive to detector running to be performed regularly.

5.4 Summary of MACRO's GC Trigger and Reconstruction Capabilities

MACRO's two GC trigger circuits operate completely independently and trigger on energy deposited in the counter, independent of counter longitudinal position. Primary energy thresholds (~6–7 MeV) and reconstruction capabilities are approximately equivalent for the two circuits. In addition the PHRASE has the ability to

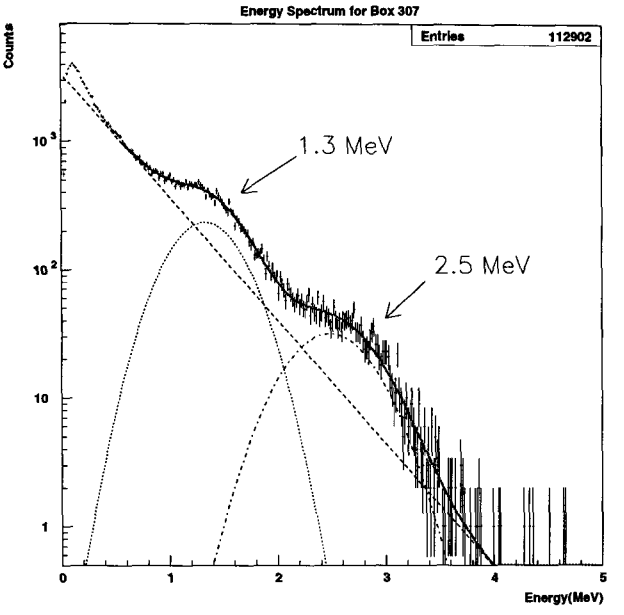

Figure 5.11: Differential low energy spectrum measured with the waveforms. (C. Walter).

lower its energy threshold to the 1.5 MeV level following a 7 MeV trigger (Sections 6.5 and C.1.3), in order to be able to capture the secondary neutron from a primary $\bar{\nu}_e$ absorption.

The PHRASE energy resolution in MACRO horizontal counters is approximately ~10% at 10 MeV and ~15% at 2.5 MeV [79]; it is somewhat worse for vertical counters. The ERP energy resolution, after readjustment, is similar to the PHRASE resolution above ~6 MeV. At 10 MeV, about half of the energy resolution comes from "instrumental" sources; the remainder is due to photoelectron statistics (about 20 photoelectrons per MeV).

Time resolution for the measurement of times between two tankends in a single counter is about 0.5 ns for both the ERP (0.7 ns for the PHRASE), which yields a position resolution of ~10 cm for muon energies (~15 cm for 10 MeV events). This position uncertainty contributes a few percent to the energy resolution.

(Section C.1.4). The absolute time of any PHRASE event with respect to UT must be reconstructed; Section 7.1.4 gives details of the procedure. For the time periods

when the PHRASE external clock was phase-locked to the UTC signal, absolute times of PHRASE events can be known to $\sim$100 μs with respect to UT; when time fits to muons are required for absolute time reconstruction, the accuracy is not quite as good. ERP GC events have absolute times reconstructed using muons to $\sim$20–50 μs with respect to the UT clock signal and therefore absolute times are known with respect to UT to $\gtrsim 100\mu$s.

Dead time for both trigger circuits is very low. For the ERP, the dead time on each supermodule for each individual GC event stored is 250 μs (the time it takes for the RS to store the information in the GC buffer). A longer $\sim$1 s dead time is introduced for a single supermodule (one sixth of the detector) for every GC buffer readout, about once every 5–10 minutes. PHRASE overall dead time (4 ms per module per primary trigger) is such that there is less than 1% loss of events even for acquisition rates of 50 Hz.

Chapter 6 Detecting Gravitational Collapse Neutrinos with MACRO

This chapter will examine in detail the capabilities of the MACRO detector for detecting neutrinos from gravitational collapse.

6.1 The Expected Signal in MACRO

As discussed in Section 3.2, MACRO's 0.56 kton of scintillator allows for excellent sensitivity to $\bar{\nu}_e$ via the inverse beta decay reaction 3.2, as well as some limited sensitivity to elastic scattering reactions and the neutral current excitation of ^{12}C.

The signal formalism given in reference [83] will be used here. In general, the rate of detected events expected from a supernova at distance d kpc is given by

$$\frac{dN_{det}}{d\epsilon\ dt} = \frac{N_t \sigma \eta(\epsilon) N_{src}(\epsilon, t)}{4\pi d^2} \tag{6.1}$$

where N_{det} represents the number of events detected, ϵ is the neutrino energy, t is time in seconds, σ is the interaction cross section, $N_{src}(\epsilon, t)$ is the number of neutrinos per unit energy and time from the supernova, N_t is the number of target particles, and $\eta(\epsilon)$ is the detector efficiency as a function of energy. For the case of the most important scintillator neutrino detection reaction, inverse beta decay (equation 3.2), the detected particle is a positron with total energy $\epsilon_e = \epsilon - Q$, where $Q = 1.29$ MeV. To first approximation, for this reaction,

$$\sigma = \frac{\sigma_0 \epsilon_e p_e}{m_e^2}, \tag{6.2}$$

where p_e is the positron momentum, $\sigma_0 = 2.38 \times 10^{-44}$ cm^2, and m_e is the mass of

the electron. N_t is the number of protons in the target,

$$N_t = 6.7 \times 10^{31} f M, \tag{6.3}$$

where M is the total target mass in kton, and f is the ratio of the fraction by mass of free protons in the target material to the fraction by mass of free protons in water. For liquid scintillator (with chemical formula C_nH_{2n}), $f = 0.14/0.11$.

We assume that the stellar core radiates as a blackbody, with the time dependence of $N(\epsilon, t)$ coming in from the evolution of the blackbody temperature with time (cooling):

$$N_{src}(\epsilon, t) = \frac{A_0 \epsilon^2}{e^{\epsilon/T(t)} + 1}. \tag{6.4}$$

$T(t)$ gives the evolution of the blackbody temperature with time t after core collapse. N_0, the total number of neutrinos emitted from the gravitational collapse, is given by

$$N_0 = \int_0^\infty \int_0^\infty N_{src}(\epsilon, t) d\epsilon dt, \tag{6.5}$$

so

$$A_0 = \frac{N_0}{(F_2(0) \int_0^\infty T(t')^3 dt')} \tag{6.6}$$

where $F_2(0) = \int_0^\infty dx x^n/(exp(x) + 1) = 1.803$.

Rearranging the above expressions and substituting the appropriate constants, we obtain:

$$\frac{dN_{det}}{d\epsilon\, dt} = f \left(\frac{0.2}{\text{MeV}^2}\right) \left(\frac{50\ kpc}{d}\right)^2 \left(\frac{M}{kton}\right) \left(\frac{N_0}{10^{58}}\right) \eta(\epsilon) F(\epsilon, t), \tag{6.7}$$

where

$$F(\epsilon, t) = \frac{\epsilon^2(\epsilon - Q)\sqrt{\epsilon^2 - 2Q\epsilon + Q^2 - m_e^2}}{F_2(0)(\int_0^\infty (T(t'))^3 dt')\,(e^{\epsilon/T(t)} + 1)}\ \text{MeV}^2 \tag{6.8}$$

$T(t)$ may be obtained from a fit of the SN1987A neutrino data. A power-law cooling parameterization given in reference [83] is used in the following calculations:

$$T(t) = T_s(1 + at/n)^{-n}, \tag{6.9}$$

where the SN1987A best-fit parameters (from a joint-likelihood fit to the Kamiokande II and IMB data) are $n = 0.5$, $a = 0.116$ s^{-1}, $T_s = 4.08$ MeV and $N_0 = 0.78 \times 10^{58}$. This parameterization is shown in Figure 6.1: the blackbody temperature decreases from 4.08 MeV to 1.9 MeV over 15 seconds.

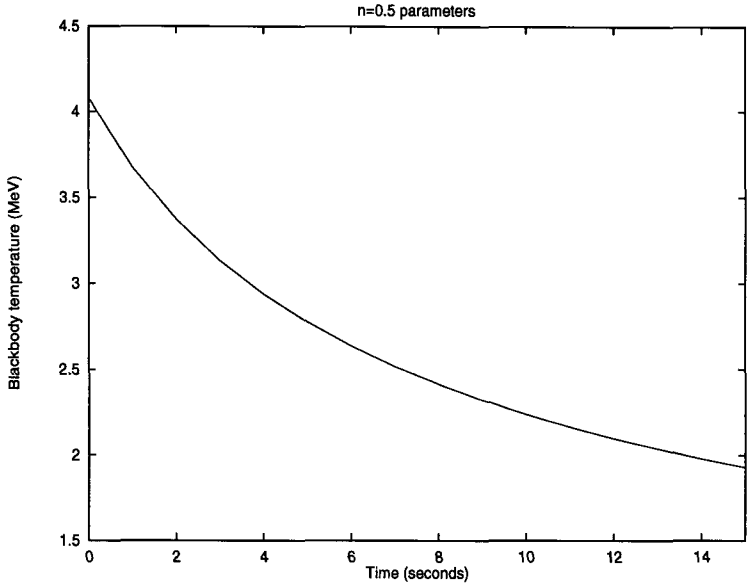

Figure 6.1: Blackbody temperature as a function of time for the SN1987A best-fit power law cooling parameterization, equation 6.9.

As a simplification, in equation 6.7 we will use the approximation that detector efficiency is a step function in energy, with 90% efficiency above threshold energy, i.e.

$$\eta(\epsilon_d) = 0, \ \epsilon_d < E_{th} \tag{6.10}$$

$$= 0.9, \ \epsilon_d \geq E_{th} \tag{6.11}$$

where in this case ϵ_d is the energy of the detected particle, and E_{th} is the energy threshold of the detector. Detailed Monte Carlo studies [79, 84], taking into account the leakage of positron energy from MACRO's high surface area counters, have shown this to be a reasonable approximation.

Substituting into 6.7 and integrating over neutrino energies and time, we get the number of detected events at a given time t after collapse as a function of detector

energy threshold,

$$N_{det}(E_{th},t) \;=\; Af\int dt\int_{E_{th}+Q}^{\infty} d\epsilon \frac{\epsilon^2(\epsilon-Q)\sqrt{\epsilon^2-2Q\epsilon+Q^2-m_e^2}}{(\int_0^\infty (T(t'))^3 dt')\,(e^{\epsilon/T(t)}\;+\;1)} \tag{6.12}$$

where

$$A \;=\; 0.2\left(\frac{50\text{ kpc}}{d}\right)^2\left(\frac{M}{\text{kton}}\right)\left(\frac{N_0}{10^{58}}\right)(F_2(0))^{-1}\text{ MeV}^{-2} \tag{6.13}$$

We can now substitute relevant MACRO parameters. Figures 6.2 and 6.3 show the results of the integration in equation 6.12: Figure 6.2 shows the total number of inverse beta decay events seen as a function of time for $E_{th} = 7$ MeV, for $d = 10$ kpc and $d = 20$ kpc. Figure 6.3 shows the number of events seen in the first 20 seconds as a function of detector energy threshold for the same two distances.

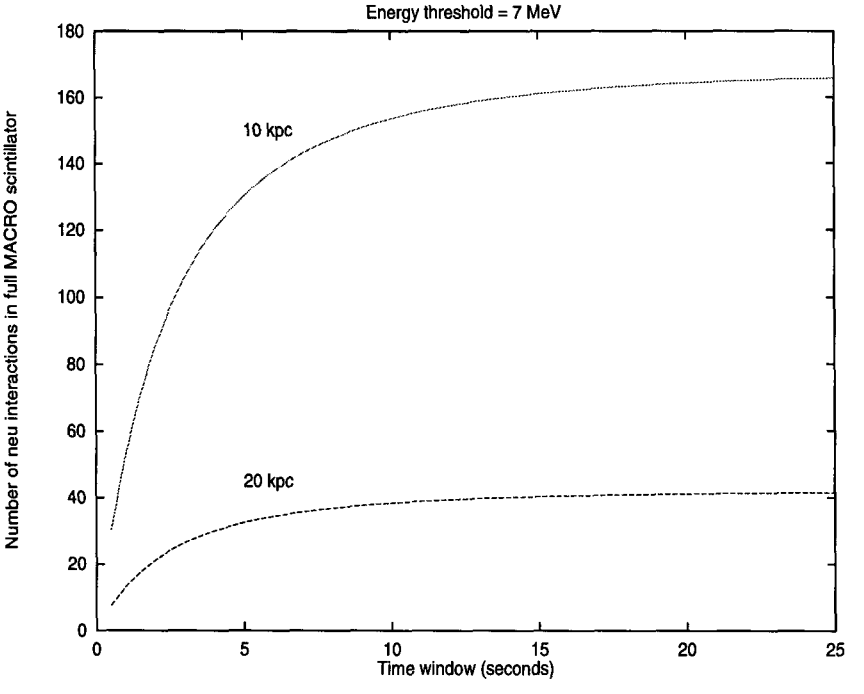

Figure 6.2: Calculated number of inverse beta decay interactions seen in MACRO as a function of time since core collapse, for an energy threshold of 7 MeV, and for GC distances of 10 and 20 kpc. (The numbers of neutrino interactions are simply scaled by $d_1^2/d_2^2 = 1/4$ for the two distances.)

Figure 6.4 shows the expected neutrino and positron differential energy spectra in liquid scintillator. Figure 6.5 shows the expected energy spectra for four (unequal)

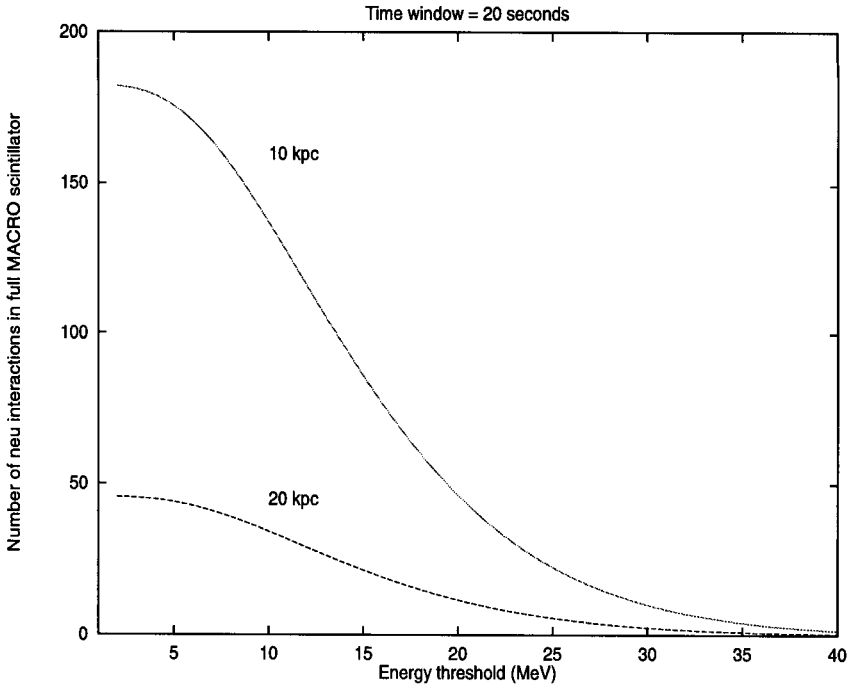

Figure 6.3: Calculated number of inverse beta decay interactions in MACRO as a function of energy threshold, for a 20 second time interval and for GC distances of 10 and 20 kpc. (The numbers of neutrino interactions are simply scaled by $d_1^2/d_2^2 = 1/4$ for the two distances.)

time slices, showing the softening of the spectrum with time.

Similar calculations can be done for electron scattering and carbon excitation (references [85, 86]).

Table 6.1 gives a summary of the number of events expected from a gravitational collapse at 10 kpc.

Reaction Type	Number of Events Expected
$\bar{\nu}_e + p \rightarrow e^+ + n$	160
$^{12}C + \nu_x \rightarrow {}^{12}C + \nu_x' + \gamma(15.11\ MeV)$	10
$\nu_x + e^- \rightarrow \nu_x + e^-$	2

Table 6.1: Expected numbers of events for the most important GC neutrino reactions in MACRO, for a GC at 10 kpc, at a 7 MeV energy threshold.

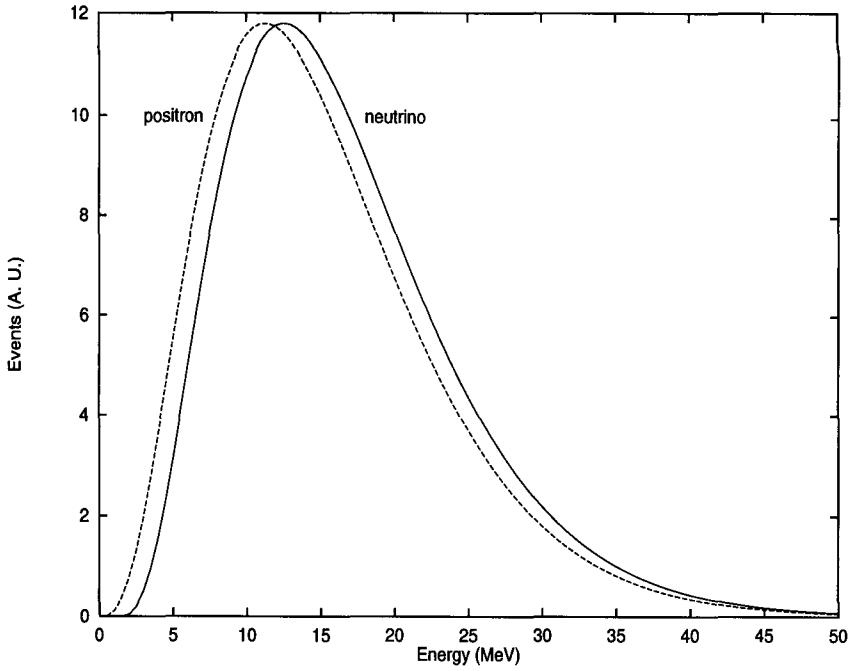

Figure 6.4: Differential energy spectra for neutrinos (right) and positrons (left) in scintillator, integrated over time, for best-fit SN1987A parameters.

6.2 Backgrounds

What limits the sensitivity of the MACRO detector for detecting bursts of GC neutrino events is the rate of background counts which can fake clusters of hits in time from random fluctuations. The various types of background will be discussed in this section.

There are three general classes of background for the detection of GC neutrino events in MACRO: cosmic ray muons, radioactivity from the surrounding rock and concrete and instrumental background (e.g. electrical discharges). In addition, products from muon-induced spallation may contribute.

6.2.1 Cosmic Ray Muons

The rate of cosmic ray muons reaching the detector is reduced by the rock overburden by a factor of about 10^6. The rate observed is approximately 1 muon per supermodule per 30 seconds. Most (~95%) muon events can be easily identified and eliminated

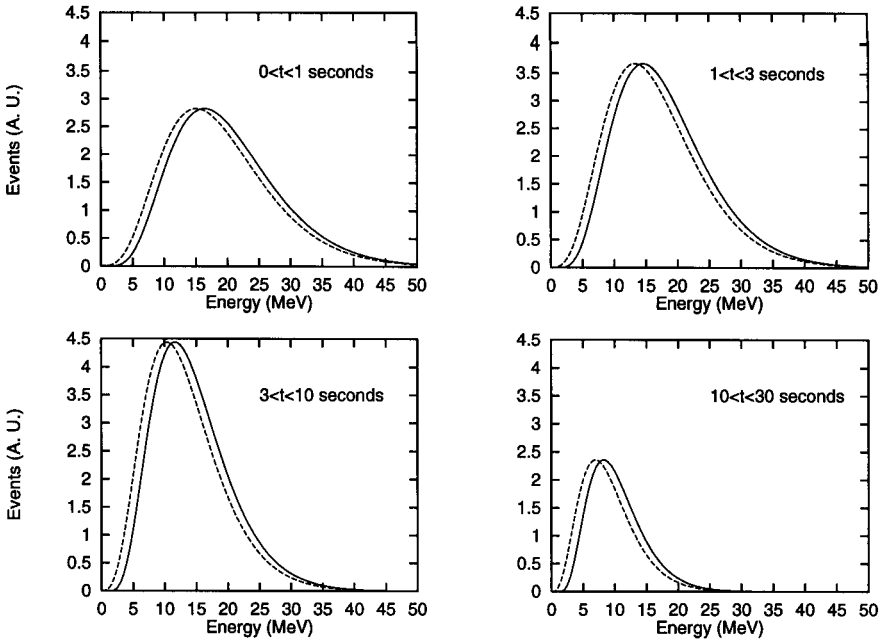

Figure 6.5: Differential energy spectra for neutrinos and positrons in scintillator, for different (unequal) time slices, for best-fit SN1987A parameters.

from a GC burst search data sample. The specific details of the veto cuts used for suppressing muons from the data sample will be given in Section 7.1.5; here, a general description of the cuts will be given.

- Multi-box coincidences in the scintillator. Through-going muons have very nearly $\beta = 1$ and so muon events hitting the scintillator counters will be separated in time by less than 270 ns (the time of flight for maximum path length within the detector), whereas the events from a GC are expected to be separated by at least milliseconds, even during the first few seconds when their rate is highest (unless the GC occurs very nearby). The particles from muon-induced showers are also generally fast and deposit energy within the counters within tens of nanoseconds of the muon event.

- Streamer tube information. Streamer tube tracks also identify muon events. When tracks are unavailable, large numbers of hits in either the wires or the strips can be indicative of the passage a muon.

- Energy deposition. Through-going muons also leave an average of 40 MeV in a horizontal counter for a typical pathlength, and GC neutrino energies are expected to be mostly in the range 10-20 MeV, so a large (> 20 MeV) energy loss can indicate a muon. However, this criterion is not used in this thesis, lest signals from anomalously-high neutrino energy collapses be eliminated. The data analysis in this thesis has no upper energy cut.

There always remains some background from cosmic rays that cannot be eliminated by criteria such as those listed above. For instance, some muons only clip part of the detector or part of the scintillator counter, so that only a single counter is hit, and a track is not clearly visible and/or a small number of streamer tubes are hit. In addition, muon energy loss may appear small due to a small path length in the counter.

6.2.2 Radioactivity

The most significant background for the detection of GC neutrinos comes from radioactive decays which happen in the rock and concrete surrounding the detector. Radioactivity present in the building materials of the detector also contributes. Such radioactivity events populate the $2 - 10$ MeV energy regime, of interest for GC neutrino detection. References [87],[88],[89] and [79] give details of extensive studies of MACRO's radioactive background using the PHRASE.

This radioactivity background consists mostly of gamma rays from the ^{238}U and ^{232}Th families, which Compton scatter in the scintillator to produce light. In addition, neutrons emitted by radioactive fission and cosmic ray spallation are slowed and captured in the scintillator and detector materials.

A differential energy spectrum of the radioactivity background taken with a NaI detector in Hall B is shown in Figure 5.9. The largest bump is due to a line from ^{208}Tl; this line can be used for calibrating the energy scale of MACRO data, as was described in Section 5.3.2. The single counter counting rates in MACRO due to this background measured with the PHRASE secondary threshold amount to about

5 kHz at a 1 MeV threshold, decreasing rapidly to about a 1 Hz at 4 MeV. The spectrum cuts off dramatically at an energy threshold of around 5 MeV, at about the point where MACRO starts triggering for "primary" events. Figure 6.6 shows some integral energy spectra for MACRO data. The plot shows rate over energy threshold for ERP hits, PHRASE hits, and hits present in both (the differences will be discussed extensively in Chapter 7). Note that triggering efficiency for the ERP and for the PHRASE primary threshold drops dramatically below $\sim$ 7 MeV, so that the rates at lower energies do not approach the ones given above (which were measured using the PHRASE secondary threshold), but rather flatten out corresponding to the hardware energy threshold.

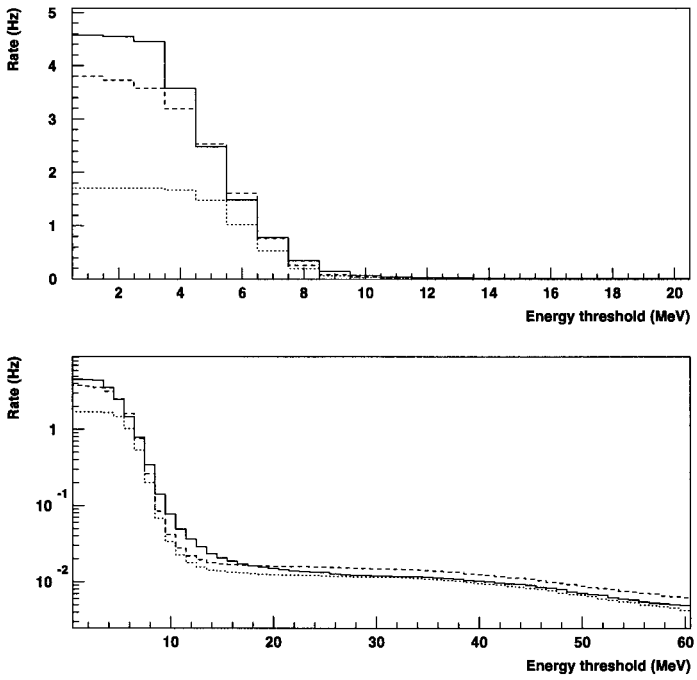

Figure 6.6: Typical integral energy spectra in the full MACRO detector, for ERP hits (solid line), PHRASE hits (dashed line) and hits triggering both the ERP and the PHRASE (dotted line). The bottom plot shows the same on a log scale out to higher energies, to show the effect of residual muons in the data sample.

Since the background rate increases so rapidly with decreasing energy, and the

expected total number of signal events from a GC event increases only slowly with decreasing energy, one can increase the signal to background ratio for an expected GC neutrino signal by making an appropriate energy cut: signal to background is optimized at energy thresholds in the range 10–15 MeV, as will be shown in Section 6.4 following. However, the secondary neutron signals at only 2.2 MeV are deep in the background and so can be detected with much less efficiency: see Section 6.5.

6.2.3 Spallation

Another potential background comes from cosmic ray muons which interact with carbon nuclei in the detector, causing spallation reactions. Reference [79] estimates the rate of such background events in MACRO to be a few thousand per year, with no appreciable impact on the data. Spallation-induced radioactive nuclei with long half-lives are also present from the passage of muons through the rock surrounding the detector; however such background is probably negligible for MACRO because the products range out before reaching the counters.

In addition, spallation events are expected be correlated in space with the inducing muon (within meters), and therefore can be rejected as GC bursts by a position uniformity criterion for a candidate burst.

6.2.4 Sparking

Occasionally, sparking can develop in the tankends as the phototube and mirror which are at high voltage discharge to nearby grounds, in spite of the measures taken to eliminate this problem (see Section 4.4.2). Internal sparking can also develop in a phototube. The sparks produce light which can be seen at one or both of the tankends. Spark pulses in a tankend can simulate low-energy pulses, and tend to come in rapid succession. However, spark burst episodes can be easily distinguished from GC bursts by the fact that the hits are very localized in space (they appear in a single counter, and in addition the reconstructed positions of spark events are close to a tankend). Chronically sparking counters are also eliminated from the data sample

for a particular time period if necessary. Section 7.4.2 gives details about such cuts for the data analysis.

6.3 Burst Search Method

The basic GC analysis burst search procedure will be outlined here; details of data reconstruction, cuts, etc. will be presented in Chapter 7. The same general method is used for both offline searches (Chapter 7) and online searches (Chapter 8).

The basic GC burst search procedure is fairly simple: ERP and PHRASE-triggered events are reconstructed and required to pass data quality and muon rejection cuts. Next, an energy cut at software energy threshold E_{th} is made. Several different software energy thresholds, ranging from 7 MeV to 15 MeV are chosen and the burst search is redone for each.

Several time windows are then chosen, typically ranging from 1 second to 20 seconds. For each time window T, events passing all cuts are looped through. For each event, the number of subsequent hits with energy exceeding the software threshold and falling within the time window T are counted: if there are n such events, the cluster is considered a *burst of multiplicity n*. If any multiplicity n has a sufficiently low Poisson probability, i.e. if

$$\mathcal{P}(n,\lambda,T) = \frac{(\lambda T)^n e^{-\lambda T}}{n!} < \mathcal{P}_{th}, \tag{6.14}$$

where $\mathcal{P}_{th}$ is the probability threshold and λ is the background rate (at energy threshold E_{th}), then the burst is considered an "interesting" candidate, and information (counters hit, energies, positions, times) about all the hits in the burst is saved for later examination.

6.3.1 Multiplicity Thresholds

The multiplicity N_{mt} corresponding to the probability threshold $\mathcal{P}_{th}$ is known as the *multiplicity threshold*, i.e. N_{mt} is the smallest n satisfying 6.14 for a given burst search.

The multiplicity threshold is calculated in advance of performing the burst search on the basis of the measured background rate λ and the chosen $\mathcal{P}_{th}$. There are two levels of multiplicity thresholds used to define GC burst candidates. A "preliminary" candidate corresponds to a Poisson probability $\mathcal{P}_{th} = 10^{-5}$. The multiplicity threshold corresponding to a preliminary candidate is denoted N_{pr}.

Preliminary burst candidates with $N > N_{pr}$ occur in MACRO a few times per month. Therefore, for the purpose of setting stringent online alarm conditions (see Chapter 8) for announcement of a burst to other observatories, this probability threshold is not sufficiently low. To define an alarm candidate in a conservative way, bursts must satisfy the condition that they are sufficiently improbable that a Poisson fluctuation burst of that multiplicity will occur with less than 0.1% probability over a 10 year time period. Such candidates will be referred to as "ten year" candidates, and the multiplicity threshold corresponding to a fluctuation probability of less than 0.001 in 10 years will be denoted N_{10yr}.

The ten year multiplicity threshold is calculated assuming that the burst search time windows are uncorrelated with each other, which is not strictly true — since the time windows start at each hit for any given burst search, they may overlap. However, as can be seen from the good agreement of uncorrelated Poisson probabilities with the data multiplicity distributions (e.g. Figure 7.29), the approximation of uncorrelated intervals is a good one. N_{10yr} is given by the smallest n such that $P_{10yr} < 0.001$. The number of "trials" for a burst is the number of hits for which time windows are opened, $\sim \lambda\mathcal{T}$, where $\mathcal{T}$ =10 years. Assuming uncorrelated intervals,

$$P_{10yr} = 1 - (P(j < n))^{\lambda\mathcal{T}}, \tag{6.15}$$

where $P(j < n)$ is the probability of $j < n$ for a single time window T,

$$P(j < n) = \sum_{j=0}^{n-1} \mathcal{P}(j, \lambda, T). \tag{6.16}$$

Table 6.2 gives N_{pr} and N_{10yr} for several different time windows, for background

rates (per 6 supermodules) of 20 mHz and 80 mHz. (As will be shown in Chapter 7, background rates for the various types of burst searches performed typically range between these values).

Time window (s)	N_{pr} 20 mHz	N_{10yr} 20 mHz	N_{pr} 80 mHz	N_{10yr} 80 mHz
1.	3	6	4	8
2.	4	7	5	9
6.	4	8	7	12
8.	5	9	7	13
10.	5	9	8	14
20.	6	11	10	17

Table 6.2: Multiplicity thresholds for N_{pr} (for a preliminary candidate) and N_{10yr} (for a fluctuation probability < 0.001 in 10 years) for the time windows used for the burst searches for this analysis, for two different background rates.

6.3.2 MACRO's Sensitivity to GC in Terms of Distance

MACRO's sensitivity to gravitational collapse neutrinos can be expressed in terms of the farthest visible gravitational collapse. The farthest visible GC event at distance d_{max} is defined as that which would produce a number of events which equal or exceed multiplicity threshold with 90% probability. d_{max} depends on the active mass M, the energy threshold E_{th} and the burst search time window T (which determine the number of signal events expected), and it also depends on the multiplicity threshold N_{mt} (which determines whether the signal event burst will be picked out as significant). The multiplicity threshold N_{mt} depends on the background rate λ_{bg} and the time window T; λ_{bg} in turn depends on E_{th} (according the the integral spectrum) and the active mass (linearly). For the calculation of d_{max}, the multiplicity threshold N_{mt} can be chosen to be either N_{pr}, which will yield the distance sensitivity for a preliminary alarm, or it can be chosen to be N_{10yr}, which will yield the distance sensitivity for a conservative candidate.

The mean number of detected signal events at distance d, $\bar{N}(d, T, E_{th}, M)$, can be obtained from equation 6.12. One can then calculate the number N_P such that

the number of detected events is $\geq N_P$ with $P\%$ probability (i.e. N_P is the number detected at $P\%$ C.L.). Assuming Poissonian statistics, N_P is given by the largest J such that

$$\sum_{j=J}^{\infty} \mathcal{P}(\bar{N}, j) \;=\; 1 \;-\; \sum_{j=0}^{J-1} \mathcal{P}(\bar{N}, j) \;\geq\; P\%, \tag{6.17}$$

where $\mathcal{P}(\bar{N}, j) = \frac{\bar{N}^j e^{-\bar{N}}}{j!}$. For these calculations, $P = 90$ is used. Setting N_P equal to N_{mt}, we obtain

$$N_{mt}(T, \lambda_{bg}(E_{th}, M)) = N_P(d, T, E_{th}, M), \tag{6.18}$$

where N_{mt} is the multiplicity threshold.

For given E_{th}, T, λ, and M, and either $N_{mt} = N_{pr}$ or $N_{mt} = N_{10yr}$, one can then solve equation 6.18 for $d = d_{max}$.

Figure 6.7 shows d_{max} as a function of active mass M, for $N_{mt} = N_{10yr}$ and for burst search parameters of $E_{th} = 12$ MeV and $T = 4$ seconds,[1] assuming a (low) background rate of 20 mHz (for the full active mass of MACRO). The top plot shows d_{max} for $N_{mt} = N_{pr}$, i.e. the preliminary candidate distance sensitivity. Figure 6.8 shows the same for a background rate of 80 mHz. The "steps" in these plots are due to the integral nature of the multiplicity thresholds. The center of the galaxy is 8.5 kpc away, the far side of the galaxy is 20 kpc away, and the Large Magellanic Cloud is 50 kpc away, out of MACRO's reach under full active mass conditions. Although a handful of events would be detected in MACRO from a GC in the LMC, the burst would not stand out above background.

Figure 6.8 shows that with about half of MACRO's mass turned on, the detector is sensitive to all of the stars in the galaxy; even with a only single supermodule, we are always sensitive to the galactic center.

Figure 6.9 shows the fraction of galactic stars in within radius R from earth [28]: essentially all stars are contained within 25 kpc. A more interesting number for our purposes than the total fraction of stars in the galaxy within radius R is the fraction of stars which are good candidates for gravitational collapse. Such candidates are young and massive, and so likely to be in regions of high heavy element abundance

[1] In Section 6.4, these parameters will be shown to provide "optimum" sensitivity.

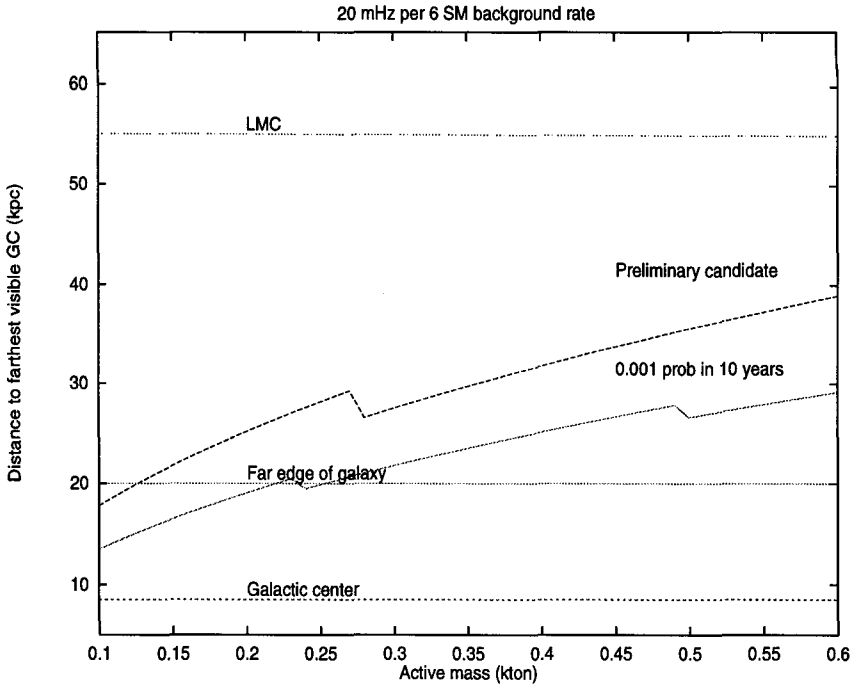

Figure 6.7: Distance to farthest visible SN1987A-like supernova as a function of active mass, assuming a background rate per six supermodules of 20 mHz. The bottom plot assumes $N_{mt} = N_{pr}$; the top plot is calculated using $N_{mt} = N_{pr}$.

("Population I" stars). Therefore, the galactic abundance of CO molecules may provide a tracer for the population of gravitational collapse candidates. The fraction of galactic CO abundance as a function of distance from Earth [90, 91] is also shown on Figure 6.9.

6.4 Optimizing Distance Sensitivity for a GC Neutrino Search

An important issue when looking for bursts of neutrino events among background events is the optimization of burst search parameters (energy threshold and time window) to achieve maximum sensitivity to gravitational collapse. As shown in the previous section, most of the events in a real GC neutrino burst are expected to have energies exceeding ~7 MeV, so decreasing the energy threshold beyond this level does not increase the signal detection efficiency much; the background rate, on the other

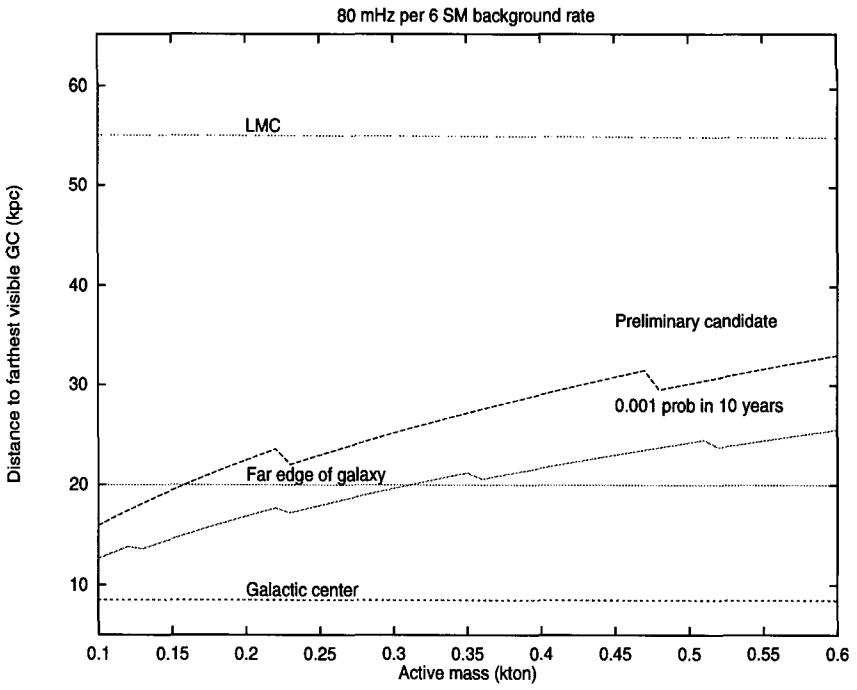

Figure 6.8: Distance to farthest visible SN1987A-like supernova as a function of active mass, assuming a background rate per six supermodules of 80 mHz. The bottom plot assumes $N_{mt} = N_{pr}$; the top plot is calculated using $N_{mt} = N_{pr}$.

hand, increases very rapidly with decreasing energy threshold.

To find the optimum E_{th} and T burst search parameters for a given assumed GC signal, we calculate the maximum distance d_{max} from equation 6.18 as a function of the parameters. To calculate d_{max}, the background energy spectrum shown in Figure 6.6 is assumed.[2] Figure 6.10 shows d_{max} as a function of energy threshold, for $T = 20$ seconds. Figure 6.11 shows the same for $T = 2$ seconds. For both cases, an energy threshold of about 12 MeV gives the best distance sensitivity.

Figure 6.12 gives d_{max} as a function of time window, for a fixed energy threshold of 10 MeV. For this case, T=4 seconds gives the best sensitivity. Figure 6.13 summarizes the situation with a plot of d_{max} as a function of both T and E_{th}.

For this gravitational collapse model, then, the best burst search parameters are T=4 seconds and E_{th}=12 MeV, assuming the background integral energy spectrum shown in Figure 6.6.

[2]For these calculations, $N_{mt} = N_{10yr}$ is used; however the results do not change if N_{pr} is used.

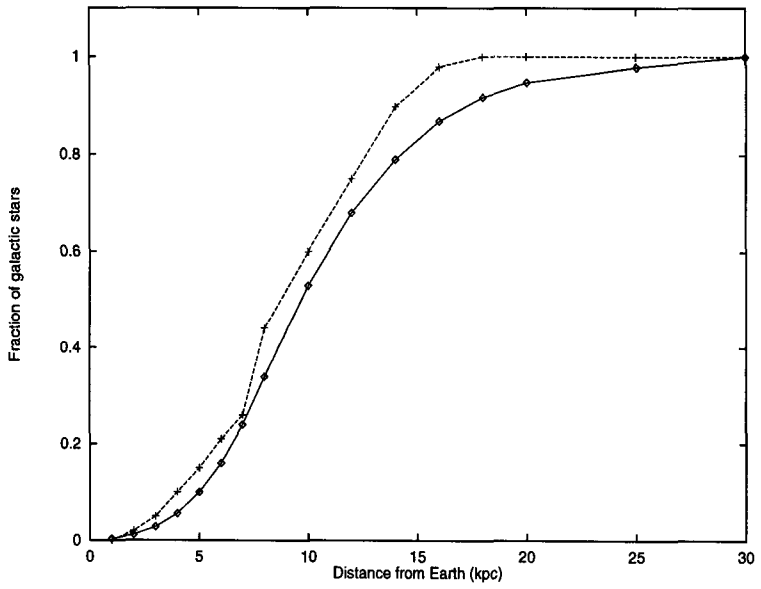

Figure 6.9: Fraction of stars in the galaxy within radius R of earth (diamonds) (from Bahcall) and fraction of CO abundance in the galaxy (crosses) (from Combs).

Not all supernovae may emit neutrinos with exactly the time and energy distributions observed for SN1987A, whose parameters were used for this calculation. Also, entirely non-SN1987A-like scenarios are not out of the question: for instance, the neutrino flux may cut off abruptly if the neutron star collapses further to a black hole state. And, of course, nature may do the unexpected. Therefore, for the best possible burst search, it is preferable to use several different time windows and energy thresholds.

6.5 Secondary Neutron Detection Capabilities

As described in Sections 3.2.3, MACRO has ability to see the neutron produced by reaction 3.2, via its 2.2 MeV fusion gamma ray. The neutron detection follows the detection of the positron after an average moderation time of 10 microseconds and an average capture time of 170 microseconds. The ability to detect secondary neutrons is unique to scintillation detectors. As described in Section C.1.3, the PHRASE trigger circuit is sensitive to the secondary neutron by means of a lowered secondary threshold after a primary energy trigger. At the secondary energy threshold of 1.5 MeV, the

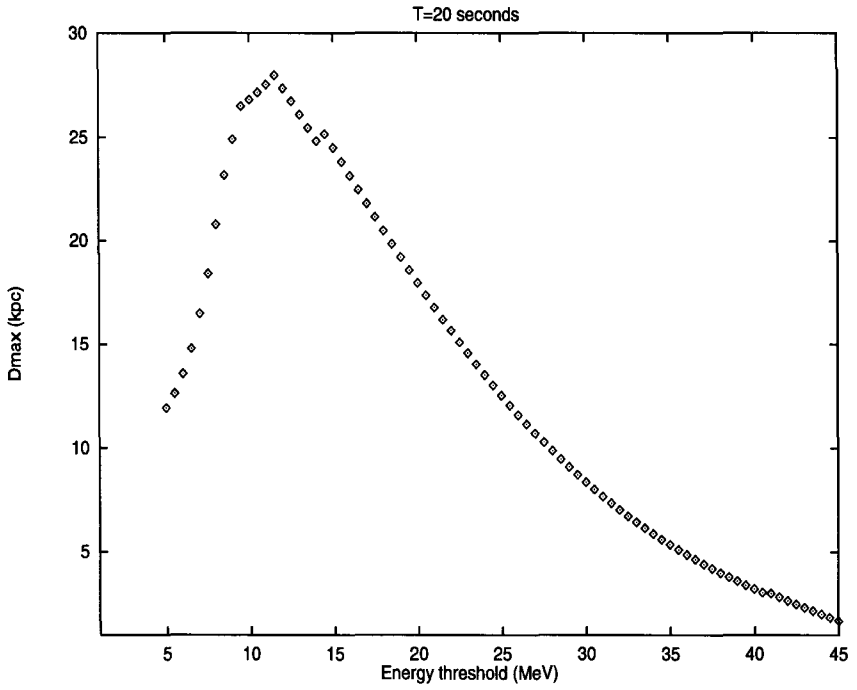

Figure 6.10: Maximum visible distance d_{max} as a function of energy threshold E_{th} for $T = 20$ seconds.

radioactivity background rate is several kHz.

Tests of the efficiency of detection of the secondary have been performed by the Pisa group using an americium-beryllium source to simulate the pattern of a primary high-energy signal followed by a time-delayed secondary signal [82, 81]. ^{241}Am is an α emitter; ^{9}Be emits neutrons upon the absorption of α particles:

$$^{9}\mathrm{Be} + \alpha \rightarrow {}^{12}\mathrm{C}^{*} + \mathrm{n}. \tag{6.19}$$

The emitted neutrons are absorbed and captured by protons in the scintillator just as GC neutrino secondaries would be. The ^{12}C in this reaction de-excites via various pathways (see Figure 6.14) giving γ-rays of various energies; 60% of the time the de-excitation is via a 4.4 MeV γ. For the special calibration runs, the primary energy threshold was lowered to 4 MeV; for this case the prompt 4.4 MeV γ is analogous to the GC neutrino $\sim$ 7 MeV primaries, and causes the lowering of the threshold to 1.5 MeV.

Am/Be sources were placed on the center parts of three MACRO scintillator

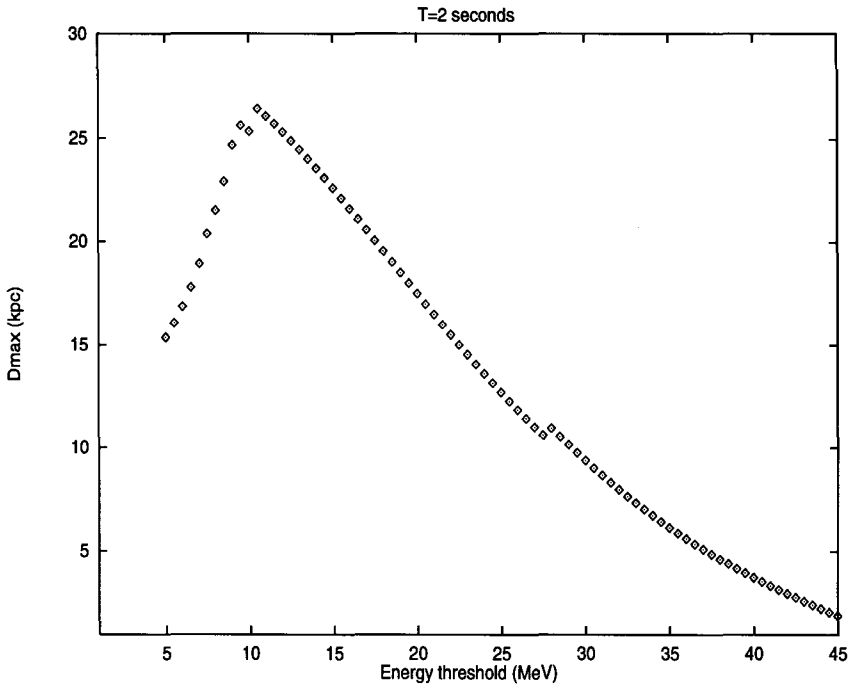

Figure 6.11: Maximum visible distance d_{max} as a function of energy threshold E_{th} for $T = 2$ seconds.

counters and the signals recorded. The resulting energy distribution well matches a Monte Carlo simulation: see Figure 6.15. The distribution of time delays between primary and secondary triggers for low energy secondaries is also as expected: it is well-described by an exponential with time constant 180 microseconds, the expected neutron capture time, superimposed on a flat background: see Figure 6.16.

In addition, the distribution of reconstructed positions for the Am/Be data shows a strong peak at the counter center where the source was located: see Figure 6.17. For this plot the radioactivity background has been subtracted. The spatial correlation between primaries and secondaries is $\sigma_z \sim 1$ m. Note that the neutrons coming from the source are not collimated and σ_z is dominated by the distance the neutrons wander in the scintillator before being absorbed. The intrinsic position resolution of the scintillator detector is actually more in the range of 10 cm.

According to the Am/Be tests, the efficiency for detection of a secondary neutron given a primary positron detection is $\sim$ 25%. In addition, the signal to background ratio during the 850 μs that the threshold is lowered can be estimated using the

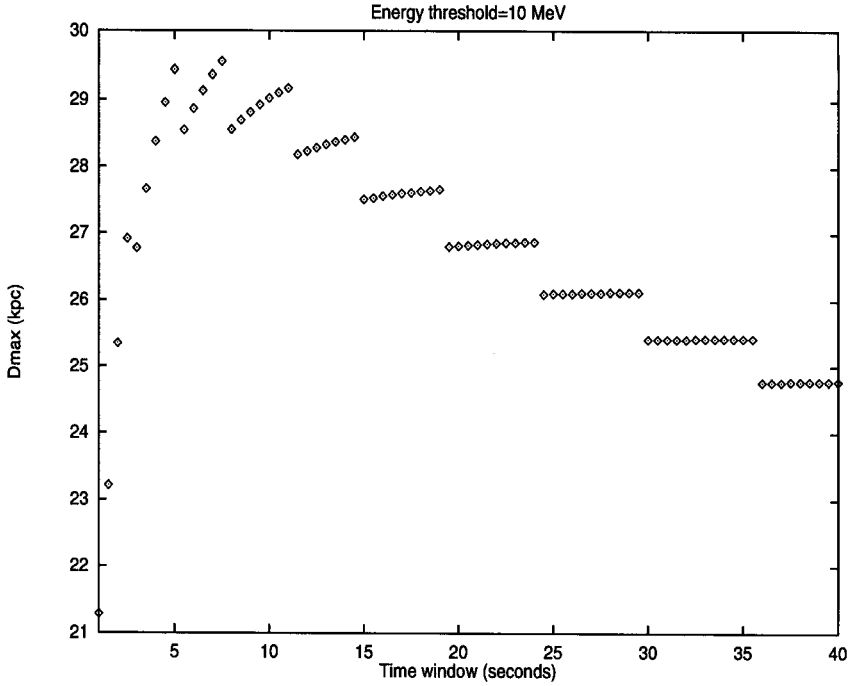

Figure 6.12: Maximum visible distance d_{max} as a function of time window T for $E_{th} = 10$ MeV.

Am/Be test to be about 2:1 after time delay and position correspondence cuts have been applied.

Secondary event analysis is not done routinely in this analysis, but may be used when a convincing candidate burst of primary events is found.

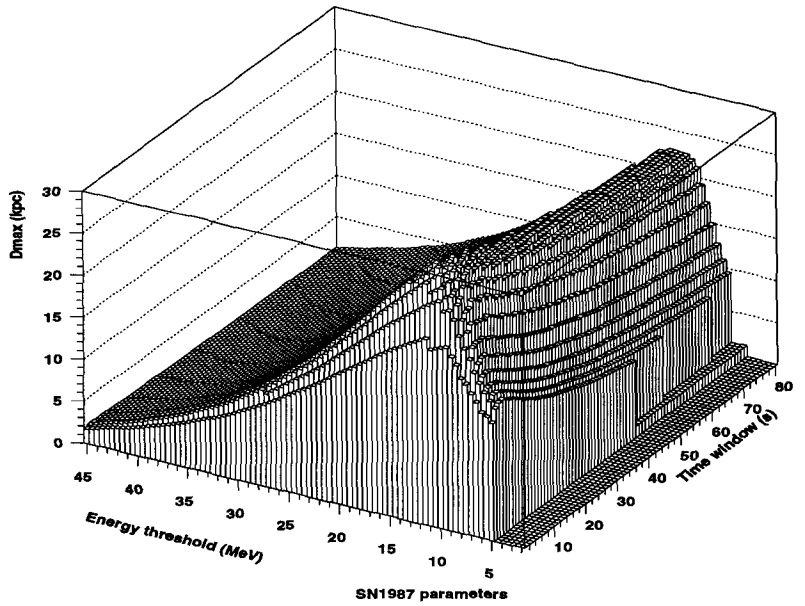

Figure 6.13: Maximum visible distance d_{max} as a function of energy threshold E_{th} and T.

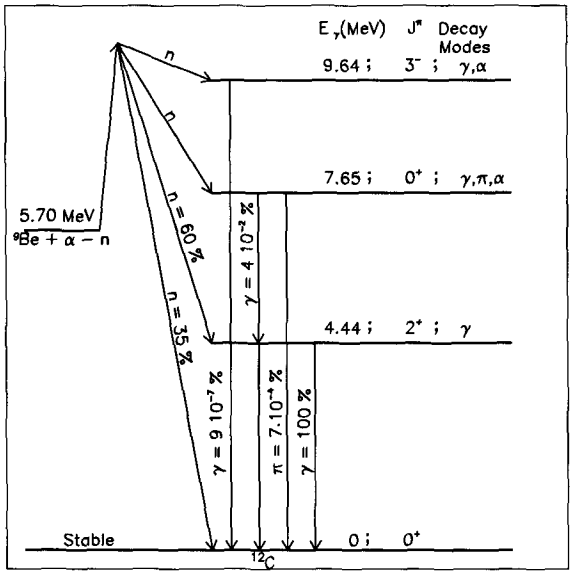

Figure 6.14: Level diagram for de-excitation of ^{12}C. (F. Cei).

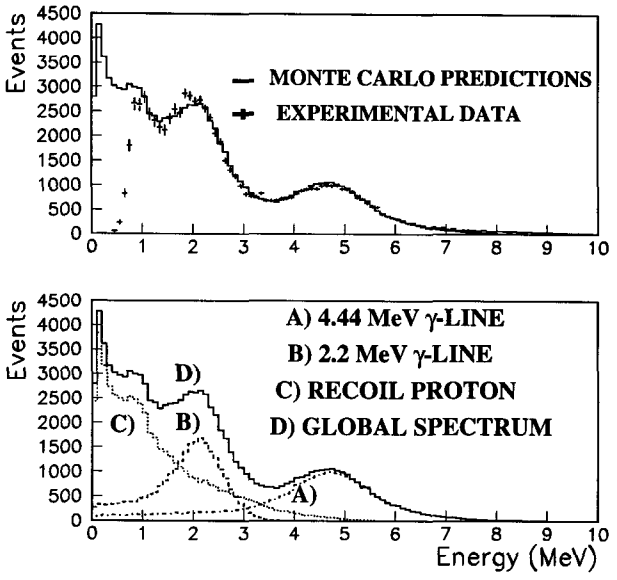

Figure 6.15: Comparison of energy distribution of Am/Be data with Monte Carlo. The bottom plot shows the breakdown of the different contributions to the simulated spectrum. (F. Cei).

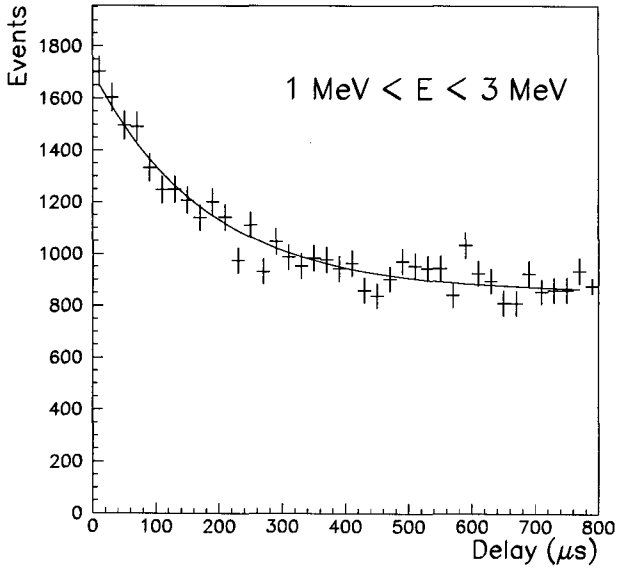

Figure 6.16: Distribution of time delays between primary and secondary events with the Am/Be source, showing the characteristic time constant of 180 microsecond superimposed on a flat background. (F. Cei).

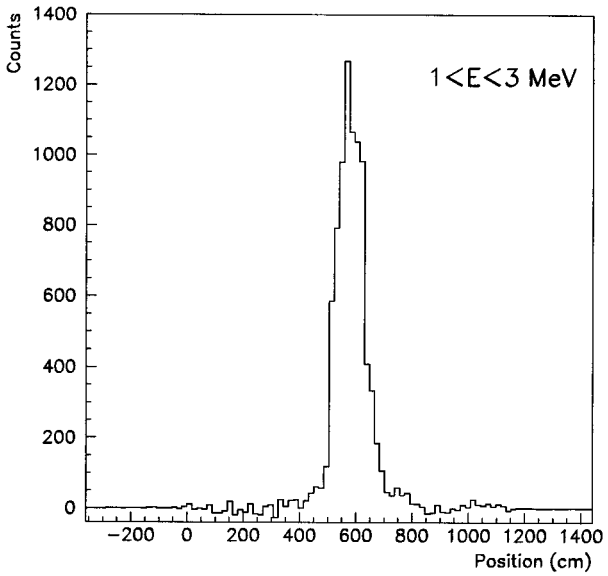

Figure 6.17: Distribution of reconstructed counter positions for the Am/Be data, with radioactivity background subtracted. (F. Cei).

Chapter 7 Data Analysis

This chapter will discuss the method and results of GC burst search data analysis performed on ERP and PHRASE triggered data, both separately and in a combined way.

7.1 Combining ERP and PHRASE data for GC Data Analysis

7.1.1 Motivation for a Combined Search

GC burst search analyses have been published for PHRASE-triggered data alone [81]. Burst search analyses may also be performed in a way which combines data from both the ERP and the PHRASE. Because the backgrounds seen by the two circuits are different due to different hardware triggering conditions (as will be discussed extensively in this chapter) a event-wise "AND" search (i.e. a search among events which triggered *both* the ERP and the PHRASE) has less background than either search separately. On the other hand, a event-wise "OR" search (i.e. a search among events which triggered *either* the ERP or the PHRASE) is likely to be more efficient. Therefore, to retain the greatest possible flexibility, the final combined ERP/PHRASE offline burst searches are performed for both an AND and an OR of the ERP and PHRASE events for runs where both systems were operational, in addition to separate ERP and PHRASE burst searches. The method for combining the ERP and PHRASE data will be described in the following subsections.

7.1.2 Farfalla DSTs

The combined ERP/PHRASE data analysis is performed making use of the FARFALLA software package [92], a convenient C++ based Data Summary Tape (DST)

production tool. The DST format is described in detail in Appendix D.

7.1.3 Initial Hit Reconstruction for the DST

After the FARFALLA nodes are created they are filled with preliminary raw information from DREAM (Section 4.6.1). This is step 1 described in Section 7.1.3. Some details of reconstruction are given below.

Decoding of Raw ERP Data

In the first ERP decoding step, the ERP counter, ADC and TDC information is extracted from the data, and the ERP clock times are reconstructed using a nominal ERP clock rate (at this point in the analysis, not yet calibrated precisely with respect to UT time.)

Information about problems with the raw ERP data is packed into an error word for each ERP hit, to be used later for data quality cuts (see Section 7.1.5 and Appendix E). See Table E.1 in Appendix E for a listing of the meaning of each bit set in the error word and the cut tolerances.

PHRASE Reconstruction

PHRASE hits are reconstructed using modified DREAM code (not yet available in the standard release) [93, 76] and standard calibration constants produced by the Pisa group, converted for use with CALMOD (Section 4.6.2). In the first DST production step, energies, positions and UT times are fully reconstructed and stored in the PHRASE FARFALLA nodes. The raw PHRASE sum pulse height values (Section 5.3) for each side of the counter are also stored.

7.1.4 Time Matching ERP and PHRASE Events

DST Production Procedure

The production of the final time-sorted and time-matched DST to be used for the burst search is accomplished in three steps.

1. *Pass 0: DREAM preliminary reconstruction*

   First, a "pass 0" intermediate DST is produced, containing PHRASE events in the order that they are processed by the standard DREAM software [93, 76]. All ERP GC buffer events are written out sorted in ERP time order. As noted above, raw ERP information and reconstructed PHRASE information is saved at this step. The pass 0 DST also contains all ERP muon trigger events, which have UT times associated with them, and streamer tube track, wire and strip hit information as well as trigger word information (and UT time information)[1] Tracking is performed using the standard DREAM package. The ST and trigger information is to be used later to reduce the muon content of the data sample (see Section 7.1.5).

2. *Pass 1: Stamping of UT times on all ERP and PHRASE hits*

   Subsequently, the pass 0 intermediate DST is processed to make a pass 1 DST: in this step, the ERP GC hits have UT times associated with them by using a fit of ERP clock time vs UT time made using the ERP muons (see also Section 8.2.3). This fit is done for each ERP GC buffer event, using the sample of ERP muons nearest in time before and after the event in the same supermodule within 600 seconds in each direction (outliers are rejected). To save CPU time, this fit is redone only for every second ERP GC event from each supermodule, and the fit parameters are stored for the next hit's time reconstruction. The quality of time matching has been shown to be negligibly degraded when a fit is done for every second event.

   A similar fit is done for the PHRASE events, to compensate for the instability of the PHRASE global external clock, which can drift tens of milliseconds over the course of a run. Since the PHRASE external clock is global to all SMs, it is not necessary to break up the fit by supermodule as for the ERP case. In pass 0, events which have more than 15 MeV reconstructed in the PHRASE are matched to ERP muons in the same counter (when such matches are present)

[1] Streamer tube and trigger information is stored in "otherTrig" FARFALLA nodes (see Appendix D).

and a fit is done to PHRASE reconstructed UT time vs ERP muon UT time. For each PHRASE hit unmatched to a pass 0 ERP muon, all the matched PHRASE hits within 600 seconds are used for the fit. For the PHRASE case, to obtain good quality time matching, it is only necessary to redo this fit for every tenth PHRASE hit, with saved fit parameters being used for time reconstruction in between fits.

3. *Pass 2: UT time sorting*

   In the final step, the pass 1 intermediate DST is converted to the final DST by sorting all the hits, both PHRASE and ERP, in UT time order. In this last step, FARFALLA nodes (PHRASE, ERP or otherTrig) with UT times within 1 ms of each other are associated in the same event.[2]

Quality of the Time Matching

Figure 7.1 shows the distribution of time differences between each ERP hit and each PHRASE hit (in the same counter) in one run on several different time scales, ranging from 1000 seconds down to 0.001 ms. This plot clearly shows the physical association of the hits, and the size of the coincidence peak gives the total number of matched hits in the run. It is clear from these plots that a 1 ms time window is appropriate for time matching between ERP and PHRASE events: there is very little accidental coincidence background on this time scale, and a negligible fraction (<0.5%) of truly matching events fail to fall within the 1 ms window.

7.1.5 Final Reconstruction and Cuts

The FARFALLA DSTs used for the burst search analysis contain raw ERP information (ADC and TDC values) and reconstructed PHRASE information (energies and positions), and UT times for both. ERP hits only undergo final reconstruction and cuts. No special cuts are performed on the PHRASE data for this analysis.

[2]They are stored in the FARFALLA event node as "children of the same event node" (see Appendix D).

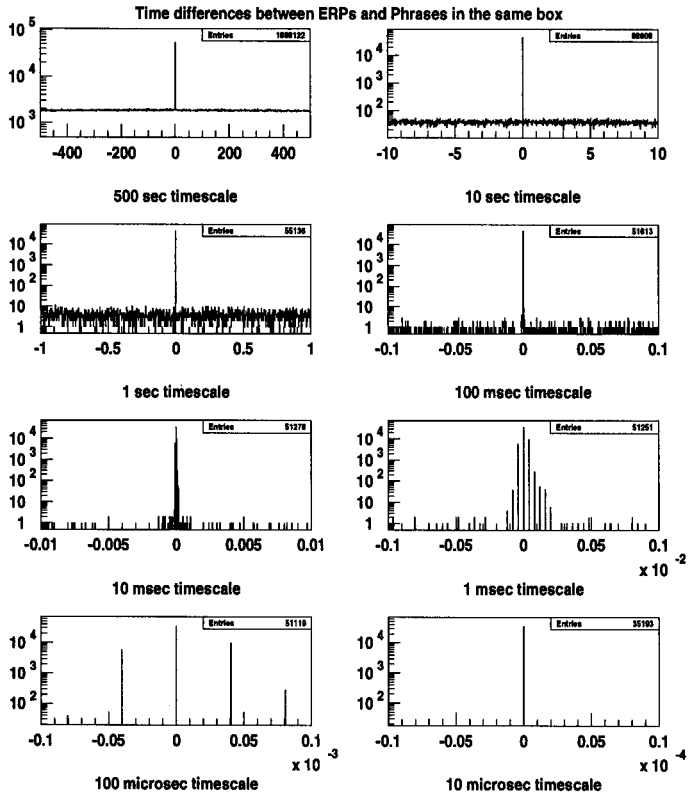

Figure 7.1: Distribution of time differences between ERP hits and PHRASE hits in the same counter for run 11033.

ERP Energy and Position Reconstruction

Reconstruction of ERP energies and positions (described in Section 5.2) is performed immediately before the burst search is performed. In general, the standard procedure described in Chapter 5 is used, with energy calibration adjustment performed for the ERP as described later in this chapter in Section 7.2.3.

Cuts on the ERP Data

Data quality and reconstruction cuts are applied to the ERP data. Appendix E.2 gives a detailed list of the cuts.

Table 7.1 shows, for a typical run (11834, livetime 6.5 hours) the numbers of events surviving after the different cuts, including the muon veto cut (Section 7.1.5) and a 10 MeV energy threshold cut. (Table E.2 in Appendix E gives a more detailed breakdown).

Requirement to pass cut	Number of events before cut	Number of events remaining after cut
Data quality good	387537	359598
z reconstructs within counter	359598	224840
ADCZ/TDCZ consistent	224840	128924
Passes muon veto	128924	107550
$E > 10$ MeV	107550	1797

Table 7.1: Effect of various cuts on numbers of events, for run 11834.

The data quality cuts are designed to eliminate bad data and calibration hits; in general they cuts remove less than 10% of the data from the initial sample. The two reconstruction cuts (the ADCZ/TDCZ consistency requirement and the position within counter requirement) actually overlap considerably in their effect. They also cut a substantial amount of data: approximately two thirds of it overall, although the fraction varies from counter to counter. Later in this chapter, these reconstruction cuts will be shown to remove background from ERP by eliminating coincident near-tankend events; the cuts will be examined in detail in Sections 7.3.2 through 7.3.4.

Vetoing Muons

Section 6.2.1 describes the muon veto cut in a general way. An event is accepted for further analysis, and is referred to as "unvetoed"[3] if it satisfies the following criteria:

- There must be no other hit of the same type (cut or uncut) in the same event, i.e. no coincidence with a hit in another counter within 1 ms. Although this cut may reduce signal size for very close GC events, it has very little effect on detection sensitivity for a standard timescale neutrino signal: for a 2 second time window, signal rates may reach ~250 Hz and bursts from sources closer than ~1 kpc would not exceed multiplicity threshold with a 1 ms coincidence cut. However, for a search over a 20 second time window, even at 0.1 kpc distance, the burst size would still exceed multiplicity threshold. (Note that anomalously short-timescale, intense signals may be eliminated by the coincidence cut; however there is no compelling reason to expect such signals.)

- There must be no coincidence within 1 ms with either a CSPAM or Bari trigger (Sections 4.5.1,4.5.2).

- There must be no coincidence within 1 ms with a ST wire or a strip reconstructed track, when tracking information is available; there must also be fewer than 10 wire hits.

Figure 7.2 shows the effect of the muon veto cut for one run: the solid line shows the integral spectrum (rate of hits over energy threshold) of events present in both the ERP and the PHRASE (matches) before the veto cut, and the dashed line shows the same after the veto has been applied. The rate of hits reconstructing to E >25 MeV (all likely to be muons) has been reduced by a factor of ~40, to approximately 15 mHz in the full detector. The rejection is not perfectly efficient due to the presence of "corner-clipping" muons which hit only one counter and cross too few planes to produce a reconstructed track or a Bari trigger.

[3]This term has a similar meaning to the term "single" used in the Pisa gravitational collapse analyses; however this thesis will use the term "unvetoed" to avoid confusion with the term "single peak" used in this chapter to refer to waveforms.

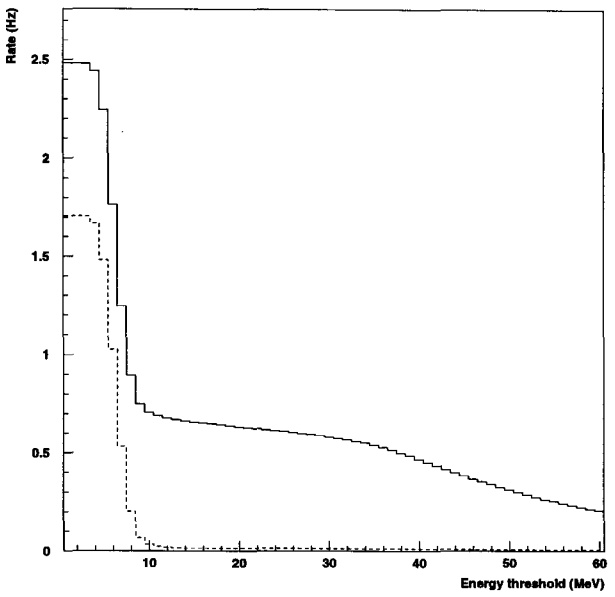

Figure 7.2: Integral energy spectrum (rate of hits exceeding energy threshold) of matched hits before and after muon veto. (See Figure 6.6 for the rates of unvetoed hits on a log scale).

7.2 Results of Event-by-Event ERP and PHRASE Comparison

Before doing a combined ERP/PHRASE burst search, it is important to compare the ERP and PHRASE data on an event-by-event basis, in order to understand the different backgrounds and efficiencies of the two systems. This section will describe an event-by-event ERP/PHRASE comparison, using standard (independent) ERP and PHRASE energy and position reconstruction.

7.2.1 ERP and PHRASE Matches and Mismatches

The sample of ERP events does not match perfectly to the sample of PHRASE events. For example, for run 11834, there are 385787 ERP hits (cut and uncut) and 114288 PHRASE hits. Of these, 88751 are matches. There are 297036 ERP hits

with no corresponding time-matched PHRASE hit, and 25537 PHRASE hits with no corresponding ERP hit. The fraction of matches varies as a function of energy threshold; most mismatches occur at low energies. The origin of the mismatches will be discussed in detail in the Section 7.3. First, the events present in both the ERP and the PHRASE will be considered. The following section will compare ERP and PHRASE standard reconstructions for the sample of matched events.

7.2.2 Comparison of Energy and Position Reconstructions

For matched ERP and PHRASE events, the reconstructed energies and positions compare reasonably well, as will be shown in the following sections. Figure 7.3 shows a plot of PHRASE reconstructed energy versus ERP reconstructed energy for the time-matched hits in a single run, for energies up to 80 MeV. The muon peak and the radioactivities are clearly visible on this plot. Figure 7.4 shows the same for energies less than 10 MeV.

This plot has a few features worth examining in more detail:

- There are a few more sparsely populated lines lying away from the main line (these are difficult to see on the plot shown; they become more visible with higher statistics.) In all cases these can be traced to calibration problems with individual counters.

- A subset of hits have high (muon-level) reconstructed energy in the ERP but low reconstructed energy in the PHRASE: this is visible as the lighter, near-horizontal line present below the main line on this plot. These events are understood to be due to a hardware problem in the PHRASE which cause blocklets (Section C.1.2) to be dropped from the data stream for high energy deposition events. Such events can be flagged in the DREAM reconstruction code (Section 7.1.3). These represent about 4% of the hits with reconstructed energy >30 MeV in the ERP (~8% if E >30 MeV ERP hits with no matched PHRASE hits are counted) . This problem is relatively unimportant for gravitational collapse studies due to the fact that the missed-blocklet events tend to have larger

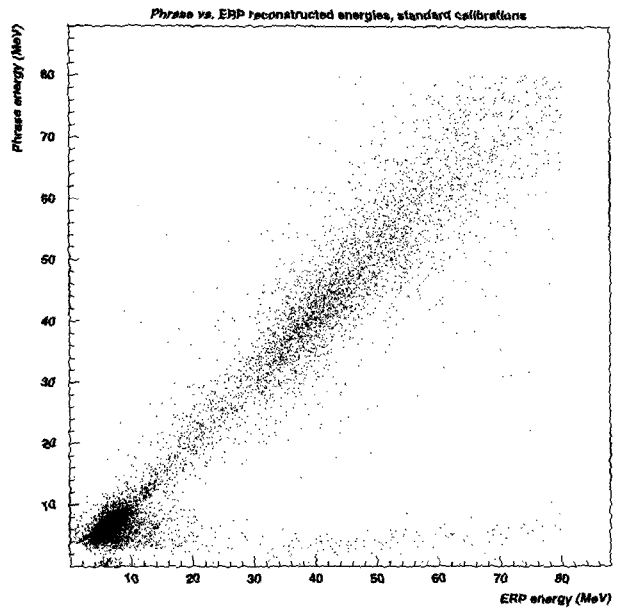

Figure 7.3: PHRASE reconstructed energy vs. ERP reconstructed energy, for all counters in run 11033. Energies were reconstructed using standard calibration constants for both the ERP and the PHRASE. This plot represents hits for only part of a run, due to plot saturation.

energy deposition than expected for gravitational collapse signal events.

The reconstructed event positions for matched ERP/PHRASE pairs also compare quite well. Figure 7.5 shows a plot of PHRASE reconstructed position versus ERP reconstructed position for the time-matched hits in a single run (timing positions are used here). The top plot of Figure 7.10 shows the distribution of differences between reconstructed energies in the ERP and the PHRASE: the mean of the distribution is -0.2 MeV and the sigma is 0.9 MeV. The agreement can be improved by an energy adjustment procedure as will be shown in the next section.

7.2.3 Adjustment of Energy Calibrations

For nearly all counters, the ERP and PHRASE reconstructed energies are related approximately linearly, and typically differ by ~1 MeV in the 5 to 15 MeV range.

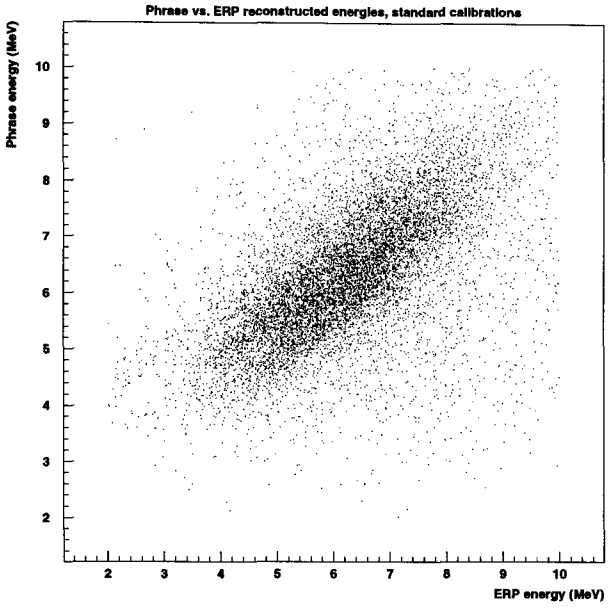

Figure 7.4: PHRASE reconstructed energy vs. ERP reconstructed energy, for all counters in run 11033, in the low energy regime. Energies were reconstructed using standard calibration constants for both the ERP and the PHRASE.

For most cases, the slope of the line is close to one; however the intercept is not zero. The origin of the discrepancy is not completely clear; it may be due to incorrectly determined pedestals (charge values at zero energy) in either the ERP or the PHRASE or perhaps both. However, the explanation probably has to do with a systematic problem with the determination of the ERP pedestals (extrapolated ADC value for zero light, see Section 5.2.3) using the lasers. The ERP intercept at zero light does not match the independently determined PHRASE pedestal, possibly due to problems with the reference phototube (which may have been operating in a non-linear regime for at least some lasers over many calibration runs).

In addition, for some anomalous counters (a few percent) there is a discrepancy of several MeV between ERP and PHRASE reconstructed energies, although the two measurements still have a linear relationship. These correspond to the outlying lines in Figure 7.3. For most of these cases, for a given hit, the ERP energy reconstructs to

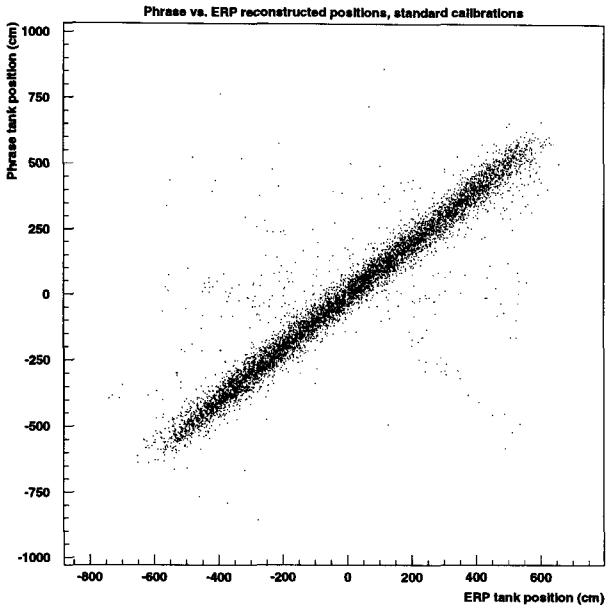

Figure 7.5: PHRASE reconstructed position versus ERP reconstructed position for matched events.

a higher value than the PHRASE energy (for the worst cases, 10 MeV higher). The consequence of having a few such anomalous counters is that at a given reconstructed energy threshold the ERP rate may be much higher than the PHRASE rate, which can affect the burst searches significantly.

For this reason, in order to provide consistent rates at a given energy threshold for a combined ERP/PHRASE burst search analysis, the ERP calibration constants are adjusted in order that ERP and PHRASE reconstructed energies match each other. The PHRASE energy scale has been chosen as the standard because PHRASE energy calibrations, based on the 2.6 MeV Tl line (Section 5.3.2) have been optimized for low energy measurements, whereas the ERP energy calibrations have not.

The charges measured by each circuit on each side of the counter— the raw ADC value for the ERP (Section C.2) and the charge response-corrected sum pulse height for the PHRASE (Section 5.3) — are compared for one counter in Figure 7.6. The figure shows that there is a linear relationship between the two measurements for

ERP ADC values less than about 800 counts. The relationship becomes non-linear at large (muon level) pulse heights, corresponding to 1000–2000 ERP ADC counts. In addition there is ERP ADC saturation at very large pulse heights, as shown in the top figure. However we are concerned primarily with the ~5–20 MeV regime: the bottom figure shows a blow up of the low energy regime, where the linear relationship is well satisfied.

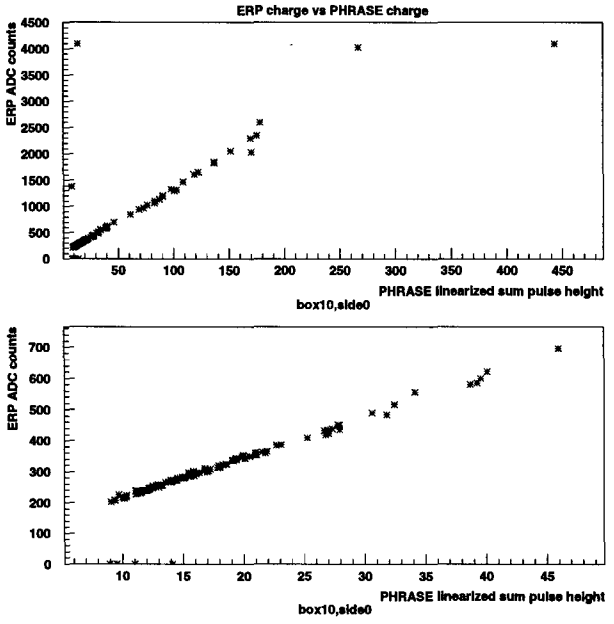

Figure 7.6: Top: ERP raw ADC value as a function of PHRASE charge response corrected sum pulse height, over a wide range of pulse charges, for one counter. Muon charge levels correspond to approximately 1000-2000 ERP ADC counts. Bottom: a blowup of the regime corresponding to lower energies relevant for gravitational collapse studies. The extrapolated ERP signal is finite at zero PHRASE signal.

To adjust the ERP energy calibration constants in order that ERP and PHRASE rates are comparable at the same reconstructed energy, the following procedure is used.

First, for each side of each counter, a fit is made to

$$sph \;=\; A[g(ADC - ped)] \;+\; B, \tag{7.1}$$

where *sph* is the PHRASE linearized sum pulse height, *ADC* is the ERP raw ADC value, g is the (standard) ERP gain calibration constant (see Section 5.2.3), *ped* is the ERP pedestal, and A and B are the linear fit parameters. Figure 7.7 shows an example of such a fit.

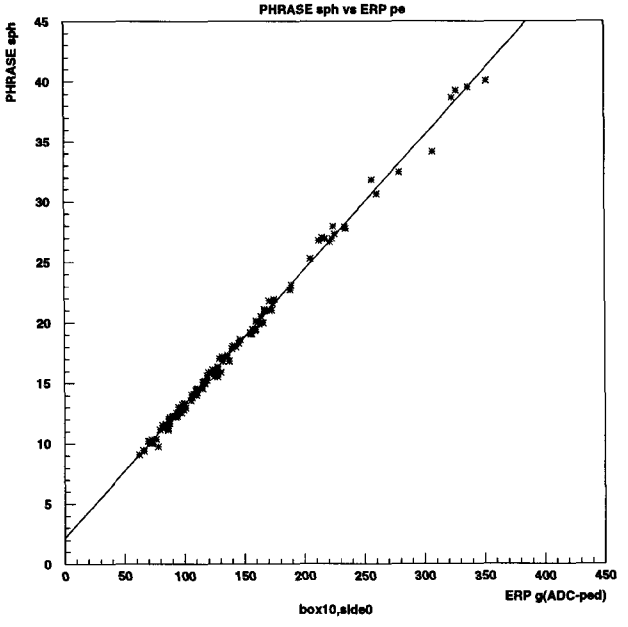

Figure 7.7: Linear fit of PHRASE sph vs ERP "photoelectrons" for ERP calibration constant adjustment.

In order that the adjusted ERP and PHRASE energies be consistent:

$$E_p \;=\; \frac{sph}{R_p} \;=\; \left(\frac{Ag(ADC - ped) + B}{R_p}\right) \;=\; \frac{kE_e}{R_e}, \tag{7.2}$$

where E_p is the reconstructed PHRASE energy, R_p is the PHRASE response correction (a function of counter longitudinal position z), E_e is the ERP reconstructed energy, R_e is the ERP response correction and $k = R_p/R_e$ is a scaling constant taking

into account the normalization of the response corrections.[4]

Then, in order to reconstruct $E_e = E_p$, one can define a new ERP pedestal ped' and a new gain g' (to be used in equation 5.8 in place of ped and g) using the fit parameters A and B:

$$ped' = ped - \frac{B}{Ag} \tag{7.3}$$

$$g' = \frac{Ag}{k}. \tag{7.4}$$

Typically, adjusted pedestals differ from the standard ones by ~10–20 counts, and adjusted gains differ from standard ones by ~5–10%.

Figure 7.8 shows ERP energy vs. PHRASE energy for a single counter with the ERP energy reconstructed using the standard ERP constants (top) and the modified constants calculated from equations 7.3 and 7.4 (bottom). Figure 7.9 shows the same plot after ERP calibration constant adjustment for all counters for a run. The worst individual counter anomalies have been eliminated, and for the other counters the energies match much better. The bottom plot of Figure 7.10 shows the distribution of ERP/PHRASE energy differences after readjustment: the sigma has narrowed to 0.36.

Note that after readjustment, ERP energies reconstruct to higher values on average than PHRASE energies. This can be seen in Figure 7.9. This is due to the longer effective integration window of the ERP, which means that the ERP is more likely to pick up uncorrelated low-level radioactivities during its integration time. This effect will be discussed in more detail later in this chapter.

The tankend-by-tankend linear relationships do change somewhat for each calibration set change, and so the linear fits are redone when either the ERP or PHRASE calibration database set changes. For each calibration run change, the good run nearest in time is chosen for which all six supermodules were present in both the ERP

[4]In practice the ratio k is not perfectly constant as a function of z for all counters: there often are some 10–20% deviations near the ends of the counters, probably due to the $1/z^2$ term in the ERP response parameterization, equation 5.9. The value of k is nominally calculated at the center of the counter.

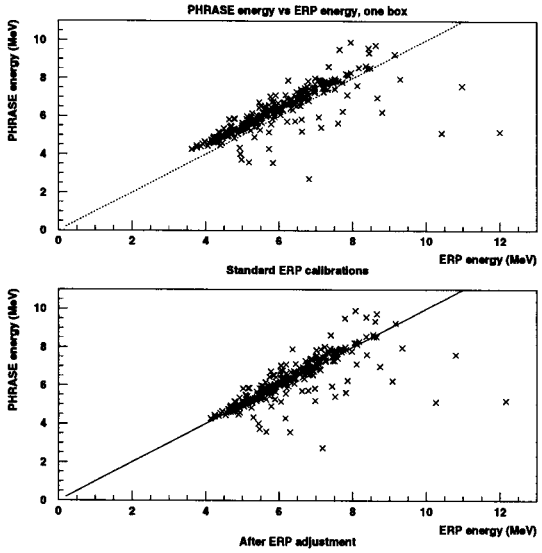

Figure 7.8: ERP vs. PHRASE reconstructed energy with the standard ERP constants (top) and the ERP constants modified to conform to PHRASE energies (bottom) for one counter. The lines show $y = x$.

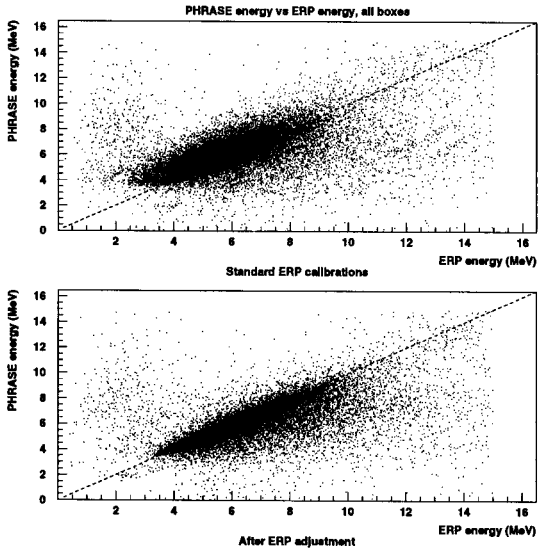

Figure 7.9: ERP vs. PHRASE reconstructed energy with the standard ERP constants (top) and the adjusted ERP constants (bottom) for all counters. Note the asymmetry: a given matched hit is likely to have $E_{erp} > E_{phr}$. The lines show $y = x$.

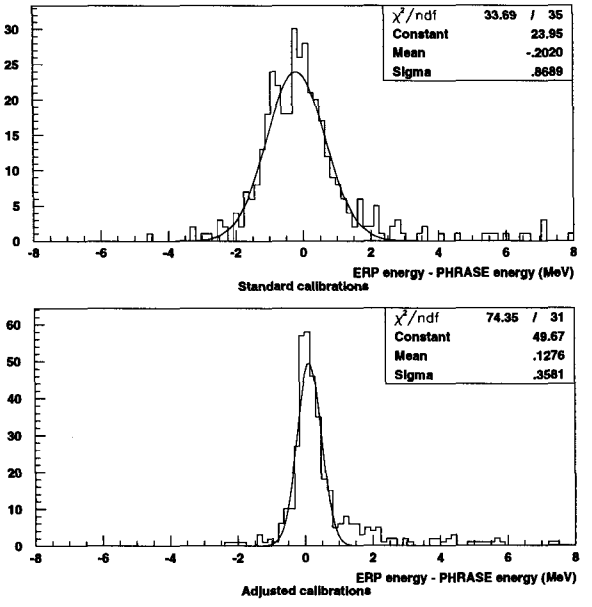

Figure 7.10: Distribution of differences between ERP reconstructed positions and PHRASE reconstructed positions, for matched events with ERP hits passing cuts, for energies <16 MeV. For the top plot, standard ERP calibrations were used and for the bottom plot adjusted constants were used.

and the PHRASE, and the data from this run is used for the fits for each tankend. Modified ERP pedestal and gain constants are then generated for that calibration run. The reconstructions have been shown to be stable in between calibration runs.

7.3 ERP-PHRASE Mismatches

In this section, the events which are "mismatched", i.e. ERP hits which have no corresponding PHRASE hits, and PHRASE hits which have no corresponding ERP hits, will be studied to better understand backgrounds and efficiencies of the two circuits.

7.3.1 Some Definitions

Here some terminology will be introduced for the purpose of discussion of matched and mismatched events:

- **MATCH:** An event containing both an ERP and a PHRASE event in the same counter within 1 ms.
- **LONE ERP:** An ERP hit with no PHRASE partner in the same box within 1 ms.
- **LONE PHRASE:** A PHRASE hit with no ERP partner passing cuts in the same counter within 1 ms.

The ERP and PHRASE trigger circuits use different methods for determining energy and triggering. The two circuits are more likely to have different efficiencies at low energies ($E < 10$ MeV) where both circuits are more likely to be inefficient. For hits with energies much less than about 10 MeV, we can expect position-dependent inefficiencies in both the ERP and the PHRASE. Therefore, we expect most mismatched events, both lone PHRASEs and lone ERPs, to have low energies.

Figure 7.11 shows the rates (in the whole detector) of matches, lone ERPs and lone PHRASEs as a function of energy threshold, i.e. integral spectra for each of the three classes of events. The energy threshold used for the matched hits is the average of the ERP and PHRASE reconstructed energies for the pair.

The ERP and the PHRASE are nominally expected to be efficient in the 10–20 MeV regime, which is the regime most important for the detection of GC neutrinos. Therefore mismatched events with greater than 10 MeV reconstructed energy merit further study.

7.3.2 Effect of the Cuts on the Mismatch Rates

Rates of matches and mismatches are very strongly affected by the cuts applied to the ERP data described in Sections 7.1.3 and 7.1.5. As shown in Figure 7.12, lone ERP

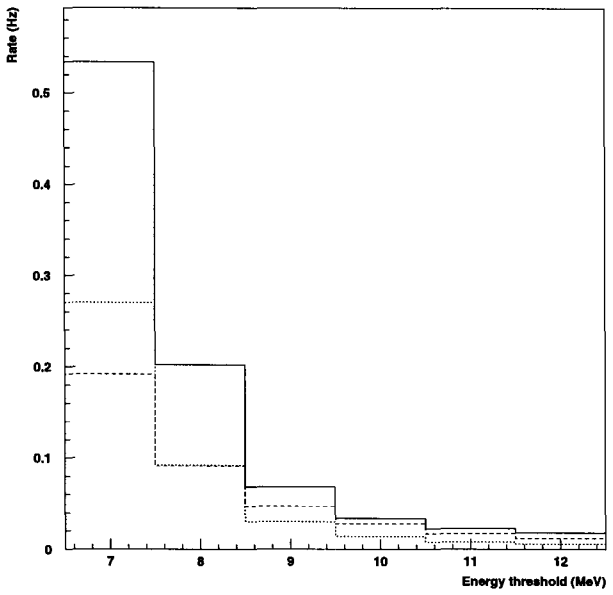

Figure 7.11: Integral spectra of ERP/PHRASE matches (dashed line), lone PHRASEs (dotted line), and lone ERPs (solid line).

rates are much higher among ERP hits failing cuts than among ERP hits passing cuts. This effect will be studied in the following sections.

7.3.3 Waveforms of Low Energy Events

Special ERP GC Waveform Runs

Several special runs were performed in order to obtain more detailed information to study the lone ERPs. For this run, the ERP low energy trigger was used to stop the custom 200 MHz waveform system for the appropriate channels, to allow explicit viewing of waveforms of the mismatched events.[5] This was accomplished by means of a set of special LUTs (see Section C.2.3) for which the Ehigh trigger bits were set to be identical to the normal Elow trigger bits. Under normal run conditions ERP Ehigh trigger causes readout of the waveforms (Section 4.5.1) for 1 ms following the trigger,

[5]Note that under normal circumstances 200 MHz waveforms are not recorded for GC ERP trigger or PHRASE events.

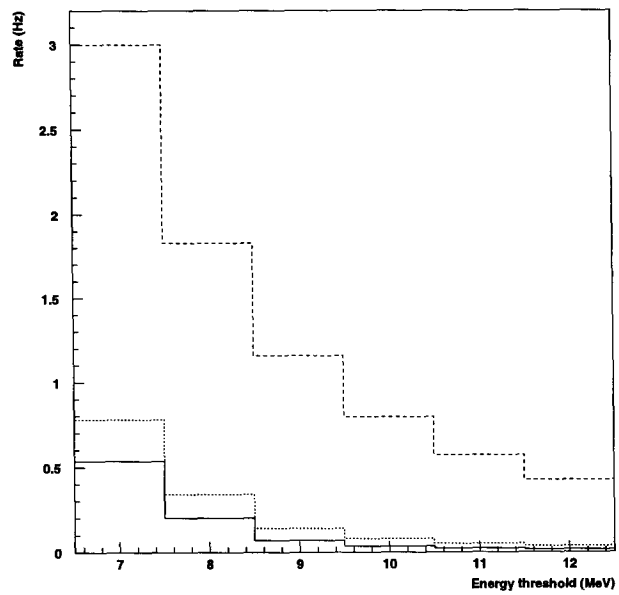

Figure 7.12: Integral spectra of ERP/PHRASE matches (solid), ERP hits passing cuts (dotted), and ERP hits not passing cuts (dashed).

so for the special runs most Elow triggers caused 1 ms worth of WFD readout.[6]

The special runs were performed in December 1995; five runs of about 10–15 minutes each were taken. The run numbers of the special runs were 11369 (December 6, 1995), and 11414 through 11417 (December 13, 1995).

"Anecdotal Evidence": multiple pulses in the ERP

A visual scan of the waveforms in the special runs shows some "anecdotal" answers to the question of what the lone ERP mismatches are: many lone ERPs, especially those failing reconstruction cuts, appear to be multiple coincident radioactivity events. Figure 7.13 shows a typical example. On the other hand, ERP hits which are matched to

[6]In practice, for the special runs, only about 80% of Elow triggers caused a waveform readout due to high deadtime from the computer busy signal inhibit of Ehigh readout (Section C.2.4) while the computer was dealing with the waveforms. Also, note that PHRASE hits only had 200 MHz waveform information associated with them if they were matched to ERP hits with waveforms, since the PHRASE triggers did not directly cause 200 MHz waveform readout.

PHRASE hits and which pass reconstruction cuts (Section 7.1.5) appear to be associated with waveforms which have clear, single peaks; the ADCZ/TDCZ consistency requirement cut appears to get rid of most of the multiple peaks. Figure 7.14 shows an example of a waveform for an ERP event which passes cuts. In the following, a "peak" will be defined as one individual pulse, corresponding to one radioactivity event.

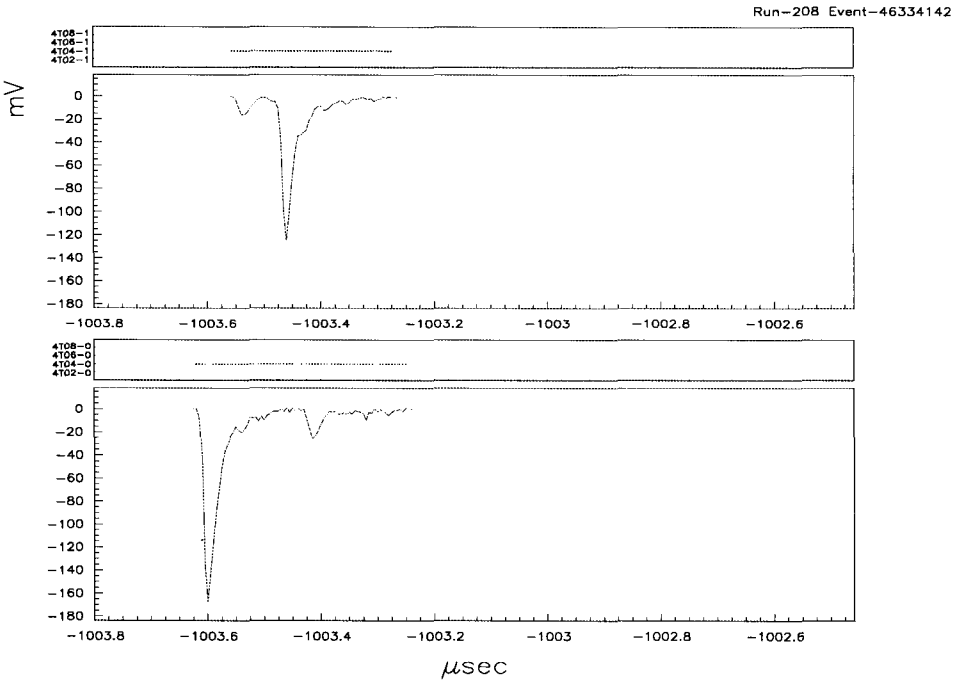

Figure 7.13: Example of a waveform of a multiple event triggered on by the ERP: the two waveforms represent the two sides of the same counter. The waveform shows two separate low energy events within about 200 ns, one near the 0-end of the counter (on the left in the picture) and the other near the 1-end of the counter (on the right in the picture).

These multiple events are mostly double radioactivity events, each with energy of a few MeV, which reconstruct to a higher energy than either of the individual pulses in the waveform. A illustrative sketch of such a double near-tankend radioactivity event is shown in Figure 7.15.

The fact that the ERP triggers on such events but the PHRASE does not is consistent with the expected behavior of the two circuits. For the ERP case, if the

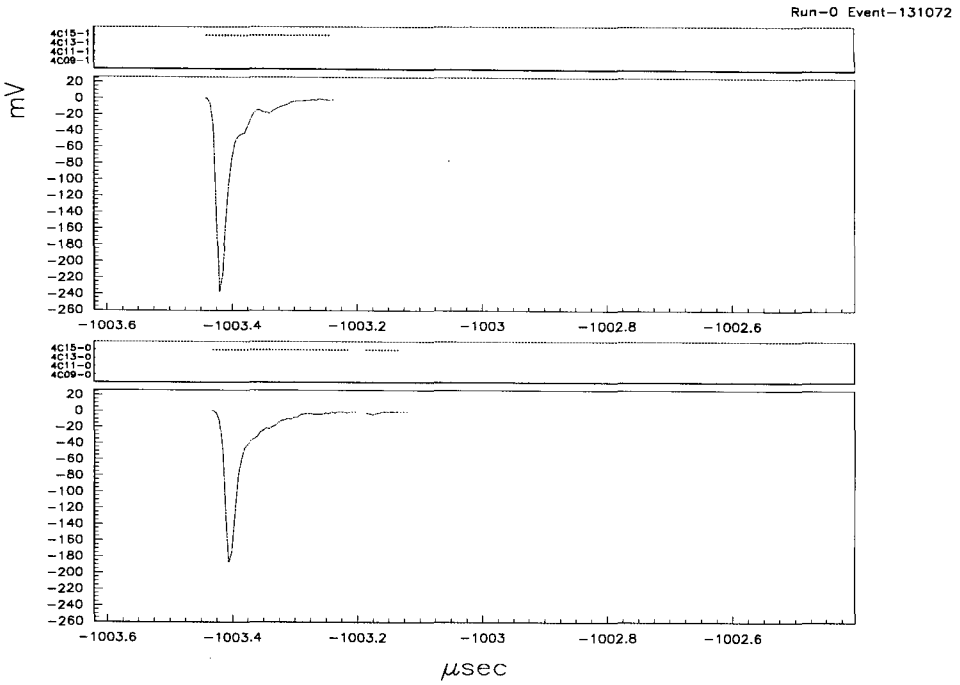

Figure 7.14: Example of a single peak waveforms, corresponding to an ERP trigger hit which passed cuts.

individual pulses on each side exceed a discriminator threshold (65-130 mV, depending on channel) within 270 ns of each other, the pulses on each side will be integrated over at least a 150 ns interval. The ERP may then trigger because the energy value in its LUT corresponding to two integrated pulse charges may exceed energy threshold, even though neither individual event in the multiple event has sufficient energy to trigger. The PHRASE, however, is less likely to trigger on a double event because its energy trigger requires a physically consistent pair of pulses within a coincidence time window of ~80 ns (see Section C.1.1).

It is qualitatively clear from a scan of the waveform pictures for these runs that:

1. The ERP picks up more multiple radioactivity hits than the PHRASE, and

2. the standard cuts on the ERP (in particular the ADCZ/TDCZ consistency requirement) suppress the multiples.

However, to make these statements quantitative and to evaluate the effect of the cuts on overall efficiency of the ERP, it is necessary to count peaks and perform

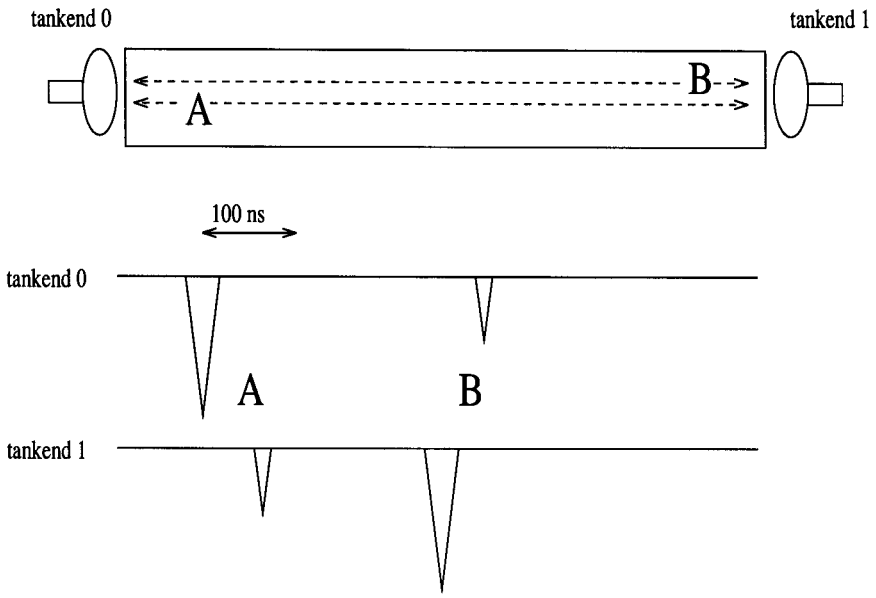

Figure 7.15: Sketch representing accidental coincidences of low energy radioactivity near by the two ends of the counter, such that the pulse size of each individual pulse appears large at the near tankend.

systematic surveys of the lone ERPs passing and failing cuts.

Peak Counting Algorithms

Towards this end, an algorithm was developed to count peaks in the waveforms, i.e. evaluate how many separate pulses (radioactivity events) were present in each ERP-triggered waveform. This task is quite difficult to perform accurately, due to pulse pile-up: peaks occurring near to each other in time overlap each other and are hard to distinguish from one another. However, one can estimate the efficiency of any given algorithm by comparing the results of the peak-counting algorithms to "by-eye" counts.

Several algorithms for peak-counting were tested. The most successful of these uses the following method: first, peaks are counted on each side of the counter separately by looking for local maxima and minima. Next, a simple numerical average (rounding up) of the number of peaks on the two sides is taken, $N_p = \frac{N_1+N_2}{2}$. This method tends to underestimate the number of peaks in the waveform. Comparing

to a "by-eye" scan of 100 events, this algorithm distinguishes between single and multiple peaks correctly 79% of the time. When the requirement for correctness was relaxed to what would be qualitatively "reasonable" for an algorithm to determine, the algorithm distinguished between singles and multiples correctly 93% of the time. Tables 7.2 and 7.3 summarize the results of the peak counting algorithm test.

	No. of peaks counted by eye	
No. of peaks counted by algorithm	1	2
1	29	21
2	1	48
3	0	1

Table 7.2: Results of peak counting algorithm test, comparing numbers of peaks counted by eye to number of peaks counted by the algorithm.

	No. of peaks counted by eye	
No. of peaks counted by algorithm	1	2
1	44	6
2	1	48
3	0	1

Table 7.3: Results of peak counting algorithm test, comparing numbers of peaks counted by eye to number of peaks counted by the algorithm, for the case where the by eye count evaluated the number of peaks it would be "reasonable" for an algorithm to be able to count.

Peak Multiplicities in the ERP and the PHRASE

Next, the peak counting algorithm was applied to obtain distributions of N_p for the ERP and the PHRASE events (with waveforms) under different conditions. Figure 7.16 the shows the distribution of N_p for all ERP hits (with waveforms present, passing cuts or not), compared to the distribution for all PHRASE hits (with waveforms present). These plots clearly show that the ERP is more likely to pick up multiple peak events than the PHRASE.

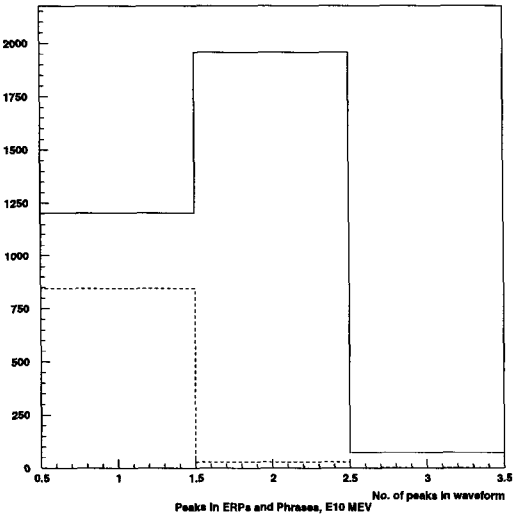

Figure 7.16: Distribution of numbers of peaks in the waveforms of ERP hits (solid line), compared the numbers of peaks in the waveforms of PHRASE hits (dashed line), for the events in the special waveform runs with E>10 MeV.

From these plots it can be seen that for all ERP hits with $E > 10$ MeV the ratio of the number of hits with single peaks to the number of hits with multiple peaks ($\frac{N_{Np=1}}{N_{Np>=2}}$) is about 2:3 whereas for PHRASE hits the same ratio is about 17:1. The fraction of multiples picked up by the ERP is much higher than for the PHRASE.

7.3.4 Effect of the Cuts on the ERP Data on Peak Distributions

Next, the effect of cuts on the ERP data was examined: Figure 7.17 shows the distribution of N_p for ERPs passing all cuts, along with the distribution for uncut ERPs. Approximately 5/6 of uncut ERPs are multiples whereas only $\sim 1/7$ of ERPs passing cuts are multiples. Figure 7.18 considers the ADCZ/TDCZ cut alone: for events failing this cut, multiples outnumber single peaks by a factor of $\sim$4.

Looking at the effect of the ADCZ/TDCZ consistency cut in another way, Figure 7.19 shows ADCZ-TDCZ for single peaks and for multiples (for all ERPs). Clearly,

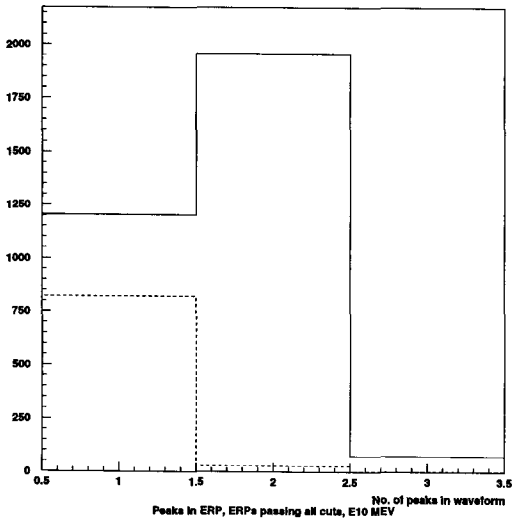

Figure 7.17: Distribution of numbers of peaks for ERP hits passing cuts (dashed line) compared to the distribution for all ERP this (solid line).

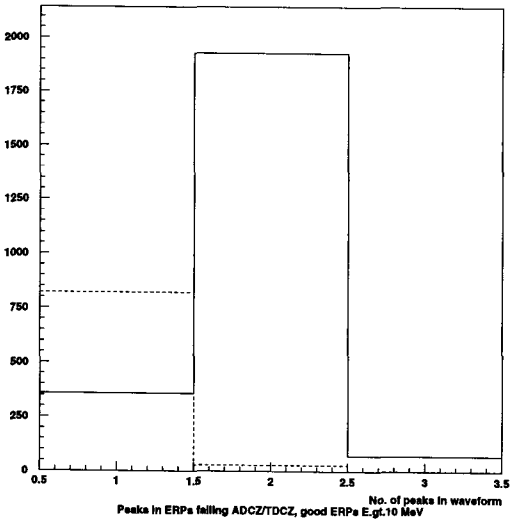

Figure 7.18: Distribution of numbers of peaks for ERPs passing the ADCZ/TDCZ consistency cut (dashed line) compared to those failing (solid line).

the effect of the ADCZ-TDCZ cut is to reject multiples.

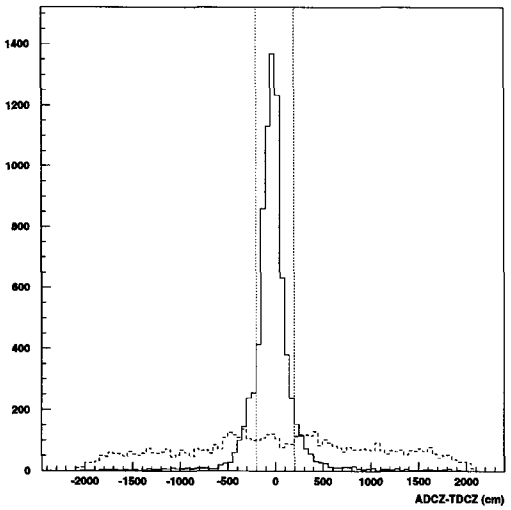

Figure 7.19: Distribution of ADCZ-TDCZ for events with waveforms with $N_p = 1$, and waveforms with $N_p >= 2$. The vertical dotted lines show the cut values.

Evaluating cut efficiency

Waveform information may be used to evaluate the efficiency of the ERP cuts (in particular the ADCZ/TDCZ consistency cut which rejects multiples.)[7] To determine cut efficiency, we must define an unbiased "signal" sample and find the fraction of signal events which pass cuts. According to Figure 7.18, if one assumes that the requirement "$N_p = 1$" is a good measure of "signal", it is necessary to go out to ADCZ-TDCZ= 400 cm to obtain 90% efficiency. However, due to deficiencies in the peak-counting algorithm (in particular, inability to resolve peaks which are close in time), $N_p = 1$ is a poor "signal" criterion. Additional selection criteria may be required in order to choose a good "signal" sample. To define a sample for evaluating

[7]The cut requiring the position to be reconstructed inside the counter is performed before ADCZ/TDCZ cut for historical reasons; however nearly all events rejected by this cut are also rejected by the ADCZ/TDCZ cut.

cut efficiency, we require $N_p = 1$ AND a match with the PHRASE.[8] The ADCZ-TDCZ distribution for the signal sample defined in this way is shown in Figure 7.20.

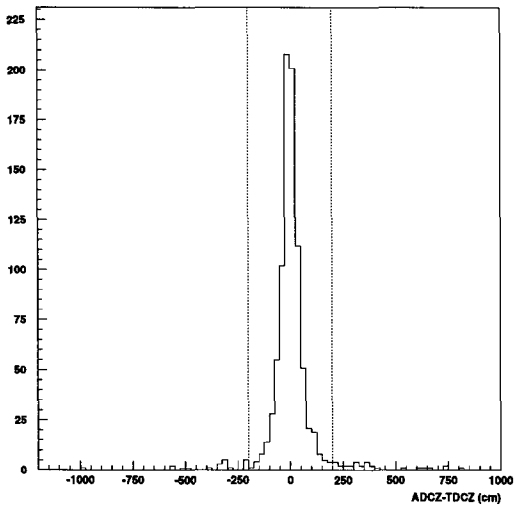

Figure 7.20: ADCZ-TDCZ distribution for events with $N_p = 1$ and a matched PHRASE event, for $E_{erp} > 10$ MeV.

Defining signal in this way, the cut efficiency is given by the ratio R of number ERP events passing cuts to the total number of events in the signal sample.

Efficiency as a function of cut value A, where the ADCZ/TDCZ consistency requirement is $|ADCZ - TDCZ| < A$ is shown in Figure 7.21. The efficiency value at the current cut value of $A = 200$ cm is found to be $\sim 90\%$.

Optimizing the cut values

To choose an optimum cut value A, one must balance efficiency versus background: the looser the cut, the better the efficiency for capturing signal but the higher the background, and therefore the higher the multiplicity threshold for a burst search and the the lesser the sensitivity (and conversely).

To evaluate the trade-offs, the following are computed:

[8]This signal criterion may possibly be biased: for instance, perhaps selecting PHRASE-matched events biases against near-tankend events which may have a different ADCZ-TDCZ distribution than normal events. However, there is no reason to believe any such biases have a significant effect.

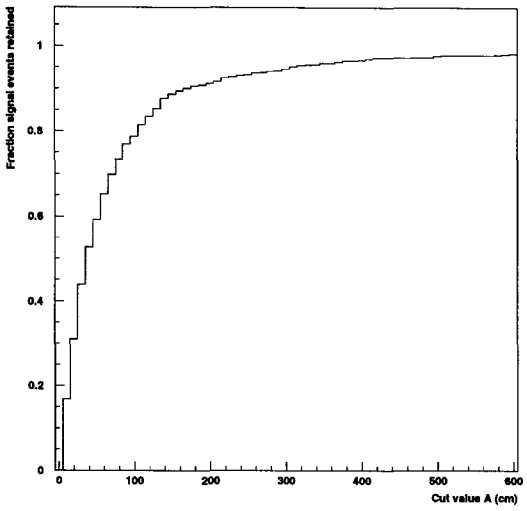

Figure 7.21: Efficiency as a function of cut value A; hits are accepted if $|ADCZ - TDCZ| < A$.

1. The rate of unrejected ERPs as a function of $|ADCZ - TDCZ|$ cut value A, to get the multiplicity threshold $N_{mt}(A)$ for a chosen set of burst search parameters.[9] For this study a 6 second time window was chosen, and the Poisson probability threshold for determining the multiplicity threshold was chosen to be 10^{-5}.

2. The expected signal detection probability: for a signal of S neutrino interactions, the probability P of seeing at least N_{mt} events out of S, for each event having efficiency ϵ of detection. P is given by

$$P = \sum_{n=M}^{S} \mathcal{P}_n(\epsilon, S) \tag{7.5}$$

where $\mathcal{P}_n(\epsilon, S)$ is the probability of seeing n out of S events, given probability

[9] $N_{mt} = N_{pr}$ was used here (see Section 6.3.1); however the choice of $N_{mt} = N_{pr}$ or $N_{mt} = N_{10yr}$ does not affect the results of the cut optimization.

ϵ of seeing each.

$$\mathcal{P}_n(\epsilon, S) = \begin{pmatrix} S \\ n \end{pmatrix} \epsilon^n (1-\epsilon)^{S-n} \tag{7.6}$$

P is a function of cut value A, through the efficiency $e(A)$ and $N_{mt}(A)$.

Next, one finds the minimum S, S_{min}, such that $P > 90\%$ for a given A. Figure 7.22 shows S_{min} for 90% detection as a function of A. The minimum S_{min} on this plot should give the cut value A_{opt} where signal detection is optimized. The plot shows a dramatic drop in S_{min} from $A = 10$ to $A = 100$ cm, a long slow minimum around $A = 100 - 250$ cm, and a very slow rise up to loose cut values of ~ 600 cm. There is a weak dependence on chosen burst search parameters: Figure 7.23 shows additional S_{min} versus A plots for 1 and 20 second time windows. A_{opt} shows a slight shift to to left (low A) for longer burst search time windows (since background is more important on the long time scale). In all cases the chosen cut value of 200 cm is in the valley: this chosen value is somewhat conservative, in the sense that the background is low enough that there is very little loss of sensitivity while we are certain to remain in efficient regime.

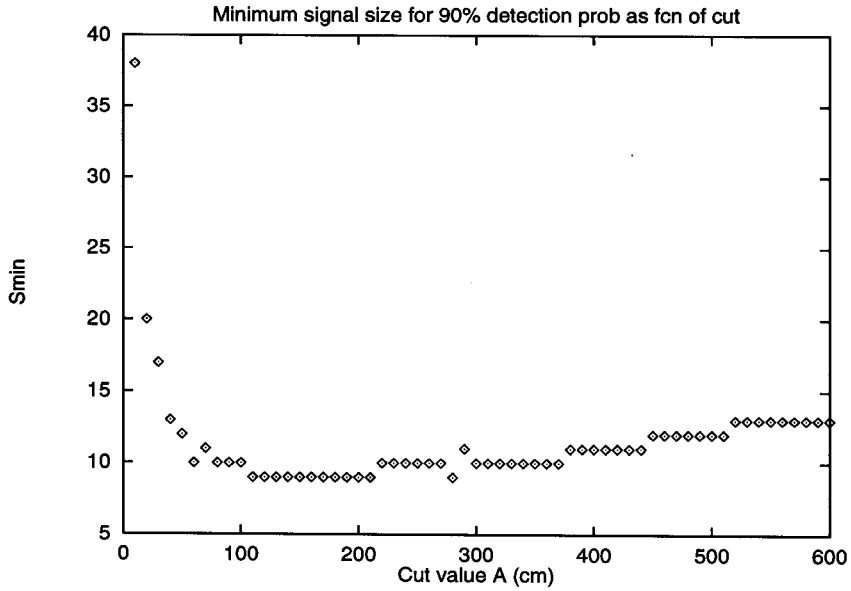

Figure 7.22: S_{min} for 90% detection as a function of cut value A.

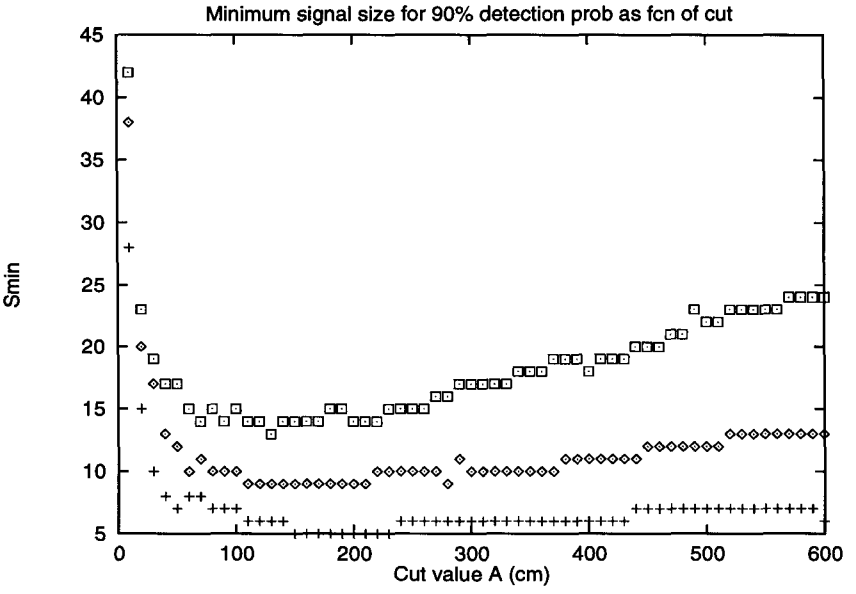

Figure 7.23: S_{min} for 90% detection as a function of cut value A for different burst search parameters. The top plot corresponds to a 20 second burst search time window, the middle plot to a 6 second window, and the bottom plot to a 1 second time window.

The question of the physical origin of the multiples — whether they are correlated radioactivities or simply uncorrelated near tankend accidentals — is considered in Appendix F.

7.3.5 Trigger Efficiencies

Rates of mismatched events can give some idea of relative trigger efficiencies of the ERP and the PHRASE. However, evaluating such efficiencies (at a given energy threshold) is somewhat complicated by the fact that ERP and PHRASE reconstructions differ, and the average energy $E_{avg} = (E_p + E_e)/2$ (used for the combined event-wise burst searches, Section 7.4.1) differs from both E_p and E_e. For a given hit, the E_e is likely to be higher than E_p; therefore the sample of matched hits with $E_e > 10$ MeV is different from the sample with $E_p > 10$ MeV, and both samples are different from the one used for the combined burst search (Section 7.4.1).

Table 7.4 gives numbers of matches and mismatches for run 11834, for a given

sample of PHRASEs with $E_p > 10$ MeV, and for a given sample of ERPs with $E_e > 10$ MeV.

PHRASEs $E_p > 10$ MeV	Total Number	728
	No ERP partner	89
	With ERP passing cuts $E_e > 10$ MeV	348
	With ERP passing cuts $E_e < 10$ MeV	89
	With ERP failing cuts $E_e > 10$ MeV	106
	With ERP failing cuts $E_e < 10$ MeV	96
ERPs $E_e > 10$ MeV passing cuts	Total number	1598
	No PHRASE partner	655
	With PHRASE $E_p > 10$ MeV	348
	With PHRASE $E_p < 10$ MeV	595

Table 7.4: Breakdown of matches and mismatches, for unvetoed hits.

Some lone PHRASEs actually do have ERP partners, but the ERP partners do not pass cuts. Other lone PHRASEs ("true lone PHRASEs") have no ERP partners at all. One may use the fraction of true lone PHRASEs to estimate the trigger efficiency of the ERP (and vice versa): according to Table 7.4, the fraction of true lone PHRASEs gives $89/728 = 13\%$ ERP trigger inefficiency. Similarly, the fraction of true lone ERPs gives $655/1598 = 40\%$ PHRASE trigger inefficiency. However, these estimates should be considered extreme upper limits on inefficiency; there is indirect evidence that lone ERPs and true lone PHRASEs mostly represent extra background (e.g. multiples or other low-energy events from an inefficient regime mis-reconstructed as having high energies) in each circuit, rather than signal events seen in one system but missed by the other system. For instance, it is likely that the great majority of the lone ERPs passing cuts are near-tankend multiples (as described in the previous sections) that are not rejected by the cuts. For the special WFD run described in Section 7.3.3, only 5% of single-peak ERP hits passing cuts had no PHRASE partners.

For the true lone PHRASE case the situation is less clear due to lack of independently measured waveform information for PHRASE-only triggers. However, some evidence suggests that the lone-PHRASE events are less likely to be "real" than

matched PHRASE events. For the run studied, true lone PHRASE hits tend to be bunched in certain counters (~40 out of 450). However, these counters do not appear to be inefficient (i.e. have low rates) in the ERP. For counters containing true lone PHRASEs, the average rate of matches is about the same as for counters containing no true lone PHRASEs (2.3 vs 2.1 hits per box).

Therefore, more realistic trigger inefficiency estimates are in the 5–10% range at 10 MeV, for both systems.

7.3.6 Final Data Sample

Figure 7.24 shows energies and positions for the final samples of hits used for the burst searches (matches with $E_{avg} = (E_p + E_e)/2 > 10$ MeV, PHRASEs with $E_p > 10$ MeV and ERPs with $E_e > 10$ MeV), for run 11834. Note the excess of hits near the tankends, which is especially pronounced in the ERP case. There are several reasons for this excess: first, energies are more likely to be misreconstructed near the tankends due to the steepness of the response curve (i.e. a small position difference can cause a relatively large energy error). In addition, background rejection is worse near the ends of the counter. Rejection of muons using ST information is slightly more inefficient near the tankends; more importantly (especially for the ERP case), rejection of multiples using the ADCZ/TDCZ cut becomes inefficient near the counter ends because ADCZ is constrained to be within the counter (by its definition, equation 5.10).

7.4 Burst Search Analysis

7.4.1 Searches

The general GC burst search procedure has already been outlined in Section 6.3.

For most runs during the time period analyzed, ERP and PHRASE circuits were running on all six supermodules and viewing MACRO's full active mass. However, because they operate independently, in the most general case, the ERP and the PHRASE view different active masses. For many runs, either the ERP or the

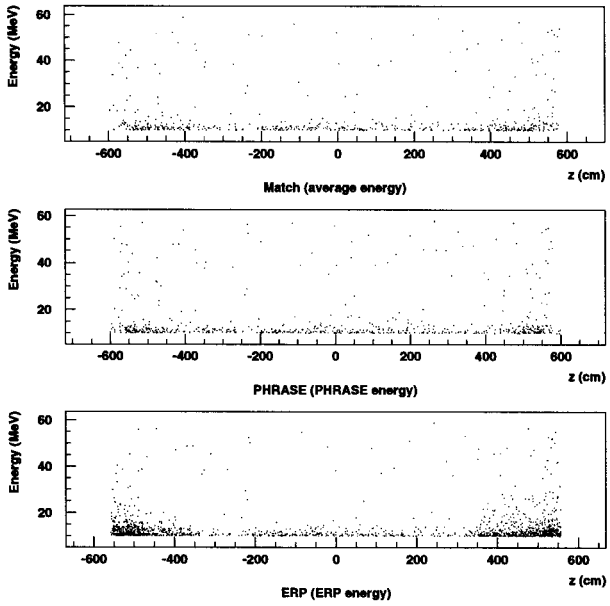

Figure 7.24: Scatterplot of reconstructed energy vs. counter longitudinal position for the sample of unvetoed hits, for matched events with $E_{avg} > 10$ MeV (top plot), PHRASE hits with $E_p > 10$ MeV (middle plot) and ERP hits with $E_e > 10$ MeV (bottom plot).

PHRASE was off on some or all supermodules. This most commonly happens during calibration runs, for which calibrations are performed on one microVAX on the main acquisition, while the PHRASE acquisition system is kept running on the other two microVAXes. In addition, for either trigger system, sometimes supermodules or microVAXes are down due to hardware problems or for maintenance.

To deal with the situation of different active masses in a combined ERP/PHRASE analysis, four types of searches are performed:

1. An ERP-only search: a search among all ERP events (unvetoed and passing cuts) with $E_{erp} > E_{th}$, where E_{erp} is the ERP reconstructed energy (adjusted), for runs and active masses where ERP was present.

2. A PHRASE-only search: a search among all PHRASE events (unvetoed) with $E_{phr} > E_{th}$, where E_{phr} is the PHRASE reconstructed energy, for runs and

active masses where PHRASE was present.

3. A combined "event-wise" AND search: a search among all unvetoed matched events (i.e. hits present in *both* ERP and PHRASE), for $E_{avg} > E_{th}$, where $E_{avg} = (E_{erp} + E_{phr})/2$, for runs and active masses where both ERP and PHRASE were present.

4. A combined "event-wise" OR search: a search among both matched and unmatched events (i.e. hits present in *either* ERP or PHRASE), for $E_{avg} > E_{th}$ for the matched events, $E_{erp} > E_{th}$ for the lone ERP hits and $E_{phr} > E_{th}$ for the lone PHRASE hits, for runs and active masses where both ERP and PHRASE were present.

Note that the combined event-wise AND and OR searches are done only for runs/supermodules with *both* ERP and PHRASE present in the data stream, i.e. for a "run AND" (strictly, an "active mass AND"). The "run OR" case (either ERP or PHRASE present in the run/supermodule) is effectively covered by the ERP-only and PHRASE-only search cases. The term "combined search" will refer to both the event-wise AND and the event-wise OR; the term "separate searches" will refer to the ERP-only and PHRASE-only searches.

For example: for a run with the ERP running on supermodules 1 through 4 and the PHRASE running on supermodules 3 through 6, the combined searches (event-wise ANDs and ORs) will be performed on the two supermodules in common, 3 and 4. An ERP-only search will be performed on supermodules 1 through 4, and a PHRASE-only search will be performed on supermodules 3 through 6.

Each search was done for four different energy thresholds (7, 10, 12, and 15 MeV) and six different time windows (1, 2, 6, 8, 10, and 20 seconds).

7.4.2 Data Selection

The time period starting on July 24, 1995 and ending on February 8, 1996 was analyzed. For this period, the entire detector was instrumented with both ERP and

PHRASE circuits. The start time was chosen to correspond to the introduction of the new data storage technology of DLT tapes (Section 4.5.4), for which analysis can be performed a factor of ~2 more quickly.

Run Cuts

Runs listed as calibration runs according to the standard logs were skipped (note that calibrations are usually done on a single microVAX at a time and that PHRASE is kept running on the other microVAXes during calibrations, to minimize dead time.)

Runs with livetimes < 5 minutes with total hit rates more than $\sim 2\sigma$ above the nominal mean rate (for the time period) were excluded.

A few runs with problems according to the data-taking logbook (for instance, with high voltage system problems) were skipped.

For the combined searches, the OR and AND livetimes were required to be consistent within 500 seconds; if not, the separate searches only were done for the run. The purpose of this run cut is to eliminate runs for which either the ERP or PHRASE turned off during the run; for such cases, appropriate background rates would be incorrectly calculated.

There was no attempt to do ERP/PHRASE time matching for runs on the main and backup acquisitions which might have been running independently on the same active mass during the same time period; such run time overlaps represent less than 1% of the data. (ERP and PHRASE separate searches were done for such cases.)

Box and Supermodule Cuts

In addition to the global run cuts, individual counters or supermodules were occasionally excluded on a run by run basis, according to the following conditions:

- Individual "hot" counters were excluded from the burst search sample if the rate for the run was greater than ~ 30 times the average rate for a counter for the run, in either the ERP or the PHRASE.

- Individual supermodules were excluded from the burst search for the following cases:

  - For the combined searches, runs were excluded for which the total number of hits in the ERP <2000 for the run, and <1000 for the PHRASE.[10] Note that this cut effectively excludes very short runs from the combined searches. (This cut does not affect the separate searches, although as mentioned above, very short high rate runs may be excluded for the separate searches by the run cuts.)
  - The total rate for the supermodule >3 times the average rate per supermodule (such conditions usually correspond to problems with the data).

  The counter and supermodule cuts were performed independently for the ERP-only and PHRASE-only searches. However, if a counter or supermodule was excluded from either of the separate searches, it was also excluded for the combined searches.

  The counter and supermodule cuts affected less than 3% of the data.

7.4.3 Rates

A plot of rates as a function of run number for the time period is shown in Figure 7.25, for the combined searches. The ERP and PHRASE rates for the separate searches are shown in Figure 7.26.

The gaps in this plot do not generally indicate dead time: usually they correspond to sets of calibration run numbers or sets of very short runs that were skipped. The change in rates starting at about run 11380 corresponds to a PMT gain resetting.

[10]The count criteria are scaled by the active mass fraction for the north and south faces of the detector, which are treated as separate supermodules.

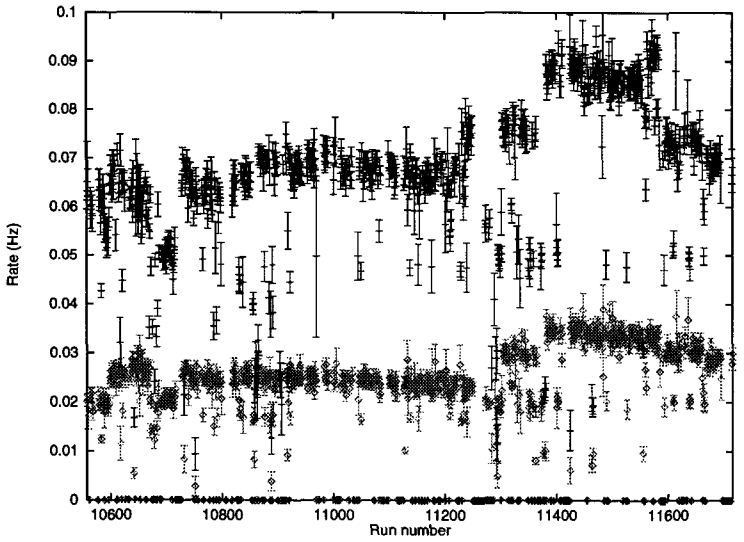

Figure 7.25: Combined search rates as a function of run number, for the OR search (top), the AND search (bottom).

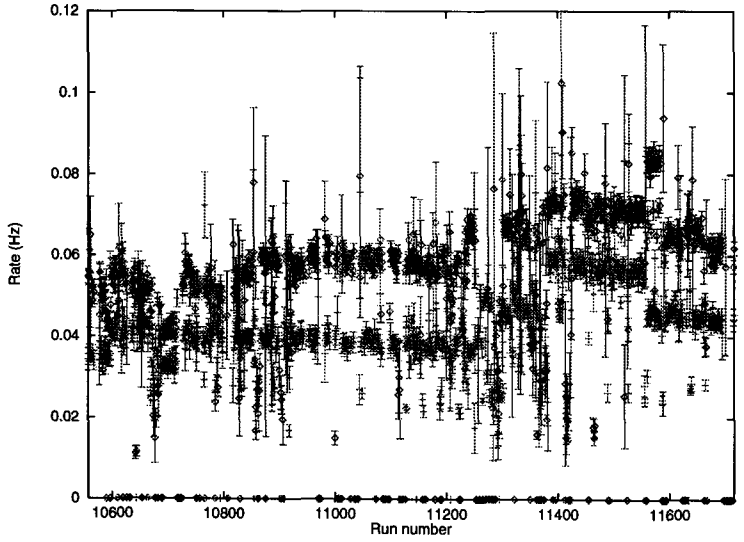

Figure 7.26: Separate search rates as a function of run number, for the ERP-only search (top) and the PHRASE-only search (bottom). Short runs were less likely to be cut for separate searches than for the combined search.

7.5 Results

7.5.1 Active Mass

The active mass as a function of time for the period is shown in Figure 7.27, for the PHRASE-only search, the ERP-only search and for the combined search. For each day, the active mass is an average over runs, weighted by relative livetime. Note that the active mass in these plots is normalized by total livetime, not total real time.

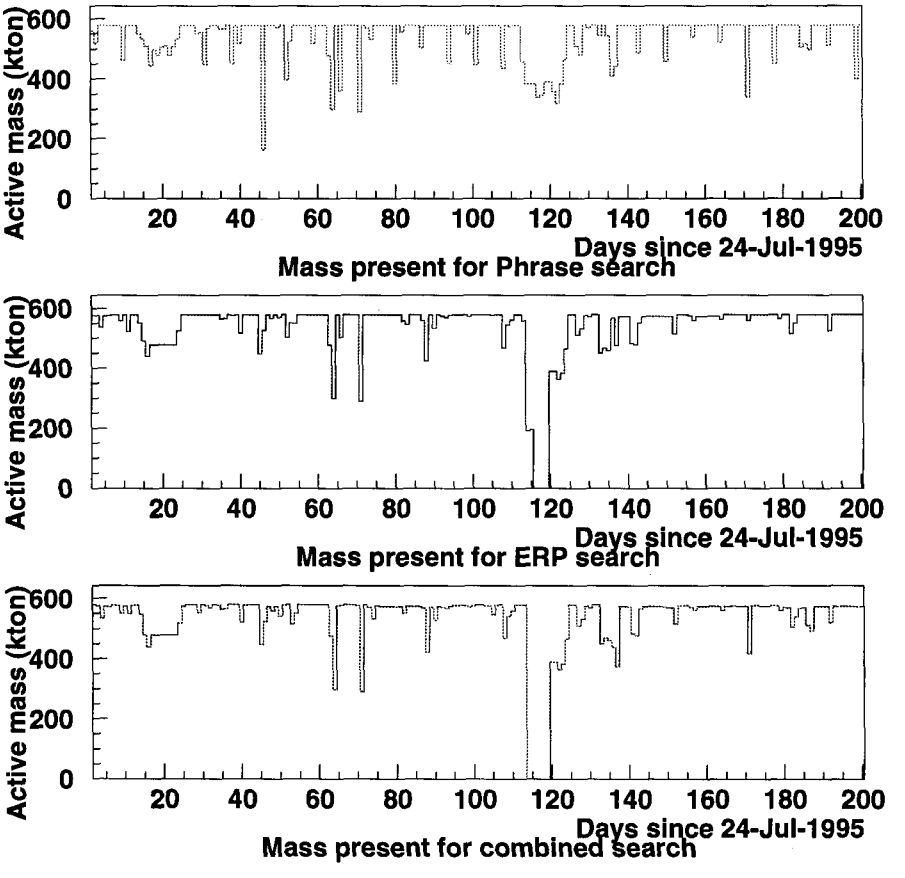

Figure 7.27: Active mass present for the PHRASE-only, ERP-only and combined searches as a function of days since July 24 1995.

7.5.2 Fraction Up-time

The "fraction up-time" over the analyzed time period, i.e. the percent of the time at least one supermodule was active for the search, is shown in Figure 7.28 for the different searches. The bottom plot shows the percent of time that either ERP or PHRASE had at least one supermodule active: this translates to the fraction of time MACRO was sensitive to a gravitational collapse.

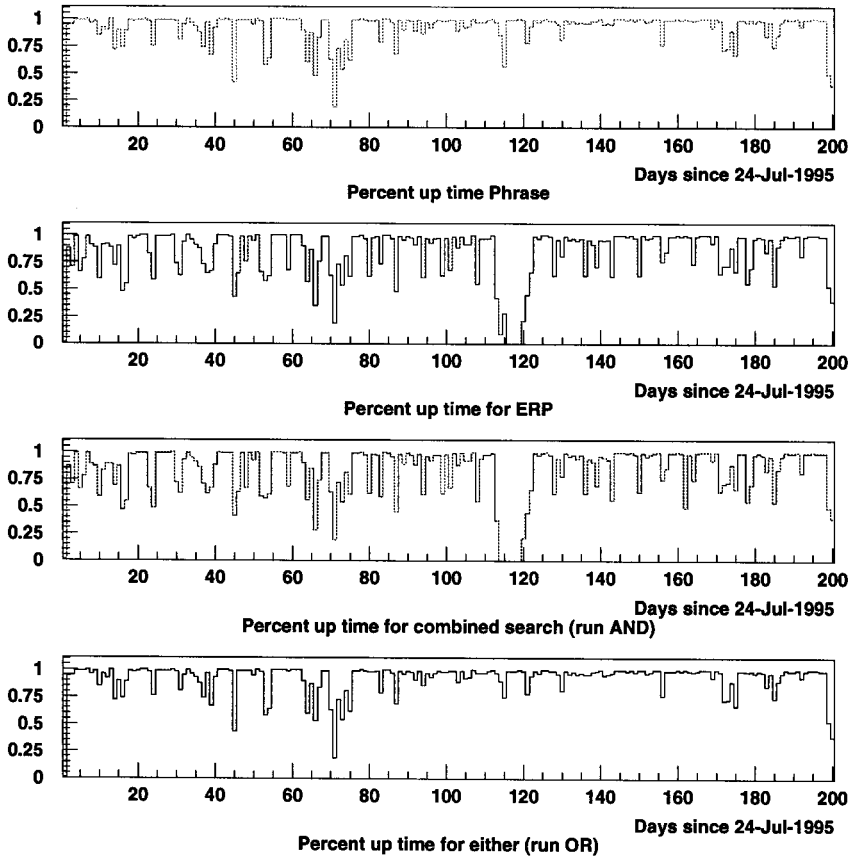

Figure 7.28: Fraction up-time for the PHRASE-only search, the ERP-only search, the combined search (run AND) and the run-OR (either ERP or PHRASE active).

The total livetime fractions corresponding to the four plots are: 92.7% for the PHRASE-only search, 84.0% for the ERP-only search, 82.8% for the combined search

(the run-AND) and 93.4% for the run-OR.

For both the up-time and active mass plots, the hole in the ERP and run-AND data plots from day 113 to day 119 corresponds to a period of detector maintenance (primarily photomultiplier tube gain resetting). As can be seen from the top and bottom plots, during most of this time, the PHRASE was kept running on some of the active mass to minimize dead time for GC detection.

7.5.3 Multiplicity Distributions

For each of the four burst search types (the two separate and the two combined), multiplicity distribution histograms are accumulated for each energy threshold and time window. The histograms are then compared to Poissonian predictions for each run, based on the background rate (for the burst search) for that run. For a given burst search, independent probabilities in each time window are assumed, which is a very good approximation for all but the longest time windows and highest rates (since for those cases, the time windows opened for the search are likely to overlap with each other). The histograms for the data and the Poisson predictions for all runs are then summed to give the total multiplicity distributions for the time period.

In addition information is written to disk for all bursts with Poisson probability $< 10^{-5}$ (10^{-8} for the 7 MeV search, which has much higher background rates). These files are scanned by hand.

Figures 7.29 and 7.30 show examples of multiplicity distributions along with Poissonian predictions for the event-wise AND and OR cases for the period under consideration, for an energy threshold of 10 MeV and for all 6 time windows used. There are no significant deviations from Poissonian predictions. The expected signal for a gravitational collapse event at the center of the galaxy would lie far to the right on the multiplicity axis for any of these plots: for example, for a 2 second time window a signal multiplicity of $\sim$100 events would be expected.

Figure 7.31 shows the same set of multiplicity distributions for the PHRASE-only search, and Figure 7.32 for the ERP-only search, again for a 10 MeV energy

threshold. Again, there are no significant deviations from Poissonian predictions. A similar pattern is seen for the burst searches at the other energy thresholds. Therefore, no gravitational collapse burst candidates were observed for the period.

7.5.4 Physics Results

The total livetime for the run-OR search was 186.8 days; this corresponds to a 90% C.L. limit on the rate of gravitational collapse in the galaxy of <4.5 per year. During the entire livetime of this search, MACRO was always sensitive to SN1987A-like neutrino bursts at the center of the galaxy (corresponding to the worst case of only one active supermodule); however for > 95% of the livetime, at least 1/3 of the detector was running, making MACRO sensitive to a SN1987A-like burst anywhere in the galaxy (see Figure 6.8). Other GC real-time neutrino detectors (Section 3.2.3) live during this search period were Kamiokande III, LVD and Baksan.

Other GC searches with MACRO have been performed on either ERP or PHRASE data separately; none have turned up any significant bursts. The results of a PHRASE-only search were published in reference [81]. This search covered a 29 month period starting on October 9, 1989; the first supermodule prototype was used for most of it, although a few-month period also included the lower parts of supermodules 2 and 3. Results from other PHRASE searches can be found in references [94] (December 15, 1992 through February 1, 1993, lower parts of 5 supermodules), [79] (July 27, 1994 through January 31, 1995, 4-6 supermodules online), and [95] (February 1, 1995 through February 1 1996, full active mass). Results of an ERP-only search with the full active mass covering the time period from November 22, 1995 to April 10, 1996 can be found in reference [84].

The GC rate limit from this thesis is not competitive with published limits of long-running experiments such as Baksan (<0.41 per year) and IMB (< 0.71 per year) [96], or the combined limit from Kamiokande, Baksan, Mont Blanc and IMB [13] of <0.08 per year. However, combined ERP/PHRASE data analysis continues. If MACRO's total livetime for a GC search is ten years, a GC rate limit of <0.23 per year can be

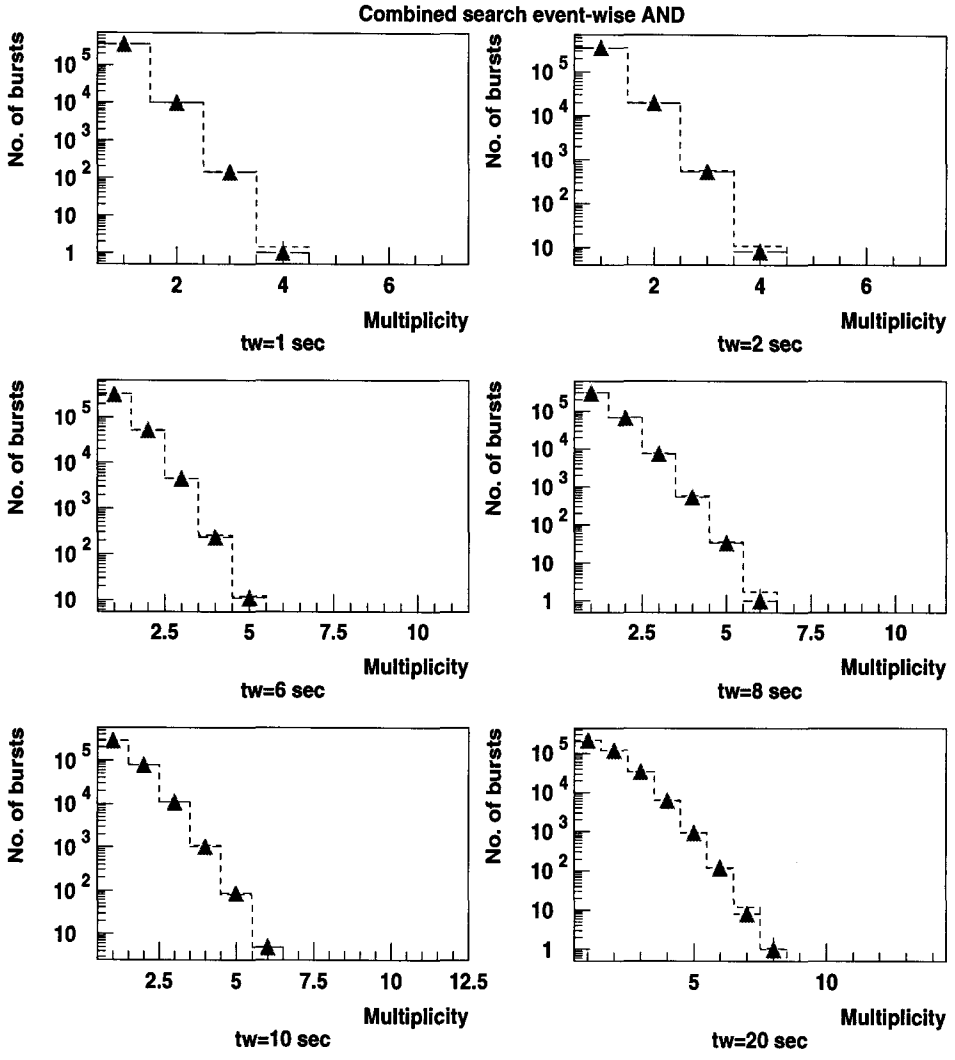

Figure 7.29: Multiplicity distributions (triangles) plus Poissonian predictions (dashed line) for an event-wise "AND" of ERP and PHRASE hits (E> 10 MeV) for the whole time period. The time windows used for the searches are 1, 2, 6, 8, 10, and 20 seconds.

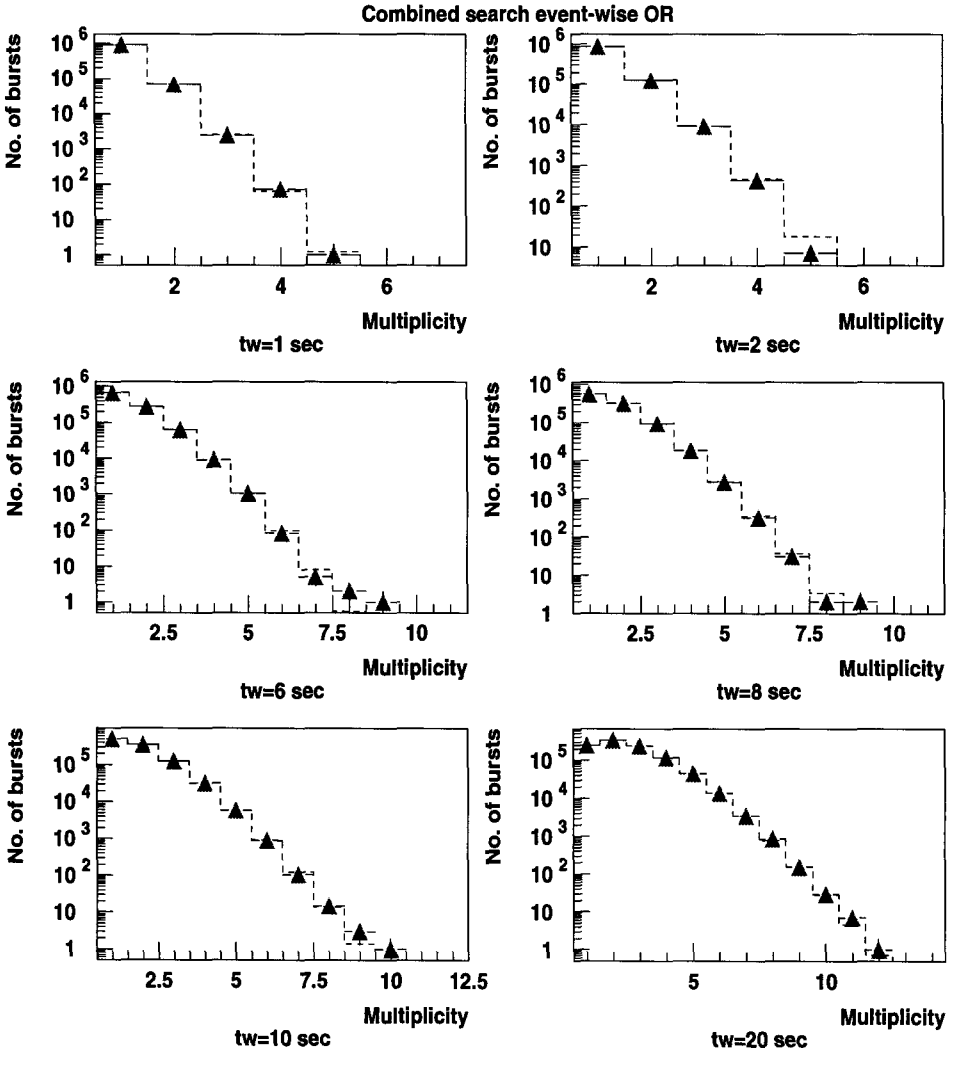

Figure 7.30: Multiplicity distributions (triangles) plus Poissonian predictions (dashed line) for an event-wise "OR" of ERP and PHRASE hits (E> 10 MeV) for the whole time period. The time windows used for the searches are 1, 2, 6, 8, 10, and 20 seconds.

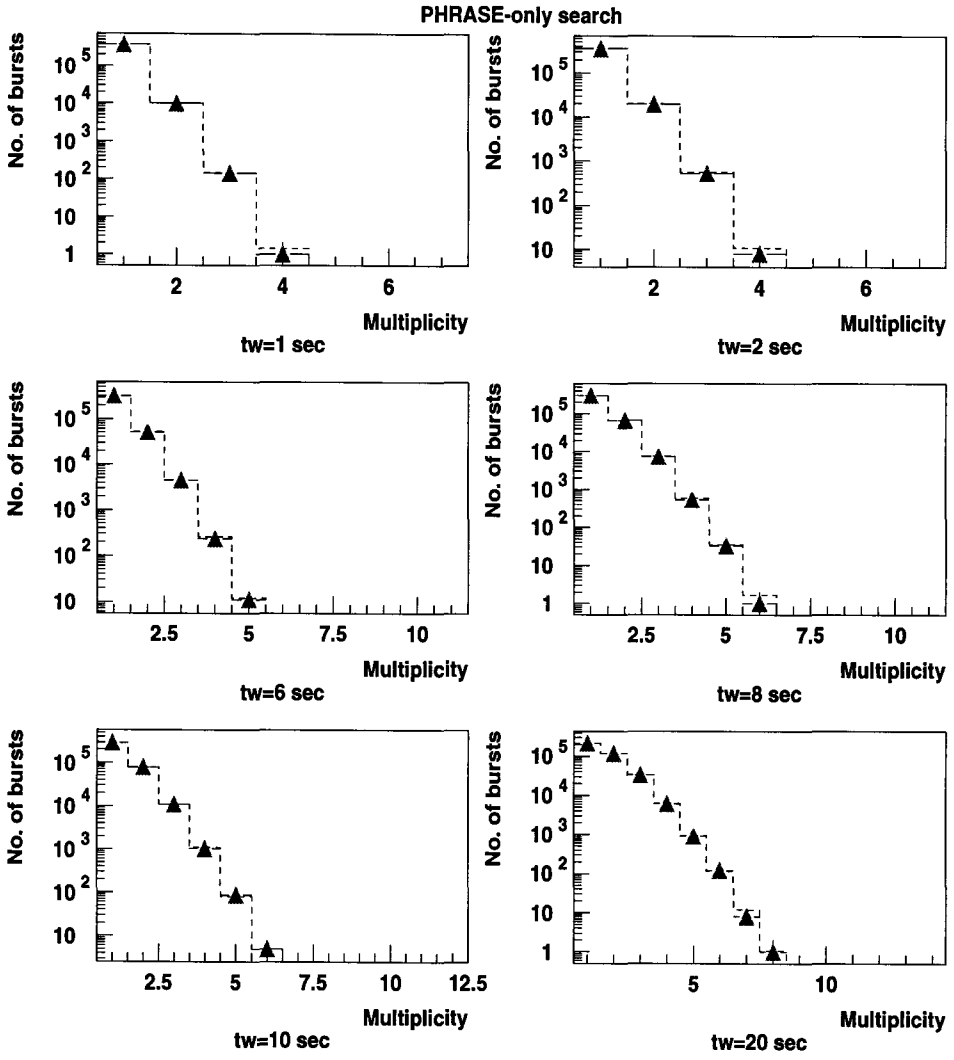

Figure 7.31: Multiplicity distributions (triangles) plus Poissonian predictions (dashed lines) for the PHRASE-only search (E> 10 MeV) for the whole time period. The time windows used for the searches are 1, 2, 6, 8, 10, and 20 seconds.

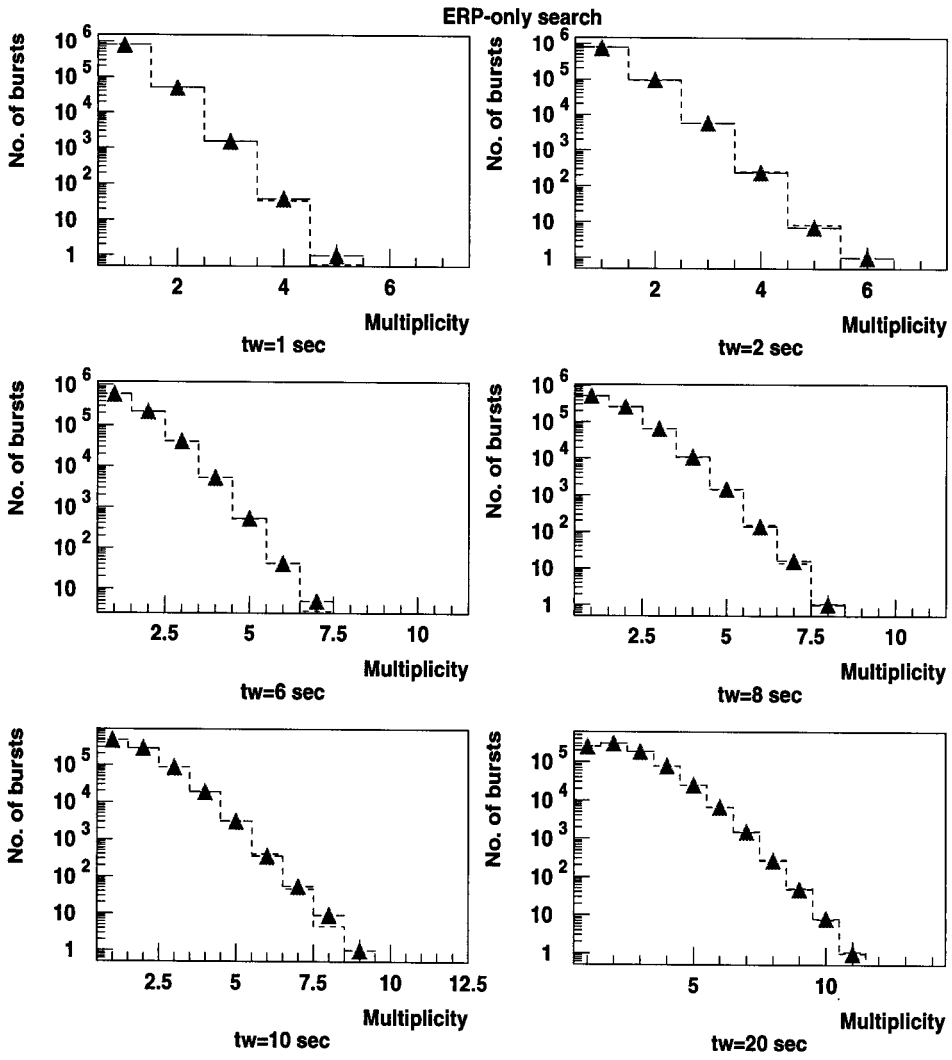

Figure 7.32: Multiplicity distributions (triangles) plus Poissonian predictions (dashed lines) for the ERP-only search (E> 10 MeV) for the whole time period. The time windows used for the searches are 1, 2, 6, 8, 10, and 20 seconds.

reached.

Chapter 8 Online Monitoring

As was pointed out in Chapters 2 and 3, a neutrino signal from a gravitational collapse can be detected hours or even days ahead of the corresponding optical signal. A prompt detection of a neutrino burst could alert optical astronomers to the possibility that a collapse event had occurred within the galaxy. Early optical detection can be very valuable for studies of the early light curve. Although certainly information about the direction from which the neutrino burst came would be very helpful to optical astronomers, the simple knowledge that a burst had occurred, as could be provided by MACRO, would be of great value.

Furthermore, there are several detectors in the world which are sensitive to gravitational collapse neutrinos. If one of them sees a gravitational collapse neutrino burst, workers at the other experiments should be informed so that the data can be searched for a corresponding burst. A coincidence of bursts would provide even more plausible evidence that a gravitational collapse event had occurred. A network of optical astronomers interested in supernovae and physicists working on underground gravitational collapse neutrino detectors is being established to provide prompt warnings of candidates for gravitational collapse events in the galaxy (see Section 8.3).

For these reasons, an online data monitoring system which checks the incoming data in real time for the presence of supernova-like bursts of events is desirable. MACRO has two separate, completely independent, gravitational collapse monitoring systems, for the ERP and the PHRASE. Both will be described here, although the ERP monitor software will be described in considerably more detail than the PHRASE monitor because it represents the work of this thesis.

8.1 The PHRASE Monitor

8.1.1 The PHRASE Monitor System: SNM

The PHRASE monitor system was set up by the University of Pisa group and is described in detail in reference [81]. The PHRASE online gravitational collapse monitor runs on a dedicated VAXstation which employs special "spy" software to look at events coming in from the three PHRASE acquisition microvaxes (see Section 4.5.4). The "spy" implementation means that the monitor process runs at a lower priority than the PHRASE acquisition; although the monitor's efficiency for collection of events may be less than 100%, the priority given to the PHRASE acquisition ensures that the efficiency with which the data are acquired and written to disk by the PHRASE acquisition is not compromised. The PHRASE monitor program, SNM, reconstructs the energies and positions and times of events from all six supermodules as they are read by the acquisition. Events are labeled as "coincidences" if they have neighboring PHRASE events in time within 320 ns or are associated with streamer tube triggers within 5 μs [1] "Unvetoed" hits are those which have no coincidences with neighboring PHRASE events or with streamer tube triggers.[2] The software keeps track of current rates of all unvetoed hits within the past two hours. After a software energy cut of 10 MeV, a burst search similar to the offline one (Section 6.3) is performed on the hits surviving cuts. The time windows used are 0.125, 0.25, 0.5, 1, 2, 4, 8, 16, 32, and 64 seconds. Multiplicity thresholds are recalculated every two hours. Any bursts of sufficiently low Poisson probability (10^{-5}) generate an alarm. Figure 8.1 shows the online display of the SNM program.

A spy system similar to SNM, called LSCM, is also used as a diagnostic tool for the general health of the PHRASE system and the scintillator system as a whole. A display on the terminal of the PHRASE monitor VAXstation (see Figure 8.2) shows

[1] The Bari trigger signals (Section 4.5.2) are plugged into spare channels of the PHRASE, so that ST information is available for the PHRASE monitor despite the fact that the PHRASE runs with an independent acquisition system.

[2] Note that terminology varies somewhat on the two sides of the Atlantic. "Unvetoed" hits are referred to as "singles" in the Pisa PHRASE analyses, and "clusters" in Pisa analyses are referred to as "bursts" in the ERP. In this thesis the ERP terminology will be used for consistency's sake.

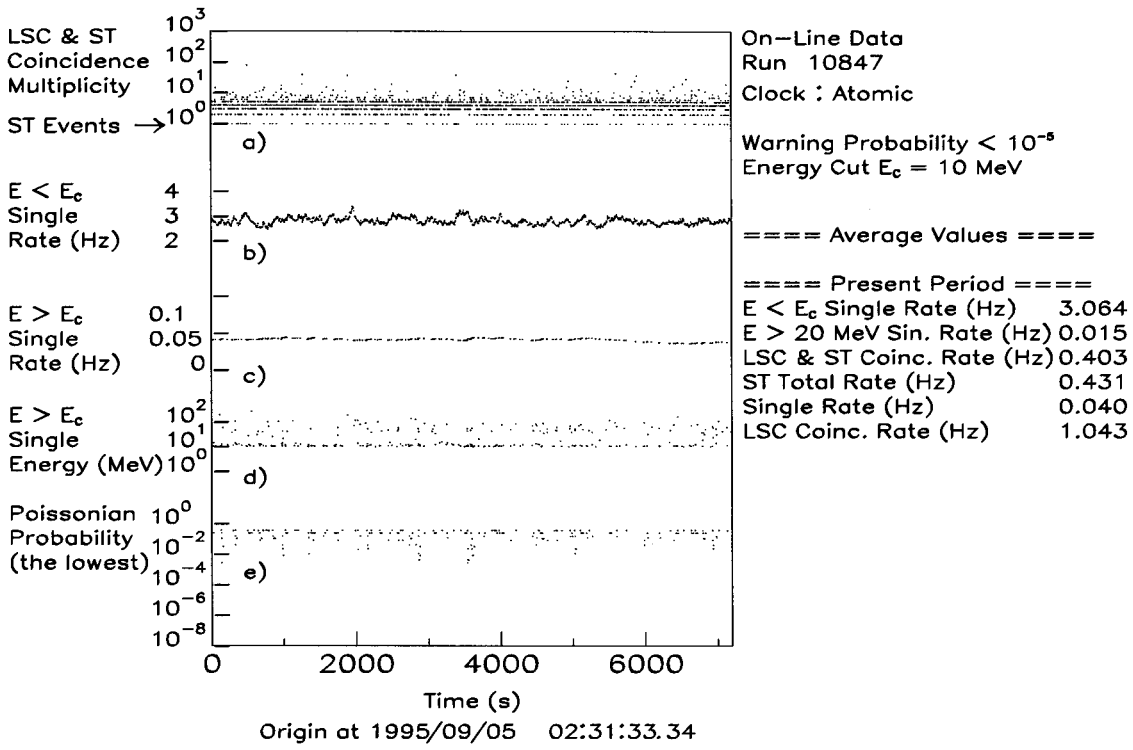

Figure 8.1: Example of a PHRASE monitor online display, for run 10847. "LSC" stands for "liquid scintillator counters" (i.e. PHRASE counters), and "ST" for streamer tubes. The top plot shows counter multiplicities for coincidences between PHRASE and streamer tube triggers, as a function of time. The second plot gives rates of unvetoed ("single") hits for hits failing the energy cut (at 10 MeV); the third plot shows shows rates of unvetoed hits passing the energy cut. The fourth plot gives the energies of the unvetoed hits, and the bottom plot gives the running Poisson probability (the minimum probability of the time windows searched.) Rate information for the above quantities is summarized on the right; also given is the LSC and ST trigger coincidence rate (counting all counters in an event), the total ST trigger rate, and the LSC coincidence rate (rate of counters in coincidence with each other.) (F. Cei).

the current PHRASE unvetoed hit rates as a function of time for each supermodule. Anomalous detector conditions often show up on this monitor as deviations in the rates. SNM also continually outputs the event information it processes to disk in DST (data summary tape) format, containing energies, positions and times of all events. In addition, a full offline burst search PHRASE analysis is performed at the end of each run. The job which performs the post-run analysis has access to all of the events on disk, and so is not subject to loss of events as the online spy job is.

8.1.2 PHRASE Monitor Alarm Output

When an alarm condition is met, the PHRASE monitor takes several actions. Electronic mail is sent out to a mailing list of interested parties (both in Italy and in the US) containing a summary of information about the bursts. An example of such an alarm message is shown in Appendix G. The program immediately tries to contact an expert via the online alarm system. The standard output files (the DST and a graphics file containing summary plots of the information, similar to Figure 8.1) are closed ten minutes after the time of the alarm, in order to accept any possible "late" signal events.

8.1.3 The PHRASE Monitor Online Alarm System

The PHRASE monitor online alarm system consists of a cellular phone with a modem link combined with a laptop computer. This system is operational in Italy only. The PHRASE monitor VAXstation places a call to the cellular phone if a low probability alarm condition is met, corresponding to a burst in any time window. There is always an "on-call" physicist on duty in Italy, who is responsible for carrying the phone and computer with him and responding to any alarms. If an alarm is received, the physicist must log on (via the cellular link if necessary) to the Gran Sasso computer and check the data files. The program continues to try to call every two minutes until there is a response.

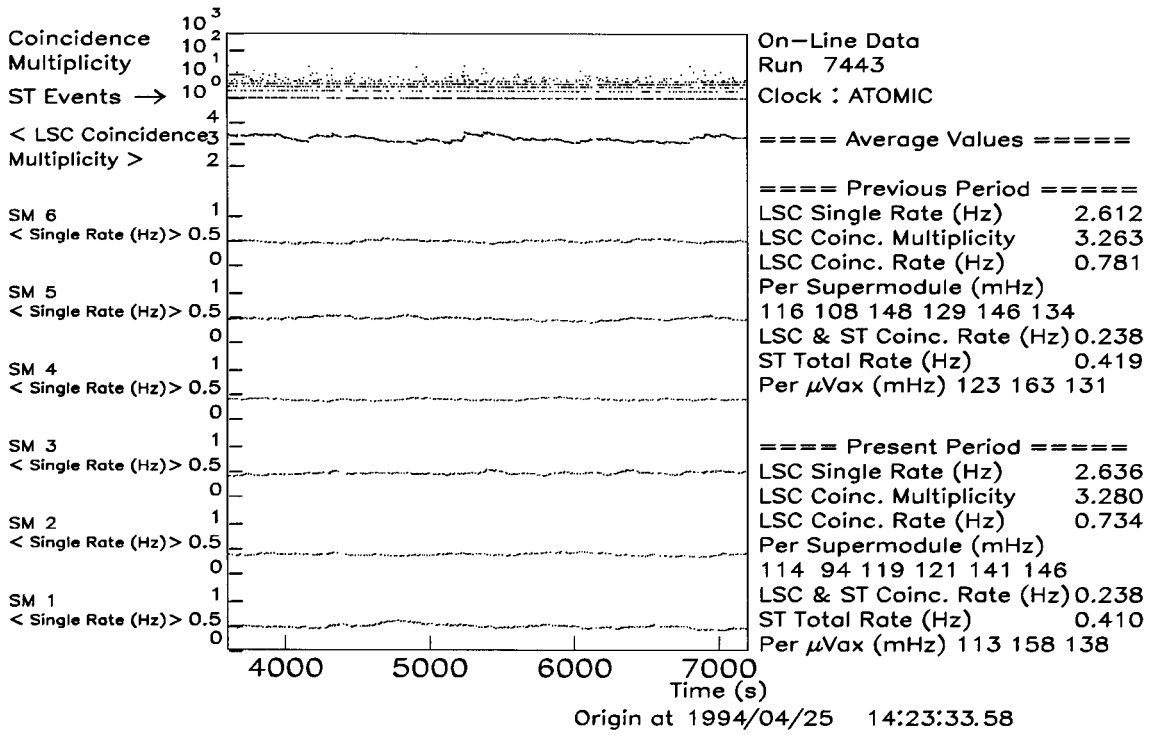

Figure 8.2: LSCM online display. Rates of unvetoed hits for each supermodule as a function of time, as well as multiplicities of coincidences and average multiplicities in the top plot. Information is summarized on the right (see caption of Figure 8.1 for definitions) for both the period shown and for the equal time period immediately previous.
(F. Cei).

8.1.4 PHRASE Monitor Performance

Event Collection Efficiency

Since a spy process is not allowed to affect the dead time of the main acquisition, it necessarily runs at lower priority and may lose some events if the rate of new events is high. Under normal rate circumstances, the low priority PHRASE monitor spy process loses very few events (a few percent). At high rates, such as would be expected for a gravitational collapse ($\sim$ 50 Hz for a center of galaxy event), the spy process still has 90% efficiency for collecting events. Therefore, even for a high-rate case the monitor would still register a burst far above background. Note that the PHRASE main acquisition still writes events to disk with better than 99% efficiency even for 50 Hz data rates.

Alarms Received

The performance of the PHRASE monitor will be briefly described for a one year period, from February 1 1995 to February 1 1995. This period is examined closely in reference [95]. 65 alarms were found online by the SNM program during this period. The PHRASE alarms are classified by the experts as follows:

- *"Good":* These are interpreted as true Poissonian fluctuations of background counts.
- *"Firing counters":* These are bursts caused by high rate counters (due to noise of various kinds).
- *"Synchronization losses":* These are cases where a problem occurred with the global PHRASE synchronization pulse (Section 5.3.1), so that PHRASE event times cannot be correctly reconstructed and therefore muons cannot be rejected.
- *"Calibration pulses":* These are bursts caused by LEDs or laser pulses firing during the run.

- *"Low initial rate":* These alarms are due to a miscalculation of the background rate for the case when a run starts with a different number of active supermodules than the previous run had (during the first two hours of the run, the rate from the previous run is used.) This problem has recently been fixed in software by counting the number of supermodules present in the PHRASE.

The period mentioned above had 24 "good" alarms, 23 total of "firing counters","synchronization loss" and "calibration" alarms, and 18 "low initial rate" alarms.)

8.2 The ERP Monitor

8.2.1 Requirements for an ERP Online Monitor

As described in detail in Section C.2, each supermodule's Readout Supervisor produces a full GC buffer which is read out every several minutes. Since a rather large block of ERP GC information is read out at relatively infrequent intervals, an online monitor program which scans the data for bursts must necessarily have very good efficiency. A single GC buffer lost from the data stream can represent a large amount of information; therefore the goal of an online monitor is to have an efficiency for collecting buffers of as close to 100% as possible.

8.2.2 General Scheme

A full analysis of a GC buffer including a search for bursts within it can be relatively time-consuming. If a "spy process" is used to collect GC buffers from the acquisition, the long analysis time may cause problems for buffer collection efficiency, since events coming in can be missed if the analysis program is busy doing something other than collecting events.

The general scheme for solving the long analysis time problem is to have two sets of programs. The first is a set of programs, called the RCDGC programs. These make use of special spy process software, the RCD library routines, written by F. Ronga and A. Marini [97]. These RCDGC programs capture events containing ERP GC

triggers from the acquisition and then send the GC buffers via a VMS mailbox virtual device [98] to a detached analysis process called GC_ANALYSIS. GC_ANALYSIS reconstructs the buffer events, searches them for bursts and then sends an alarm to interested parties if a large burst is found. The advantage of this software configuration is that the RCDGC buffer collection programs are dedicated to the task of collecting buffers and sending them along to the analysis process. Writing the buffers to the mailbox is very fast (tens of ms per buffer). Since the mailbox contains a queue of several buffers, the analysis program can be relatively slow, as long as the average time taken for analysis is less than the average time between GC buffer readouts. See Figure 8.3 for a diagram of the general scheme of the software.

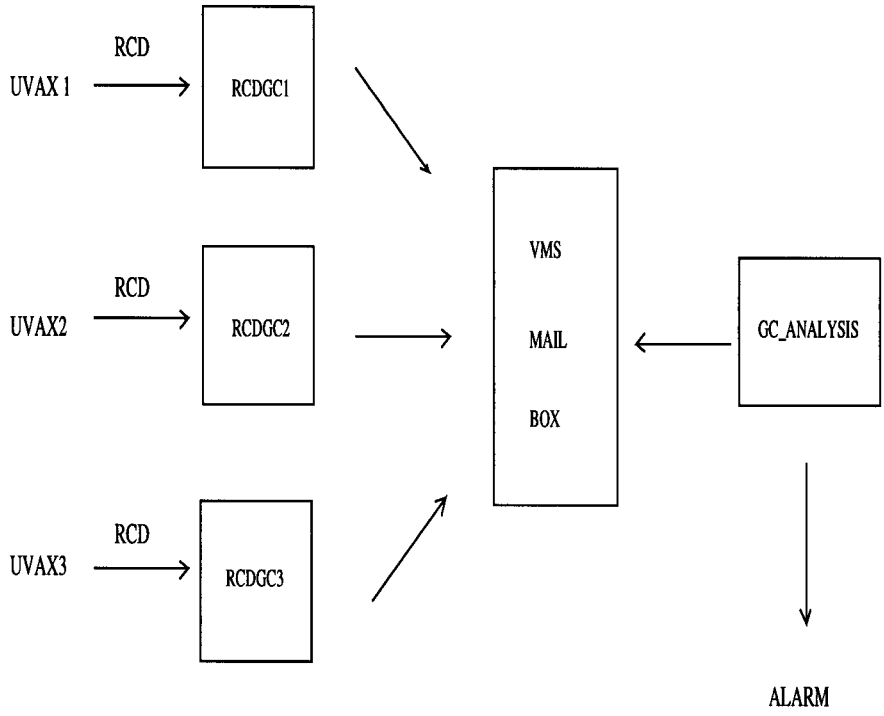

Figure 8.3: General scheme of the ERP GC monitor software.

There is one RCDGC process per main acquisition microvax, which reads events directly from the microvax, for a total of three independent RCDGC processes. These three processes all write to the same VMS mailbox, and the single detached analysis process reads from the mailbox.

When it starts up, a master program called SENTINEL initially launches the individual microvax RCDGC processes and the detached process. Subsequently, it

watches over the processes continuously. It checks them every few minutes and relaunches any processes that have disappeared (due to microvax reboot, rare program crashes, etc.)

The ERP monitor programs run on MACRO's auxiliary acquisition computer VXMACB. They run continuously, and the master program SENTINEL gets started up whenever VXMACB does.

Technical details about the ERP GC monitor software are available in references [99, 100, 101].

8.2.3 The ERP GC Monitor Data Analysis Process

The ERP GC monitor data analysis procedure is quite similar to the standard offline data analysis procedure already described in Chapter 7.

Event Reconstruction and Initial Cuts

Essentially the same reconstruction is done in the monitor as is done for the offline analysis, and the same initial data quality cuts are applied as described in Section 7.1.3. Standard calibration constants are used for reconstruction (with no readjustment performed for the online software at this time, although this may change).

The Six Supermodule Burst Search

The ERP GC buffers fill up and read out every 5–10 minutes. Since the six supermodules' supervisors operate independently and provide ERP GC buffers at different times, it is necessary to synchronize and time-sort the hits before performing a burst search on the full active mass. This is a reasonably easy problem to solve offline, because all of the data from all supermodules for all times is available on disk for sorting. However the task of combining and time-sorting the ERP GC buffers is a much more difficult one to perform online due to the chunk-like nature of the ERP GC readout: at any given time not all of the GC buffers may have read out. In addition, some supermodules or microvaxes may not be present and the program has

no way of knowing this in advance. Also, an online full-detector search GC monitor program must know how to deal with missing GC buffers.

UT time Fit

The first step toward doing a full-detector burst search is to synchronize (in software) the six supermodules' ERP clocks and convert the ERP clock times to UT times. This is done in essentially the same manner as for the offline analysis as described in Section 7.1.4. However instead of doing frequent fits during the run, only a small set of ERP muons (10 per supermodule) are used to calibrate the ERP clock for each run. Over a ~5 minute period at the beginning of each run, the RCD buffer collection processes collect a sample of ERP muon hits for which both ERP clock times and UT times are available. For each supermodule, a double precision least squares fit is done to

$$UT = A_i * ERP + B_i, \tag{8.1}$$

where UT and ERP are the UT and ERP clock times respectively for the muons collected for the ith supermodule, and A_i and B_i are the fit parameters. A_i and B_i are saved and used subsequently to convert GC buffer ERP clock times to UT times.

The fit gives reconstructed UT times good to within one or two milliseconds after five or six hours (a typical run length), as shown in Figure 8.4. This accuracy is fully adequate for the purpose of a full-detector burst search, as will be shown later in this section.

The ERP clock calibration drift results both from errors in the clock calibration fit and intrinsic ERP clock drift (possibly due to temperature variations). Note that a double precision fit is used; otherwise the drift becomes dominated by errors in the fit and becomes unacceptably large over the course of a run: a time drift over 5 or 6 hours larger than the time coincidence cut window of 4 ms (see Section 8.2.3) becomes unacceptable.

If fewer than 10 ERP muons have been collected for a supermodule by the time the first GC buffer for that supermodule reads out, then the UT time fit is forced and done using the available muon data. After at least 10 muons have finally read out,

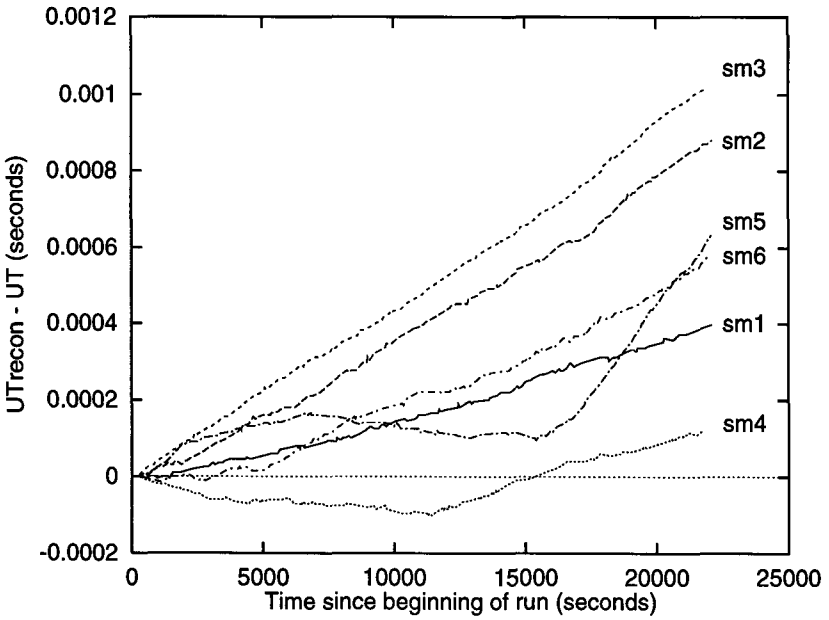

Figure 8.4: Typical ERP clock drift over a run for the case when the ERP clocks are calibrated with muons at the beginning of the run, for all six supermodules. This plot was made using ERP muons from run 11578. The x-axis represents actual time during the run. The y-axis gives the difference in seconds between reconstructed UT time using the ERP clock calibration and the actual UT time of the muon. The maximum drift over the course of the run is approximately a millisecond.

the fit is then redone. After the required number of ERP muons have been collected, the RCD processes look only for GC buffers and ignore muons.

Note that the RCD buffer collection efficiency decreases if the RCD processes must wait for ERP muons continuously. This is the reason for the collection of only a small sample of muons at the beginning of each run. In principle, the fit precision could be increased and the clock calibration drift decreased by collecting additional small samples of muons throughout the course of a run (perhaps every couple of hours); however, this is not strictly necessary because a single fit at the beginning of a run has been shown to be adequate.[3]

Combining and Time-Sorting Hits

[3]If run lengths ever increase significantly, the collection of mid-run muons will be implemented.

After the GC buffers hits have had their positions and energies reconstructed and have had UT times stamped on them, the separate supermodule buffers must be combined and the hits sorted in order of UT time. This is accomplished at the end of the decoding and reconstruction step for all the hits in each buffer.

For each supermodule, information for three GC buffers' worth of hits ($818 * 3 = 2454$ hits) is kept in memory, in an array for each supermodule. Reconstructed energy, position, time and error code information is stored for each hit.

All hits, whether cut or not, are included in these arrays. An additional "full-detector" array containing pointers (array indices in FORTRAN) to these hits is maintained. As each GC buffer is processed, the array indices pointing to each hit are stored in the full-detector array such that the successive hits in the full-detector array point to separate supermodule array data *in UT time order.*

After the time-ordered indices for a GC buffer have been stored in the full-detector array, the final cuts are performed (see Section 8.2.3.) An additional array, the "non-cut" array, is filled: this contains pointers to pointers to good hits, i.e. indices of the full-detector array elements which point to the non-cut hits in the individual-supermodule arrays (in UT time order). Figure 8.5 shows a diagram illustrating this structure.

The buffers are filled in a circular fashion and old events are deleted as new events get added.

Final Cuts

After the full-detector buffer of pointers to hits in UT time order has been filled, the final set of cuts is performed.

1. **Time coincidence cut:** At this point the final time coincidence cut is applied: any hit with a UT time which is within 4 ms of its nearest time neighbor (whether the neighbor passes cuts or not) in the full-detector array gets labeled as cut and so its array index does not end up in the noncut array. This cut is designed primarily to eliminate muons from the data sample, as well as to eliminate calibration events and shower hits (see Section 7.1.5.) The time

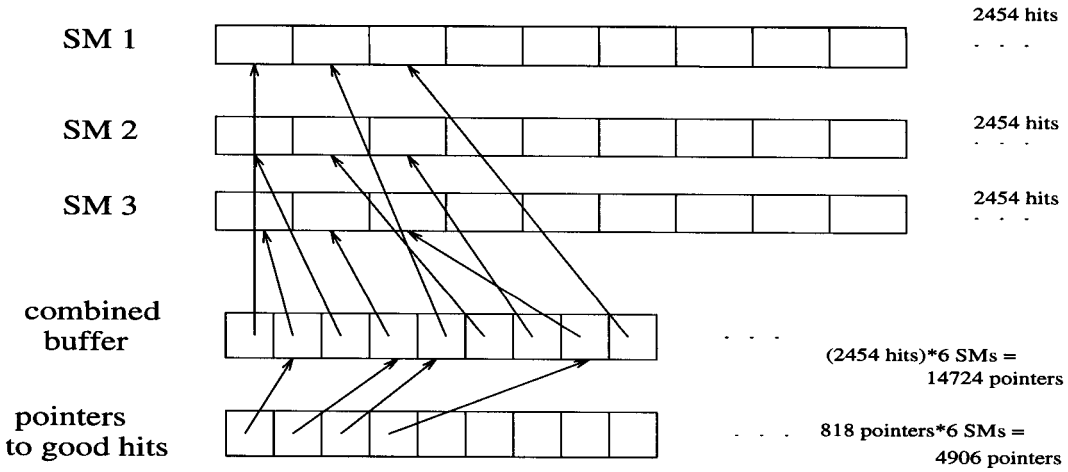

Figure 8.5: Buffer structure for combining, time-sorting and performing cuts on the ERP GC buffers, simplified to show only three supermodules. Each counter represents a hit or a pointer to a hit. The first "all hit" buffers contain all hits for a supermodule (cut and non-cut). The "full-detector" array contains indices of all of the hits in the all-hit buffers in UT time order. The "noncut" array contains the indices of the full-detector buffer elements which point to hits which pass all cuts. The full-detector burst search is performed by stepping through all of the elements of the final array.

coincidence cut is done on the full-detector buffer in order to eliminate inter-supermodule muons which might hit only one counter per supermodule. The 4 ms coincidence time window was chosen to allow for typical ERP clock calibration drift over the course of a run (see Section 8.2.3), without eliminating signal bursts except for extremely close supernovae. Expected signal rates in the first, most intense, two seconds of a GC burst reach ~250 Hz at a collapse distance of about 4 kpc; however, calculations show that over a 20 second interval the number of signal events surviving a 5 ms coincidence cut only dips below multiplicity threshold at a distance closer than about 0.2 kpc.

2. **Energy cut:** A software energy cut of 10 MeV is applied (during very early monitor running it was 7 MeV). This energy threshold is approximately the threshold that optimizes the signal to background ratio for standard gravita-

tional collapse models.

The Bari Fake Box

In July 1995 the "Bari box" was added to the ERP for the purpose of improving muon rejection for the GC monitor, especially inter-supermodule muon rejection. The output of the Bari trigger (Section 4.5.2) for each microvax was plugged into one of the ERP "fake box" inputs, previously used for ERP calibration purposes (as described in Section 5.2). With the Bari box in the data stream, all events in coincidence with any Bari streamer tube trigger get cut automatically by the counter coincidence cut. The following example illustrates why the use of the Bari fake box is an improvement over the simple counter coincidence cut for cutting inter-supermodule muons, for the full-detector burst search case when the search is done before all supermodules have read out and been added to the full-detector buffer, e.g.:

> Consider an inter-supermodule muon making one hit in supermodule 3 and one hit in supermodule 4. If the supermodule 4 buffer reads out before the supermodule 3 buffer, then the full-detector search will not reject the supermodule 4 hit when it is doing the search on supermodule 4, if there is no Bari box.

Also, some fraction of truly single-box muons can be rejected from the burst search data stream using the Bari box time coincidence, for the cases where there are enough streamer tube planes hit to form a Bari trigger.

Searching for Bursts

Once the events from a buffer have been stored in memory and time-sorted, burst searches are performed on all events pointed to by the indices in the noncut array. First, a single supermodule burst search is performed on the hits in the GC buffer that just read out, and subsequently a full-detector burst search is performed on all hits present in the full-detector arrays (spanning the whole time period available in memory.)

1. **Single Supermodule Burst Search** The burst search algorithm is basically the same as the one described in 6.3: all hits passing cuts are stepped through,

and the number of subsequent good hits within the given time window are counted up to give the multiplicity n of the trial burst. If n exceeds the pre-calculated multiplicity threshold corresponding to a given Poisson probability $\mathcal{P}_{th}$, a preliminary alarm condition is set; what is done with the burst candidate is described later in this section. The multiplicity thresholds corresponding to each time window and supermodule are calculated prior to the single supermodule burst search (after each buffer readout) based on current rate information. The Poisson probability threshold $\mathcal{P}_{th}$ is read from a file; $\mathcal{P}_{th}$ has been set to 10^{-5} over most of the history of the monitor.

The burst search is done for six different time windows (1, 2, 6, 8, 10 and 20 seconds) at an energy threshold of 10 MeV. For each supermodule and each time window, histograms of the multiplicities are accumulated and written out at the end of the run.

2. **Full-Detector Burst Search**

The burst search is performed on all hits present in the full-detector arrays after every individual supermodule ERP GC buffer readout. Note that this means that for a given time period being searched, not all supermodules may be present in the arrays (even though they are live and producing data). For each hit being considered, the number of supermodules present in the full-detector buffer is determined. This is done by keeping track of the times of the first and last hits present for each supermodule in the full-detector buffer: for each hit it is determined whether the time of that hit falls within each supermodule's time window.

This method of "burst searching everything currently in memory" also means that the same intervals of time are searched repeatedly, with differing combinations of supermodules present each time. One consequence of this procedure is that a real gravitational collapse burst in the data may get picked up more than once, as subsequent supermodules read out and get added to the full-detector data stream. To compensate, alarm messages are sent out only for bursts which

are "better" than any previous ones for the same time period: see the notes on "burst consolidation" later in this section.

The burst search algorithm is similar to the one for the single-supermodule search, although the multiplicity threshold used depends on the particular combination of supermodules present, as described in the following section.

The north and south face data are ignored by the ERP monitor. The endcaps represent less than 3% of MACRO's active mass, and the buffer readout is too infrequent to be of much use for the full-detector burst search: by the time the N/S faces have read out, the other supermodules' events for most of the time period represented in a endcap buffer will have already cleared the full-detector burst search buffers in the program's memory. In addition, the endcap active mass is too small for an "single supermodule" search of only north or south face data to be very significant.

Multiplicity Thresholds

Multiplicity thresholds are calculated regularly at run time based on the current rate of good (uncut) hits. After each GC buffer is read in, the current rate for each supermodule is calculated (using the number of good hits in that supermodule since the beginning of the run and the time since the beginning of the run; if the time since the beginning of the run is less than two hours, the last run's rate for that supermodule is used.) This rate is then used to determine a burst multiplicity threshold for each time window based on a constant Poisson probability threshold, as described in 6.3 and above.

The appropriate supermodule's rate is used for the individual supermodule burst search. For the full-detector burst search, the rate and corresponding multiplicity threshold is determined in advance for each possible combination of supermodules, and then as the burst search proceeds through the full-detector buffer the multiplicity threshold used is the one corresponding to the appropriate supermodule combination and time window.

Dealing with an Alarm Condition

Final Software Filtering

If a burst of hits with multiplicity exceeding threshold is found, for either the single or full-detector burst search, an alarm procedure is started. But before sending out any alert messages, there are some additional checks on the data.

Spark Checks

First, the burst is put through some "spark catching" code, which makes sure that an alarm burst is not dominated by a particular counter which may have an anomalously high rate. The burst is considered to be "sparks" if more than one half of the hits in the burst come from a single counter (although as is often the case the physical cause of the high-rate counter is not sparking at all).

A summary file is written to disk if a burst is identified as "sparking", containing the same information as for a legitimate burst (see Appendix G). However, for a "sparking" burst, no email is sent out.

"Burst Consolidation"

Next, for bursts found with the full-detector burst search, a burst consolidation check is performed. The program keeps track of the times and properties of bursts for which alarms have recently been sent out. As noted previously, since in the full-detector burst search the same time interval is searched repeatedly, a given real burst could generate several alarms in succession.

If an alarm has already been sent out for a burst at a given time, the program will only send out another alarm for a burst within 30 seconds of the first if the subsequent burst satisfies the following conditions:

- It is present in a greater number of supermodules AND having a lower Poisson probability, OR
- It has a much lower Poisson probability ($<.01$ of the previous minimum Poisson probability for the time period.)

In other words, a less significant or fewer-supermodule burst than the previous burst will not have an alarm message sent out for it.

If the burst passes these tests, the alarm procedure proper gets launched: files get written, email gets sent, and a message goes out to the GC alarm beeper. The alarm procedure in the following section.

Alarm Output

When an alarm condition passes all filters, a text file giving detailed information about the burst and the events contained in it is written to disk, set up for easy viewing. An example is shown in Appendix G. For single-supermodule bursts, a PAW [102] ntuple is written which contains information for all hits in the GC buffer which contains the burst (or the most recent GC buffer for the case when a burst straddles buffers), including those which were below energy threshold or cut for some reason. For full-detector bursts, the ntuples contain all hits (cut and non-cut) in the time interval between the first and last hits of the burst. Appendix G gives a summary of the information contained in the ntuple.

The Online Alarm System

Alarm Email

When a GC alarm burst is found, messages are sent out to the people on the prompt alarm mailing list. The message consists of a summary string giving important properties of the burst. Appendix G gives the contents of the string.

The information encoded in the burst summary string is intended to give some idea of the urgency of the alarm, e.g. a burst of just one hit over multiplicity threshold in one supermodule only might not be worth investigating immediately.

The same message string is sent to pagers in the US. The beeper address is the first address on the prompt alarm mailing list.

A limit is imposed on the number of mail messages that can be sent out: no more than four messages per supermodule per run will be sent, to avoid a flood of mail due to some detector or software problem (although experience has not shown this to be a problem.)

The Pager System

At present the ERP online GC alarm system consists of two pagers in the United

States. One pager in California, leased from the SkyTel company, has been operational since December 1994. The pager (a standard model made by Motorola) can receive up to 16 electronic mail messages of 240 characters each. The email sent to the pager must go via a commercial electronic mail provider. ATTmail was shown to be the most reliable provider. The range over which the SkyTel pager can receive messages includes most cities in the United States. There are no SkyTel transmitting stations in Italy at this time. A second pager in Michigan, also capable of receiving email messages, has been operational since April 1996.

The person carrying a pager is responsible for responding immediately to any alarm, which entails logging on to VXMACB and checking the alarm text files and/or the ntuples, and communicating with others if the burst looks sufficiently interesting. Reference [101], gives some additional technical information about the beeper system.

When a burst of events is found, the monitor software sends email via two network routes for redundancy:

- Route 1: Mail sent directly from VXMACB via SMTP mail protocol.
- Route 2: Mail sent out of the tunnel from VXMACB to VAXGS via DECNET first, then sent out from VAXGS.

Since the email is sent twice, any alarm causes two separate pages.

8.2.4 ERP GC Monitor Performance

The various parts of monitor operation have been tested in various ways. There are two important components to overall ERP GC alarm efficiency: the efficiency with which the monitor software picks up buffers from the acquisition (the RCD efficiency), and the efficiency with which an alarm will actually reach the beeper (and the collaborators) if a burst over multiplicity threshold is found.

RCD Efficiency Tests

The RCD buffer collection efficiency is defined as the ratio of the number of GC buffers processed by the monitor to the number of GC buffers present on disk (excluding the north and south face buffers). This is monitored regularly. While the efficiency was very good (>95%) during the early period (with occasional low values), it declined in the fall of 1995: see Figure 8.6. This decline was eventually understood to be related to the addition of the waveform digitizers to the acquisition, which caused a greater load on the entire system, as well as increased batch queue use on VXMACB for data quality monitoring purposes, which began at around that time.

In any case, the poor RCD inefficiency problem was cured by having the ERP monitor queue priority increased so that both the RCDGC processes and the detached analysis process have priority over the standard jobs running in the batch queue. Figure 8.6 shows typical efficiencies before and after the queue priority change.

Beeper/Internet efficiency tests

The second important efficiency consideration is the efficiency with which an alert is received after the monitor software has decided to send one. This alarm efficiency depends on network connections as well as the efficiency of the SkyTel system.

To test these efficiencies, during early 1995 the monitor ran with lowered multiplicity thresholds in order to obtain a large sample of alarms. During these test runs, multiplicity thresholds were set such that 3–5 alarms from accidental coincidences of background events were generated per week. For a total of 18 "fake" alarms occurring during the month of January 1995, Figure 8.7 shows a histogram of the time delay between the time of the first event in the burst and the time that the alarm message arrived at the pager. The average response time delay was 8 minutes, and the maximum time delay was 20 minutes. The overall response time delay for this test was in fact dominated by the ERP GC buffer readout time (5-10 minutes).

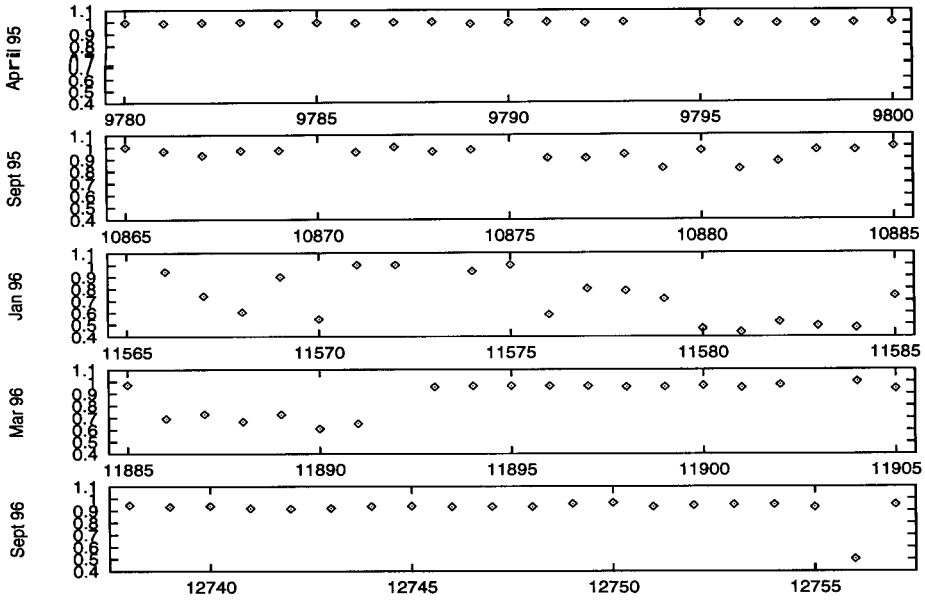

Figure 8.6: RCD efficiency as a function of run number, for several different time periods. (Note: zero efficiency for a given run usually means it was a short run with no buffers read out for that run.) Early in 1995 (top plot), the efficiency was very good (>95%). In late 1995 through early 1996, the efficiency declined; the fourth plot shows the increase in efficiency at run 11893 when the queue priority was increased. The fit plot shows some recent running.

History

Testing of the ERP monitor software started in 1993, and early versions had only the single supermodule search. The full-detector six supermodule burst search version of the ERP monitor has been running since early 1995, and has been stable at maximum efficiency since March 1996. Table 8.1 shows a summary of ERP GC monitor history.

Figure 8.8 shows the active mass seen by the ERP monitor as a function of time, starting January 1, 1995 (shortly after the monitor first turned on with the full-detector six supermodule search). Figure 8.9 focuses on the "fully efficient" period starting on March 9 1996, up to July 27 1996. As for Figure 7.27, the active mass for a given day is the average for all runs on that day, weighted by relative livetime, with the normalization given by total livetime (not real time).

Figure 8.10 shows the percent of time that the ERP monitor was processing data

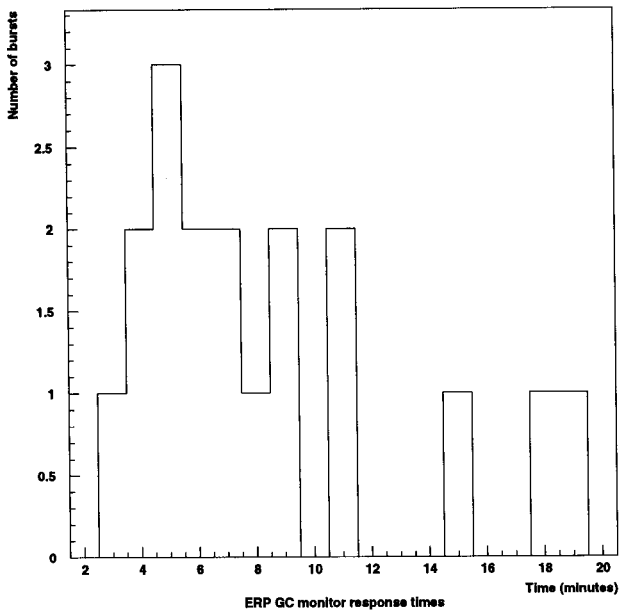

Figure 8.7: Histogram showing time differences between the first event time in a candidate burst and the time that an alarm message appeared on the SkyTel pager, for 18 different "fake" alarms.

from at least one supermodule, starting March 9, 1996.

Alarms Received

A total of 106 alarms have been received since the ERP monitor starting running in January 1995; of these, 17 have been during the stable period from March 1996 through July 1996.

At present, none of the PHRASE alarms have matched the ERP alarms during the time periods that both were active. This is not unexpected. The ERP "good" background sample differs from the PHRASE background: the typical background rate for six supermodules at 10 MeV is about 60 mHz (after cuts), as opposed to about 40 mHz for the PHRASE. As discussed at length in Section 7.3, the extra rate in the ERP is primarily due to extra accidental coincidences of near tankend events. Multiplicity thresholds will be therefore set differently for the two triggers.

Dates	Notes
1992-1993	Early testing
May-June 1993	Version 1.0 running, single SM search and email alarm only
1993	Attico counters added to ERP
1993-94	Full-Detector burst search software development
1994	First tests of beeper
December 1994	Version 2.0, full-detector burst search, beeper alarm system online
January 1995	Alarm tests with lowered thresholds
May 1995	macro-erpgc mailing list started
July 1995	Bari box added
Fall 1995	Decrease in RDC efficiency due to VXMACB batch activity
March 1996	Queue priority increase solves efficiency problem
April 1996	RCD hangup problem solved
up to present	Continued running, continual minor upgrades

Table 8.1: ERP GC monitor running history.

For example, consider a search in an 8 second time window. For an ERP background rate of 60 mHz and a PHRASE background rate of 40 mHz, the multiplicity thresholds for a preliminary candidate are 7 and 6 hits respectively. According to Table 7.4, any given PHRASE hit with $E_p > 10$ MeV has a ~348/728=47% probability of being observed as an ERP hit with E_e >10 MeV; in addition there is an ERP buffer collection inefficiency factor of ~0.95. Given a burst of 6 hits at multiplicity threshold in the PHRASE, the probability that all 6 hits will be considered in the ERP monitor burst search is $(0.46 * 0.95)^6 = 0.007$. At least one additional ERP hit with $E_e >$ 10 MeV in the time interval is still needed to exceed ERP multiplicity threshold. The rate of ERPs with no PHRASEs (with $E_p > 10$ MeV) at $E_e > 10$ MeV is ~(655+595)/1598*0.60, so the probability of one lone ERP hit or more in 8 seconds is only $1 - e^{-(.047)*8} = 0.3$. Therefore the probability of an alarm in ERP being correlated with a given PHRASE alarm is $\sim 10^{-3}$. Note, however, that the fact that

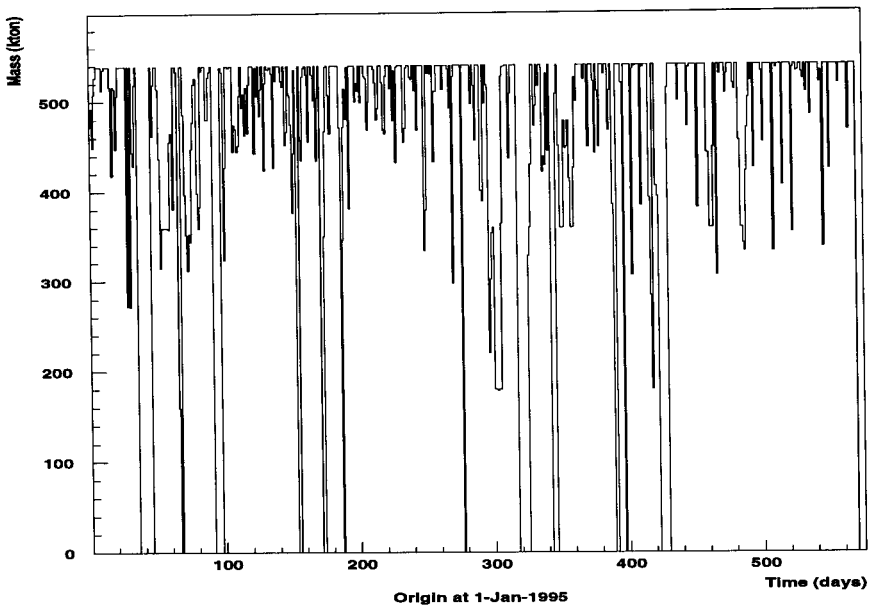

Figure 8.8: Active mass seen by the ERP monitor, for the whole time period starting January 1, 1995. For each day, the active mass is an average over runs, weighted by relative livetime.

background fluctuations are unlikely to be correlated does *not* mean that signal bursts will not be correlated.

In addition, the ERP monitor is not subject to exactly the same types of non-Poissonian background alarms as the PHRASE is. For instance, there is no global ERP clock (synchronization between the supermodules being done in software using muons) so the "synchronization loss" classification does not apply to the ERP. In addition, the ERP employs an automatic veto which rejects alarms for which more than one half of the hits in the burst occurred in the same scintillator counter (the "spark check"); this cut suppresses many of the "firing counters" type alarms (although for these bursts ERP information is still written to disk). Calibration alarms from LED or laser light in the counters are also strongly suppressed for the ERP monitor due to signals from the calibration fake counters which fire spare channels in the ERP, so that calibration events are automatically removed from the data sample by the counter coincidence cut. And finally, the "low initial rate" type alarms seen in the ERP are rare, because the background rate is always calculated on a per-supermodule

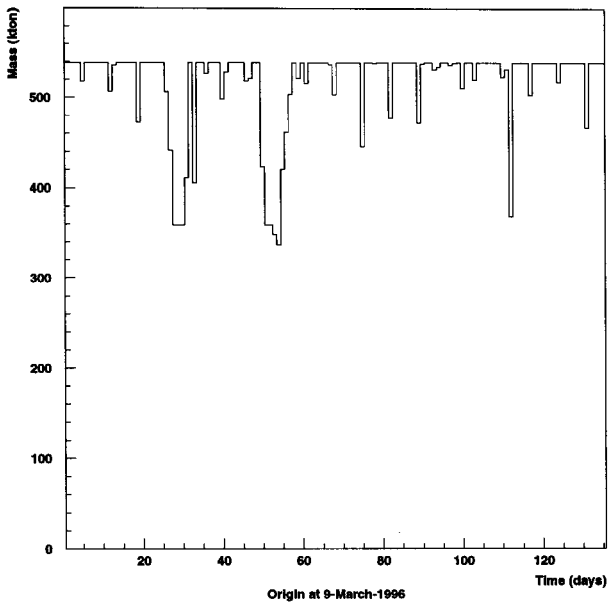

Figure 8.9: Active mass seen by the ERP monitor, for the efficient time period starting March 9 1996.

basis (although in principle such a problem with the background calculation could occur if the rate of a particular supermodule increases suddenly.)

The ERP alarms have been classified as either "good background fluctuations" or "non-uniform", i.e. bursts for which the position distribution across the detector was clearly non-uniform (due to firing counters, high voltage fluctuations, etc.) 61 were classified as non-uniform and 45 as good fluctuations.

The energy distribution of the events in the candidate bursts in shown in Figure 8.11; clearly, unvetoed muons remain in the data sample.

8.3 Alarm Procedure

Several detectors with excellent capabilities for recording GC neutrino events such as SuperKamiokande and SNO, have recently turned on or will be turning on in the near future. Many people have proposed that the different neutrino observatories communicate information about neutrino burst candidate detection (e.g. [22, 103]). In particular, employing a coincidence between detectors could increase sensitivity for

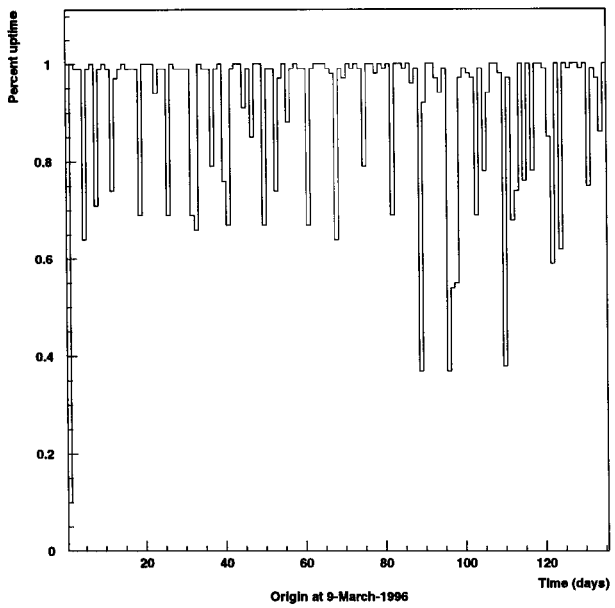

Figure 8.10: Percent of the time the ERP monitor was active, for the efficient time period.

small signals. In addition, for a high statistics burst it may be possible to determine the direction of the source using information from more than one detector, which would be enormously useful for alerting astronomers.

MACRO's participation would valuable to such a neutrino telescope network. The exact burst criteria required in order to alert such a network (astronomers and other neutrino telescopes) are currently under consideration by the MACRO collaboration. The aim is to have in hand a set of *quantitative* criteria, published in advance, which define an unambiguous neutrino signal. Some distance sensitivity may be sacrificed in order to be conservative about an alarm. The following types of criteria are under consideration (exact details are currently being be worked out):

- The Poisson probability of the multiplicity in the given time window must be very low for a conservative candidate. A false alarm would be generated with probability less than 0.001% every ten years for the given burst search, i.e. $n \geq N_{10yr}$ will be required.

- There must be no anomalous conditions on the detector which may cause non-

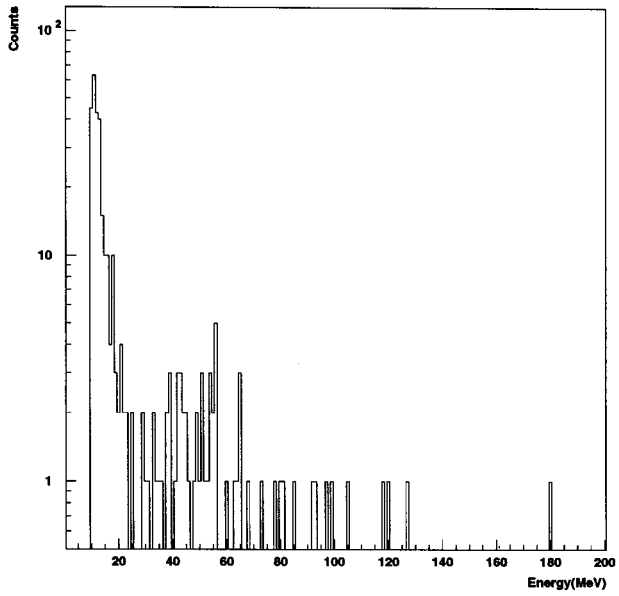

Figure 8.11: Energy distribution of events present in "good" ERP monitor burst candidates.

Poisson background (e.g. no LED or laser calibrations in progress, no power fluctuations recorded). A checklist of specific conditions is being developed.

- The position distribution of hits across the apparatus must be uniform. This is a powerful criterion for rejecting non-Poisson background, which in almost all cases causes hits localized in space (e.g. tankend sparking, LED's, high voltage fluctuations, etc.)

- Energy and time distributions may possibly be required to be consistent with the expected gravitational collapse signal. However this condition will not be stringent in order not to reject signals from non-standard collapse physics.

The exact conditions under which and AND or an OR of ERP and PHRASE alarms would be required are under examination. The estimated total response time required is 1–2 hours.

Chapter 9 Conclusions

The MACRO detector, although built to detect monopoles and other supermassive, highly ionizing particles, also has good capabilities for stellar collapse neutrino detection. From a GC at 10 kpc, approximately 180 neutrino events with energies >7 MeV are expected in MACRO's 560 tons of liquid scintillator on a time scale of tens of seconds. The full active mass of MACRO is sensitive to a burst of neutrinos from a gravitational collapse beyond the opposite edge of our galaxy.

A burst search using information from both of MACRO's GC trigger systems has been performed, over the time period starting on July 24, 1995 and ending February 8, 1996. This search is more sensitive than previous MACRO searches using either trigger system alone. The total livetime for GC detection was 0.51 yr for this period. No neutrino burst candidates were observed over this time, and the time structure of event multiplicity distributions was consistent with Poissonian predictions. Therefore there were no gravitational collapse events within 20 kpc during the live period of this search. This result corresponds to a limit on the rate of gravitational collapse in our galaxy of <4.5 per year at 90% C.L.. Combined trigger data analysis work is ongoing.

MACRO is also capable of providing an early warning of a GC event to optical astronomers. Two redundant supernova alarm systems, one in Italy and one in the United States, are set up to react to the observation of a candidate burst within a few hours of its occurrence. In the near future, MACRO expects to join a world-wide network of neutrino observatories (including SuperKamiokande, SNO, AMANDA and others): a detection of a neutrino burst by several independent experiments could provide confirmation of a weak signal or perhaps yield directional information which would enormously increase the value of an early warning to optical astronomers.

Bibliography

[1] R. M. Bionta *et al.*, Phys. Rev. Lett. **58**, 1494 (1987).

[2] T. Haines *et al.*, Nucl. Instr. Meth. A **264**, 28 (1988).

[3] K. S. Hirata *et al.*, Phys. Rev. D **38**, 448 (1988).

[4] E. N. Alekseev *et al.*, JETP Lett. **45**, 589 (1987).

[5] M. Aglietta *et al.*, Europhys. Lett. **3**, 1315 (1988).

[6] R. P. Harkness and J. C. Wheeler, in *Supernovae*, edited by A. G. Petschak (Springer-Verlag, New York, 1990).

[7] S. E. Woosley and T. A. Weaver, Ann. Rev. Astron. Astrophys. **24**, 205 (1986).

[8] R. Bowers and T. Deeming, *Astrophysics I: Stars* (Jones and Bartlett Publishers, Inc., Boston, 1984).

[9] W. Hillebrandt, in *Supernovae*, edited by A. G. Petschak (Elsevier, Les Houches, 1991).

[10] H. A. Bethe and J. R. Wilson, Astrophys. J. **295**, 14 (1985).

[11] A. Burrows *et al.*, Astrophys. J. **450**, 830 (1995).

[12] D. H. Clark and F. R. Stephenson, Mon. Not. R. Astr. Soc. **179**, 87 (1977).

[13] G. A. Tammann *et al.*, Astrophys. J. Suppl. **92**, 487 (1994).

[14] D. A. Leahy and X. Wu, Publ. Astron. Soc. Pac. **101**, 607 (1989).

[15] R. Narayan and J. P. Ostriker, Astrophys. J. **352**, 222 (1990).

[16] D. R. Lorimer *et al.*, Mon. Not. R. Astron. Soc. **263**, 403 (1993).

[17] S. Wakatsuki *et al.*, Astrophys. J. **392**, 628 (1992).

[18] W. D. Arnett *et al.*, Astrophys. J. **339**, L25 (1980).

[19] J. N. Bahcall and T. Piran, Astrophys. J. **267**, L77 (1983).

[20] K. U. Ratnatunga and S. van den Bergh, Astrophys. J. **343**, 713 (1989).

[21] D. Hartmann *et al.*, Astron. Astrophys. Suppl. Ser. **97**, 219 (1993).

[22] A. Burrows *et al.*, Phys. Rev. D **45**, 3361 (1992).

[23] J. R. Wilson, in *Numerical Astrophysics*, edited by J. Centrella, J. LeBlanc and R. Bowers (Jones and Bartlett, Boston, 1985), p. 422.

[24] S. Bruenn, Phys. Rev. Lett. **59**, 938 (1987).

[25] E. Myra and A. Burrows, Astrophys. J. **364**, 222 (1989).

[26] A. Burrows, Astrophys. J. **334**, 49 (1988).

[27] S. Ying *et al.*, Phys. Rev. D **40**, 3211 (1989).

[28] J. N. Bahcall, *Neutrino Astrophysics* (Cambridge University Press, Cambridge, 1990).

[29] M. Fukugita *et al.*, Phys. Lett. B **212**, 139 (1988).

[30] C. Bari *et al.*, Nucl. Instr. Meth. A **264**, 5 (1988).

[31] E. N Alekseev *et al.*, JETP **77**, 339 (1993).

[32] C. Athanassopoulos, *et al.*, Phys. Rev. Lett. **75**, 2650 (1995).

[33] M. Aglietta *et al.*, Nuov. Cim. C **9**, 185 (1986).

[34] C. Arpesella *et al.*, Borexino at Gran Sasso, Proposal for a Real Time Detector for Low Energy Solar Neutrinos (1994).

[35] F. Boehm *et al.*, Proposal for the San Onofre Neutrino Oscillation Experiment (1994).

[36] R. M. Bionta *et al.*, Phys. Rev. Lett. **51**, 27 (1983).

[37] Y. Suzuki, Nucl. Phys. B **35**, 273 (1994).

[38] G. T. Ewan, Nucl. Instr. Meth. A **314**, 373 (1992).

[39] P. Cennini *et al.*, Icarus II, A Second-Generation Proton Decay Experiment and Neutrino Observatory at the Gran Sasso Laboratory (1993).

[40] D. B. Cline, Ann. N. Y. Acad. Sci. **647**, 413 (1991).

[41] B. T. Cleveland *et al.*, Nucl. Phys. B Suppl. **38**, 47 (1995).

[42] P. Anselmann *et al.*, Phys. Lett. B **285**, 376 (1992).

[43] A. I. Abazov *et al.*, Phys. Rev. Lett. **67**, 3332 (1991).

[44] J. Engel *et al.*, Phys. Rev. Lett. **67**, 426 (1991).

[45] D. N. Schramm and J. W. Truran, Phys. Rep. **180**, 89 (1989).

[46] D. N. Spergel and J. N. Bahcall, Phys. Lett. B **200**, 366 (1988).

[47] A. Burrows, Astrophys. J. **334**, 891 (1988).

[48] Heidelberg-Moscow Collaboration, LANL preprint hep-ex 9502007 (unpublished).

[49] J. N. Bahcall and M. H. Pinsonnealt, Rev. Mod. Phys. **64**, 885 (1992).

[50] C. Weinheimer *et al.*, Phys. Lett. B **300**, 210 (1993).

[51] O. G. Ryazhskaya *et al.*, in *Proceedings of the 23rd ICRC* (University of Calgary, Calgary, 1993), Vol. 4, p. 380.

[52] B. Adeva *et al.*, Phys. Lett. B **275**, 209 (1992).

[53] C. E. Rolfs and W. S. Rodney, in *Cauldrons in the Cosmos* (The University of Chicago Press, Chicago, 1988), p. 90.

[54] O. G. Ryazhskaya *et al.*, Nucl. Phys. B Suppl. **35**, 454 (1994).

[55] I. Goldman *et al.*, Phys. Rev. Lett. **60**, 1789 (1988).

[56] C. S. Lim and W. J. Marciano, Phys. Rev. D **37**, 1368 (1988).

[57] W. D. Arnett *et al.*, Ann. Rev. Astron. Astrophys. **27**, 629 (1989).

[58] J. Kristian *et al.*, Nature **338**, 234 (1989).

[59] K. S. Hirata *et al.*, Phys. Rev. Lett. **58**, 1490 (1987).

[60] E. Bellotti, Nucl. Instr. Meth. **A264**, 1 (1988).

[61] S. D. Drell *et al.*, Phys. Rev. Lett. **40**, 644 (1983).

[62] S. Ahlen *et al.*, Phys. Lett. B **357**, 481 (1995).

[63] S. Ahlen *et al.*, Phys. Rev. D **46**, 895 (1992).

[64] S. Ahlen *et al.*, Phys. Rev. D **46**, 4836 (1992).

[65] S. Ahlen *et al.*, Astrophys. J. **412**, 301 (1993).

[66] S. Ahlen *et al.*, Phys. Lett. B **249**, 149 (1990).

[67] S. Ahlen *et al.*, Phys. Rev. Lett. **69**, 1860 (1992).

[68] C. Walter, Internal MACRO memo/PUB, Technical report, Caltech (unpublished).

[69] S. Ahlen *et al.*, Nucl. Instr. Meth. A **324**, 337 (1993).

[70] J. Hong *et al.*, Internal MACRO memo draft, Technical report, Boston University (unpublished).

[71] G. Battistoni *et al.*, Nucl. Instr. Meth. A **279**, 137 (1989).

[72] W. E. Earle, Internal MACRO memo 1030/91, Technical report, Boston University (unpublished).

[73] E. Kearns, Internal MACRO memo 1004/94, Technical report, Boston University (unpublished).

[74] G. Battistoni *et al.*, Internal MACRO memo 1001/88, Technical report (unpublished).

[75] J. Musser *et al.*, Internal MACRO memo 1006/93, Technical report, Indiana University (unpublished).

[76] K. Scholberg, Internal MACRO memo draft, Technical report, Caltech (unpublished).

[77] J. Musser, Internal MACRO memo draft, Technical report, University of Michigan (unpublished).

[78] J. Musser and A. Habig, Internal MACRO memo draft, Technical report, Indiana University (unpublished).

[79] F. Cei, Ph.D. thesis, Scuola Normale Superiore, 1996.

[80] A. Baldini *et al.*, Internal MACRO memo, Technical report, University of Pisa (unpublished).

[81] S. Ahlen *et al.*, Astropart. Phys. **1**, 11 (1992).

[82] A. Baldini *et al.*, Internal MACRO memo 16/90, Technical report, University of Pisa (unpublished).

[83] S. A. Bludman and P. J. Schinder, Astrophys. J. **326**, 265 (1988).

[84] R. Baker, Ph.D. thesis, University of Michigan, 1996.

[85] A. Baldini *et al.*, Internal MACRO memo 17/90, Technical report, University of Pisa (unpublished).

[86] A. Baldini *et al.*, Internal MACRO memo 20/91, Technical report, University of Pisa (unpublished).

[87] A. Baldini *et al.*, Internal MACRO memo 8/93, Technical report, University of Pisa (unpublished).

[88] A. Baldini *et al.*, Internal MACRO memo 3/95, Technical report, University of Pisa (unpublished).

[89] A. Baldini *et al.*, Internal MACRO memo 3/91, Technical report, University of Pisa (unpublished).

[90] C. Bower and R. Heinz, personal communication, 1995.

[91] F. Combs, Ann. Rev. Astron. Astrophys. **29**, 195 (1991).

[92] B. Nolty and C. Walter, in *Computing in High Energy Physics '94*, edited by S. C. Loken (Lawrence Berkeley Laboratory publication, San Francisco, 1994).

[93] A. Baldini *et al.*, Internal MACRO memo 22/91, Technical report, University of Pisa (unpublished).

[94] The MACRO collaboration *et al.*, in *Proceedings of the 23rd ICRC* (University of Calgary, Calgary, 1993), Vol. 4, p. 472.

[95] M. Ambrosio *et al.*, MACRO/pub memo 1996/3, Technical report (unpublished).

[96] R. S. Miller *et al.*, Astrophys. J. **428**, 629 (1993).

[97] A. Marini, Internal MACRO memo 30/92, Technical report, Frascati (unpublished).

[98] VMS System Services manuals, Technical report (unpublished).

[99] K. Scholberg and A. Habig, Internal MACRO memo 1008/93, Technical report, Caltech, Indiana University (unpublished).

[100] K. Scholberg and A. Habig, Internal MACRO memo draft, Technical report, Caltech, Indiana University (unpublished).

[101] K. Scholberg, Internal MACRO memo draft, Technical report, Caltech (unpublished).

[102] R. Brun *et al.*, Technical report (unpublished).

[103] D. Cline *et al.*, in *Proceedings of the Supernova Watch Workshop* (PUBLISHER, Santa Monica, 1990).

[104] K. Scholberg, Internal MACRO memo 1019/93, Technical report, Caltech (unpublished).

[105] K. Scholberg, Internal MACRO memo 1012/94, Technical report, Caltech (unpublished).

[106] Pisa group, Internal MACRO memo, Technical report, University of Pisa (unpublished).

[107] F. Bourgeois, Nucl. Instr. Meth. **219**, 153 (1984).

[108] J. Musser, Internal MACRO memo draft, Technical report, Indiana University (unpublished).

[109] K. Scholberg, Internal MACRO memo draft, Technical report, Caltech (unpublished).

Appendix A Tank Naming Convention

Individual MACRO scintillation counters[1] are named according to a standard format, $XAYY$. X is a digit indicating the supermodule number, A a letter indicating which scintillator plane contains the counter: B for bottom, C for center, T for top, E for east, W for west, N for north and S for south. YY is a two-digit number indicating the counter number within the plane and supermodule: horizontal planes have counters numbered 01 through 16 (17 for the top layer) from north to south, and vertical planes have counters numbered 01 through 14 from bottom to top (01 through 07 for the north and south planes which have the upper part of the plane open). So, for example, counter 4E09 is in the east plane of supermodule 4, in the upper part of the plane, 9 counters from the bottom. In addition, tankends are designated 0 or 1 according to which end is closer to the origin of the standard MACRO coordinate system. (The origin is located at the northwest corner of MACRO, the y-axis runs east-west and the x-axis runs north-south.) A standard number for calibration database purposes is also assigned to each counter, ranging from 1 to 584.

[1] In this thesis the terms "counters", "boxes" or "tanks" will be used interchangeably to refer to the scintillator counters.

Appendix B Photomultiplier Gain Setting

The gains of the phototubes have been set using various methods. The most consistent way involves flashing an LED (Section 4.4.2) in the counter at the single photoelectron level and recording the spe spectrum with a LeCroy qVt multichannel analyzer [104]. For EMI tubes, the spe spectrum has a clearly visible peak (Figure B.1), and the gain can be set such that the difference between the peak and pedestal channels on the qVt corresponds to a consistent charge value. The qVt procedure is more complicated for Hamamatsu tubes than for EMI tubes: in this case there is no visible peak in the qVt spectrum (Figure B.2), and the background (measured with a non-LED run) must first be subtracted out of the LED spectrum and a correction made for the presence of multiple photoelectron signals in the spectrum. For the Hamamatsu case, the gain is set such that the average charge value for an spe signal falls in a particular qVt channel.

However, the qVt method is quite time-consuming and disruptive to detector running, and in practice it has been found to be more efficient to set the gains "by-eye", by looking at the spe signals directly on an analog oscilloscope and setting the voltage such the the bright spe band falls at predetermined voltage level (making sure that the gain-setter is able to set a consistent level). LEDs are not necessary for this method.[1]

Relative phototube gains can be checked by measuring tankend singles rates; see references [87, 105].

[1]This method is effective only for EMI phototubes with well-defined spe signals; Hamamatsus require the qVt method for effective gain-setting.

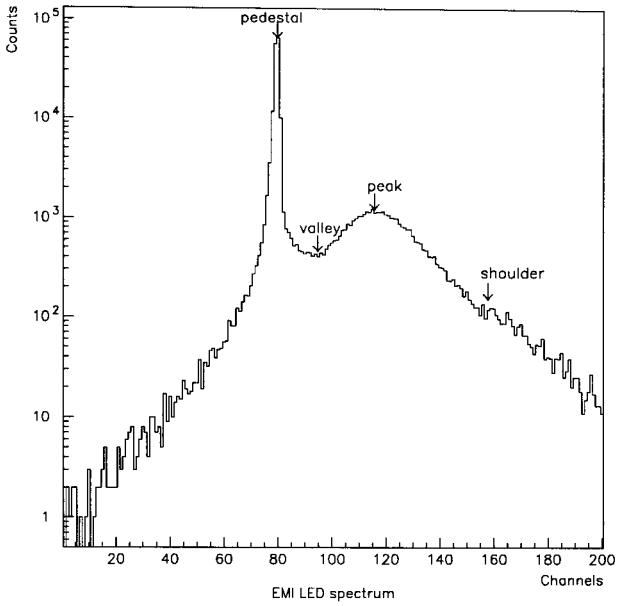

Figure B.1: An EMI single photoelectron qVt spectrum, showing pedestal, valley, peak and a slight second photoelectron shoulder to the right of the peak. The gain of the phototube is set so that the most likely spe pulse (out of the MACRO fanout) has a peak voltage of 4 mV.

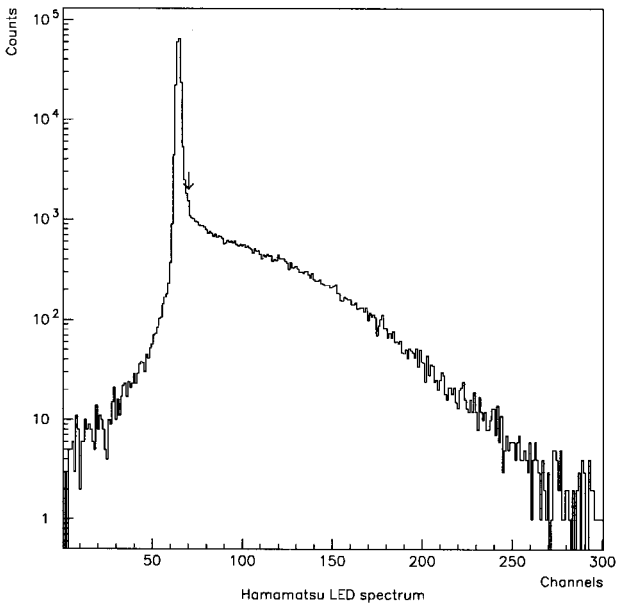

Figure B.2: Hamamatsu spe qVt spectrum, before pedestal subtraction.

Appendix C Gravitational Collapse Trigger Electronics

There are two main trigger systems in MACRO sensitive to GC neutrinos. Both do online compensation for light attenuation in the counter in order to provide a trigger based on energy deposition in the counter, independent of position in the counter. The PHRASE (Pulse Height Recorder and Synchronous Encoder) performs the attenuation correction in with an analog circuit, whereas the ERP (Energy Reconstruction Processor) performs the light attenuation correction digitally using lookup tables.

The two systems have fundamentally different approaches and so provide redundancy and independent checks of efficiency. This section will discuss in detail the features of these two trigger systems.

C.1 The PHRASE

The PHRASE trigger and waveform recording system was designed, built and installed by the members of the Pisa group of the MACRO experiment. It was designed with the detection of GC neutrinos as its main purpose, and so is optimized for recording low energy (7-20 MeV) events. Detailed descriptions of this circuit can be found in references [69] and [106].

A block diagram showing the general operation of the PHRASE circuit is shown in Figure C.1.

PHRASE modules are double-width Camac modules, each serving both sides of two counters, with signals arriving from the fanouts. At the front-end, the signal is split in two: one copy is used to make trigger decisions while the other copy goes to the PHRASE waveform digitization section (not to be confused with MACRO's 200 MHz waveform digitizer, Section 4.5.1).

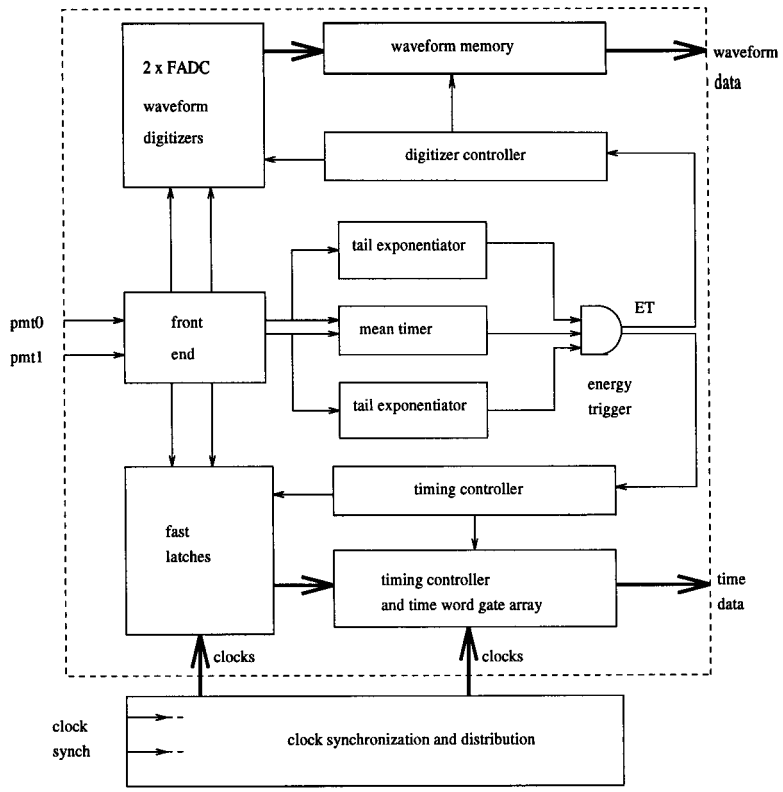

Figure C.1: Block diagram showing the organization of the PHRASE circuit.

C.1.1 The Energy Trigger

The PHRASE provides triggers for events at a constant energy threshold regardless of position of the hit within the counter (to first approximation.) This is done using an analog compensation for light attenuation within the counter. The analog light attenuation compensation exploits the nearly exponential nature of the light attenuation in the counter.

For an event which deposits energy E at a longitudinal counter position z (where $z = 0$ is the center of the counter), according to the simplest assumption of exponential light attenuation, the pulse heights a_L and a_R seen by the left and right side phototubes respectively are given by

$$a_L = kE \exp\left(-\frac{z}{\lambda}\right), \tag{C.1}$$

$$a_R = kE \exp\left(+\frac{z}{\lambda}\right), \tag{C.2}$$

where k is a constant, and λ is the attenuation length of the scintillator.

If the signals from each side of the counter arrive at times t_L and t_R and their peak heights are allowed to decay exponentially with time constant τ, starting from their times of arrival, the exponentially-decayed pulse heights on each side, A_0 and A_1, as a function of time t (for t greater than the arrival time of the pulse on that side) can be written

$$A_L = kE \exp\left(-\frac{z}{\lambda}\right) \exp\left(-\frac{t - t_L}{\tau}\right) \tag{C.3}$$

$$A_R = kE \exp\left(+\frac{z}{\lambda}\right) \exp\left(-\frac{t - t_R}{\tau}\right). \tag{C.4}$$

If the particle hits the counter at time t_0, then we can write

$$t_L = \frac{\frac{L}{2} - z}{v} + t_0 \tag{C.5}$$

$$t_R = \frac{\frac{L}{2} + z}{v} + t_0, \tag{C.6}$$

where v is the velocity of light in the counter and L is the length of the counter.

Substituting this expression this into equation C.3, we get for the decaying amplitudes A_L and A_R as a function of time,

$$A_L = kE \exp\left(-\frac{z}{\lambda}\right) \exp\left(-\frac{t - \frac{L}{2v} - \frac{z}{v} - t_0}{\tau}\right) \tag{C.7}$$

$$A_R = kE \exp\left(+\frac{z}{\lambda}\right) \exp\left(-\frac{t - \frac{L}{2v} + \frac{z}{v} - t_0}{\tau}\right). \tag{C.8}$$

To remove the position dependence in these equations, we can then choose the exponential decay time constant

$$\tau = \lambda / v. \tag{C.9}$$

In this case,

$$A_L = kE \exp\left(-\frac{t - \frac{L}{2v} - t_0}{\tau}\right) \tag{C.10}$$

$$A_R = kE \exp\left(-\frac{t - \frac{L}{2v} - t_0}{\tau}\right). \quad \text{(C.11)}$$

The "mean time", $t_{mt} = \frac{t_L + t_R}{2}$, can also be written, using equations C.5 as

$$t_{mt} = t_0 + \frac{L}{2v}, \quad \text{(C.12)}$$

so we can rewrite equation C.10 as

$$A_L = kE \exp\left(-\frac{t - t_{mt}}{\tau}\right) \quad \text{(C.13)}$$

$$A_R = kE \exp\left(-\frac{t - t_{mt}}{\tau}\right). \quad \text{(C.14)}$$

These last two equations mean that *at a fixed time t with respect to the mean time* the pulse heights on each side of the counter are *proportional to energy only* (provided $t > max(t_L, t_R)$).

What this means from a practical point of view is that if one adds an exponential tail with time constant τ given by equation C.9, and one generates a signal occurring at a fixed time with respect to t_{mt} (as per equation C.12, i.e. a time independent of longitudinal position of the event), then at that time the pulse heights A_L and A_R can be simply discriminated to yield a trigger that depends only on energy deposition in the counter and is independent of longitudinal position z. This is how the PHRASE circuit accomplishes its position-independent energy trigger (although the position independence is not perfect due to the deviation of the light attenuation function from a simple single exponential: trigger rates can vary by up to a few tens of percent as a function of position, with the non-uniformity being more pronounced near the ends of the counter).

The Mean Timer

In order to implement the energy trigger described in the preceding subsection, a signal occurring at the mean time t_{mt} is required: this signal is generated by the

"mean timer" part of the PHRASE circuit. The copy of the signal which goes to the trigger decision section is first amplified and discriminated. The discriminator thresholds can be set by Digital to Analog Converter (DAC) via Camac over a $0-100$ mV range; currently they are set at 30 mV. During the time that the input signals on each side are over threshold, the outputs of the discriminator are used to charge a linear ramp, such that

$$V_L = V_i - \alpha(t - t_L) \tag{C.15}$$

$$V_R = V_i - \alpha(t - t_R) \tag{C.16}$$

where V_i the initial voltage and α are constants, i.e. on each side, the output of the ramped charge is then proportional to the time since the leading edge of the input pulse. The outputs of the voltage ramps V_L and V_R for the two sides of the counter are summed resistively:

$$V_s = \frac{V_L + V_R}{2}. \tag{C.17}$$

The summed signal V_s is then discriminated. The time t_* at which V_s reaches a preset voltage threshold V_{th} is given by

$$t_* = \frac{V_i - V_{th}}{\alpha} + \frac{t_L + t_R}{2}. \tag{C.18}$$

The time t_* then equals the mean time $t_{mt} = \frac{t_L+t_R}{2}$ plus a constant offset $T_0 = (V_i - V_{th})/\alpha$, which can be set by choosing α, V_i and V_{th}.

The mean timer signal resets itself and both voltage ramps (with the minimum mean timer signal width being 20 ns). Therefore, if one side of the counter does not fire the discriminator, setting $V_R = V_i$ in the above equations gives a mean timer signal at time

$$t_{reset} = \frac{2(V_i - V_{th})}{\alpha} + t_L, \tag{C.19}$$

i.e. at time $2T_0$ after t_L. The value of $2T_0$ is set to be 80 ns, to allow comfortably

for light propagation time in the counter ($\sim$ 60 ns). This means that the effective coincidence window between the two ends of the counter in the PHRASE is $\sim$ 80 ns, in contrast to the ERP coincidence window of 270 ns (see Section C.2.2).[1]

The Tail Exponentiator

Next, to add an exponential tail to the signals on each side of the counter as in equation C.3, the signals go through the "tail exponentiator" part of the circuit: this is an emitter follower circuit driving a capacitor. After the peak of the signal, the emitter follower turns off and the capacitor discharges through a resistor. The time constant of the exponential discharge is chosen according to equation C.9: $\tau \sim$60 ns; the same value is used for all channels.

If, when the mean timer signal arrives, the exponential tails of both sides of the counter are above a particular threshold, an energy trigger (ET) is formed. It stays on for at least 20 ns and thereafter for as long as the pulses remain above threshold.

Figure C.2 shows a timing diagram demonstrating the relative timing of these signals.

C.1.2 PHRASE Waveform Digitization

When an energy trigger (ET) occurs, the pulse waveforms on each side of the counter are saved. The waveform digitizers used are special units developed at CERN [107], called GARBO and FATGA. The sampling rate is 100 MHz. The digitization occurs continuously and is stored in a circular buffer regardless of whether an energy trigger occurs. The data is stored in units of "blocklets": each blocklet contains 16 digitizations and covers a 160 ns time period. When an energy trigger occurs, the blocklet previous to the one being written when the ET occurred is saved after a time delay of 80 ns.

If an energy trigger extends over a period of time, blocklets up to a limit of 15 continue to be stored: this can cover a time period of from 2400 ns to 1 second,

[1] This difference has relevance for comparing background rates in the ERP and PHRASE; see Section 7.3.3.

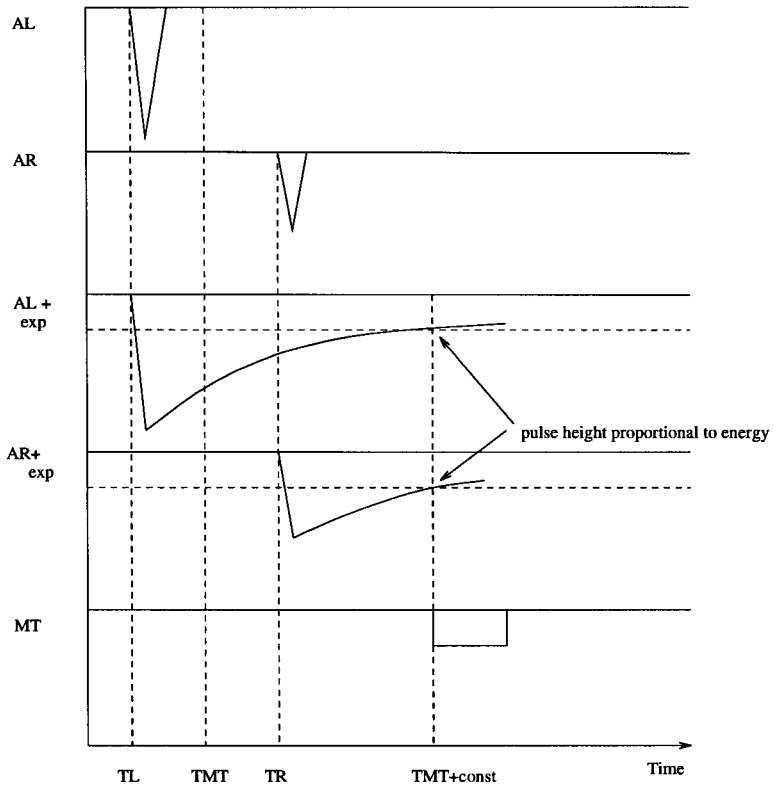

Figure C.2: Timing of PHRASE energy trigger signals.

depending on the number and length of the pulses digitized. Time words are also stored for each blocklet as described later in this section.

C.1.3 The Secondary Threshold

The energy threshold is effectively lowered to its secondary level of 1.5 MeV when an energy trigger occurs. This "special time" during which low energy pulses are recorded continues for 850 microseconds.

C.1.4 PHRASE Timing

A custom-built external clock unit distributes the same 100 MHz signal to all PHRASE modules. This external clock signal has been phase-locked to the laboratory's 10 MHz atomic clock signal (Section 4.5.3) since early 1996; before that the time measured by this clock was subject to drift of up to tens of milliseconds with respect to UTC over the course of a several-hour run (see Section 7.1.4).

The PHRASE makes use of a special custom gate array chip to manage the time words recorded for each set of digitizations. An internal 24-bit counter (the "GA clock") with a period of 80 ns is driven by the external clock: this gives the internal "GA time" with a rollover period of 80 ns $\times 2^{24} \sim 1.3$ seconds. The GA chip also accepts 24 bits of external "fast clock" time words.

The "fast clock" time words are derived from the external global 100 MHz signal, which drives 4-bit counters whose binary bits are converted to Gray code (allowing phase error free asynchronous latching). The bits in these fast counters are latched for each blocklet.

An additional 1.6 ns accuracy is obtained from the 10 ns period signal using the "phase-split clock" idea: two copies of the external 10 ns signal are delayed by 1.6 ns and 3.2 ns, so that the 10 ns period is divided into six equal periods each with a unique corresponding bit pattern (a Johnson code pattern). These three bits plus an additional connecting bit to resolve phase ambiguities are added to the four Gray code fast clock bits, giving a total of 8 fast clock bits per counter side per time word. There are three of these time words latched per blocklet: one for the left side of the counter, one for the right side, and a "flag" word (for the time of the blocklet change). A total of 24 bits of fast clock information per blocklet are latched at the time of blocklet change.

The 24 bits of GA clock information plus the 24 bits of fast clock information (total 48 bits, or 3 shortwords) are written into memory in the gate array, and are read out for each recorded blocklet.

In addition, the PHRASE "header time" is written for each "PHRASE" (set of blocklets, corresponding to one or several hits in one or more counters), which is a readout of the UT clock signal. The header time is recorded when each PHRASE is read out by the microVAX, and so it may incorporate delays of up to tens of milliseconds with respect to the actual times of the hits. The delays will depend on how many channels were read out as part of the PHRASE event.

All channels of the PHRASE system over the whole detector are driven by the same external 100 MHz clock. They are synchronized by a common SYNC signal

which sets all internal counters to zero at the beginning of each run.

In summary, the relative times of PHRASE events can be known to 1.6 ns. The absolute time of any PHRASE event with respect to UT must be reconstructed; Section 7.1.4 gives details of the procedure. For the time periods when the PHRASE external clock was phase-locked to the UTC signal, absolute times of PHRASE events can be known to $\sim$100 μs; when time fits to muons are required for absolute time reconstruction, the accuracy is not quite as good.

C.1.5 PHRASE Data Acquisition

In addition to the standard three data acquisition microVAXes, three microVAXes are dedicated to serving the PHRASE. The main acquisition VAX computer receives data from these microVAXes and combines them with the rest of the MACRO data to be stored on disk. Even when none of the other microVAXes are in acquisition, the PHRASE system is set up to be still able to run independently; see Section 4.5.4.

C.2 The ERP

The ERP system was designed, built and installed primarily by the University of Michigan group. It is a general-purpose ADC/TDC system which serves as MACRO's main scintillator muon trigger as well as a gravitational collapse trigger. It is described in references [69] and [108].

The ERP's GC event detection capabilities differ from the PHRASE's in three major respects: first, the light attenuation correction done to provide a consistent energy trigger across the counter is done in a digital way, via lookup tables (LUTs). Second, integrated charge and common-stop TDC timing information is saved, rather than waveforms. Finally, unlike the PHRASE, the ERP does not provide a threshold lowering feature and is not sensitive to the 2.2 MeV secondary γ ray following a neutrino-induced position created by the fusion of the neutron (equation 3.2) with a proton in the scintillator.[2]

[2]However, the ERP muon trigger causes readout of the 200 MHz waveforms for a 1 ms period

C.2.1 Overview of ERP Operation

A separate ERP system serves each supermodule, with the north and south faces of the detector having their own separate ERP systems. The ERP system comprises three main types of modules. Signals from the two sides of the counter go from the fanout into the *Sample and Hold* (S/H) modules, which, after a first level discrimination, integrate the signals and hold the charge and timing information. If there is a coincidence between the two sides of the counter, a "pretrigger" signal is formed and flash ADCs (FADCs) perform a preliminary digitization of the charge of the signals. The pretrigger and the FADC information is then sent on to the *Trigger Processor* (TP) module. The TP uses the FADC values for the two sides of the counter as inputs to a LUT whose values correspond to events of different energies. On the basis of the lookup result, if the FADC values correspond to an energy above a particular energy threshold, then a trigger condition is generated. There are two separate energy thresholds: a "high-level" or "muon-level" trigger is generated for event energies greater than about 12 MeV; a "low-level" or "GC-level" trigger is generated for event energies greater than about 6 MeV. The exact trigger thresholds are software programmable. Of course, as for the PHRASE case, the light attenuation correction is not perfect; the the graininess of the LUT bits makes for imperfect resolution for mapping the response. (As for the PHRASE case, there can be 20-30% rate variations along the length of the counter, especially near the ends of the counter.)

If the TP decides that a trigger condition has occurred, it sends a signal to the *Readout Supervisor* module. This module contains a high quality analog to digital converter (ADC), which digitizes the charge and timing information stored in the S/H modules. It puts the digitized information in separate buffers depending on whether high or low level triggers were formed. It also contains an internal clock of 8 microseconds resolution, and it stamps this time onto each event. The digitized information is then read by the main acquisition computer via Camac.

A block diagram showing the setup for one channel of ERP is shown in Figure C.3.

following the trigger; therefore, some secondary information could be retrieved for GC neutrino-induced positions with energy greater than about 12 MeV.

The separate subsystems of the ERP will be discussed in more detail in the following subsections.

C.2.2 The Sample and Hold Modules

The S/H modules serve as the "front end" of the ERP. The electronics are housed in standard VME modules and accommodate 4 ERP channels (1 counter/2 tankends per channel) each. There are eight sample-and-hold circuits per ERP channel (four per tankend). The signals from each side of the counter are divided into four paths and put through discriminators. One copy of the signal is discriminated and a one-shot is used to provide a 270 ns gate. This gate is used to form the coincidence between the two sides of the counter, and is also used as the integration gate for the pulse charge integrating sample-and-hold circuitry. This first-level coincidence between the two tankends' ADC signals is called the "minimum bias trigger" (MBT) or "pretrigger" and is used for two main purposes: it is used to notify the trigger processor that an event requires its attention, and it is used as a common stop for the TDCs.

The ADC pulse is delayed and then integrated on a S/H circuit during the gate. A copy of the signal attenuated by a factor of 10 is also integrated. At the same time, two additional copies of the tankend's signal are processed. They are discriminated by two different discriminators, one with one half the threshold of the other (the "high-threshold" and "low-threshold" TDC discriminators respectively). The low threshold TDC discriminator value is held at a constant fraction of ~ 0.5 of the high-threshold TDC discriminator value by a potentiometer. The signals cause a start of the constant current integrator S/H circuitry, such that the integrated charge is proportional to the time difference between the start signal and the stop signal. The MBT signal, delayed by 400 ns, is then used as the common stop for the TDC constant current integrators for all the channels of the ERP system.

The "ADC" (charge integration) and "TDC" (timing) discriminator levels are individually settable by a Camac-programmable DAC for each side of each counter. (The low threshold "TDC" discriminator level is always at a constant fraction of

the high threshold TDC discriminator level.) The TDC thresholds have been set uniformly across all channels at 130 mV for the horizontals and 65 mV for the verticals (with the low threshold TDC discriminators being set therefore at ~65/32.5 mV). The ADC thresholds vary from tankend to tankend according to typical signal sizes at individual tankends: the criterion is that a 5 MeV pulse at the opposite end of the counter must be large enough to fire the discriminator, so that the longer the attenuation length of the oil, the lower must the ADC threshold be set. (Attenuation lengths do vary from counter to counter; see Section 4.4.2). The ADC thresholds have been set in the range 70-130 mV. Due to the fact that for many channels the ADC thresholds are less than the TDC thresholds, some pulses which fire the ADC threshold will not fire the high-threshold TDC discriminator; for these events, low-threshold TDC information can be used for event time reconstruction.

After the input pulse signals have been integrated, the S/H channel waits for the Trigger Processor to decide whether or not a trigger condition occurred. If no trigger occurred, the S/H channel is reset after a time delay of 200 ns.

C.2.3 The Trigger Processors

The TP modules are single-width Camac modules, each one serving four counters.

When an MBT first-level coincidence signal arrives from a S/H channel, the corresponding TP channel goes to work. After a delay to allow the signals to "settle" on the S/H integrators, the TP looks at the S/H capacitors and digitizes the charge for each tankend with an FADC. The FADC has a nonlinear response to increase its dynamic range, with values ranging from 0 to 63:

$$d_{out} = \frac{V_{in}}{(BV_{in} + V_0)}, \tag{C.20}$$

where d_{out} is the output count value, V_{in} is the input voltage, and B and V_0 are constants.

The two FADC values are then used as addresses to a 64x64 lookup table (LUT). This LUT, which has been loaded into RAM memory via Camac, has bits set for

each grid point according to whether the energy corresponding to that particular combination of pulse heights (for a unique counter position) exceeds a pre-set energy threshold. If the looked-up bit is set to 1, the trigger condition is met.

A typical LUT, with the hatched region representing the bits set to 1, is shown in figure C.4.

In fact two different bits in the LUT looked-up word are used, corresponding to two different energy thresholds. If the highest order bit in the LUT is set to 1 for a given set of signals (addresses), an "Ehigh" or "muon" trigger condition occurs. If the next to highest order bit in the LUT is set to 1, an "Elow" or "GC" trigger condition occurs. If both of these bits are set to 0, no trigger occurs, and the S/H channels are reset.

The LUT bits are set by a combined method of using calibration information for the counter to determine which bits correspond to energies greater than threshold, and a trial and error method based on examining the rates as a function of counter position for each counter (see reference [109]). The Ehigh energy threshold is set to ~12 MeV and the Elow energy threshold is set to ~6–7 MeV.

If a trigger occurs, information is sent to the Readout Supervisor (RS), which must then deal with the readout of the relevant information.

C.2.4 The Readout Supervisor

The Readout Supervisor (RS) is a single-width Camac module. There is one RS module per supermodule, and it occupies the same Camac crate as the TP modules.

When the TP tells the RS that it has a trigger, the RS action depends on whether the trigger was an Ehigh or an Elow. For an Elow trigger, the RS finds the particular S/H channels which produced the Elow trigger and digitizes the charge and timing information saved on the S/H circuitry of that channel, using a high precision ADC. One count of this ADC corresponds to about 1 pC of charge, or about .17 ns of time. The RS addresses each S/H channel (box) sequentially to find which ones triggered. Eight ADC/TDC values are digitized per triggered channel, corresponding to the

eight S/H circuits (their abbreviations follow, for reference): the charge value for each side of the counter (ADC0 and ADC1), the attenuated charge values (ADCA0 and ADCA1), the high threshold time values (TDC0 and TDC1) and the low threshold time values (TDCL0 and TDCL1).

The RS also contains the 8 μs precision ERP internal clock. For each trigger that occurs, the 32 bits of the clock counter value are written into the data for that event and stored in the GC or muon buffers along with the ADC and TDC data words. Information about which channel fired is also encoded into the data. There are a total of 10 16-bit words stored per hit.

The digitized values are stored in the "GC buffer", an 8K memory buffer which can hold information for up to 818 hits. When this buffer is full, an "Eltrig" signal is produced which goes to the RS front panel and signals the acquisition to read out the GC buffer. The readout is performed via standard Camac commands.

For a Ehigh signal (a muon trigger), the procedure is similar, except that the digitized signals are put into the "muon buffer". In this case, *all* counters which produced a trigger, whether Elow or Ehigh, have their digitized values entered into the muon buffer. Unlike the situation for an Elow signal, an Ehigh signal is sent promptly to the RS front panel to signal the acquisition to read out the event promptly. While readout is going on, which takes tens of milliseconds, further muon triggers are inhibited by the computer busy signal. However, if Elow triggers occur during the computer busy time, they can still be added to the GC buffer during this time.

The dead time on each supermodule for each individual GC event stored is 250 μs (the time it takes for the RS to store the information in the GC buffer). A longer dead time occurs more rarely: a several hundred ms dead time is introduced for that supermodule (one sixth of the detector) for every buffer readout about once every 5-10 minutes. These dead times should cause negligible loss of signal for even a close supernova.

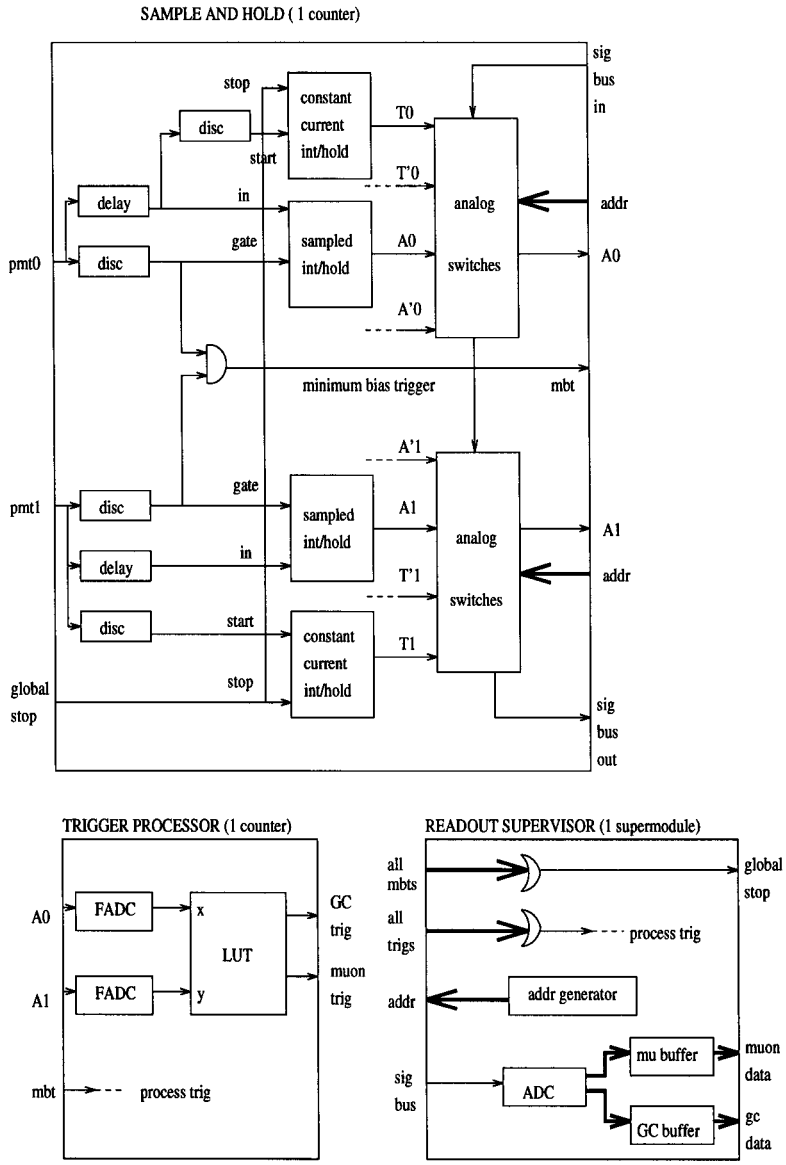

Figure C.3: Block diagram showing the organization of the ERP circuit. The labels are explained in the text. T0 and T'0 represent the high and low threshold TDC signals for side 0 of the counter (T1 and T'1 for side 1); A0 and A'0 represent the ADC and attenuated ADC signals for side 0 (A1 and A'1 for side 1).

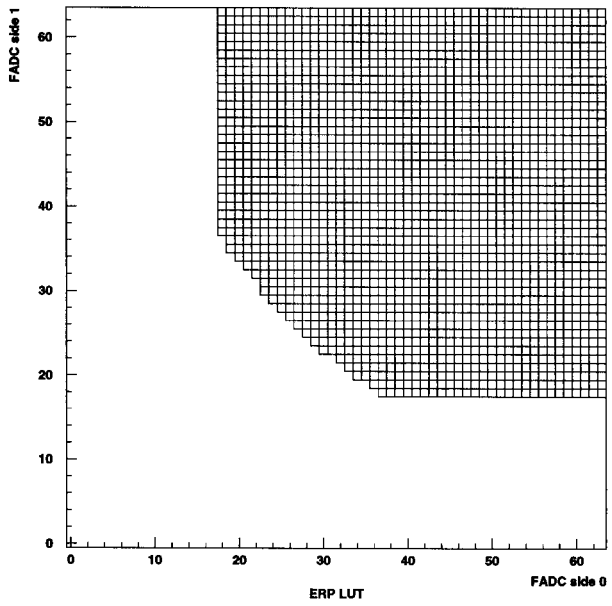

Figure C.4: An ERP lookup table. The axes represent the FADC values from each side of the counter. The hatched region indicates trigger bits that are set: events producing FADC pairs falling in the this region will cause energy triggers.

Appendix D FARFALLA DSTs

In a FARFALLA DST [92], information is written out event by event and organized into hierarchical tree structure made up of "nodes". A node is simply a data structure containing a predefined set of information; node structures and relationships can be custom-designed by the user. In a typical MACRO FARFALLA DST, an "event node" contains header information about a MACRO acquisition event, and "child" nodes associated with the event node contain information about the various MACRO triggers and equipments associated with the event.

The different kinds of data required for GC analysis are organized into custom FARFALLA nodes. For reference, types of FARFALLA nodes created for use in this analysis and their contents are listed here:

- **Raw ERP Nodes:** contain raw ERP information, i.e. counter number, ADC and TDC values, error codes, ERP clock times and UT times if available.
- **Reconstructed ERP Nodes:** in addition to raw ERP information, contain reconstructed ERP energies and positions. These are not used for the saved DST, and are only created temporarily in the final analysis steps.
- **PHRASE Nodes:** contain PHRASE counter number, sum pulse heights, UT times, reconstructed energies and positions.
- **"Other Trigger (otherTrig)" Nodes:** contain bit pattern of the trigger pattern register, i.e. information about which triggers fired for the event. Also contain wire hit, strip hit, and wire and strip track information.

Each of these FARFALLA node types are stored as "children" of FARFALLA event nodes. For the FARFALLA ERP and PHRASE node types, there is one node per hit (with each hit comprising information from both sides of the counter). For

the otherTrig node type, there is one otherTrig child per event node whenever the information is present.

In this thesis, an "event" refers to a FARFALLA event node with ERP, PHRASE or otherTrig child nodes associated with it within one 1 ms of one another. This is represented schematically in Figure D.1. This DST configuration allows convenient data analysis of matched and unmatched hits.

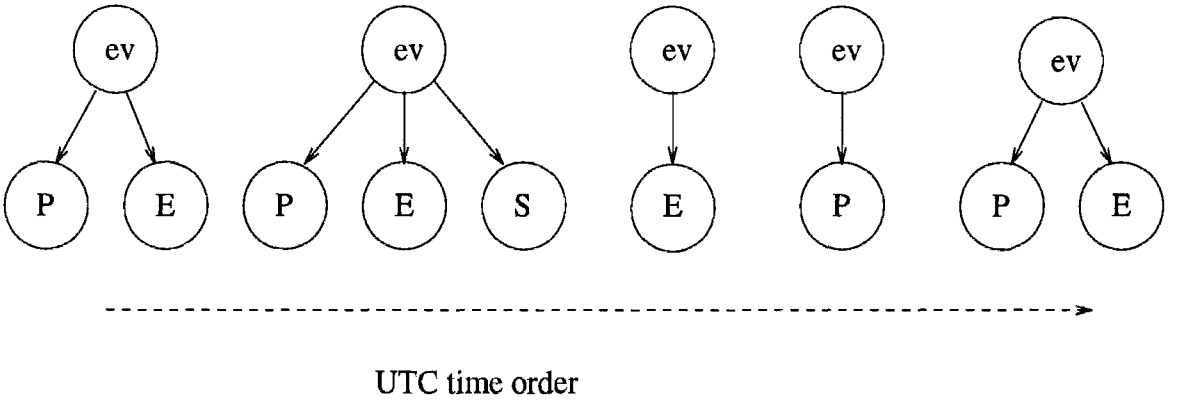

Figure D.1: FARFALLA DST structure for ERP/PHRASE GC DST. Each event node can have one or more children of types PHRASE(P), ERP(E) or other trig (S). Nodes with UT times within 1 ms of each other are gathered together as children of the same event node.

Appendix E Cuts on the ERP Data

Listed in this appendix are details about the specific cuts used on the ERP data.

E.1 ERP Hit Error Codes and Cut Tolerances

Table E.1 gives the meaning of each bit set in the ERP error word, and the cut tolerances used for the analysis of this thesis.

The first 6 bits refer to data quality and are set in the first step of FARFALLA DST production (Section 7.1.3). Bits 7 through 9 refer to the energy and position reconstruction and are not set until the final reconstruction step (see Section 7.1.5).

E.2 Cuts on the ERP Data

ERP hits are cut from the sample if they fail to satisfy the following requirements on both raw and reconstructed information (see Table E.1 for specific cut tolerances used):

E.2.1 Data Quality Cuts

1. The counter number must correspond to a real counter. The ERP "fake boxes", including the Bari box (Sections 5.2 and 8.2.3) are eliminated from the sample by this cut.

2. ADC and ADCA values must be between pedestal and overflow, for both sides of the counter.

3. Either TDCH or TDCL must be between pedestal and overflow for both sides of the counter.

4. There must be no ERP clock time reconstruction error.

Bit Set	Error	Tolerance
1	Error in decoded counter number or "fake box" counter number	1≤box≤84
2	Raw ADC error for either tankend: ADC<pedestal or ADC>overflow	ped<ADC<4095
3	Raw attenuated ADC error for either tankend: ADCA<underflow or ADCA>overflow	8<ADCA<4095
4	High threshold TDC error for either tankend: TDCH < underflow or TDCH > overflow	500<TDCH<4000
5	Low threshold TDC error for either tankend: TDCL < underflow or TDCL > overflow	500<TDCL<4000
6	ERP clock time reconstruction problem	$\Delta T < 200s$ between subsequent events in the SM
7	Bad calibration constants	ERPOK=0 and refractive index≥ 0
8	Reconstruction error: Photoelectrons<0 or calculated response correction<0 or TDC position out of counter	$pe > 0$ and $R > 0$ $\lvert z\rvert < 560$ cm
9	Reconstructed ADC position inconsistent with reconstructed TDC position	|ADCZ−TDCZ| < 200 cm

Table E.1: ERP hit error codes and cut tolerances.

5. The calibration constants must be good according to flags in the CALMOD database.

One minor deviation from the standard collaboration ERP software deserves note: if the TDCH information is over or underflow,[1] then the TDCL values are used for position reconstruction.[2]

[1]In general, TDC overflow refers to the situation where the TDC value is at or near maximum count (because it was never stopped), and TDC underflow refers to the case where the TDC value is zero or small (because it never got started).

[2]The reason for this is that the MBT discriminator thresholds can be lower than the TDCH thresholds, leading to some numbers of hits with TDCH values underflow. In principle, the TDCL information should be good for such hits although in practice sometimes it is not. See [109] for further discussion on these issues.

E.2.2 Reconstruction Cuts

1. The counter longitudinal position calculated from timing (TDCZ, from equation 5.1) must reconstruct to be geometrically inside the counter.

2. The position reconstructed from the ratio of pulse charges of the two sides (ADCZ from equation 5.10) must be consistent with timing position TDCZ.

Table E.2 shows, for a typical run (11834, livetime 6.5 hours) the numbers of events cut at each of the above steps, including the muon veto cut (Section 7.1.5) and a 10 MeV energy threshold cut.

Requirement to pass cut	Number of events before cut	Number of events remaining after cut
Counter number within range	387537	368107
ADC,ADCA within range	368107	365541
TDCH,TDCL within range	365541	359598
ERP time good	359598	359598
Calibration constants good	359598	359598
z reconstructs within counter	359598	224840
ADCZ/TDCZ consistent	224840	128924
Passes muon veto	128924	107550
$E > 10$ MeV	107550	1797

Table E.2: Effect of various cuts on numbers of events, for run 11834.

Appendix F Origin of the Multiples: Correlated or Uncorrelated?

F.1 Waveforms of the Multiples

Although the waveform study has shown that the multiple coincidences seen in the ERP but not the PHRASE are real pulses and not electronic noise of some kind, it is not immediately clear what the physical origin of these coincidence is. Are the double events correlated with each other or are they just accidental near end coincidences?

To shed light on this question, the time and position differences between the individual peaks of the multiple waveforms have been studied. However the deficiencies of the peak-counting algorithm make this study rather difficult: it is not easy to resolve peaks near each other in time which overlap partially. Figure F.1 shows a distribution of $\Delta T = t_1 - t_2$ for the multiples, where t_1 is the mean time of the peaks of the two sides of the highest energy peak, and t_2 is the mean time of the next highest energy event's peaks. This distribution is not as illuminating as could be desired: the ΔT values are spread out from -300 to 300 ns, as expected; however there is a deficit in the middle near $\Delta T = 0$, due to the inability to resolve peaks close to each other in time. However, this distribution is not clearly *inconsistent* with the pulses being uncorrelated accidentals.

Figure F.2 shows the distribution of ΔZ values for the multiple peaks, where $\Delta Z = z_1 - z_2$, z_1 is the timing position of the highest energy event, and z_2 is that of the second highest event. This plot shows that ΔZ is more likely to be long (near the counter length, positive or negative) than short, i.e. the two events in a multiple are likely to be both near the counter ends. This plot is consistent with the hypothesis that the individual events in the multiple event are uncorrelated accidentals.

The fact that ΔZ is likely to be $\sim$10 m (i.e. individual events both being near the

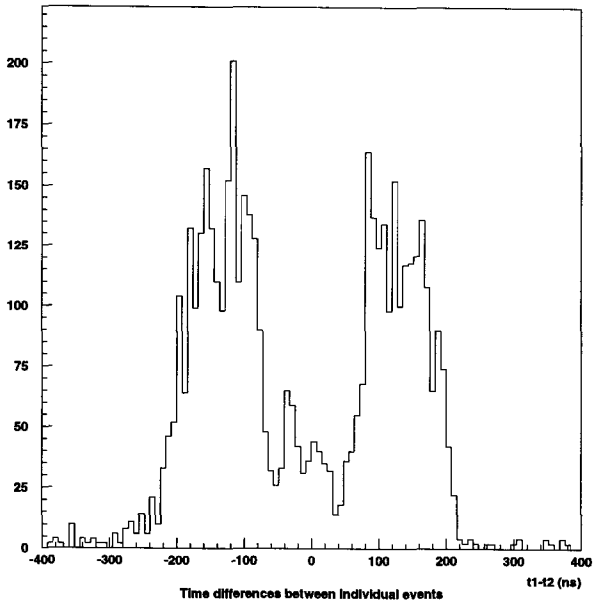

Figure F.1: Distribution of time differences between individual events of a multiple peaks.

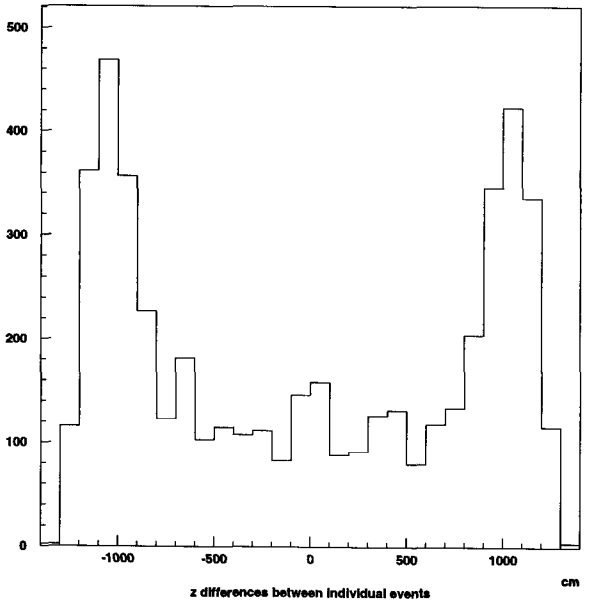

Figure F.2: Distribution of longitudinal position differences between individual multiple peaks of a multiple event.

ends of the counters) suggests that the events are indeed uncorrelated: it is unlikely that correlated particles can physically travel that far from each other on a ~300 ns timescale.

F.2 Expected Rate of Uncorrelated Accidentals

The expected rate R_{acc} of uncorrelated accidentals on the two sides of the counter occurring within coincidence window τ and reconstructing to energy $> E_{th}$ can be calculated approximately from

$$R_{acc} = 2 \int \int \tau f(v) f(u) du dv, \tag{F.1}$$

where u and v are pulse heights seen on the two sides of the counter, $f(u)$ is the differential pulse height spectrum, and the integral is over the region in $u - v$ space where $E(u, v) > E_{th}$ (analogous to the region in LUT space with the trigger bits set: see Figure C.4). The integral can be written:

$$R_{acc} = 2 \int_C^\infty F(g(u, E_{th})) \tau f(u) du, \tag{F.2}$$

where u is the pulse height on one side of the counter, $v = g(u, Eth)$ is a function which gives the pulse height v on the opposite side of the counter such that the reconstructed energy $E = E(u, v) = E_{th}$ (g can be calculated from the light attenuation response curve), the function $F(v)$ is the integral pulse height spectrum, i.e. the rate on one side of the counter of pulses with pulse height $> v$. The integral is over pulse heights u, where u goes from C, the minimum pulse height on the opposite end for an energy trigger, to infinity. The pulses are assumed to be uncorrelated.

This formula is an approximation for the rate of accidentals in the ERP to the extent that it neglects that the ERP actually integrates pulse charge for each side of the counter, and does not measure pulse heights. It also assumes equal photomultiplier gains on the two sides of the counter.

In addition, because response curves and singles rate spectra and LUTs do vary

quite significantly from counter to counter, it is important to measure explicitly the functions F and g for a particular counter before doing the calculation. The calculation was performed for a single MACRO counter for which the function $F(v)$ (the singles rates as a function of discriminator threshold) was measured carefully for each side of the counter. The response curve was measured by capturing muon pulses with a digital oscilloscope in order to determine a parameterization of the function g. Muons were also used to determine the energy scale for this function. These parameterized functions were substituted into equation F.2 (with appropriate corrections made for ERP front end response). The results gave an expected accidentals rate of 1.5 mHz at a 10 MeV reconstructed energy threshold, and an expected rate of 35 mHz at a 6 MeV energy threshold. These numbers are roughly consistent with the observed rates of ADCZ/TDCZ mismatches for the same counter during the time period when the measurements were made: 3 mHz at 10 MeV reconstructed energy threshold and 25 mHz at a 6 MeV energy threshold.[1] Therefore, it is plausible that the near-tankend events are uncorrelated accidental coincidences.

[1]Note that the rates of ADCZ/TDCZ mismatches can vary from a few mHz to a few tens of mHz from counter to counter. As would be expected, the rates tend to be higher for the attico counters, where the attenuation lengths are lower (see Section 4.4.2).

Appendix G Alarm Output

G.1 Phrase Monitor Alarm Output

G.1.1 Alarm Email Summary

The following shows an example of the email message mailed to the interested parties when a Phrase monitor alarm condition is met:

```
****************************************
WARNINGS FOR CLUSTER(S) DURING RUN009390
****************************************
25/02/1995-06:06:27.38:
PROBABILITY = 2.437717E-06; RATE(Hz) = 4.486111E-02
WARNING! BOX 6T14: BURST DURATION = 32 sec; MULTIPLICITY 11; E = 65 MeV
FULL CLUSTER INFORMATION: U.T.,BOX,DELAY(s),E(MeV)
   1)  25/02/1995-06:05:56.31   5C09(173)    0.0000     11.
   2)  25/02/1995-06:05:57.73   5E06(470)    1.4258     11.
   3)  25/02/1995-06:06:00.54   3C04(136)    4.2295     11.
   4)  25/02/1995-06:06:01.40   3C06(138)    5.0953     10.
   5)  25/02/1995-06:06:02.12   1W02(302)    5.8090     11.
   6)  25/02/1995-06:06:06.99   6T07(287)   10.6858     15.
   7)  25/02/1995-06:06:08.05   6B16( 96)   11.7468     11.
   8)  25/02/1995-06:06:14.17   6W11(391)   17.8672     11.
   9)  25/02/1995-06:06:15.69   6T09(289)   19.3777     12.
  10)  25/02/1995-06:06:26.04   5W02(366)   29.7317     10.
  11)  25/02/1995-06:06:27.38   6T14(294)   31.0688     65.
```

G.2 ERP Monitor Alarm Output

G.2.1 Text File

Various output is written to disk in the case of an alarm: an example of the text file written is given below.

```
 Run Number        11186
 Event Number   15732
 Number of bursts found            1
*****************************************************
 BURST FOUND IN SEVERAL SM
 Burst Number:            1
 Time Window:            6 seconds
 Total number of hits in the time interval:          38
 Number passing all cuts:            6
 SM combination number:          48
 Supermodules present for burst search:
 SM 1: N SM 2: N SM 3: N SM 4: N SM 5: Y SM 6: Y
 Background rate:   2.8130261E-02
 Multiplicity threshold:            5
 Poisson probability:   9.43E-07           6

ERP clock time (UT-corrected) of first hit in burst:      30409.7619
Julian Day of first hit in burst:    2450022.535685427
UT time of first hit in burst: 01-11-1995 00:51:23.2209097
```

Hit Number	Index	Box	Time	Energy	Position	Type
1	733	459	0.0000	10.80	405.56	8
12	383	513	0.9137	10.32	517.46	8
18	738	414	1.6285	10.19	550.46	8
21	388	568	1.9224	64.87	-114.74	0
22	389	516	2.1043	10.54	352.31	0
38	396	580	5.7041	17.51	77.50	8

```
*****************************************************
```

All hits during the time window of the burst:

Hit Number	Index	Box	Time	Energy	Position	Type	Cut
1	733	459	0.0000	10.80	405.56	8	
2	375	524	0.0616	5.04	-520.46	8	*
3	376	556	0.2761	0.00	-648.85	136	*
4	734	465	0.4108	0.00	569.02	128	*
5	377	564	0.5100	5.00	-219.82	8	*
6	735	498	0.6111	0.00	0.00	1	*
7	378	506	0.6121	39.16	-351.57	0	*
8	379	522	0.6121	46.55	-525.37	0	*
9	380	598	0.6121	0.00	0.00	25	*
10	381	571	0.6121	66.61	-228.12	0	*
11	382	572	0.6121	119.71	-214.84	0	*
12	383	513	0.9137	10.32	517.46	8	
13	384	577	1.1643	0.00	0.00	24	*

```
 14      736      419      1.1867      8.76      -459.91      0  *
 15      385      554      1.2053      0.00      -332.06    264  *
 16      737      432      1.4209      0.00       746.36    136  *
 17      386      575      1.5447      0.00      -756.57    136  *
 18      738      414      1.6285     10.19       550.46      8
 19      387      518      1.7432      7.05       -30.88      0  *
 20      739      428      1.8430      7.26      -443.92      0  *
 21      388      568      1.9224     64.87      -114.74      0
 22      389      516      2.1043     10.54       352.31      0
 23      740      443      3.3440      4.92       181.99      0  *
 24      741      472      3.4117      0.00      1125.77    136  *
 25      742      421      3.5486      3.34       406.14      8  *
 26      390      580      3.7264      0.00         0.00     24  *
 27      743      498      3.8814      0.00         0.00     25  *
 28      744      475      3.8814     46.33      -415.75      0  *
 29      745      476      3.8814     31.95      -382.99      0  *
 30      746      455      3.8814     40.42      -515.88      0  *
 31      391      598      3.8824      0.00         0.00      1  *
 32      747      419      3.9360      0.00      1356.86    128  *
 33      392      575      4.6357      0.00       781.55    136  *
 34      393      566      5.2371      0.00     -1680.55    136  *
 35      394      570      5.2664      0.00     -1562.25    136  *
 36      748      414      5.4884      3.74      -314.03      8  *
 37      395      539      5.6686      0.00       757.33    136  *
 38      396      580      5.7041     17.51        77.50      8
*********************************************************
```

Explanations of the information given in this file follow:

1. **Run number:** The run number the burst was found in.

2. **Event number:** The event number of the GC buffer in which the burst was found. For single-SM bursts, this is the event number of the first GC buffer containing the burst. For combined-SM bursts, this is the event number of the last GC buffer to be read out containing hits in the burst.

3. **Number of bursts:** The total number of (possibly overlapping) bursts found. For a combined-SM burst, only the "most significant" burst will be shown (see Section 8.2.3); for a single-SM burst, all overlapping bursts in the buffer will be listed.

4. **Burst number:** If multiple overlapping bursts were found, this is the number of the burst.

5. **Time window:** The time window in seconds for this burst.

6. **Total number of hits:** The total number of hits in the burst time interval, including both cut and non-cut hits.

7. **Number passing all cuts:** The number of hits in the burst time interval which passed all cuts, i.e. the hits which were used for the burst search. This is the multiplicity of the burst (+1).

8. **SM combination number:** This is an integer whose binary representation indicates which supermodules were present in the burst search, i.e. if bit 1 is set, SM 1 should have been present, etc. The information contained in the SM combination word is written out "longhand" in the next entry.

9. **Supermodules present:** For the combined burst search, this is the set of supermodules that were present in the combined buffer for this burst search. In this example, the burst was found in supermodules 4 and 5.

10. **Background rate:** This is the rate of good hits current at the time of the burst (the sum of the rates of the individual supermodules present for the search). This is the rate that was used to calculate the multiplicity threshold.

11. **Multiplicity threshold:** This is the multiplicity threshold that was used for the burst search.

12. **Poisson probability:** This is the Poisson probability of the burst given the background rate and multiplicity.

13. **ERP clock time:** This the "synchronized" ERP clock time of the first hit in the burst, i.e. it is the time in seconds since the beginning of the run, corrected to UT time using the muon UT time fit information (see Section 8.2.3).

14. **Julian Day:** This is the UT time of the first hit in the burst, expressed in Julian days.

15. **UT time:** This is the UT time of the first hit in the burst, expressed in standard format.

16. Next, a list of all the hits in the burst in UT time order is given. First, each hit in the burst which passed cuts and was included in the burst search is listed. The information given for each hit is:

    - *Hit Number:* This is the relative index of the hit in the combined buffer, starting from the first hit in the burst.
    - *Index:* This is the GC buffer index of the hit, i.e. the position of the hit in its GC buffer. Note that these indices are not necessarily sequential for hits in different SMs.
    - *Box:* The CALMOD counter number of the hit.
    - *Time:* The time of the hit in seconds referenced from the first hit in the burst.
    - *Energy:* The reconstructed energy of the hit, in MeV.
    - *Position:* The counter position of the hit (TDC position only) in cm; a TDC position of zero corresponds to the center of the counter.
    - *Type:* The error code of the hit (see Section 7.1.3).

    After the "good hits" are written out, each hit in the buffer (the individual SM or combined buffer) between the first and last hits of the burst has its information written out, including all hits that were cut. This "all hits" list has an additional "Cut" column. A "*" in this column indicates that the event was cut and not used for the burst search (for any reason).

    The hits which were cut are inspected as well as the hits which passed all cuts, to take into account the case of a very high rate burst for which a large fraction

of hits may have failed the time coincidence cut (see Section 8.2.3).

G.2.2 PAW Ntuple

A PAW [102] ntuple is also written to disk for an ERP monitor alarm. The contents of the ntuple are given in Table G.1:[1]

Name	Meaning
BOXNUM	CALMOD counter number
ERPTIME	UT-corrected ERP time in seconds (time since beginning of run)
X	TDC position
ENERGY	reconstructed energy in MeV
N	index of hit in buffer
TYPE	error code
CUT	= 1 if hit was cut = 0 if hit passed cuts

Table G.1: Ntuple contents.

G.2.3 Alarm Email

The summary string sent out as email to the mailing list and to the pager has the following format:

$A - B - C - D - E - F - G - H$

where:

A is the run number,

B is the event number of the GC buffer ,

C gives the supermodule number for a single-SM burst, or in the case of a burst in more than one SM it will be the letter C (for "combined"),

D gives the number of hits in the burst, including the first

E gives the time window, in seconds, of the burst,

[1]Note that the raw information for each hit is not saved and written to the ntuple due to program memory constraints.

F gives the index (within the GC buffer) of the first hit in the burst,

G is $-nint(\log_{10}(\mathcal{P}))$, where $\mathcal{P}$ is the Poisson probability of the burst based on the current background rate,

H is the multiplicity threshold (N_{pr}) used for this burst search i.e. there had to have been at least $H + 1$ counts in the time window (including the first) in order for an alarm to have been triggered.

Appendix H Glossary

This glossary contains terms used in this thesis which may be unfamiliar to many readers. These terms are defined in the text but are compiled here for the reader's convenience. Included are MACRO-specific terms used within the collaboration (or invented specifically for this analysis) and also standard astrophysical terms used in the thesis which may be unfamiliar to physicists. In addition, some commonly used acronyms and symbols are given.

A: ADCZ/TDCZ cut value, such that an event is retained if $|ADCZ - TDCZ| < A$ (Sections 7.1.5, 7.3.4).

Active mass: The total mass of scintillator viewed by the electronics at any given time (Section 7.5.1).

ADC: Analog to Digital Converter.

ADC0: ERP raw unattenuated ADC value for side 0 of the counter (Section C.2.2).

ADC1: ERP raw unattenuated ADC value for side 1 of the counter (Section C.2.2).

ADC0A: ERP raw attenuated ADC values for side 0 of the counter (Section C.2.2).

ADC1A: ERP raw attenuated ADC values for side 1 of the counter (Section C.2.2).

ADCZ: Counter longitudinal position from pulse height ratio (equation 5.10).

Alarm condition: A condition set in the monitor programs if a burst is found with Poisson probability $< 10^{-5}$; various actions are then taken (Sections 8.2.3, 8.1.2, 8.3).

Attenuated ADC: See ERP attenuated ADC.

Attenuated reference ADC: The ADC digitizing the attenuated reference phototube signal (Sections 4.4.2, 5.2.3).

Attenuated reference phototube: For the ERP laser pedestal calibration, the phototube looking at attenuated laser light (Sections 4.4.2, 5.2.3).

Attico: The upper part of the detector, including the top horizontal layer and the planes of upper six vertical counters. (Section 4.4.2).

Attico verticals: The vertical counters between the central and top horizontal layers (Section 4.4.2).

Bari box: ERP fake box with the Bari trigger as input (Section 8.2.3).

Bari trigger: Streamer tube 4-plane muon trigger (Section 4.5.2).

Blocklet: A set of 16 digitizations in a PHRASE waveform (Section C.1.2).

Box: A scintillator counter (Appendix A).

Breakout: The time at which a supernova shock wave hits the neutrinosphere, when neutrinos formed in the wake of the shock are free to stream out. Corresponds to a burst in the neutrino luminosity (Sections 2.2.6, 3.1.2).

Burst: A grouping of hits in time within a predefined time window (Section 6.3), known as a "cluster" in Pisa analyses.

Burst consolidation: For the ERP monitor, the check of whether alarms have already been sent out for a burst in a given time period (Section 8.2.3).

Burst Search: A search for clusters of hits in time among selected events, by opening time windows for each hit and counting subsequent hits within the time window. For each burst search, a particular data sample (e.g. ERP only), energy threshold and time window is chosen (Section 6.3).

CALMOD: Standard MACRO software package for storing and manipulating calibration constants (Section 4.6.2).

Charge respone function: Function relating PHRASE sum pulse height to input pulse charge (also known as the linearization function) (Section 5.3.2).

Coincidence: PHRASE hits in coincidence with other hits within 320 ns or in coincidence with streamer tube triggers within 5 μs (Section 8.1.1).

Combined searches: For the offline data analysis described in Chapter 7, event-wise AND and event-wise OR burst searches performed for runs and active masses were both the ERP and the PHRASE were running (Section 7.4.1).

Computer busy: Signal produced by the acquisition microVAXes while they are processing an event; used as an inhibit for the ERP muon trigger (Sections 4.5.4, C.2.4).

CSPAM: Muon trigger for coincidence within a 1 μs window between planes of scintillator (Section 4.5.1).

DAC: Digital to Analog Converter.

Delayed explosion: Explosion for which a slow mechanism, such as neutrino heating, revives the shock wave and powers the supernova explosion (Sections 2.2.7, 3.1.3).

Distance sensitivity: The distance d_{max} such that a burst at that distance would exceed multiplicity threshold with 90% probability (Section 6.3.2).

DREAM: Standard MACRO collaboration software package (Section 4.6.1).

DST: Data Summary Tape.

Effective index of refraction: n_{eff}, such that the velocity of light in the counter is c/n_{eff}, taking into account optical properties of the scintillator and the various ray paths from the site of energy deposition to the phototube (Section 5.2.2).

Ehigh: See ERP muon trigger.

Elow: See ERP GC trigger.

ERP: Energy Reconstruction Processor (Sections 4.5.1, C.2).

ERP attenuated ADC (ADC0A, ADC1A): The ERP ADC value for input signals attenuated by a factor of 10 (Section C.2.2).

ERP clock: Clock internal to each ERP Readout Supervisor with a 8 μs period (Section C.2.4). There is a separate ERP clock for each supermodule.

ERP time: Time measured with the ERP internal clock (Section C.2.4).

ERP cuts: Cuts on raw and reconstructed ERP information described in Sections 7.1.3 and 7.1.5.

ERP gain: ERP "photoelectrons" per ADC count (Section 5.2.3).

ERP GC trigger: ERP hit satisfying the lower level energy threshold ($\sim$ 7 MeV), stored in the GC buffer which is read out every 5-10 minutes (Section C.2).

ERP monitor: ERP spy software for online monitoring for GC bursts (Section 8.2).

ERP muon trigger: ERP hit satisfying the higher level energy threshold ($\sim$ 12 MeV), stored in the muon buffer which is read out promptly and stamped with a UT time (Section C.2).

ERP-only search: A burst search among ERP events only (Section 7.4.1).

ERP pedestal: ERP ADC counts at zero light, measured using the laser (Section 5.2.3).

ERP "photoelectrons": *pe* calculated according to 5.8, proportional to the number of photoelectrons for the phototube.

ERP unattenuated ADC (ADC0, ADC1): The ERP ADC value for unattenuated input signals (Section C.2.2).

ET: Energy Trigger for the PHRASE (Section C.1.1).

Explosion: The process by which the star's material gets disrupted after the bounce of the collapsing core (Sections 2.2.7, 3.1.3).

Event: For the purpose of the data analysis in this thesis, a group of hits associated within 1 ms of each other.

Event node: FARFALLA data structure containing information for one event. Each event node generally contains child nodes containing ERP, PHRASE, trigger or streamer tube information, associated within 1 ms (Section D).

Event-wise AND: A burst search among events present in both the ERP and the PHRASE, performed for time periods and active masses when both the ERP and the PHRASE were running (Section 7.4.1). Part of the combined search.

Event-wise OR: A burst search among events present in either the ERP or the PHRASE, performed for time periods and active masses when both the ERP and the PHRASE were running (Section 7.4.1). Part of the combined search.

FADC: Flash-ADC. For the ERP, FADCs are used to digitize input signals to use as addresses to the LUTs (Section C.2). The PHRASE uses FADCs for its waveform digitization (Section C.1).

Fake box: Spare channel in the ERP accepting non-phototube signals for calibration purposes (Section 5.2.2) or muon veto (Section 8.2.3).

FARFALLA: A C++ software package used for DST production (Section D), making use of hierarchical data structures.

FARFALLA node: Data structure used in FARFALLA (Section D).

Fraction up-time: The fraction of time that at least one system was viewing at least one supermodule of active mass (Section 7.5.2).

Gate Array (GA) clock: PHRASE internal clock with 80 ns period driven by global clock (Section C.1.4).

GC: Gravitational Collapse.

GC_ANALYSIS: ERP monitor detached process for analysis and burst search performance (Section 8.2.2).

GC buffer: 818-hit buffer containing ERP GC trigger information (Section C.2).

Global PHRASE clock: PHRASE external clock with 10 ns period driving all PHRASE modules (Section C.1.4).

Header time: UT clock time stamped on PHRASE events at readout (Section C.1.4).

High threshold TDC values (TDC0, TDC1): The ERP TDC values corresponding to the higher discriminator threshold (Section C.2.2), typically 100 mV for horizontal counters.

Horizontal counter: Counter included in one of the horizontal layers of scintillator (Section 4.4.1).

Hit: For the PHRASE, refers to one primary-threshold triggered waveform pulse in one counter, usually corresponding to a single muon or radioactivity event. For the ERP, refers to one signal (two-end coincidence) in one counter, corresponding to one set of digitizations.

Inverse beta decay: For GC neutrino studies, the capture of an antineutrino on a proton, equation 3.2.

Large Magellanic Cloud (LMC): A small galaxy which is part of the Local Group of galaxies gravitationally bound to our own galaxy. Site of SN1987A, 50 kpc away (Section 3.4).

LED: Light Emitting Diode.

Light curve: Supernova luminosity as a function of time (Chapter 2).

Linearization function: In Pisa analyses, PHRASE charge response function relating sum pulse height to pulse charge (Section 5.3.2).

Liquid Scintillator Counter Monitor (LSCM): PHRASE data quality monitoring software (Section 8.1.1).

LMC: Large Magellanic Cloud.

Lone ERP: An ERP hit with no PHRASE partner in the same counter in the same event (Section 7.3).

Lone PHRASE: An PHRASE hit with no ERP partner passing cuts in the same counter in the same event (Section 7.3).

Lookup Table (LUT): For the ERP, a digital table in which trigger information is stored. Pulses from the two sides of a counter are digitized with FADCs and the values used as x-y inputs to the LUT in order to make a trigger decision (Section C.2.3).

Low threshold TDC (TDC0L, TDC1L) values: The ERP TDC values corresponding to the lower discriminator threshold (Section C.2.2), typically 50 mV for horizontal counters.

LSC: Liquid Scintillator Counters.

LSCM: Liquid Scintillator Counter Monitor (Section 8.1.1).

Main acquisition: Data acquisition serving all of MACRO's electronics, with the exception of the PHRASE (Section 4.5.4).

Match: Hit present in both the ERP and the PHRASE in the same counter within 1 ms (Section 7.3).

MBT: Minimum Bias Trigger in the ERP (Section C.2.2), also referred to as the pretrigger.

MicroVAX: Computer performing data acquisition services for a group of two supermodules; often refers to the two supermodules themselves (Section 4.5.4).

Minimum Bias Trigger (MBT): The ERP signal from the Sample and Hold modules indicating a coincidence within 270 ns between the two ends of a counter. The delayed MBT is also used as the TDC common stop (Section C.2.2).

Mismatch: A hit present in either the ERP or the PHRASE but not the other trigger circuit, i.e. a lone ERP or a lone PHRASE (Section 7.3).

MU: Mr. Universe.

Multiple event: A waveform with two or more peaks present, indicating two or more particles in the waveform (Section 7.3.3).

Multiplicity: The number of hits in a given predefined time window following an event (Section 6.3.1).

Multiplicity threshold: The multiplicity required in order for a burst to be considered a candidate (Section 6.3.1). Two levels of multiplicity thresholds, "preliminary" (N_{pr}) and "ten-year" (N_{10yr}) are used.

Muon buffer: Buffer containing ERP muon trigger information (Section C.2).

Neutrinosphere: The spherical shell at radius r_ν, separating regions which are opaque to and transparent to neutrinos, i.e. the radius at which the density of matter is such that the distance between that radius and infinity is one neutrino interaction mean free path. For $r < r_\nu$, a neutrino is trapped, whereas for $r > r_\nu$ a neutrino is free to propagate outward (Section 2.2.4).

Neutrino flash: See Breakout.

Neutronization burst: See Breakout.

otherTrig nodes: FARFALLA nodes containing streamer tube and trigger pattern information (Section D).

pe: Photoelectrons (see ERP photoelectrons).

Peak: An individual waveform pulse, corresponding to one particle's energy deposition (Section 7.3.3).

PHRASE: Pulse Height Recorder and Synchronous Encoder (Sections 4.5.1, C.1).

PHRASE acquisition: MicroVAXes and acquisition system serving the PHRASE system, independent of the main acquisition (Section 4.5.4).

PHRASE monitor: PHRASE spy software for online monitoring for GC bursts (Section 8.1.1).

PHRASE nodes: FARFALLA nodes containing reconstructed PHRASE information (Section D).

PHRASE-only search: A burst search among PHRASE events only (Section 7.4.1).

PMT: Photomultiplier Tube.

Preliminary candidate: A burst with a multiplicity exceeding multiplicity threshold N_{pr}, such that the Poisson probability in the time window is less than 10^{-5} (Section 6.3.1).

Pretrigger: ERP Minimum Bias Trigger (MBT) (Section C.2.2).

Primary threshold: $\sim$ 7 MeV energy threshold for the PHRASE; events exceeding it cause lowering of the energy threshold to the secondary level (Sections 4.5.1,C.1).

Primary: Event satisfying the primary PHRASE threshold (Sections 4.5.1,C.1).

Population I stars: Young, massive, hot and bright stars, found in the arms of spiral galaxies (Section 2.1.)

Population II stars: Older, low mass stars, found in the disks of spiral galaxies (Section 2.1).

Prompt explosion: Explosion for which the shock wave itself powers the disruption of stellar matter (Sections 2.2.7, 3.1.3).

Raw ERP nodes: FARFALLA nodes containing raw ERP information (Section D).

RCDGC processes: ERP monitor processes dedicated for GC buffer collection (Section 8.2.2).

RCD libraries: Software for online spy monitoring (Section 8.2.2).

Readjustment: Procedure for adjusting standard ERP pedestals and gains so that ERP and Phrase energies are comparable (Section 7.2.3).

Readout Supervisor (RS): ERP system module which performs high-quality digitization and readout of signals stored in the Sample and Hold ERP modules (Section C.2.4).

Reconstructed ERP nodes: FARFALLA nodes containing raw and reconstructed information (Section D).

Reference phototube: See attenuated reference phototube.

Reference ADC: See attenuated reference ADC.

Response function: Function describing the light attenuation in a counter, i.e. relative light as a function of longitudinal distance of the source from the phototube (Sections 5.2.3, 5.3.2).

RS: Readout Supervisor.

Run-AND: Periods of time for which both the ERP and the PHRASE were operated on the active masses under consideration, for which combined searches can be performed (Section 7.4.1). Strictly, it is an "active-mass AND" since only part of the active mass of the detector may have a combined search done for any given time period.

Sample and Hold (S/H): The ERP front-end circuit, which performs a first level discrimination, integrates the signals and holds charge and timing information for later readout by the Readout Supervisor (Section C.2.2).

Secondary threshold: $\sim$ 1.5 MeV energy threshold for the PHRASE; events exceeding the primary threshold cause lowering of the energy threshold to the secondary level for a time period of 850 μs (Sections 4.5.1,C.1).

Secondary: Event satisfying the secondary PHRASE threshold (Sections 4.5.1,C.1).

SENTINEL: ERP monitor process for management of the RCDGC and GC_ANALYSIS processes (Section 8.2.2).

Separate searches: ERP-only and PHRASE-only burst searches (Section 7.4.1).

S/H: Sample and Hold.

Single: An unvetoed hit (Section 7.1.5) (term used in the Pisa analyses).

Single peak: A hit with a waveform with a single peak, presumably corresponding to a single particle (Section 7.3.3).

Single supermodule burst search: For the ERP monitor, the burst search among events in the GC buffers from individual supermodules (Section 8.2.3).

Full-detector search: For the ERP monitor, the burst search among hits in the GC buffers from all supermodules combined (Section 8.2.3).

SNM: Supernova Monitor (see PHRASE monitor).

Sparks: For the ERP monitor, any burst with more than half of the hits in a single counter, not necessarily corresponding to physical sparking in a tankend (Section 8.2.3).

spe: Single Photoelectron.

Special time: The time during which the PHRASE secondary threshold is lowered in order to accept fusion γ rays (Section C.1.3).

sph: Sum Pulse Height.

"Spy" process: Online monitoring process which examines data at a lower priority than the main data acquisition. Efficiency for data collection may be less than 100% but efficiency with which data is written to disk is not compromised (Chapter 8).

Standard calibrations: ERP calibration constants generated by the University of Indiana group (Section 5.2).

ST: Streamer Tubes.

Sum pulse height (sph): For the PHRASE, the sum of the individual digitizations of a waveform (Section 5.3.1).

Supermodule: One sixth of the MACRO detector, instrumented to operate alone if necessary (Section 4.4.1).

Supernova: A highly energetic explosion resulting in the disruption of a star's matter (Chapter 2).

Supernova Monitor (SNM): The PHRASE monitor software (Section 8.1.1).

Synchronization loss: An error condition for the PHRASE, for which a problem occurred with the PHRASE global clock synchronization (Section 8.1.4).

Tank: A scintillator counter (Appendix A).

Tankend: End chamber of a counter containing the phototubes, separated from the main scintillator and filled with clear mineral oil (Section 4.4.2).

TDC: Time to Digital Converter.

TDC0: ERP raw high threshold TDC value for side 0 of the counter (Section C.2.2).

TDC1: ERP raw high threshold TDC value for side 1 of the counter (Section C.2.2).

TDC0L: ERP raw low threshold TDC value for side 0 of the counter (Section C.2.2).

TDC1L: ERP raw low threshold TDC value for side 1 of the counter (Section C.2.2).

TDCZ: Counter longitudinal position from timing (equation 5.1)

Ten year candidate: A burst with a multiplicity exceeding N_{10yr}, such that the probability of a fluctuation of that multiplicity is less than 0.001 in 10 years, assuming uncorrelated time windows (Section 6.3.1).

Thallium line method: Method of setting the low energy scale for the PHRASE by using the change in slope of the PHRASE secondary energy spectrum to define the location of the 2.2 MeV ^{208}Tl γ line (Section 5.3.2).

Timewalk: Correction to measured pulse times due to the effect of different relative threshold-crossing times for different pulse sizes (Sections 5.2.2, 5.3.1).

Time window: The time window for counting hits for determining burst multiplicity for a burst search (Section 6.3).

TP: Trigger Processor.

Tracks: Streamer tube tracks corresponding to muons reconstructed by the DREAM software package (Sections 4.5.2, 4.6.1). Tracks are reconstructed in both wire and strip views.

Trigger Processor (TP): Modules in the ERP system which digitize the signals from the two ends of a counter with an FADC and use FADC the values as addresses for a LUT to determine whether or not a trigger condition should be set (Section C.2.3)

Type I supernova: Supernova with no hydrogen lines and a peaked light curve. The standard model is a white dwarf which has lost its hydrogen envelope and accreted matter from a companion until a thermonuclear explosion is ignited (Section 2.1).

Type II supernova: Supernova with hydrogen lines in its spectrum, and typically a broad light curve. The standard model is a gravitational collapse event (Section 2.1).

Unattenuated reference ADC: The ADC digitizing the unattenuated reference phototube signal (Sections 4.4.2, 5.2.3).

Unattenuated reference phototube: For the ERP laser pedestal calibration, the phototube looking at unattenuated laser light (Sections 4.4.2, 5.2.3).

Unvetoed hit: An hit which passes the muon veto cuts described in Section 7.1.5. The term "single" is used in Pisa analyses to refer to unvetoed hits.

Vertical counter: Counter included in one of the vertical layers of scintillator (Section 4.4.1).

VXMACB: MACRO's auxiliary acquisition computer, which runs data monitoring jobs and the ERP monitor software (Section 4.5.4).

WFD: Waveform Digitizer.

Waveform Digitizer (WFD): MACRO's custom 200 MHz waveform digitizer system (Section 4.5.1), not to be confused with the PHRASE internal 100 MHz waveform digitizer.

UT clock Laboratory atomic clock signal with 100 ns period and 100 μs accuracy with respect to Universal Time (Section 4.5.3).

z: Counter longitudinal position, measured from center of counter.

Z: Distance from tankend along tank.

Appendix I The MACRO Author List

The MACRO Collaboration

M. Ambrosio[12], R. Antolini[7], G. Auriemma[14,a], R. Baker[11], A. Baldini[13], G. C. Barbarino[12], B. C. Barish[4], G. Battistoni[6,b], R. Bellotti[1], C. Bemporad[13], P. Bernardini[10], H. Bilokon[6], V. Bisi[16], C. Bloise[6], C. Bower[8], S. Bussino[14], F. Cafagna[1], M. Calicchio[1], D. Campana[12], M. Carboni[6], M. Castellano[1], S. Cecchini[2,c], F. Cei[13,d], P. Celio[14],V. Chiarella[6], A. Corona[14], S. Coutu[11], G. De Cataldo[1], H. Dekhissi[2,e], C. De Marzo[1], I. De Mitri[9], M. De Vincenzi[14,f], A. Di Credico[7,14], O. Erriquez[1], C. Favuzzi[1], C. Forti[6], P. Fusco[1], G. Giacomelli[2], G. Giannini[13,g], N. Giglietto[1], M. Grassi[13], A. Grillo[7], F. Guarino[12], P. Guarnaccia[1], C. Gustavino[7], A. Habig[8], K. Hanson[11], A. Hawthorne[8], R. Heinz[8], J. T. Hong[3], E. Iarocci[6,h], E. Katsavounidis[4], E. Kearns[3], S. Kyriazopoulou[4], E. Lamanna[14], C. Lane[5], D. S. Levin[11], P. Lipari[14], R. Liu[4], N. Longley[4], M. J. Longo[11], Y. Lu[15], G. Ludlam[3], G. Mancarella[10], G. Mandrioli[2], A. Margiotta-Neri[2], A. Marini[6], D. Martello[10], A. Marzari-Chiesa[16], M. N. Mazziotta[1], D. G. Michael[4], S. Mikheyev[7,i], L. Miller[8], M. Mittelbrunn[5], P. Monacelli[9], T. Montaruli[1], M. Monteno[16], S. Mufson[8], J. Musser[8], D. Nicoló[13,d], R. Nolty[4] C. Okada[3], C. Orth[3], G. Osteria[12], O. Palamara[10], S. Parlati[7], V. Patera[6,h], L. Patrizii[2], R. Pazzi[13], C. W. Peck[4], S. Petrera[10], N. D. Pignatano[4], P. Pistilli[10], V. Popa[2,l], A. Rainó[1], J. Reynoldson[7], F. Ronga[6], A. Sanzgiri[15], F. Sartogo[14], C. Satriano[14,a], L. Satta[6,h], E. Scapparone[2], K. Scholberg[4], A. Sciubba[6,h], P. Serra-Lugaresi[2], M. Severi[14], M. Sitta[16], P. Spinelli[1], M. Spinetti[6], M. Spurio[2], R. Steinberg[5], J. L. Stone[3], L.R. Sulak[3], A. Surdo[10], G. Tarlé[11], F. Tassoni[14], V. Togo[2], V. Valente[6], C. W. Walter[4] and R. Webb[15]

1. Dipartimento di Fisica dell'Università di Bari and INFN, 70126 Bari, Italy
2. Dipartimento di Fisica dell'Università di Bologna and INFN, 40126 Bologna, Italy
3. Physics Department, Boston University, Boston, MA 02215, USA

4. California Institute of Technology, Pasadena, CA 91125, USA

5. Department of Physics, Drexel University, Philadelphia, PA 19104, USA

6. Laboratori Nazionali di Frascati dell'INFN, 00044 Frascati (Roma), Italy

7. Laboratori Nazionali del Gran Sasso dell'INFN, 67010 Assergi (L'Aquila), Italy

8. Depts. of Physics and of Astronomy, Indiana University, Bloomington, IN 47405, USA

9. Dipartimento di Fisica dell'Università dell'Aquila and INFN, 67100 L'Aquila, Italy

10. Dipartimento di Fisica dell'Università di Lecce and INFN, 73100 Lecce, Italy

11. Department of Physics, University of Michigan, Ann Arbor, MI 48109, USA

12. Dipartimento di Fisica dell'Università di Napoli and INFN, 80125 Napoli, Italy

13. Dipartimento di Fisica dell'Università di Pisa and INFN, 56010 Pisa, Italy

14. Dipartimento di Fisica dell'Università di Roma "La Sapienza" and INFN, 00185 Roma, Italy

15. Physics Department, Texas A&M University, College Station, TX 77843, USA

16. Dipartimento di Fisica Sperimentale dell'Università di Torino and INFN, 10125 Torino, Italy

a Also Università della Basilicata, 85100 Potenza, Italy

b Also INFN Milano, 20133 Milano, Italy

c Also Istituto TESRE/CNR, 40129 Bologna, Italy

d Also Scuola Normale Superiore di Pisa, 56010 Pisa, Italy

e Also Faculty of Sciences, University Mohamed I, B.P. 424 Oujda, Morocco

f Also Dipartimento di Fisica, Università di Roma III, Roma, Italy

g Also Università di Trieste and INFN, 34100 Trieste, Italy

h Also Dipartimento di Energetica, Università di Roma, 00185 Roma, Italy

i Also Institute for Nuclear Research, Russian Academy of Science, 117312 Moscow, Russia

l Also Institute for Atomic Physics, 76900 Bucharest, Romania